OPTICAL PROCESSING USING PHOTOREFRACTIVE CRYSTALS

Thesis by

Jeffrey Winston Yu

In Partial Fulfillment of the Requirements

for the Degree of

Doctorate of Philosophy

California Institute of Technology

Pasadena, California

1988

(Submitted March 21, 1988)

This thesis is dedicated to my parents, Albert and Jane, and to my fiancee, Catherine Hayes, whose unwavering love and support have made my stay at Caltech an enjoyable and rewarding experience.

ACKNOWLEDGEMENTS

I would like to dedicate this thesis to my parents, whose support in my graduate studies was invaluable. I am also indebted to my fiancee Cathy for her support and encouragement. In addition, I would like to thank my advisor, Professor Demetri Psaltis, for investing his time and effort in me during my stay at Caltech.

I am deeply indebted to the past and present members of the Optical Information Processing Group. Among them, I would like to thank Dr. John Hong and Fai Mok who have made valuable contribution to my work. In addition, I would liketo thank Dr. Armand Tanguay, Jr., Dr. Richard Johnson, and Dr. Abdellatif Marrakchi for their collaborative efforts on the Photorefractive Incoherent to Coherent Converter. I also thank Dr. Kelvin Wagner, Dr. Eung Gi Paek, Dr. Hyuk Lee, David Brady, Mark Niefeld, Scott Hudson, Alan Yamamura, and Xiang Guang Gu for their numerous helpful discussions.

I am also grateful for administrative help that I received from Mrs. Helen Carrier, Mrs. Odessa Myles, Mrs. Linda Dozsa, and Mrs. Su McKinley. I also gratefully acknowledge that my fourth year at Caltech was financially supported in part by a fellowship grant from the TRW Program in Advanced Technologies Program.

ABSTRACT

The ability of photorefractive crystals to holographically record an optical image in real time allows one to use them in a variety of optical information processing systems. A number of such systems are presented in this thesis. To form the ground work used in analyzing the performance of photorefractive optical processors, a comparison between the Kukhtarev and Moharam models was done. The regimes where each model sufficiently predicted the response of the photorefractive crystal was determined. In addition, a new model based on a higher perturbation expansion of Kukhtarev's material equation is presented. This method allows one to numerically derive the profile of the space charge field recorded in the crystal and predict the regime where the Kukhtarev and Moharam models are most accurate.

Three optical processing systems are presented. The first, a photorefractive incoherent to coherent converter (PICOC), utilizes a photorefractive crystal as a spatial light modulator. Both the Kukhtarev and higher expansion models were used to analyze the performance of the converter. In the second example, the use of a photorefractive crystal as a time integrating detector is presented. By utilizing this crystal in an acousto-optic time integrating correlator, the output correlation is presented without the bias inherent in standard time integrating architectures. This allows one to utilize the full dynamic range of the output detector, thereby increasing the processing gain of the system. The third example utilizes a pho-

torefractive crystal in a VanderLugt correlator. Standard VanderLugt correlators using planar holograms have been used successfully in pattern classification. In this thesis, we will derive the capacity of this system and demonstrate that by using a photorefractive crystal as the storage medium, the volume holographic properties of the crystal results in an increase in the capacity of the system. In addition, the angular selectivity of the crystal allows one to perform multi-category classification. The effect of using a volume hologram in a VanderLugt correlator is analyzed and experimental results presented.

TABLE OF CONTENTS

I. INTRODUCTION

I.1 Optical Processing Systems

Optical information processing systems have been used to implement operations that are useful in solving a variety of problems. Among these accomplishments are optical correlators [1-3], spectrum analyzers [4,5], synthetic aperture radar processors [6,7], and associative memories [8,9]. Any optical processing systems can be subdivided into three basic components. These are the input, output and processing stages (Fig. 1.1). A major issue in the construction of the three stages is the availability of optical materials to perform the task of each stage.

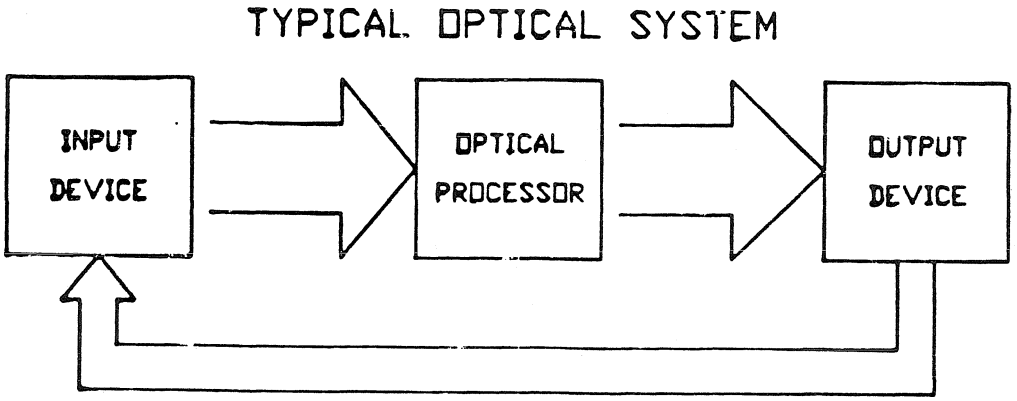

Fig. 1.1 Typical Optical System

The input stage receives information from an external source and converts it to either coherent or incoherent light. If the original information is itself optical, it is necessary for the input stage to receive the light originating from the source and convert it into a form usable by the optical processor (usually coherent light). A number of devices, commonly refered to as spatial light modulators (SLMs), have been developed to perform the input task. These SLMs are sensitive to the light detected from the source and modulate an optical parameter such as the polarization, refractive index, or transmitivity of the material. Another light beam, usually a coherent beam, is used to readout this perturbation resulting in the information from the light source being transferred onto the coherent beam. The coherent form of the original image is then suitable for further processing. Photographic film is an example of a device which uses amplitude modulation to convert images to their coherent replicas. The necessity for high speed converters is important when the information must be processed in real time. Some devices which have this ability are the Hughes Liquid Crystal Light Valve (LCLV) [10], the Pockels Readout Modulator (PROM) [11], PRIZ [12], and the Microchannel Spatial Light Modulator (MSLM) [13]. The LCLV uses liquid crystals to modulate the polarization of the light while the remaining examples utilize the buildup of a local space charge field to modulate the refractive index through the electro-optic effect. Another type of SLM are thermoplastics [14] which utilize the temperature change induced by the

incident light to modulate the refractive index of the material.

There are often situations where the information being received is electronic in nature. In this case, the input device is required to convert the electronic signal into a modulation of a light beam. These devices are sensitive to the electric field induced by the signal and produce modulation of a light sensitive parameter in the material. The electronic signal is then converted to its optical replica by reading out the induced parameter modulation with an auxillary beam. Devices capable of performing this have been fabricated utilizting the acousto-optic (AOD) [15], electro-optic [16], and the magneto-optic effects (MOD) [17]. The AOD converts the input electrical signal to a propagating acoustic wave. Through the piezo-electric effect, this acoustic wave in turn modulates the refractive index of the material. Similarly, in an electro-optic modulator, the electro-optic effect is utilized to convert the input signal to a refractive index modulation of the material. The major limitation of both these devices is that processing is limited to one-dimensional signals. In spite of this, these modulators have been used successfully in optical procesing of video and radar images [18-20]. The MOD, in contrast, is capable of converting electronic signals into a two dimensional binary image. This device utilizes the magnetic field induced by the electrical signals to vary the magnetic orienation of the pixels in the MOD. Through the Faraday effect, these pixels in turn rotate the polarization of the incident light in one of two directions, depending on the orientation of the

induced magnetic field. By detecting the output polarization of the incident light, the electronically generated image is transferred onto the coherent light beam.

The output stage of an optical processing system, like the input stage, has a clearly defined objective: to convert the post-processed optical information into a usable output. In most applications, the output of the optical system is simply converted into an electronic signal to be represented on a video monitor or recorded in an electronic computer. This can be accomplished through the use of optical detectors and/or video cameras. In some applications, however, the output device must convert the processed information to another optical beam, as in the case where a number of optical processing units are to be cascaded or when a feedback loop is present in the system. In this situation, spatial light modulators or optical amplifiers are used to maintain an all-optical system.

Unlike the input and output stages, the objective in the processing stage of an optical processing system is varied. The requirements of the processing stage differ with the task the system is being required to perform. As a result equal attention must be given to the design, as well as the materials and devices, used in constructing the processing unit. The required devices in the processing stage are for the implementation of the three basic processes: storage, nonlinear operations and interconnections. In this situation, the design objective is to develop a method of arranging the available components in order to accomplish the assigned processing

task.

One major drawback to implementing an information processing system optically is a lack of materials. The common factors which determine the usability of material for optical processing are its ability to modulate an optical parameter (*e.g.* phase, amplitude, or polarization) of an incident light beam in a controllable manner, the ability to implement these changes of the optical parameters within reasonable energy and time constraints, as well as the ease of manufacturing these devices in either large numbers or very dense structures. A promising material, which is the focus of this thesis, is the photorefractive crystal. These crystals have the property that light incident on them induces a change in the refractive index of the material. This property, coupled with the material's high spatial bandwidth and relatively fast response time, has resulted in its use as an efficient rewriteable volume phase hologram. This in turn has resulted in a wide variety of application which utilize photorefractive crystals in optical processing systems, some of which are presented in this thesis. The basic mechanism of the photorefractive effect is presented in the next section. In addition, an overview of optical processing systems which utilize photorefractive materials is presented.

I.2 The Photorefractive Effect

I.2.1 The Basic Mechanism

In a photorefractive crystal, photoionizable trapping sites exist within the crys-

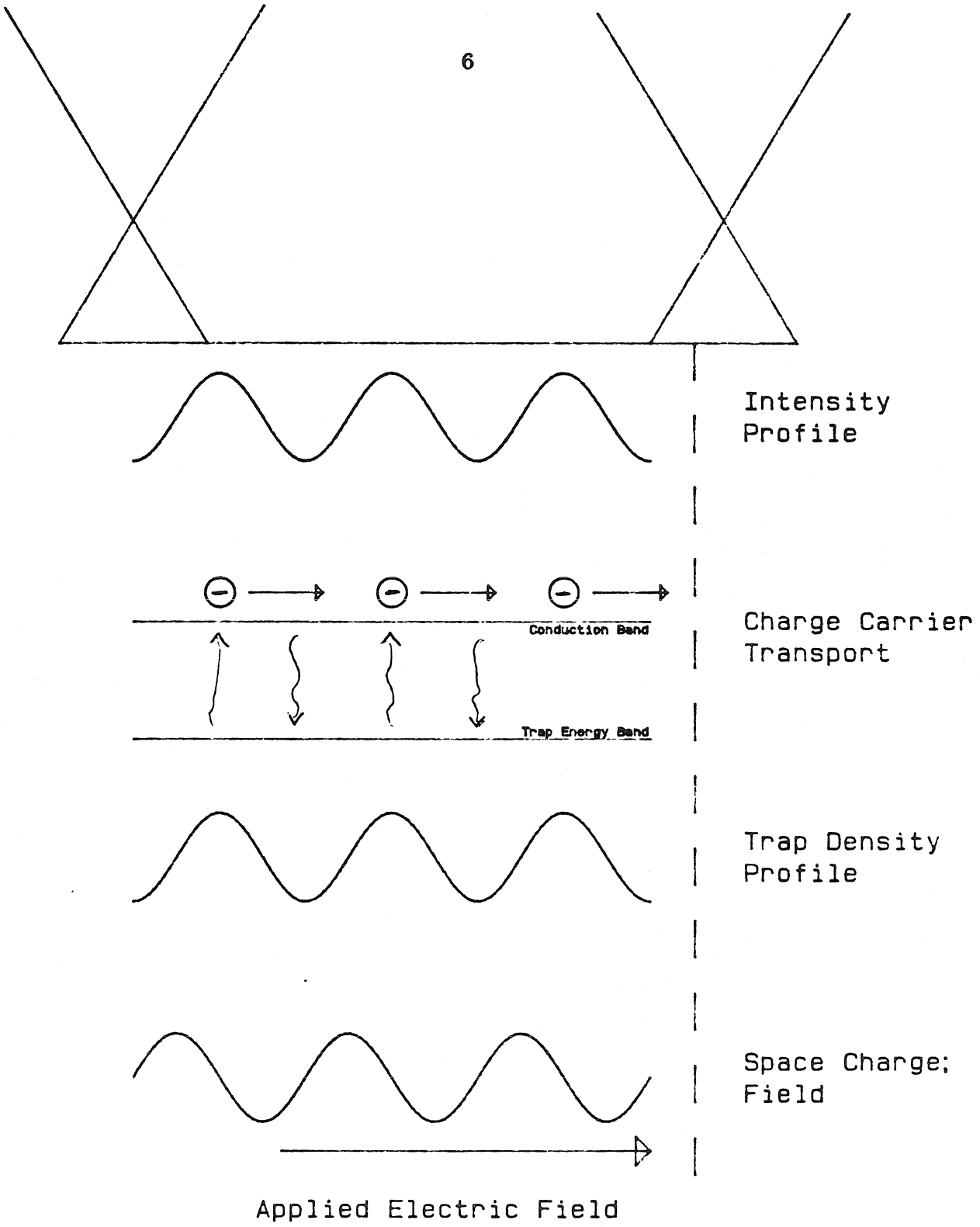

Fig. 1.2 The Photorefractive Effect

tal (Fig. 1.2) which are neutrally charged in the dark. When a light beam is incident on the crystal these trap sites are ionized and electrons are excited into the conduction band (or holes into the valence band depending on the transport mechanism) leaving positively ionized donors. These electrons are transported to regions where the light intensity is low either through diffusion or drift resulting from either an external or photovoltaic field. In these dark regions, the electrons are retrapped producing a net negative charge locally. The result is the build-up of a space charge field in the crystal which has the same spatial dependence as the pattern of light intensity exposing the crystal. This field in turn induces a change in the refractive index through the linear electro-optic effect which results in a phase hologram being written in the crystal.

In addition to the donor trap sites discussed above, acceptor traps which normally do not contain an electron are present in the photorefractive crystal. When a light intensity pattern is incident on the crystal, regions of bright intensity develop a net positive charge, while regions of low intensity will collect electrons. Upon turning off the light, these electrons can no longer remain in the conduction band (since most photorefractive crystals are insulators) and recombine with both ionized donors and acceptor sites in the region. As a result, the local space charge field remains even after incident light is no longer illuminating the crystal. In essence, the photorefractive material has recorded a phase hologram of the incident inten-

sity pattern. Erasure of the hologram can be performed by illuminating the crystal with a uniform light beam. In this case, the uniform beam excites electrons into the conduction band which through transport effects is distributed uniformly over the crystal. As a result any spatial variation in the space charge field is removed and the hologram is erased. The holographic rewriting capability results in a great potential of using photorefractive crystals for optical information processing systems, some of which will be reviewed below.

I.2.2 Survey of Photorefractive Research

Study of the photorefractive effect began with the discovery of optical damage in lithium niobate crystals ($LiNbO_3$) [21]. Ashkin *et al.* noticed that the refractive index change in the crystal was proportional to the amount of intensity incident on the material. The potential for utilizing this intensity dependent index perturbation was first realized by Chen, LaMacchia and Fraser [22,23] who demonstrated that holograms could be written, stored and erased in lithium niobate. Since that time photorefractive properties have been found in a variety of other crystals. These commonly used materials can be subdivided into three categories: ferroelectrics, silinites, and semiconductors. Ferroelectric crystals are usually insulators and to some degree exhibit photovoltaic properties. Among the ferroelectric materials in which the photorefractive effect has been observed are lithium niobate ($LiNbO_3$) [22], lithium tantalate ($LiTaO_3$) [23], potassium tantalate niobate (KTN) [24], bar-

ium titanate ($BaTiO_3$) [25], strontium barium niobate (SBN) [26], and barium sodium niobate ($Ba_2NaNb_5O_{15}$) [27]. The silinites on the other hand are normally paraelectric and exhibit no photovoltaic properties. These material are characterized by faster response time at the expense of lower diffraction efficiency. The photorefractive crystals which fall into this category are: bismuth silicon oxide (BSO) [28], bismuth germanium oxide (BGO) [28], and bismuth titanium oxide (BTO) [29]. The photorefractive properties in semiconductor materials have been studied relatively recently. At present, gallium arsenide (GaAs) [30] and indium phosphide (InP) [31] crystals have been used in photorefractive two- and four-wave mixing experiments. Both these crystals are most sensitive in the near infrared and demonstrate a very fast response time compared to the insulators (silenites and ferroelectrics). In addition because of its semiconductive nature, information recorded in these crystals generally decays faster than the insulators.

Research in the field of photorefractive effects and material have developed on three parallel but distinct tracks: 1) the development and improvement of optical characteristics in photorefractive materials, 2) the formulation of a mathematical model for the photorefractive effect and 3) use of photorefractive materials in optical systems.

Since the discovery of the photorefractive effect in bulk crystals, much effort has been made to improve the characteristics of the materials such as diffraction

efficiency, sensitivity, and response time. One method of accomplishing this is by doping the photorefractive material with impurities in order to increase the concentration of traps, thereby increasing the sensitivity of the material. Lithium niobate crystals doped with iron [32], rhodium [33], copper [34], uranium [35], cesium [34], manganese [34] or nickel [35] have shown improvements over the crystal in its pure form. Other examples of enhanced photorefractive crystals are BSO doped with transition metals [35], cesium-doped SBN [36] and chromium-doped GaAs crystals [37]. Another method of improving the characteristics of a photorefractive crystal is by varying the experimental conditions, *e.g.*, as applying an electric field to enhance the diffraction efficiency of the material [38]. Other improvement methods include experiments which demonstrate fixing by thermal [39] or electrical means [40], utilizing an auxillary photovoltaic crystal to generate an applied field [41], recording information with high energy very short optical pulses [42] and using moving gratings [43] or alternating applied fields [44] to improve the phase conjugate reflectivity of the crystal.

In conjuction with the efforts to enhance the photorefractive effect in various crystals, much work has been done to formulate a mathematical model through which the response of a photorefractive crystal can be accurately predicted. This work is important in order to determine the limitations of photorefractive materials and the experimental conditions such as incident wavelength and intensity which

result in a better response by the material. A number of theories have been proposed [45-47] and are discussed in greater depth in chapter II. In addition, two of these models, the Moharam and Kukhtarev models, are reviewed in the chapter.

The final track of photorefractive research has been the use of these material in various optical systems. The high spatial bandwidth and relatively fast response time of photorefractive crystals allows one to utilize these materials as real time, reusable, phase transparencies in holographic applications. Photorefractive crystals in optical information processing systems are often utilized in this manner.

Early applications of photorefractive crystals included using them in holographic systems [48,49]. Later uses of the material utilized these holographic recording properties to design phase conjugate mirrors [50-52] and resonators [53,54] to perform aberration correction of optical wavefronts. Other uses of photorefractive crystals include performing image arithmetic operations, such as image subtraction [55] and division [56], and image processing, such as edge enhancement [57], contrast reversal [58], image correlations [59], and speckle removal [60]. In addition, systems which utilize these crystals have been demonstrated to perform real time interferometry [61], laser beamsteering [62], optical motion detection [63], and light amplification [64].

I.3 Outline of Thesis

The following chapter reviews some of the mathematical models used to quanti-

tatively describe the photorefractive effect. Two models, the Moharam and Kukhtarev models, are described in detail. A new model based on a higher order perturbation expansion of the Kukhtarev material equation is presented. Using this model and its numerically simulated results, comparisons between the Moharam, Kukhtarev, and higher order models are made.

The use of a photorefractive crystal as an input device is demonstrated in chapter 3. Specifically, the high spatial bandwidth and the relatively fast response time of a BSO crystal is utilized to construct a spatial light modulator. A mathematical model is formulated to predict the response of the photorefractive incoherent to coherent converter and to determine the characteristics of this device.

In chapter 4, a photorefractive crystal is utilized as an output device, specifically as a time integrating detector for an acousto-optic correlator. In a standard time integrating acousto-optic architecture which uses CCDs, the output correlation is presented with bias. This results in a limitation on the effective dynamic range of the correlator. In a photorefractive crystal, light that is without spatial variation does not produce a cumulative bias signal and hence when the BSO crystal is used as the integrating detector, the correlation signal can be recorded and read out without bias. Important characteristics such as linearity, dynamic range, and integration time are also discussed in this chapter.

The use of photorefractive crystals as components in the processing stage of an

optical processing system is demonstrated in chapter 5 The use of photorefractive crystals as a storage medium for a pattern recognition system is discussed. A VanderLugt correlator is used to perform the classification, and the capacity of this architecture using a planar hologram as the filter is derived. By replacing the planar hologram with a volume element, such as a photorefractive crystal, the filter begins to demonstrate a degree of angular selectivity. The effect of replacing the planar filter with a volume hologram is experimentally demonstrated and analyzed. It is expected that because storage occurs in three dimensions, the capacity of the volume VanderLugt correlator will be higher than that of the planar correlator. It will be demonstrated, however, that this increase in capacity is achieved at the expense of a loss in the shift invariance of the correlator.

References for Chapter 1

1. A. VanderLugt, "Signal Detection by Complex Spatial Filtering", *IEEE Trans. Inf. Th.*, **IT-10**, 139 (1964).
2. R. A. Sprague and C. L. Koliopoulos, "Time Integrating Acousto-optic Correlator", *Appl. Opt.*, **15**, 89 (1976).
3. K. Bromley, "An Optical Incoherent Correlator", *Appl. Opt.*, **21**, 35 (1974).
4. A. VanderLugt, "Interferometric Spectrum Analyzer", *Appl. Opt.*, **20**, 2770 (1981).
5. D. Psaltis and D. Casasent, " Time and Space Integrating Spectrum Analyzer", *Appl Opt.*, **18**, 3203 (1981).
6. E. N. Leith, "Quasi-Holographic Techniques in the Microwave Region", *IEEE. Proc.*, **59**, 1305 (1971).
7. M. Haney and D. Psaltis, "Acousto-Optic Techniques for Real Time SAR Imaging", *SPIE*, **542-26** (1985).
8. N. Farhat, D. Psaltis, E. Paek and A. Prata, "Optical Implementation of the Hopfield Model", *Appl. Opt.*, **24**, 1469 (1985).
9. E. Paek and D. Psaltis, "Optical Associative Memory using Fourier Transform Holograms", *Opt. Eng.*, **26**, 428 (1987).
10. W. P. Bleha, L. T. Lipton, E. Wiener-Arnear, J. Grinberg, P. G. Reif, D. Casasent, H. B. Brown and B. V. Markevitch, "Application of the Liquid Crys-

tal Light Valve to Real-Time Optical Data Processing", *Opt. Eng.*, **17**, 371 (1978).

11. B. A. Horowitz and F. J. Corbett, "The PROM - Theory and Applications for the Pockels Readout Optical Modulator", *Opt. Eng.*, **17**, 353 (1978).

12. M. P. Petrov, A. V. Khomenko, M. A. Krasin'kova, V. I. Marakhonov and M. G. Shlyagin, *Sov. Phys. Tech. Phys.*, **26**, 816 (1981).

13. C. Warde, A. M. Weiss, A. D. Fisher and J. I. Thachara, "Optical Information Processing Characteristics of the Microchannel Spatial Light Modulator", *Appl. Opt.*, **20**, 2066 (1981).

14. W. S. Colburn and E. N. Tompkins, "Improved Thermoplastic Photoconductor Devices for Holographic Recording", *Appl. Opt.*, **13**, 2934 (1974).

15. N. J. Berg and J. N. Lee, eds. "Acousto-Optic Signal Processing" *Marcel Decker*, New York (1983).

16. A. Yariv and P. Yeh *Optical Waves in Crystals*, Ch. 7 *J. Wiley and Sons*, New York (1984).

17. W. E. Ross, D. Psaltis and R. H. Anderson, *Opt. Eng.*, **22**, 485 (1983).

18. E. G. Paek, C. H. Park, F. Mok and D. Psaltis, "Acoustooptic Image Correlators", *SPIE*, **638-05** (1986).

19. D. Psaltis and J. Hong, "Adaptive Acousto-optic Filter", *Appl. Opt.*, **23**, 3485 (1984).

20. D. Psaltis, E. G. Paek and S. S. Venkatesh, "Optical Image Correlation with a Binary Spatial Light Modulator", *Opt. Eng.*, **23**, 698 (1984).

The Photorefractive Effect

21. A. Ashkin, G. D. Boyd, J. M. Dziedzic, R. G. Smith and A. A. Ballman," Optically Induced Refractive Index Inhomogeneities in $LiNbO_3$ and $LiTao_3$", *Appl. Phys. Lett.*, **9**, 72 (1966).

22. F. S. Chen, J. T. LaMacchia and D. B. Fraser, "Holographic Storage in Lithium Niobate", *Appl. Phys. Lett.*, **13**, 223 (1968).

23. F. S. Chen, "Optically Induced Change of Refractive Indices in $LiNbo_3$ and $LiTaO_3$", *Jour. Appl. Phys.*, **40**, 3389 (1969).

24. F. S. Chen, "A Laser Induced Inhomogeneity of Refractive Indices in KTN" *Jour. Appl. Phys.*, **38**, 3418 (1967).

25. R. L. Townsend and J. T. LaMacchia, "Optically Induced Refractive Index Changes in $BaTiO_3$", *Jour. Appl. Phys.*, **41**, 5188 (1970).

26. J. B. Thaxter, "Electrical Control of Holographic Storage in Strontium Barium Niobate", *Appl. Phys. Lett.*, **15**, 210 (1969).

27. J.J. Amodei, D. L. Staebler and A. W. Stephens, "Holographic Storage in Doped Barium Sodium Niobate ($Ba_2NaNb_5O_{15}$)", *Appl. Phys. Lett.*, **18**, 507 (1971).

28. J. P. Huignard and F. Micheron, "High Sensitivity Read-Write Volume Holo-

graphic Storage in BSO and BGO Crystals", *Appl. Phys. Lett.*, **29**, 591 (1976).

29. BTO

30. M. B. Klein, "Beam Coupling in Undoped GaAs at 1.06μm Using the Photorefractive Effect", *Opt. Lett.*, **9**, 350 (1984).

31. A. M. Glass, A. M. Johnson, D. H. Olson, W. Simpson and A. A. Ballman, "Four-Wave Mixing in Semi-Insulating InP and GaAs Using the Photorefractive Effect", *Appl. Phys. Lett.*, **44**, 948 (1984).

32. G. A. Alphonse and W. Phillips, "Read-Write Holographic Memory with Iron-Doped Lithium Niobate", *Ferroelectrics*, **11**, 397 (1970).

33. A. Ishida, O. Mikami, S. Miyazawa, and M. Sumi, "Rh-doped $LiNbO_3$ as an Improved New Material for Reversible Holographic Storage", *Appl. Phys. Lett.*, **21**, 192 (1972).

34. W. Phillips, J. J. Amodei, and D. L. Staebler, "Optical and Holographic Storage Properties of Transition Metal Doped Lithium Niobate", *RCA Rev.*, **33**, 95 (1972).

35. N. I. Katsavets, E. I. Leonov, V. M. Orlov and E. B. Shardin, "Holographic Recording in Doped Bismuth Silicate and Germanated Crystals", *Sov. Tech. Phys. Lett.*, **9**, 183 (1983).

36. K. Megumi, H. Kozuka, M. Kobayashi and Y. Furihata, "High Sensitive Holographic Storage in Ce-doped SBN", *Appl. Phys. Lett.*, **30**, 631 (1977).

37. G. Albanese, J. Kumar and W. H. Steier, "Investigation of the Photorefractive Behavior of Chrome-Doped GaAs by Using Two-Beam Coupling", *Opt. Lett.*, **11**, 650 (1986).

38. Y. Ohmori, Y. Yasojima and Y. Inuishi, "Control of Optical Damage in Reduced $LiNbO_3$ by External Applied Field", *Appl. Phys. Lett.*, **25**, 716 (1974).

39. J. Amodei, W. Phillips and D. L. Staebler, "Improved Electro-optic Materials and Fixing Techniques for Holographic Recording", *Appl. Opt.*, **11**, 390 (1972).

40. F. Micheron and G. Bismuth, "Electrical Control of Fixation and Erasure of Holographic Patterns in Ferroelectric Materials", *Appl. Phys. Lett.*, **20**, 79 (1972).

41. J. P. Huignard and F. Micheron, "Conrtol of Sensitivity to Hologram Storage in $LiNbO_3$ Using an Accessory Photovoltaic Crystal", *Opt. Comm.*, **16**, 80 (1976).

42. C. T. Chen, D. M. Kim and D. Vonder Linde, "Efficient Hologram Recording in $LiNbO_3$:Fe Using Optical Pulses", *Appl. Phys. Lett.*, **34**, 321 (1979).

43. S. I. Stepanov, V. V. Kulikov and M. P. Petrov, "Running Holograms in Photorefractive $Bi_{12}SiO_{20}$ Crystals", *Opt. Comm.*, **44**, 19 (1982).

44. S. I. Stepanov and M. P. Petrov, "Efficient Unstationary Holographic Recording in Photorefractive Crystals Under an External Alternating Electric Field", *Opt. Comm.*, **53**, 292 (1985).

45. M. G. Moharam, T. K. Gaylord, R. Magnusson and L. Young, "Holographic Formation in Photorefractive Crystals with Arbitrary Electron Transport Lengths", *Jour. Appl. Phys.*, **50**, 5642 (1979).

46. N. V. Kukhtarev, V. B. Markov, S. G. Odulov, M. S. Soskin and V. L. Vinetskii, "Holographic Storage in Electrooptic Crystals: I Steady State", *Ferroelectrics*, **22**, 949 (1979).

47. J. Feinberg, D. Heiman, A. R. Tanguay, Jr. and R. W. Hellwarth, "Photorefractive Effects and Light Induced Charge Migration in Barium Titanate", *Jour. Appl. Phys.*, **51**, 1297 (1980).

48. J. B. Thaxter and M. Kestigian, "Unique Properties of SBN and their Use in Layered Optical Memory", *Appl. Opt.*, **13**, 913 (1974).

49. L. D'Auria, J. P. Huignard, C. Slezak and E. Spitz, "Experimental Holographic Read-Write Memory Using 3-D Storage", *Appl. Opt.*, **13**, 808 (1974).

50. J. P. Huignard, J. P. Herriau, P. Aubourg, and E. Spitz, "Phase Conjugate Wavefront Generation via Real-Time Holography in $Bi_{12}SiO_{20}$", *Opt. Lett.*, **4**, 21 (1979).

51. J. Feinberg, and R. W. Hellwarth, "Phase Conjugating Mirror with Continuous Wave Gain", *Opt. Lett.*, **5**, 519 (1980).

52. B. Fischer, M. Cronin-Golomb, J. O. White and A. Yariv, "Real Time Phase Conjugate Windows for One-Way Optical Field Imaging Through a Distor-

tion", *Appl. Phys. Lett.*, **41**, 141 (1982).

53. J. F. Lam and W. P. Brown, "Optical Resonators with Phase Conjugate Mirrors", *Opt. Lett.*, **5**, 61 (1980).

54. M. D. Ewbank and P. Yeh, "Frequency Shift and Cavity Length in Photorefractive Resonators", *Opt. Lett.*, **10**, 496 (1985).

55. Y. H. Ja, "Real Time Image Subtraction in Four-Wave Mixing with Photorefractive $Bi_{12}GeO_{20}$ Crystals", *Opt. Comm.*, **42**, 377 (1982).

56. Y. H. Ja "Real Time Image Division in Four-Wave Mixing with Photorefractive $Bi_{12}GeO_{20}$ Crystals", *Opt. Comm.*, **44**, 24 (1982).

57. J. Feinberg, "Real Time Edge Enhancement Using the Photorefractive Effect", *Opt. Lett.*, **5**, 330 (1980).

58. R. Grousson and S. Mallick, "Image Contrast Reversal with a Photorefractive Recording Medium", *App. Opt.*, **20**, 1719 (1981).

59. J. O. White and A. Yariv, "Real Time Image Processing Via Four-Wave Mixing in Photorefractive Medium", *Appl. Phys. Lett.*, **37**, 5 (1980).

60. J. P. Huignard, J. P. Herriau, L. Pichon and A. Marrakchi, "Speckle-free Imaging in Four-Wave Mixing Experiments with $Bi_{12}SiO_{20}$ Crystals". *Opt. Lett.*, **5**, 436 (1980).

61. J. P. Huignared and J. P. Herriau, "Real Time Double Exposure Interferometry with $Bi_{12}SiO_{20}$", *Appl. Opt.*, **16**, 1807 (1977).

62. P. D. Henshaw, "Laser Beamsteering Using the Photorefractive Effect", *Appl. Opt.*, **21**, 2323 (1982).

63. D. Z. Anderson, D. M. Lininger and J. Feinberg, "Optical Tracking Novelty Filter", *Opt. Lett.*, **12**, 123 (1987).

64. J. P. Huignard and A. Marrakchi, "Coherent Signal Beam Amplification in Two-Wave Mixing Experiments with Photorefractive $Bi_{12}SiO_{20}$ Crystals", *Opt. Comm.*,**38**, 249 (1981).

II. THE PHOTOREFRACTIVE EFFECT

In this chapter, a review of the methodology used in predicting the photorefractive effect is presented. Specifically, two theoretical models, the Kukhtarev and Moharam models, are reviewed. Each model makes a number of simplifying assumptions in order to derive an analytical solution for the photorefractive effect. These assumptions consequently determine the accuracy of the model and the operating conditions under which each model can be used. In order to compare these models with a more accurate model of the photorefractive effect, a higher order model will be derived, based on an extended perturbation expansion of the Kukhtarev material equations. Because of the inherent analytical complexity of this technique, numerical methods are used to generate a solution for the steady state regime. A comparison of these three models is then used to determine the accuracy of the analytic models.

II.1 Theoretical Framework for the Photorefractive Effect

In a typical photorefractive medium, such as those described in the previous section, the crystal is photosensitive, has a relatively large electo-optic effect, and has a high number of donor and acceptor trap sites. As shown in Figure 1.2, when an intensity pattern is incident on the photorefractive crystal, the photosensitive trap sites release electrons to the conduction band in regions where the intensity is bright. These free moving electrons are then transported through drift or diffusion effects.

Bias fields necessary to induce drift currents may either be externally applied (as in the case of BSO and BGO) or they may be present due to an internal photovoltaic effect (as in the case of Lithium Niobate and Lithium Tantalate). These electrons then recombine with trap sites in the dark regions forming a local space charge field between light and dark regions. This locally varying field induces a change in the refractive index due to the linear electro-optic effect. A number of mathematical modes have been developed in order to quantify the photorefractive effect [1-15].

Because most photorefractive applications are holographic, the models concentrate on determining the response of a photorefractive crystal to an incident intensity grating. The models can be divided into two categories. The first is a traditional holographic model where it is assumed that the grating is formed by the two incident beams. The induced space charge field and corresponding phase grating are calculated. The diffraction of the incident beams due to this grating is then computed while assuming that the diffracted beams do not significantly alter the formed grating. In the second model, which is more complete but also more complicated, all four beams (two incident and two diffracted) are considered in computing the space charge field and their collective contributions are included in the derivation of the grating formed.

In order to develop a model for the photorefractive effect, a set of material equations are used to describe the physical processes occuring in the crystal, such

as the excitation and recombination of the charge carriers (electrons or holes) and the buildup of the local space charge fields, from which the strength of the space charge field can be derived. Due to the linear electro-optic effect, this field would result in an index perturbation

$$\Delta n = \frac{r_{eff} n_0^3}{2} E_{sc}(x,t). \qquad [2.1]$$

$E_{sc}(x,t)$ is the amplitude of the space charge field and has temporal variations much slower than optical frequencies. n_0 is the refractive index of the material, and r_{eff} is the effective electro-optic coefficient for the particular direction of space charge field and readout polarization used in the experiment.

The resulting index perturbation can then be subsituted into the coupled wave equation to predict the actual light diffracted by the photorefractive crystal

$$\nabla^2 \xi + (n_0 + \Delta n(x,t))\xi = 0. \qquad [2.2]$$

In order to account for the effect of the incident and diffracted beams on the grating formation in the crystal, equation 2.2 is solved simultaneously with the material equations. In this case, the index change Δn will be dependent on the amplitude of the light beams propagating within the photorefractive crystal. The standard procedure used in analyzing this problem is to consider a thin photorefractive slab and use the material equations to calculate the index perturbation based on the amplitude strength of the beams incident on the slab. The amplitude strength

of the light beams in the crystal can then be found by solving the coupled wave equation, with the refractive index change being explicitly dependent on the light amplitudes. A number of techniques have been used to analyze this diffraction process in photorefractive media [9-15].

In considering the response of a thin photorefractive slab, an important characteristic is the inherent phase shift between the incident intensity grating and the induced refractive index grating. This phase shift leads to an energy exchange between the two incident beams resulting in interesting effects such as self-amplification [16] and optical bistability [17]. Under certain operating conditions (i.e, high applied field and low spatial frequencies), the phase shift is small or the crystal is thin, there is very little energy exchange between the readout and diffracted beams. In this case, the diffraction efficiency of the index grating is [9]

$$\eta = sin^2(\Delta n_1 L). \qquad [2.3]$$

It is assumed that the incident readout beam is perfectly Bragg matched to the index grating and Δn_1 is the amplitude of the fundamental Fourier component of the induced index grating. L is the thickness of the photorefractive media. Thus, it is only important to determine the strength of the fundamental component of the induced space charge field in order to predict the diffraction efficiency of the recorded phase grating.

In this chapter, we will concentrate on models of the first category, the thin

slab (*i.e.*, we will neglect self diffraction effects). Our theory must predict three things. Firstly, it must successfully determine the magnitude of the induced index change. This is important in predicting the diffraction efficiency of the holographic grating. Secondly, the phase difference between the index grating and the incident intensity grating must be accurately modeled since this parameter will determine the fidelity with which signals are recorded in the optical processors considered in this thesis. Lastly, the model must be able to predict the temporal behavior of the photorefractive process in order to determine the write and decay rates of dynamic holograms in the crystal.

A number of mathematical models have evolved along with the research in photorefractive materials [1-8]. The models of Moharam *et al.* [3] and Kukhtarev *et al.* [4] will be reviewed below. Both models utilize a set of material equations through which the induced space charge field is derived. Through equation 2.1 and 2.3, the index perturbation and resulting diffraction efficiency can then be found. The major difference between these two models and subsequent analytical studies is the accuracy through which the material equations are modeled. In the Moharam case, it is assumed that an infinite number of trapping sites exist in the crystal. This assumption allows one to derive an analytical solution for the space charge fields in the steady state case. However, this assumption also results in severe inaccuracies in predicting the response of the crystal to high spatial frequency

gratings. Kukhtarev sought to remedy this by incorporating the density of traps into the material equations. But because of the additional complexity, he was only able to derive an analytical solution for low modulation depth gratings.

A number of other models have been developed seeking to solve more accurate sets of material equations [5-8]. Valley [7] incorporated an additional trapping and recombination equation for acceptors and derived a dynamic solution which demonstrated more than one time constant. Ochoa *et al.* [8] incorporated the acceptor density to the Moharam model and utilized a higher order perturbation scheme to derive more accurate analytical solutions in the high modulation depth regime.

In addition, mathematical models have been used to predict the response of photorefractive crystals with moving gratings [18] and in four-wave mixing geometries [19]. Unfortunately, most recent models suffer from a high degree of complexity and present results which hide the physics of the photorefractive effect behind voluminous analytical expressions.

In order to facilitate comparison between the two analytical models and the higher order numerical model, we will consider the photorefractive effect in a BSO crystal. The material parameters for BSO used in numerical comparisons are presented in Table 2.1 on page 65.

II.2 Moharam Model

The theoretical framework derived by Moharam *et al.* [3] uses the following set of material equations

$$\frac{\partial N_D^+(x,t)}{\partial t} = g_0 I(x,t) - \frac{n(x,t)}{\tau_r} \qquad [2.4]$$

$$\frac{\partial N_D^+(x,t)}{\partial t} = \frac{\partial n(x,t)}{\partial t} - \frac{1}{e}\frac{\partial J(x,t)}{\partial x} \qquad [2.5]$$

$$E(x,t) = -\frac{1}{\epsilon}\int_0^t J(x,t)dt + G(t) \qquad [2.6]$$

$$J(x,t) = \mu e n(x,t) E(x,t) + k_B T \mu \frac{\partial n(x,t)}{\partial x} \qquad [2.7]$$

where

$I(x,t)$ is the incident intensity

$g_0 = \alpha\eta/h\omega$ (α=absorption coefficient, η-quantum efficiency, h-Planck's constant, and ω-frequency of recording light)

τ_r is the recombination time between free carriers and traps

$J(x,t)$ is the current density

k_B is Boltzmann's constant

T is the temperature

$n(x,t)$ is the charge carrier density

$N_D^+(x,t)$ is density of ionized traps

e is the unit electronic charge

μ is the charge carrier mobility

$E(x,t)$ is the space charge field

$G(t)$ is determined from the boundary condition (*i.e.* constant applied voltage constraint).

The first equation is a trap density equation incorporating the generation and recombination rates of the charge carriers. The charge balance relationship is described in the second equation while the relationship between the space charge field and the current density is expressed in the third equation. The fourth is the current density equation incorporating both drift and diffusion components.

Assume an incident intensity grating of the form

$$I(x,t) = I_0(1 + mcoskx) \qquad [2.8]$$

where I_0 is the average light intensity, m is the modulation depth and $k/2\pi$ is the spatial frequency of the grating. The resulting space charge field in the steady state regime is [3]

$$E_{sc}(x) = \frac{mE_d sinkx}{1 + mcoskx} + E_0\left[1 - \frac{\sqrt{1-m^2}}{1 + mcos(kx)}\right] \qquad [2.9]$$

where E_0 is the strength of the applied DC field and E_d is the characteristic diffusion field given by

$$E_d = \frac{k_B T k}{e}. \qquad [2.10]$$

In most applications detailed knowledge of the space charge field profile is not necessary. Since the fundamental component of the space charge field determines

the diffraction efficiency or the coupling strength, calculating the strength and phase shift of this Fourier component is essential in predicting the response of a photorefractive crystal. Decomposing equation 2.9 into its Fourier components results in a fundamental component with magnitude given by

$$E_1 = 2\sqrt{E_d^2 + E_0^2}\left[\frac{\sqrt{1-m^2}-1}{m}\right] \qquad [2.11]$$

and phase shift by

$$\phi_1 = tan^{-1}\left[\frac{E_d}{E_0}\right]. \qquad [2.12]$$

Figure 2.1 shows the magnitude of the space charge field induced in a BSO crystal as a function of the spatial frequency for various values of applied field. The modulation depth of the intensity grating incident on the crystal is assumed to be 1.0. It is interesting to note that in Figure 2.1, the induced space charge field component stays constant down to a zero spatial frequency grating. This arises because the model developed by Moharam assumes the photorefractive crystal has infinite transverse dimensions. As a result, gratings of arbitrarily low spatial frequencies and the corresponding space charge profile still maintain their structure over the transverse dimension of the crystal. In reality, however, the transverse dimension of a photorefractive crystal are finite. This results in a minimum spatial frequency that can be detected and hence recorded by the crystal. In addition, since the incident light is used to record a phase hologram, an overall change in the refractive index induced by a uniform beam (*i.e.* zero spatial frequency) will not result in a

change in the DC component of the diffracted output (as opposed to the case of an absorption hologram). Figure 2.2 shows the dependence of the phase shift between the incident intensity and induced index gratings on the spatial frequency of the intensity grating.

The major advantage of this model is its ability to determine exactly the space charge profile recorded in the crystal. Figure 2.3 shows a typical profiles predicted by this model. Figures 2.3a depicts the space charge fields for an intensity grating with modulation depth 0.9 and a spatial frequency of 100 l/mm. being recorded on a BSO crystal. In this case, an external applied field of 6kV/cm was applied to the crystal. The resulting profile shows the symmetry about the minimum intensity point, typical in the drift dominated regime. Figure 2.3b shows the profile for a grating with spatial frequency of 1000 l/mm. In this case, the space charge field shows a slight asymmetry arising from the contribution of the diffusion field (which is higher for higher spatial frequencies) to the overall recorded field. Figures 2.3c and 2.3d show the space charge field profiles for a 100 and 1000 l/mm. grating when no applied field is present. In both cases, the field pattern shows the asymmetrical distribution, typical of charge transport in the diffusion dominated regime.

The main disadvantage of this model is its inability to provide a temporal analysis of the photorefractive effect. In their paper [3], Moharam *et al.* expanded the space charge field into its spatial frequency components and solved numerically for

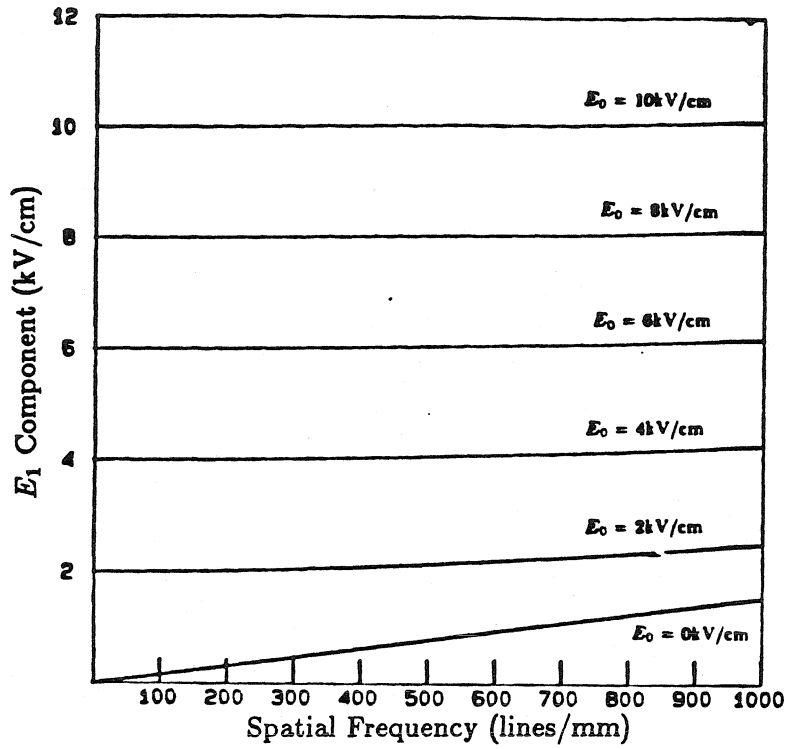

Fig. 2.1 $|E_1|$ vs Spatial Frequency (Moharam Model)

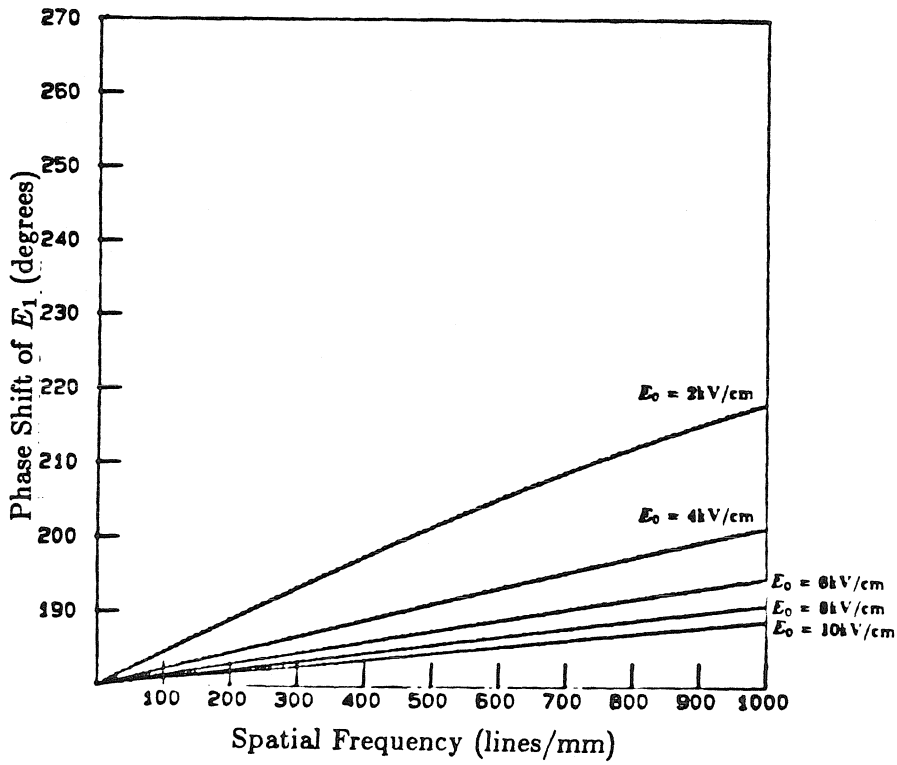

Fig. 2.2 Phase Shift vs Spatial Frequency (Moharam Model)

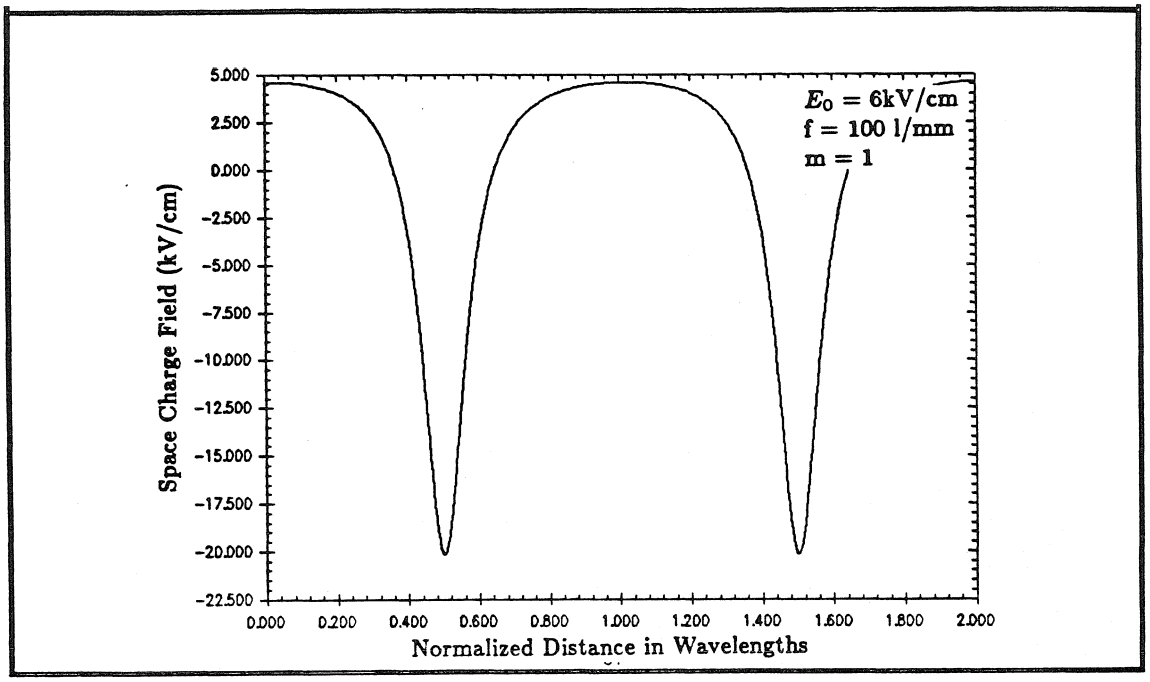

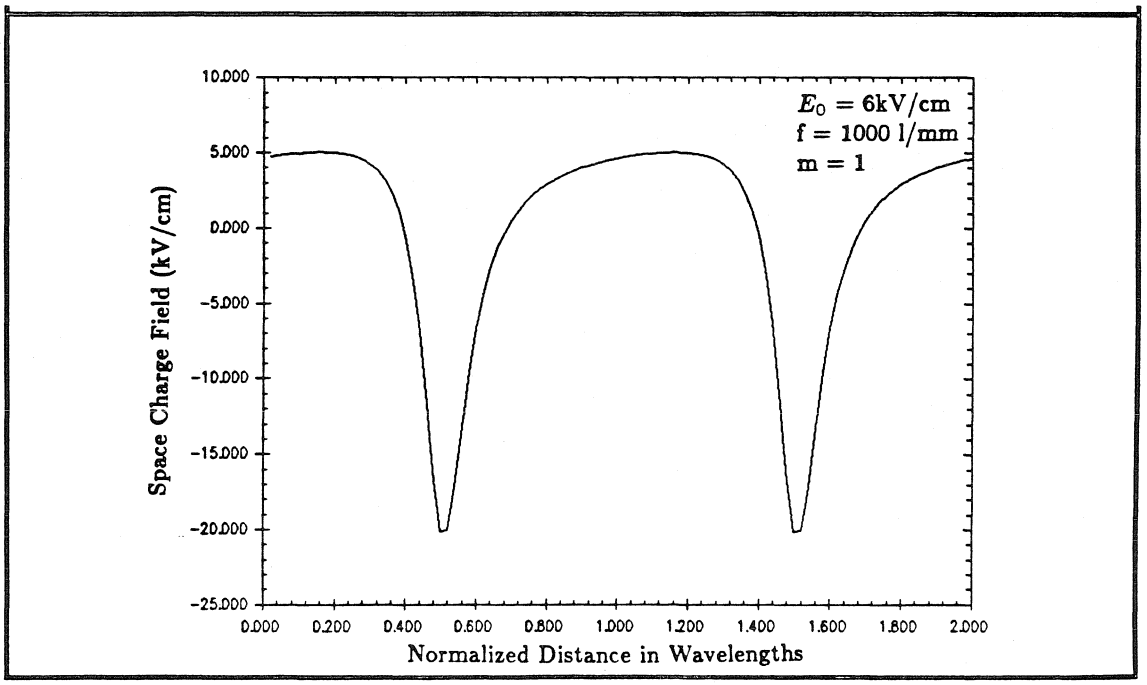

Fig. 2.3 Space Charge Field Profiles Derived from the Moharam Model

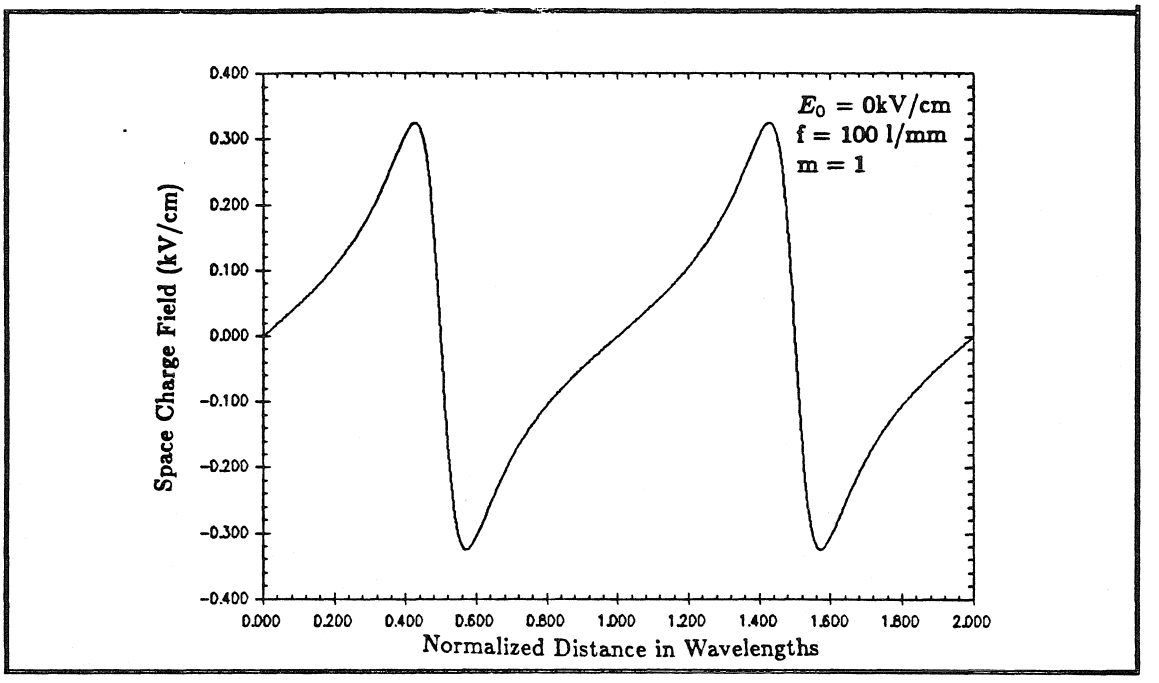
E_0 = 0kV/cm
f = 100 l/mm
m = 1
Space Charge Field (kV/cm)
0.400
0.300
0.200
0.100
0.000
-0.100
-0.200
-0.300
-0.400
0.000 0.200 0.400 0.600 0.800 1.000 1.200 1.400 1.600 1.800 2.000
Normalized Distance in Wavelengths

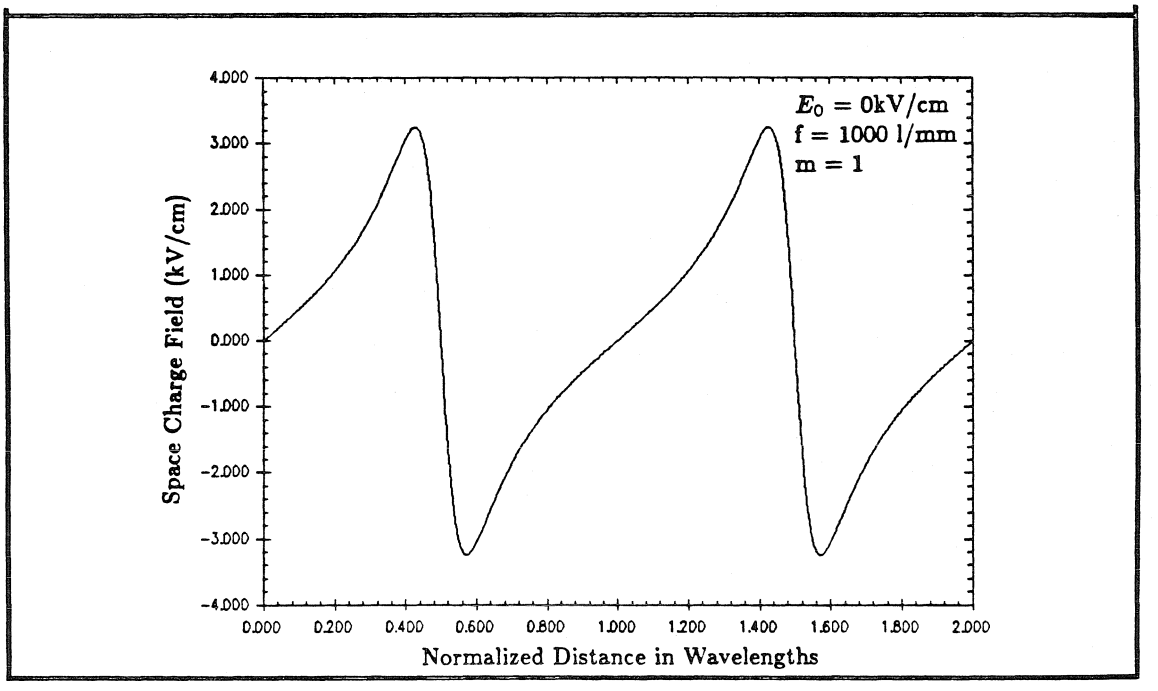
E_0 = 0kV/cm
f = 1000 l/mm
m = 1
Space Charge Field (kV/cm)
4.000
3.000
2.000
1.000
0.000
-1.000
-2.000
-3.000
-4.000
0.000 0.200 0.400 0.600 0.800 1.000 1.200 1.400 1.600 1.800 2.000
Normalized Distance in Wavelengths

Fig. 2.3 *cont*

the dynamics of the photorefractive crystal. Another disadvantage is the assumption that the recombination time τ_r is independent of the trap density. This results from an assumption that the trap density in the crystal is essentially unlimited. Consequently, the model makes incorrect predictions in the high spatial frequency regime, where the finite trap densities result in an upper limit in the space charge field that can be supported within the crystal. Kukhtarev et. al. corrected this problem by incorporating the density of trapping sites into the material equation and the recombination rate. The result of this will be reviewed in the following section.

II.3 Kukhtarev Model

The Kukhtarev model is similar to that of Moharam in utilizing a set of a material equations to predict the space charge field, and hence the index perturbation within the photorefractive material. The material equations which form the core of the Kukhtarev model are:

$$\frac{\partial N_D^+(x,t)}{\partial t} = (s_g I(x,t) + \beta)(N_D - N_D^+(x,t)) - \gamma_R N_D^+(x,t) n(x,t) \qquad [2.13]$$

$$\frac{\partial N_D^+(x,t)}{\partial t} = \frac{\partial n(x,t)}{\partial t} - \frac{1}{e}\frac{\partial J(x,t)}{\partial x} \qquad [2.14]$$

$$\frac{\partial E(x,t)}{\partial x} = \frac{e}{\epsilon}(N_D^+(x,t) - n(x,t) - N_A) \qquad [2.15]$$

$$J(x,t) = \mu e n(x,t) E(x,t) + k_B T \mu \frac{\partial n(x,t)}{\partial x} \qquad [2.16]$$

in which

N_D is the total concentration of donor-like trapping center

N_{Deq}^{+} is the concentration of ionized donor-like trapping centers in the absence of light

$N_D^{+}(x,t)$ is the concentration of ionized donor-like trapping centers

N_A is the concentration of negatively charged acceptor-like centers that compensate for the charge N_{Deq}^{+}

$n(x,t)$ is the concentration of electrons in the conduction band

$E(x,t)$ is the internal space charge electric field

e is the electronic charge

s_g is the absorption cross section at the grating beam wavelength

β is the thermal generation rate of electrons into the conduction band

γ_R is the carrier recombination constant

$I(x,t)$ is the optical intensity profile incident on the photorefractive material

$J(x,t)$ is the current density within the crystal

μ is the charge carrier mobility

k_B is Boltzmann's constant

T is the absolute temperature of the crystal

ϵ is the dielectric constant of the crystal.

Equation 2.13 describes the trapping and recombination process, while equations 2.14-2.16 are the transport, Poisson, and current density equations. The main

difference between the two models lies in the form of the recombination term in equation 2.13. In the Moharam model, the recombination term is of the from $n(x,t)/\tau_r$ which assumes that the recombination time is independent of the density of available traps. In Kukhtarev's formulation, the recombination term, $\gamma_R N_D^+ n$ assumes a recombination time of the form

$$\tau_r(x,t) = \frac{1}{\gamma_R N_D^+(x,t)}. \qquad [2.17]$$

This added terms leads to a number of important differences in predicting the space charge field recorded in the crystal. As discussed in the previous section, the simpler formulation of the trapping/recombination equation lead to a closed form solution for the space charge field in the steady state case. By removing the constant recombination time approximation in the Kukhtarev model, the additional nonlinearities that one introduced in describing the photorefractive effect can no longer be solved in closed form. As a result, Kukhtarev uses a perturbation analysis on the set of material equations to predict both the steady state and temporal response of a photorefractive crystal for low modulation depths.

Assuming again, an intensity profile of

$$I(x,t) = \begin{cases} 0 & \text{t<0} \\ I_0(1+mcosx) & \text{t>0} \end{cases}, \qquad [2.18]$$

the trap and electron densities, as well as the current and space charge fields can

be expanded in terms of their Fourier components

$$N_D^+(x,t) = N_{Deq}^+ + \sum_{r=1}^{\infty} N_{Dr}^+(t)e^{ikrx} + c.c. \qquad [2.19]$$

$$n(x,t) = n_0 + \sum_{r=1}^{\infty} n_r(t)e^{ikrx} + c.c. \qquad [2.20]$$

$$J(x,t) = J_0 + \sum_{r=1}^{\infty} J_r(t)e^{ikrx} + c.c. \qquad [2.21]$$

$$E(x,t) = E_0 + \sum_{r=1}^{\infty} E_r^+ e^{ikrx} + c.c.. \qquad [2.22]$$

In predicting the diffraction efficiency of a grating recorded in a photorefractive media, the Fourier component of most importance is the space charge field corresponding to the frequency of the intensity grating, the $E_1(t)$ component. By assuming the modulation depth of the grating profile is small, the E_1 component of the space charge field can be solved analytically be truncating each series to the first harmonic component. By utilizing a first order perturbation expansion, the resulting space charge field component is given by [4]

$$E_1(t) = -i\frac{m}{2}E_q\frac{E_0 + iE_d}{E_0 + i(E_d + E_q)}\left[1 - e^{-t/\tau}\right] \qquad [2.23]$$

where the complex rise time τ is given by

$$\tau = t_0\frac{E_0 + i(E_d + E_m)}{E_0 + i(E_d + E_q)} \qquad [2.24]$$

and E_d, E_m and E_q are the characteristic fields due to diffusion, drift and trap density limit, respectively, and are given by

$$E_d = \frac{k_B T k}{e} \qquad [2.25]$$

$$E_m = \frac{\gamma_R N_{Deq}^+}{\mu k} \qquad [2.26]$$

$$E_q = \frac{eN_{Deq}^+}{\epsilon k} \qquad [2.27]$$

and t_0 is the fundamental recombination time given by

$$t_0 = \frac{N_{Deq}^+}{\alpha N_D I_0}. \qquad [2.28]$$

The steady state value for the $r = 1$ component of the space charge field

$$E_1 = \frac{m}{2} \frac{E_0 + iE_d}{1 + (E_0 + iE_d)/E_q} \qquad [2.29]$$

One feature of equation 2.29 is the linear relationship between E_1 and the modulation depth m. This arises from the small modulation depth approximation which allows a first order space charge field solution. In the high modulation depth regime, E_1 depends on many higher powers of m.

Figure 2.4 shows the dependence of $|E_1|$ on the spatial frequency of the incident intensity grating for various applied field strengths. The material parameters for a BSO crystal (shown in Table 2.1) and a grating modulation depth of 1 are used to facillitate a comparison with the Moharam model described in the previous section. The major difference in the prediction of this model and that of Moharam (Fig. 2.1) lies in predicting $|E_1|$ in the high spatial frequency regime. In the low frequency regime, both models predict that the amplitude of the space charge field will remain at a constant value. In the Kukhtarev model, this value is equal to one half the

applied field strength multiplied by the modulation depth of the grating, whereas in the Moharam model, this value will have a nonlinear relationship with m, reaching a peak value equal to the applied field when m equals 1. However, in the high frequency regime, the Kukhtarev model predicts a decrease in the amplitude as the spatial frequency increases. This is primarily due to the finite number of trap sites present in the crystal. Specifically, for a material with an ionized trap density of N_{Deq}^{+} and a grating with spatial frequency k, Poisson's equation determines that the maximum field that can be supported is

$$E_{1max} = \frac{eN_{Deq}^{+}}{\epsilon k} = E_q. \qquad [2.30]$$

This inverse relationship between the space charge field and the grating frequency is demonstrated in the high frequency regime of Figure 2.4, where $E_q < E_0$. The Kukhtarev model, like that of Moharam, assumes a photorefractive crystal which is infinite in the transverse direction and as a result predicts the recording of a space charge field for arbitrarily low spatial frequencies.

The phase shift between the E_1 component of the space charge field and the intensity grating as a function of spatial frequency is shown in Figure 2.5. Again the results are similar to those derived by the Moharam model (Fig. 2.2) in the low frequency regime. In the high frequency regime, however, the phase shift tends toward 90^o.

Another advantage of the Kukhtarev model over the Moharam model is its

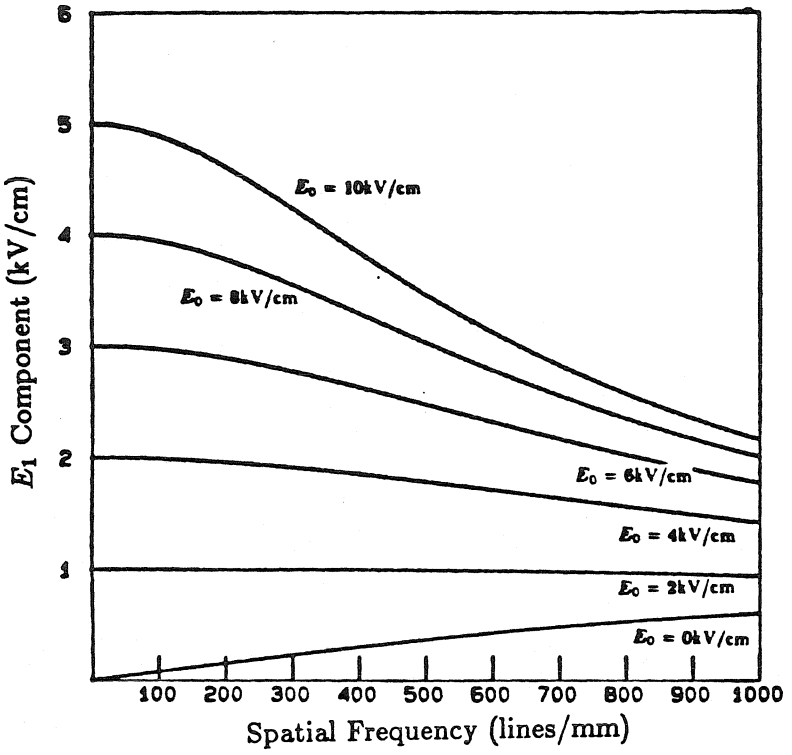

Fig. 2.4 $|E_1|$ vs Spatial Frequency (Kukhtarev Model)

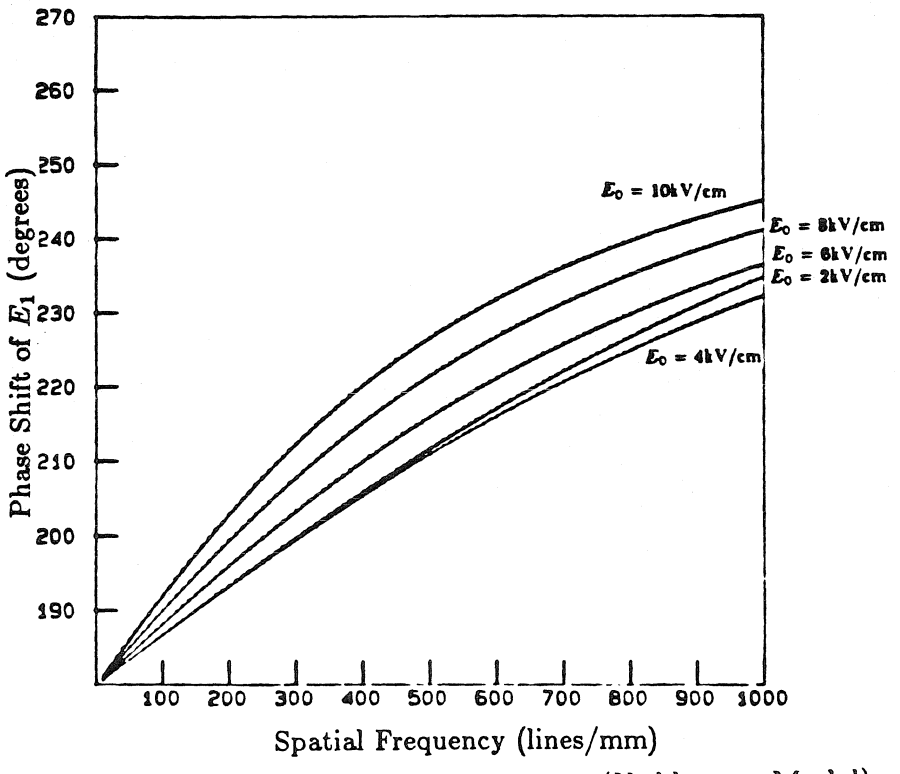

Fig. 2.5 Phase Shift vs Spatial Frequency (Kukhtarev Model)

ability to predict a closed form solution for the temporal response of the photorefractive effect. Again it must be noted that the analysis is restricted to situations where the modulation depth of the grating being recorded is small. Equation 2.24 demonstrates that when an intensity grating is incident on a photorefractive crystal, a space charge field is built up exponentially with a time constant τ given by equation 2.25. This time constant contains a number of interesting features. Firstly, τ is inversely proportional to the intensity incident on the crystal. This arises from the fact that a minimum number of photons is necessary to excite enough charges to create a index grating of fixed strength [20]. As a result, the stronger the light that is incident on the crystal, the quicker the task can be accomplished. The second interesting feature in the expression for τ is the that it contains both a real and imaginary component characteristic of an underdamped system. The writing time of the material is dependent on the real part of τ and is given by

$$t_{write} = \frac{|\tau|^2}{Re[\tau]}. \qquad [2.31]$$

This writing time is plotted as a function of spatial frequency in Figure 2.6. The light incident on the material was assumed to have a wavelength of 488 nm and a strength of 1 mW/cm^2. Figure 2.6 demonstrates two regimes for the time constant of the photorefractive material. In the low frequency regime, the response time of the crystal is very fast and rises proportionally to the spatial frequency of the grating being recorded. In the high frequency regime, however, the time constant

reaches a saturation value and becomes independent of the grating frequency. The expression for the time constant τ given in equation 2.24 can be rewritten as a function of the ionized trap density N_{D1}^{+}

$$\tau = \frac{1}{\alpha N_D I_0} N_{D1}^{+} \frac{E_0 + i(E_d + E_m)}{E_0 + iE_d)}. \qquad [2.32]$$

In BSO, for applied fields, $E_0 >$ 1kV/cm and spatial frequencies, f> 10 l/mm, $E_0 > E_d, E_m$.

The ratio of the characteristic fields in the right hand side of the equation is approximately unity. Hence, the time constant is proportional to the amount of traps N_{D1}^{+} ionized by the intensity grating. In the low frequency regime, the space charge field component E_1 that is recorded is clamped to a value equal to half the applied electric field. From Poisson's equation (Eq. 2.15, in order to maintain this constant space charge field, the number of charges that must be ionized increases with increasing spatial frequency. Since the amount of light incident on the material is also constant, the time required to excite charges is proportional to the amount of ionized traps that must be generated, hence the linear relationship between the recording time constant of the material and the spatial frequency of the grating. In the high frequency regime, the induced space charge field decreases due to the finite number of charges that can be ionized in the crystal. As a result, the number of ionized traps have reached a saturation value equal to N_{Deq}^{+}. Consequently, the time required to form the space charge grating remains constant in this regime.

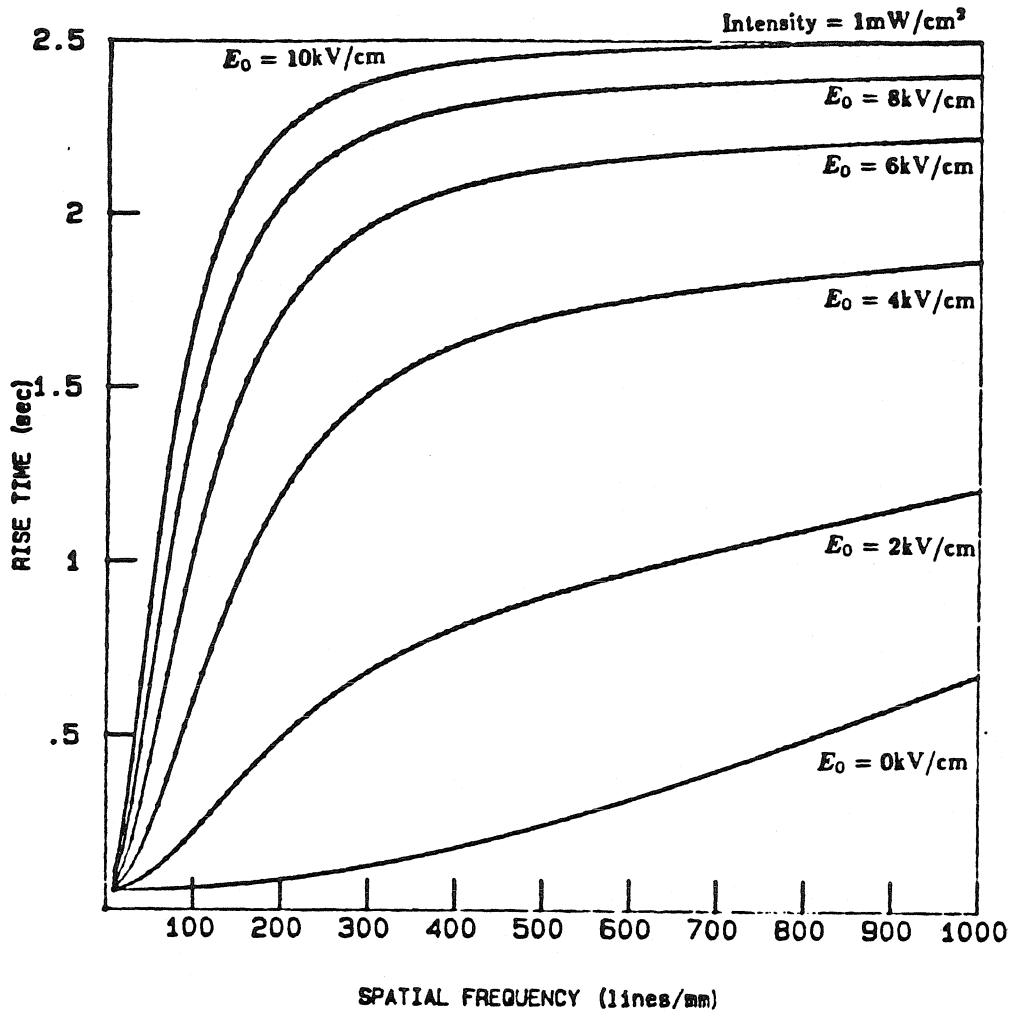

Fig. 2.6 Real Part of τ vs Spatial Frequency (Kukhtarev Model)

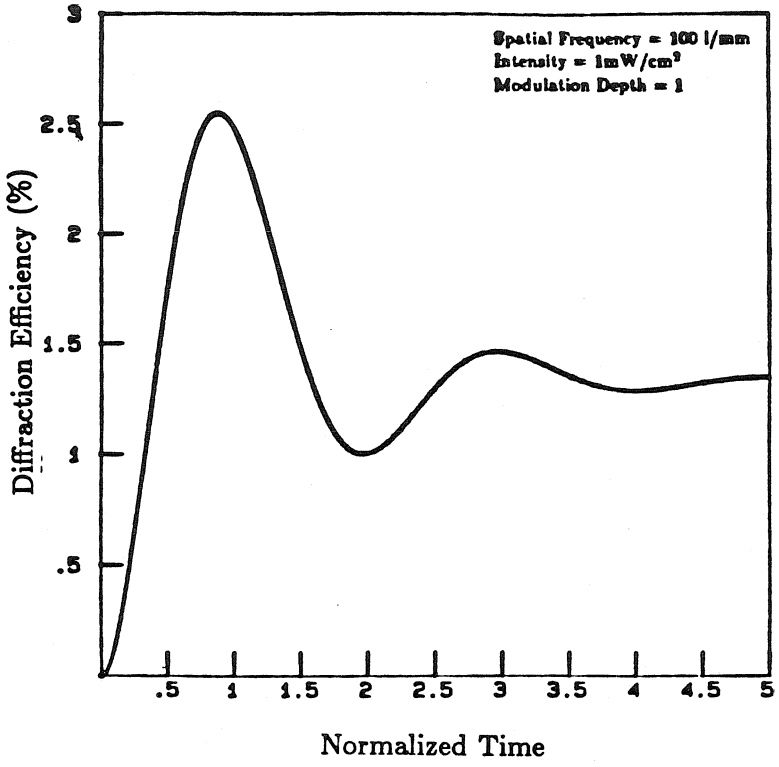

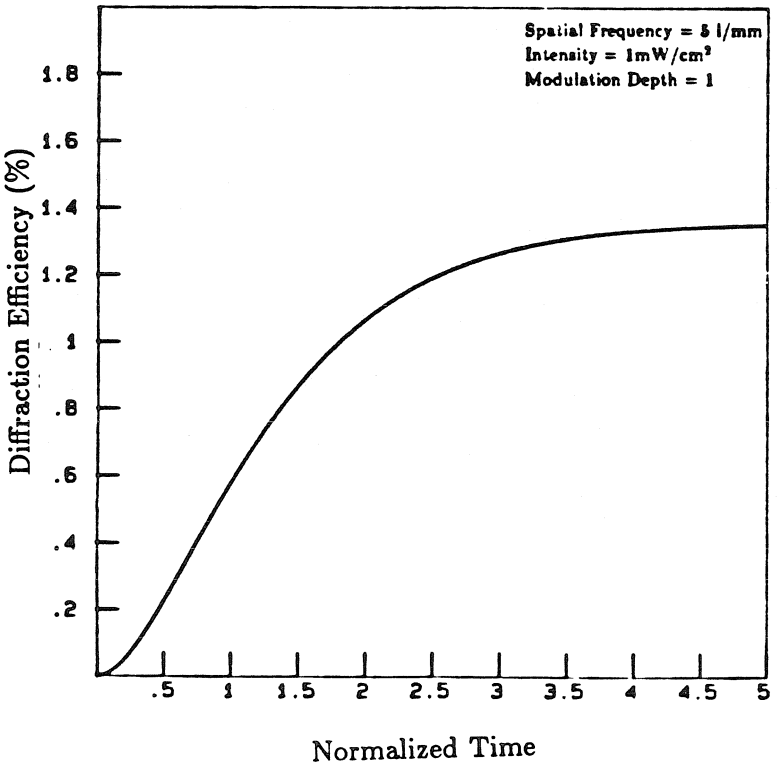

Fig. 2.7 Temporal Response of Space Charge Field: a) High Oscillatory Behavior and b)Exponential Behavior

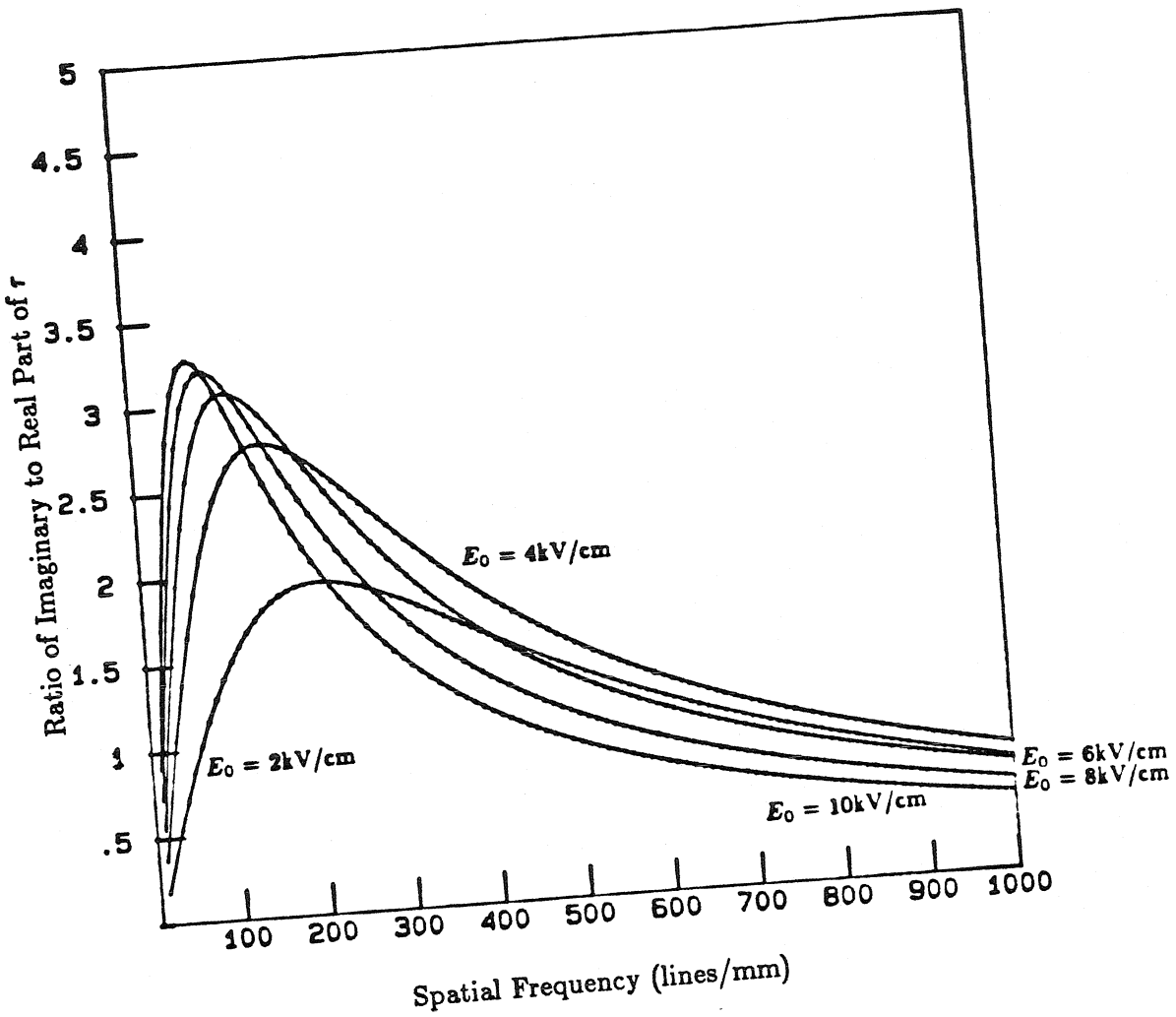

Fig. 2.8 Ratio of Real Part of τ to Imaginary Part of τ vs Spatial Frequency

The imaginary part of τ, on the other hand, results in an oscillation in the response of the crystal. Figure 2.7 shows two possible responses that may occur. The first case (Fig. 2.7a) corresponds to the recording of a grating at a spatial frequency of 100 lines/mm. In this case, the crystal exhibits a very strong oscillatory behavior. In contrast, Figure 2.7b shows the temporal behavior at 5 lines/mm and demonstrates negligible oscillatory behavior. A parameter which can be used to characterize the two cases is the ratio of the imaginary part to the real part of the time constant. In the first case, the ratio is high and as a result a number of oscillatory cycles occur before they are sufficiently damped out. In the second case, the ratio between the real and imaginary parts is low, describing the rapid damping of the oscillation term (imaginary part) by the decay term (real part). The spatial frequency dependence of the ratio between the real and imaginary parts of τ is shown in Figure 2.8. It is interesting to note that the ratio of the imaginary to real parts of the τ reaches its maximum value when the grating wavelength is equal to the drift length induced by the applied field resulting in a highly oscillatory behavior. This seems intuitively reasonable since the physical process within the crystal attempts to move the electrons from one intensity peak and recombine them with traps in the adjoining intensity peak. The recombination process results in a build-up of a field which overcompensates for the applied field. This internal field cannot be maintained and consequently decreases as electrons are transported from

regions of high space charge field. A set of damped oscillations occurs as the internal space charge field undergoes a series of overcompensation and undercompensation of the applied field.

The major disadvantage of the Kukhtarev model lies in the assumption that the modulation depth of the incident grating is small. Since the analysis is carried out only to first order, the model predicts a space charge field amplitude E_1 which is proportional to the modulation depth. However, as the modulation depth approaches unity, higher order perturbation components play an important part in predicting the recorded space charge field. In the next section, we will incorporate higher order components of the space charge field in order to extend the Kukhtarev model for higher modulation depths as well as produce profiles of the space charge field.

II.4 Higher Order Perturbation Model

The analytical model proposed by Moharam *et al.* [3] demonstrates an advantage over that of Kukhtarev *et al.* [4] by being able to predict the steady state response of the photorefractive crystal at high modulation depth. In order to combine this feature of the Moharam model, while being able to accurately predict the response of the photorefractive media in the high frequency regime, we present a higher order perturabation technique to solving Kukhtarev's set of material equations to higher order and hence higher accuracy.

As in the case of the Kukhtarev model, the space charge field, trap electron, and current densities are expanded into their Fourier series components. This method is advantageous since the important fundamental Fourier component is solved explicitly. However, because of the nonlinearities inherent in the photorefractive material equations, higher order Fourier components may affect the values of the fundamental Fourier term. Consider equation 2.13 describing the charge generation and recombination within the photorefractive crystal. The first Fourier term of the trap density (N_{D1}^{+}) can be solved by collecting terms with the same spatial frequency components such as $N_{D0}^{+}n_1$ and $N_{D1}^{+}n_0$. The inclusion of these terms were sufficient to characterize the photorefractive effect in the low modulation depth regime as demonstrated by Kukhtarev *et al.* [4]. However, since it is suspected that higher order terms have an important effect in regimes where the modulation depth approaches 1, terms such as $N_{D2}^{+}n_{-1}$ and $N_{D-1}^{+}n_2$ must be included in the solution of each component of the material parameters. In essence, the presence of higher order spatial frequencies generated by the nonlinearities in the photorefractive recording process can affect the strength of the fundamental and lower order Fourier components. The resulting expansion of each material equation will then result in an infinite set of equations corresponding to each spatial frequency components. In addition, these equations will be nonlinearly (multiplicative) coupled to one another making an analytical solution difficult to discover.

Another look at the first order solution as derived by Kukhtarev *et al.* shows a linear dependence of the material parameters to the modulation depth m. It is reasonable to assume then that higher Fourier orders, which arise through the multiplicative nonlinerities (*i.e.*, they are a product of only two unknown parameters, such as n(x,t)E(x,t)), would depend on higher powers of m. As a result, the effect of these higher order Fourier components on the fundamental component would most likely depend on even higher powers of m. Based on this motivation, we choose to further expand each Fourier component by a power series in the modulation depth, m. Hence the expressions for the space charge field, electron, trap and current densities can be written as:

$$N_D^+(x,t) = N_{Deq}^+ + \sum_{r=1}^{\infty}\sum_{s=1}^{\infty} m^s N_{Drs}^+(t) e^{ikrx} + c.c. \qquad [2.33]$$

$$n(x,t) = n_0 + \sum_{r=1}^{\infty}\sum_{s=1}^{\infty} m^s n_{rs}(t) e^{ikrx} + c.c. \qquad [2.34]$$

$$J(x,t) = J_0 + \sum_{r=1}^{\infty}\sum_{s=1}^{\infty} m^s J_{rs}(t) e^{ikrx} + c.c. \qquad [2.35]$$

$$E(x,t) = E_0 + \sum_{r=1}^{\infty}\sum_{s=1}^{\infty} m^s E_{rs}^+(t) e^{ikrx} + c.c.. \qquad [2.36]$$

The solution is found by substituting the above equations into the material equations 2.13-2.16. Terms are grouped primarily by their spatial Fourier components and then by powers in m. Solutions for lower powers in m are then used to solve for higher order terms. The above expansion is equivalent to declaring m as a perturbation parameter and solving for each Fouier-power component through successive

iteration. Because of the multiplicative nonlinearities, it relatively easy to determine which components multiply to give the Fourier and power component of interest. The method by which this expansion eases the bookkeeping is demonstrated by an example summarized below as well as in the Appendix.

As mentioned previously, most applications of photorefractive crystals only require the amplitude of the first fundamental frequency component of the space charge. Consider a steady state expansion of the first harmonic component to a second order in m. In other words, we wish to derive the first two nonzero components of $E_{1,s}$ in the steady state regime. The actual analytical derivation is presented in the Appendix but the general procedure is reviewed below.

Since the material equations describing the photorefractive process involve only a simple product between independent variables (such nN_D^+ in equation 2.13 and nE in equation 2.16), it is easy to determine which Fourier orders will combine to contribute to other Fourier components. Assume first that the DC component of the space charge field is undepleted (*i.e.* $E_{00} >> E_{10}, E_{20}$). The first term E_{11} can then be solved as a function of E_0 and yields a result identical to that derived by Kukhtarev,

$$E_{11} = \frac{m}{2} \frac{E_0 + iE_d}{1 + (E_0 + iE_d)/E_q}. \qquad [2.37]$$

This solution combines with components having the same spatial frequency to produce terms with twice the spatial frequency (i.e. terms with the Fourier component

e^{i2kx}). This term is explicitly written in the Appendix and has a dominant component proportional to m^2 (ie.$E_{20} = E_{21} = 0$). This solution in turn combines with spatial frequency components e^{-ikx} to affect terms in the fundamental frequency. Since the terms with frequency e^{i2kx} are proportional to m^2 and terms with frequency e^{-ikx} are proportional to m, they will combine to form terms in e^{ikx} proportional to m^3. Hence the first harmonic component of the space charge field will be of the form

$$E_1 = mE_{11} + m^3E_{31}. \qquad [2.38]$$

The explicit expression of E_{31} is also presented in the appendix.

It is possible to derive analytical expressions for higher order terms using these techniques; however, the results tend to be very cumbersome. Dynamic solutions are also possible, but they result in a large number of time constants yielding very little physical intuition. Consequently, utilization of the higher order model is best done by numerical simulation. By applying these numerical techniques, profiles of the space charge distribution and electric field strength within the crystal can be generated. Figures 2.9-2.14 show a number of numerically simulated trap density and space charge field profiles for various of applied field strengths, spatial frequencies, and modulation depths for a BSO crystal in the steady state regime. The trap densities depicted in these figures have been normalized to the equilibrium trap concentration which is approximately 10^{16} cm^{-3} in BSO. These calculation was

performed for 100 Fourier orders and a power series expansion in m of 100 orders. These profiles took several hours on a VAX 750 to compute.

Figure 2.9 shows the trap density and space charge field for a grating of 100 l/mm, an applied field of 6kV/cm, and a modulation depth of 1 being recorded in a BSO crystal. The trap density exhibits three distinct regions: a highly localized positive region, a highly localized negative region, and the remaining neutral region. Under these operating conditions, the drift length is approximately 9μm and translates to 0.9 in the normalized distance scale. As a result, photogenerated electrons from throughout the intensity pattern are swept into the regions where the intensity is zero. In these regions, the electrons recombine and cannot be reexcited. Consequently, a large region of negative charge collects in areas of zero light intensity. Because the applied field results in an asymetric direction for current flow (in this case the applied field is oriented toward the right), the compensating region of positive charge is located immediately to the right of the region of high negative charge. In the remaining regions, the charge density remains neutral resulting from a balance between the excitation and recombination rates. The size of localized positively and negatively charged region results from a diffusive process. Under these operating conditions, the diffusion length is approximately 0.6 μm corresponding to 0.06 distance units. This corresponds to approximately one half the width of the highly negatively charged region as well as the highly positively charged region.

The space charge field profile that is generated by the derived trap density pattern shows a comb-like field pattern. As expected the space charge field is highly non-sinusoidal and agrees with the profiles generated by the Moharam model, which are accurate in this operating regime.

Figure 2.10 shows the trap density and field strengths for E_0 = 6kV/cm, f = 1000 l/mm, and m = 1. In this case, the trap density profile is similar to that shown for the 100 l/mm case (Fig. 2.9) but with a much broader region of positively and negatively charged carriers. This broadening is attributed to an increased importance of diffusion effects as well as saturation of ionized traps. With the spatial frequency used in this case, the diffusion length is approximately 0.6 distance units. The consequence of this broadening in the trap density results in a more sinusoidal looking space charge field, as predicted by the Kukhtarev model.

Figures 2.11 and 2.12 demonstrate the case when there is no applied field (E_0 = 0 kV/cm). In this case, the modulation depth is unity and the spatial frequencies are 100 and 1000 l/mm, respectively. In the 100 l/mm case (Fig 2.11), the trap density profile is characterized by a symmetric function which is spatially limited around the region of minimum incident intensity. The width of this region is approximately one diffusion length (0.06 distance units) in each direction. This leads to the highly nonsinusoidal space charge field profile shown in the figure. In contrast, the 1000 l/mm case (Fig. 2.12) has a trap density profile which extends

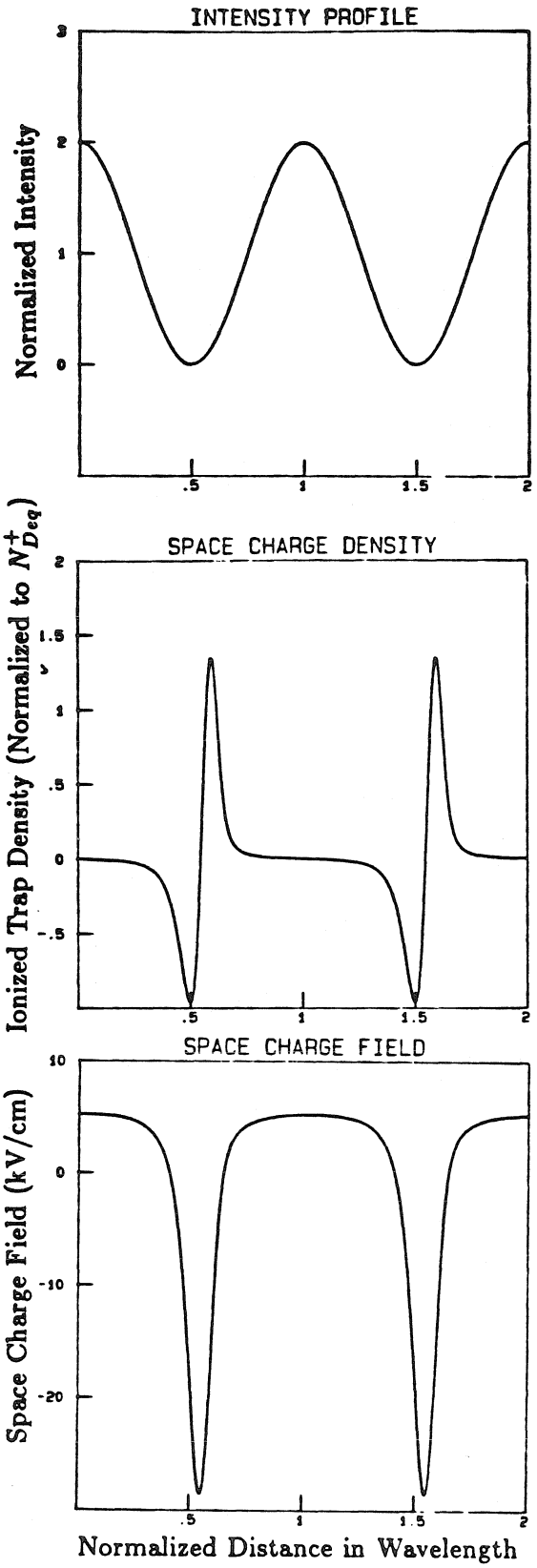

Fig. 2.9 Trap Density and Space Charge Profile of a Grating Recorded on a BSO crystal (E_0= 6kV/cm, f = 100 lines/mm, m = 1)

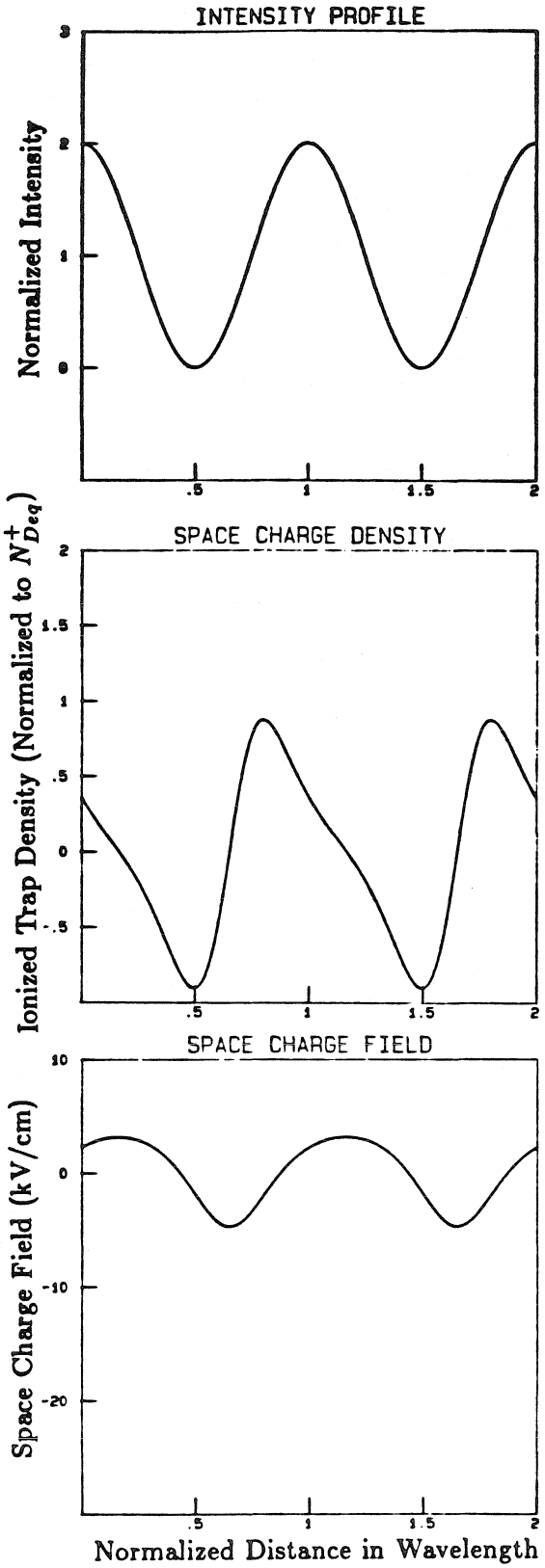

Fig. 2.10 Trap Density and Space Charge Profile of a Grating Recorded on a BSO crystal (E_0= 6kV/cm, f = 1000 lines/mm, m = 1)

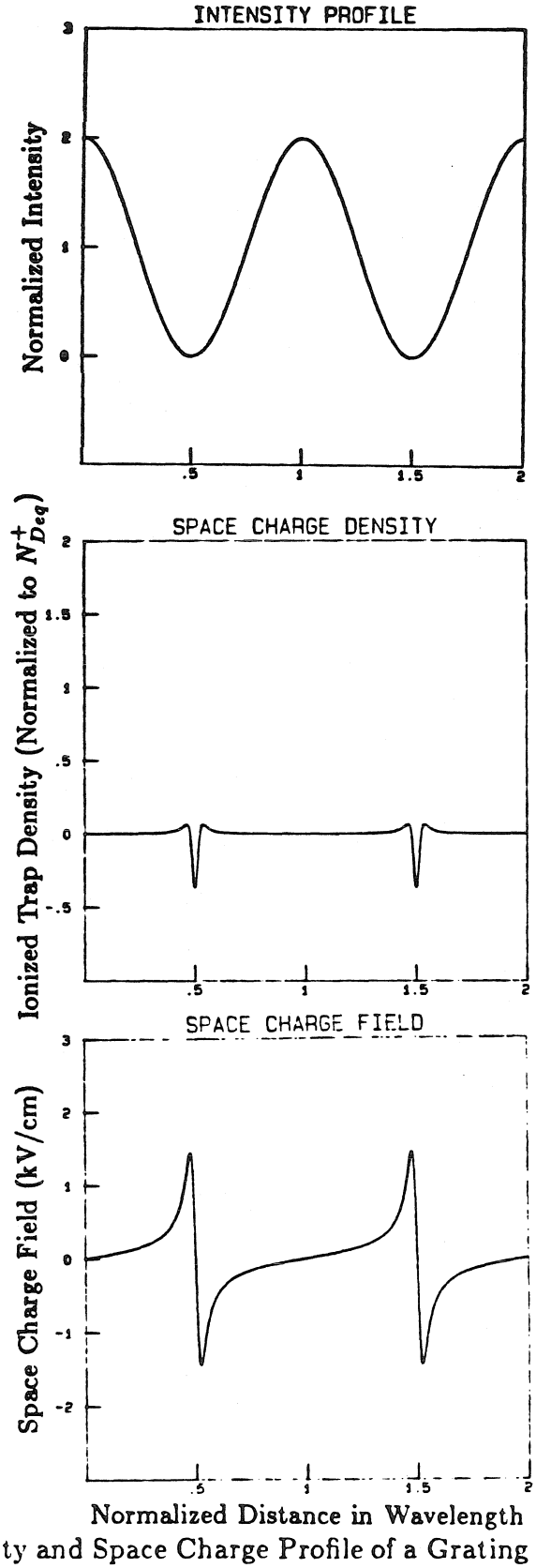

Fig. 2.11 Trap Density and Space Charge Profile of a Grating Recorded on a BSO crystal (E_0= 0kV/cm, f = 100 lines/mm, m = 1)

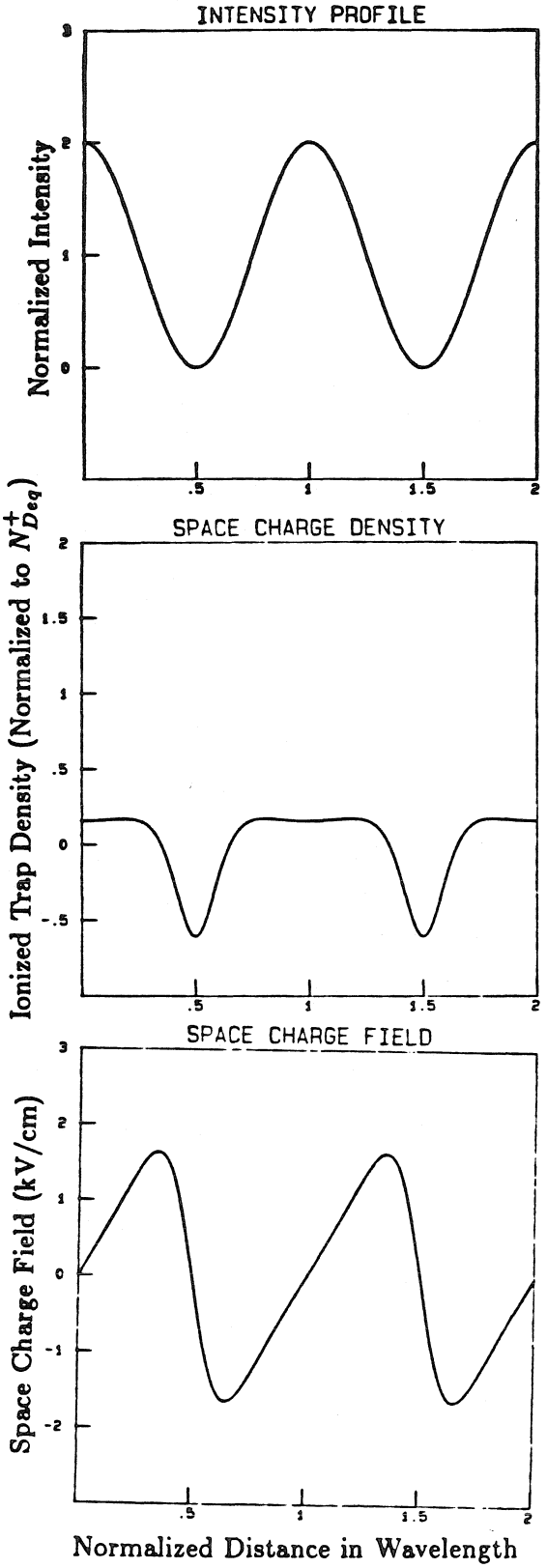

Fig. 2.12 Trap Density and Space Charge Profile of a Grating Recorded on a BSO crystal (E_0= 0kV/cm, f = 1000lines/mm, m = 1)

through the entire grating wavelength due to the larger normalized diffusion length. This results in a more sinusoidal-looking space charge field yielding a fundamental Fourier component larger than that derived from the 100 l/mm case.

Figures 2.13 and 2.14 show the space charge field profile for a 0.5 modulation depth grating being recorded at 100 and 1000 l/mm, respectively with an applied field of 6kV/cm. In both cases the space charge field is almost sinusoidal. This results because the contribution from higher Fourier orders is lessened at lower modulation depths, as expressed by the analytical derivations from the higher order model.

Figure 2.15 shows the strength of each of the Fourier components when an intensity grating of spatial frequency 100 and 1000 lines/mm is recorded in a BSO crystal. Both the drift dominated ($E_0 = 6kV/cm$) and diffusion dominated ($E_0 = 0kV/cm$) cases are plotted. As expected, the contribution of higher order harmonic components to the space charge field profile are significantly higher for low frequency gratings than high frequency gratings. In the high frequency regime, the higher order terms become negligible when compared to the fundamental component.

II.5 Comparison between the Moharam, Kukhtarev and Higher Order Models

The higher order model described in the previous section allows one to analyze the accuracy of the Moharam and Kukhtarev analytical models in the steady state

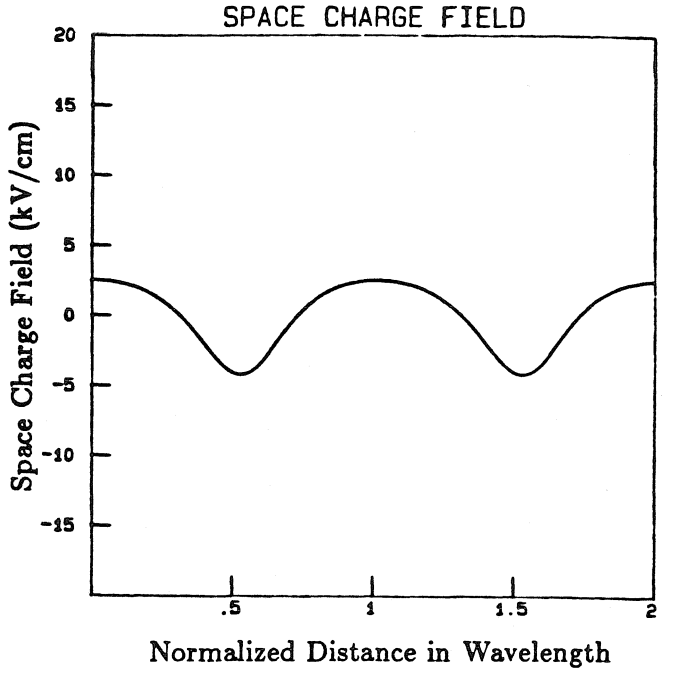

Fig. 2.13 Space Charge Profile of a Grating Recorded on a BSO crystal (E_0= 6kV/cm, f = 100 lines/mm, m = 0.5)

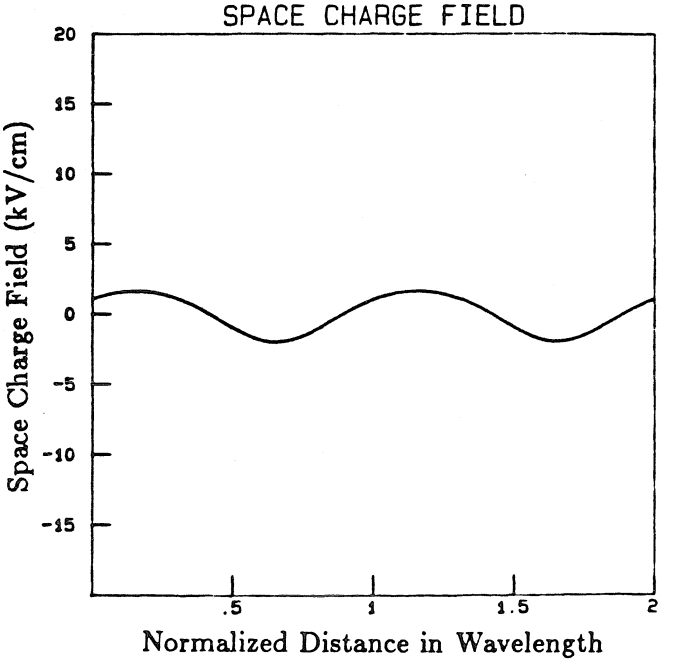

Fig. 2.14 Space Charge Profile of a Grating Recorded on a BSO crystal (E_0= 6kV/cm, f = 1000 lines/mm, m = 0.5)

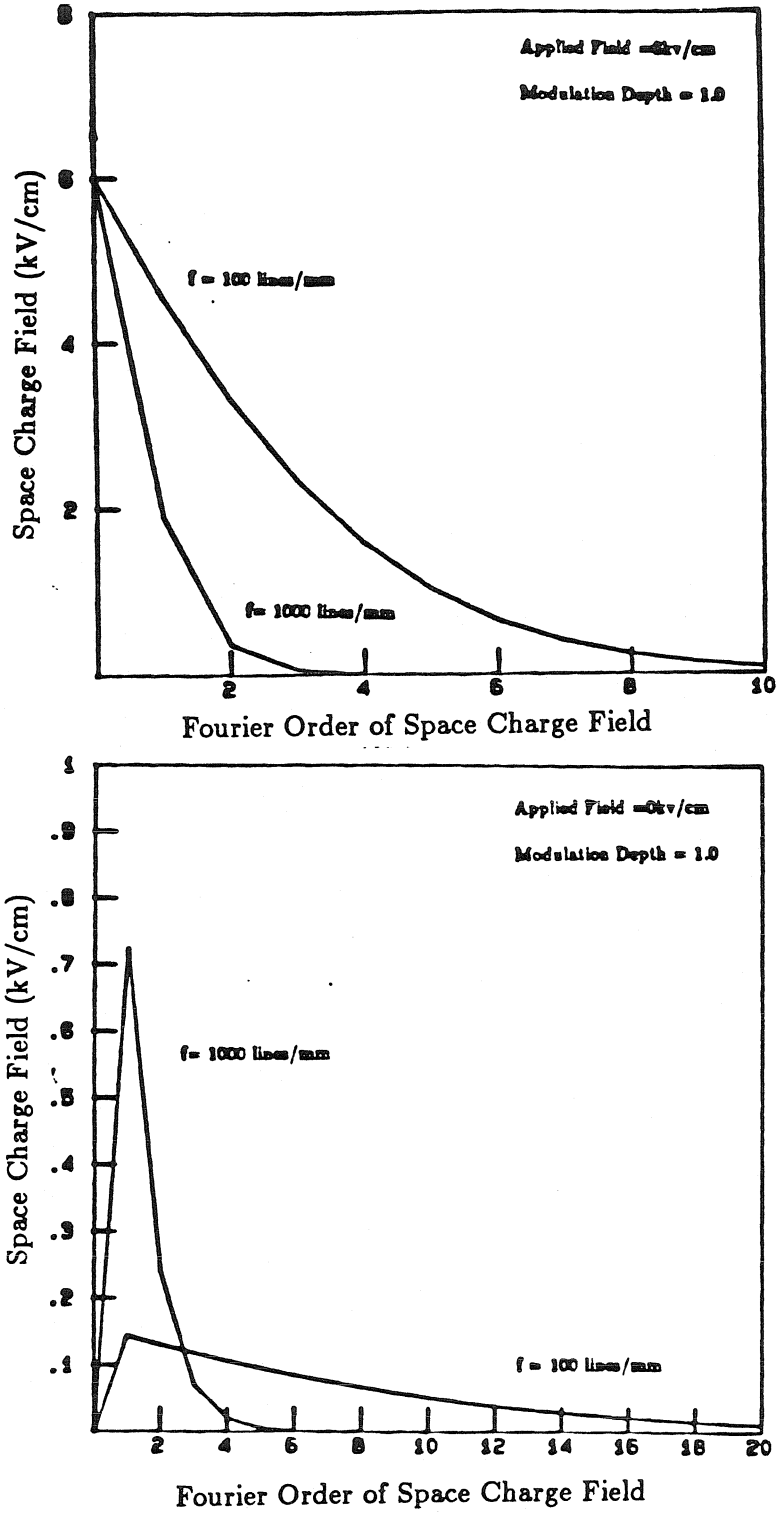

Fig. 2.15 Fourier Spectrum of Space Charge Field Profiles

regime. Figure 2.16 shows the first harmonic component of the space charge field E_1 as a function of modulation depth using all three models. In this figure a grating of 100 lines/mm recorded in a BSO crystal was simulated. As expected, both the Kukhtarev and Moharam models agree with the numerical simulations in the low modulation depth regime. However, in high modulation depth regime, the solution of the Kukhtarev model deviates greatly from the higher order solution. In contrast, the Moharam model accurately predicts the space charge field component over the full range. It is interesting to note that the Moharam model still overpredicts the actual response of the crystal due to its assumption of an infinite trap density (or constant recombination time). Figure 2.17 shows the E_1-m relationship for a 1000 line/mm grating. In this case, the Kukhtarev model shows good agreement with the numerical simulations over the full range of modulation depths. However, because of the inability of the Moharam model to predict a trap limited screening field, the model is inaccurate over the entire range.

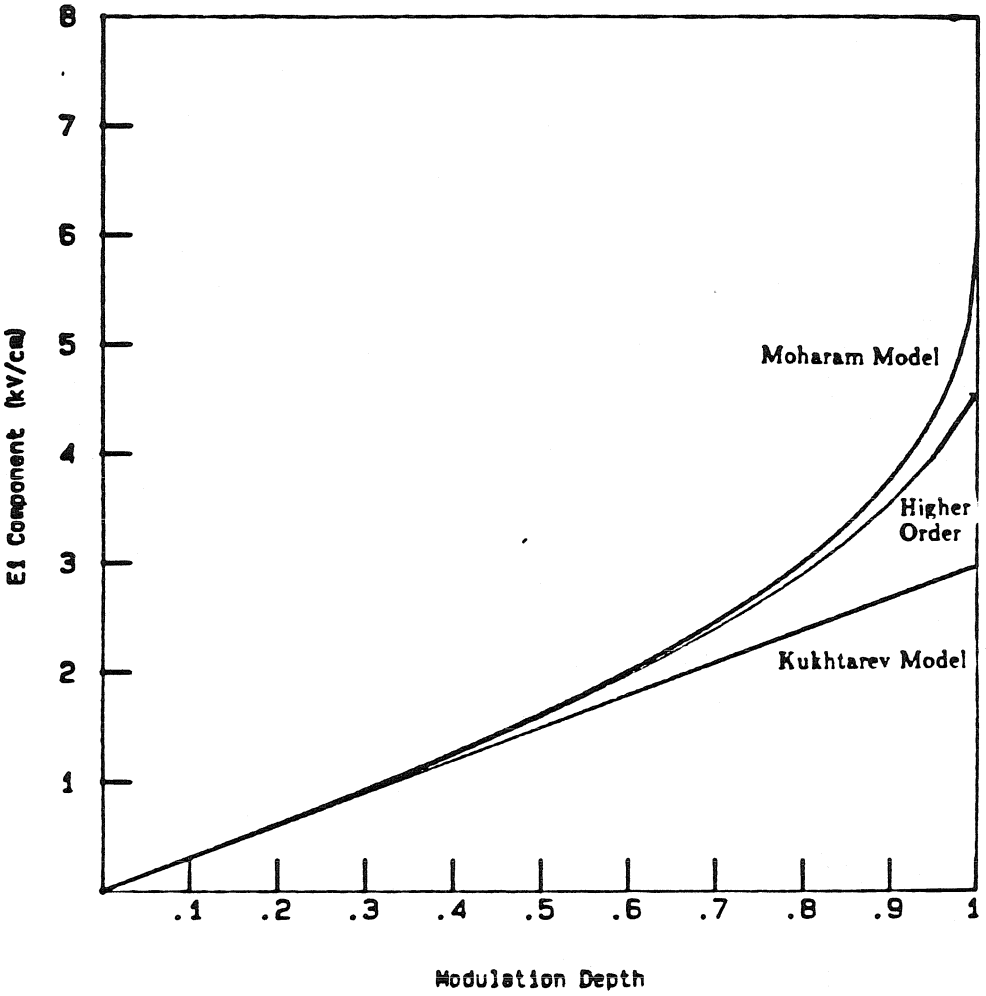

Fig. 2.16 $|E_1|$ vs Modulation Depth for Moharam, Kukhtarev and Higher Order Models at f = 100 lines/mm.

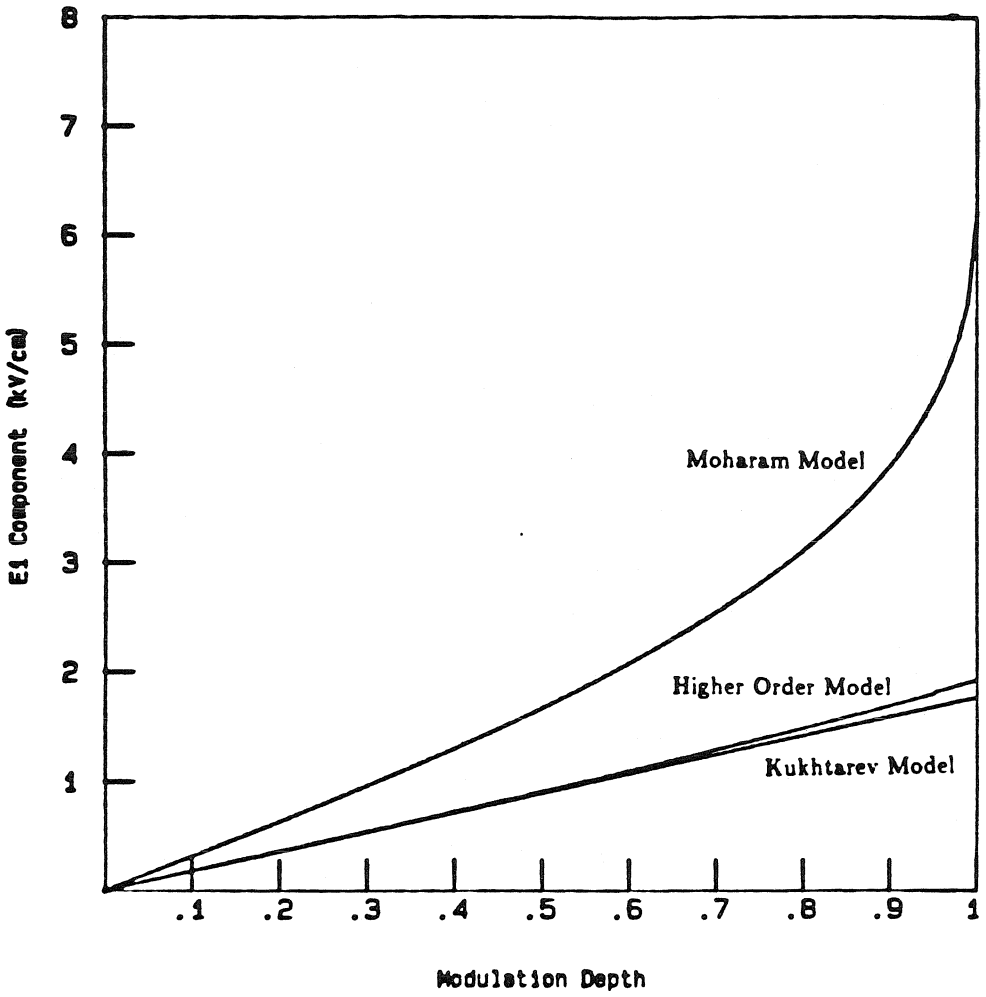

Fig. 2.17 $|E_1|$ vs Modulation Depth for Moharam, Kukhtarev and Higher Order Models at f = 1000 lines/mm.

Table 2.1 Material Parameters for Bismuth Silicon Oxide (BSO)

Parameter	Symbol	Value	Ref
Mobility	μ	$0.03 cm^2/V\text{-}s$	[24]
Carrier Lifetime	τ	$5x10^{-6}$ s	[24]
Donor-like Trap Density	N_D	$10^{19} cm^{-3}$	[24]
Dark Ionized Trap Density	N^+_{Deq}	$10^{16} cm^{-3}$	[24]
Recombination Coefficient	γ_r	$2x10^{11} cm^3/s$	[24]
Dielectric Constant	ϵ	56	[24]

		488	515	633 nm	
Index of Refraction	n_0	2.650	2.615	2.530	[23]
Optical Absorption	α	7.0	2.8	0.6 cm^{-1}	[23]
Electrooptic Coefficient	r_{41}	4.52	4.51	4.41 pm/V	[23]
Photo-Ionization Cross Section	s_g	–	0.42	– cm^2/J	[24]

APPENDIX

Second Order Expansion of the E_1 Component of the Space Charge Field in Steady State

This appendix will focus on deriving the first harmonic component of the space charge field that is induced when an intensity grating is incident on a photorefractive BSO crystal. The method described here extends the first order perturbation expansion forwarded by Kukhtarev[4] to higher orders. An explicit expression for the second order expansion of the E_1 component of the steady state space charge field will be derived.

Consider an intensity grating of the form

$$I(x) = I_0(1 + mcoskx) \qquad [A.1]$$

incident on a BSO crystal. The material equations which govern the photorefractive effect are described by equations 2.13-2.16. By combining equations 2.14 and 2.16, the steady state material equations can be written as:

$$sN_D I(x) = \gamma_r n N_D^+ \qquad [A.2]$$

$$\frac{dE}{dx} = \frac{e}{\epsilon}(N_D^+ - N_A) \qquad [A.3]$$

$$\mu e\left[n\frac{dE}{dx} + E\frac{dn}{dx}\right] + k_B T\mu\frac{d^2n}{dx^2} = 0 \qquad [A.4]$$

Equation A.4 corresponds to the fact that the time derivative of the current density is zero in the steady state regime. In order to derive an explicit expression for the

induced space charge field, the solutions to field, electron and trap densities are assumed to be of the form:

$$E = E_0 + \sum_{r=1}\sum_{s=1} E_{rs} m^s e^{irkx} + \text{c.c.} \qquad [A.5]$$

$$N_D^+ = N_{Deq}^+ + \sum_{r=1}\sum_{s=1} N_{Drs}^+ m^s e^{irkx} + \text{c.c.} \qquad [A.6]$$

$$n = n_0 + \sum_{r=1}\sum_{s=1} n_{rs} m^s e^{irkx} + \text{c.c..} \qquad [A.7]$$

Hence the amplitude of the fundamental component of the space charge field will be given by

$$E_1 = mE_{11} + m^2 E_{12} + m^3 E_{13} + ... \qquad [A.8]$$

Since m is always less than 1, we can consider m as a perturbation parameter in solving the material equations. By substituting equations A.5-A.7 in equations A.2-A.4 and collecting terms for the non-harmonic spatial components (*i.e.*, DC terms), results in the following relationship

$$n_0 = \frac{\sigma N_d I_0}{\gamma N_{Deq}^+}. \qquad [A.9]$$

Likewise by collecting terms for which r=1 and s=1, and using equations A.9, the expression for E_{11} is given by:

$$E_{11} = -i\frac{E_q}{2}\frac{E_0 + iE_d}{E_0 + i(E_q + E_d)} \qquad [A.10]$$

where $E_d = k_B T k/e$ and $E_q = eN^+_{Deq}/\epsilon k$ are the characteristic fields due to diffusion and space charge. The above expression is identical to that derive by Kukhtarev which corresponds to a first order solution of the material equations. In order to extend the solution of the fundamental component of the space charge field to second order, components with higher spatial frequencies must be incorporated into the solution. Since the nonlinearities in the material equations are simple products between the unknown variables, it is relatively easy to determine the lower order terms which affect a given higher order term. In this case, we would like to derive the higher terms in the E_1 series. The next significant term which would produce terms with spatial frequency k is a product between a term with frequency 2k and a term with frequency -k. Hence an expression for E_2 must first be derived. By collecting terms with spatial frequency 2k and substituting the first order expressions for E_1 and their complex conjugates, it can be shown that $E_{02} = E_{12} = 0$. In addition, the first nonzero component, E_{22}, is given by

$$E_{22} = i\frac{E_q}{8} K_1(1 - K_1) D_1 \qquad [A.11]$$

$$K_1 = \frac{E_0 + iE_d}{E_0 + i(E_d + E_q)} \qquad [A.12]$$

$$D_1 = \frac{E_0 + i(2E_d + E_q)}{E_0 + i(2E_d + E_q/2)}. \qquad [A.13]$$

Thus, the dominant term of the second spatial frequency component of the space

charge field is given by

$$E_2 = m^2 E_{22}. \qquad [A.14]$$

In order to solve for the second term of the fundamental Fourier components, components with spatial frequency 2k must be combined with components with spatial frequency -k. Utilizing equation A.11 and the corresponding equations for the electron and trap densities (n_{22} and N^+_{D22}) in conjunction with the conjugate expressions for E_{-11}, n_{-11}, and N^+_{D-11}, the expression for E_{13} can be derived.

$$E_{13} = -i\frac{E_q}{8}[D_1 K_1 |1 - K_1|^2 D_2 + |K_1|^2 (1 - K_1)(1 - D_1) D_3] \qquad [A.15]$$

where

$$D_2 = \frac{E_0 + i(E_d + E_q/2)}{E_0 + i(E_d + E_q)} \qquad [A.16]$$

$$D_3 = \frac{E_0 + i(E_d - E_q)}{E_0 + i(E_d + E_q)}. \qquad [A.17]$$

Through further examination of the nonlinearities in the material equation, it can be shown that $E_{14} = 0$. Hence the fundamental component of the space charge field can be written to second order as

$$E_1 = mE_{11} + m^3 E_{13} + O(m^5). \qquad [A.18]$$

References for Chapter 2

1. F. S. Chen, "Optically Induced Change of Refractive Indices in $LiNbO_3$ and $LiTaO_3$", *Jour. Appl. Phys.*, **40**, 3389 (1969).

2. J.J. Amodei, "Analysis of Transport Processes During Holographic Recording in Insulators", *RCA Rev.*, **32**, 185 (1971).

3. M. G. Moharam, T. K. Gaylord, R. Magnusson and L. Young, "Holographic Grating Formation in Photorefractive Crystals with Arbitrary Electron Transport Lengths", *Jour. Appl. Phys.*, **50**, 5642 (1979).

4. N. V. Kukhtarev, V. B. Markov, S. G. Odulov, M. S. Soskin and V. L. Vinetskii, " Holographic Storage in Electro-optic Crystals. I. Steady State", *Ferroelectrics*, **22**, 949 (1979).

5. J. Feinberg, D. Heiman, A. R. Tanguay, Jr. and R. W. Hellwarth, "Photorefractive Effects and Light Induced Charge Migration in Barium Titanate", *Jour. Appl. Phys.*, **51**, 1297 (1980).

6. S. F. Su and T. K. Gaylord, "Refractive Index Profile and Physical Process Determination in Thick Gratings in Electro-optic Crystals", *Appl. Opt.*, **15**, 1947 (1976).

7. G. C. Valley, "Erase Rates in Photorefractive Materials with Two Photoactive Species", *Appl. Opt.*, **22**, (1983).

8. E. Ochoa, F. Vachss and L. Hesselink, "Higher-order Analysis of the Photore-

fractive Effect for Large Modulation Depths", *Jour. Opt. Soc. Am. A*, **3**, 181 (1986).

9. H. Kogelnik, "Coupled Wave Theory for Thick Hologram Gratings" *Bell. Sys. Tech. Jour.*, **48**, 2909 (1969).

10. D. L. Staebler and J. J. Amodei, "Coupled Wave Analysis of Holographic Storage in $LiNbO_3$", *Jour. Appl. Phys.*, **43**, 1042 (1972).

11. V. L. Vinetskii, N. V. Kukhtarev, S. G. Odoulov and M. S. Soskin, "Dynamic Self-Diffraction of Coherent Light Beams", *Sov. Phys. Usp.* **22**, 742 (1979).

12. N. V. Kukhtarev, V. B. Markov, S. G. Odulov, M. S. Soskin and V. L. Vinetskii, " Holographic Storage in Electro-optic Crystals. II. Self Amplification", *Ferroelectrics*, **22**, 961 (1979).

13. A, Marrakchi, R. V. Johnson and A. R. Tanguay, Jr., "Polarization Properties of Photorefractive Diffraction in Electrooptic and Optically Active Sillenite Crystals (Bragg Regime)", *Jour. Opt. Soc. Am. B"*, **3**, 321 (1986).

14. L. M. Connors, H. W. Khamis and T. J. Hall, "Short Wavelength Asymptotic Framework for Wave Mixing in Photorefractive Media", *Jour. Opt. Soc. Am. A*, **2**, 1035 (1985).

15. D. Yevick and L. Thylen, "Analysis of Gratings by the Beam Propagation Method", *Jour. Opt. Soc. Am.*, **72**, 1084 (1982).

16. J. P. Huignard and A. Marrakchi, "Coherent Signal Beam Amplification in

Two-Wave Mixing Experiments with Photorefractive $Bi_{12}SiO_{20}$", *Opt. Comm.*, **38**, 249 (1981).

17. R. W. Eason and A. M. C. Smout, "Bistability and Noncommutative Behavior of Multiple-Beam Self-Pulsing and Self-Pumping in $BaTiO_3$", *Opt. Lett.*, **12**, 51 (1987).

18. J. P. Huignard and A. Marrakchi, "Coherent Signal Beam Amplification in Two Wave Mixing Experiments with Photorefractive $Bi_{12}SiO_{20}$ Crystals", *Opt. Comm.*, **38**, 249 (1981).

19. J. F. Lam and W. P. Brown, "Optical Resonators with Phase Conjugate Mirrors", *Opt. Lett.*, **5**, 61 (1980).

20. Ph. Refregier, L. Solymar, H. Rajbenbach and J. P. Huignard, "Two Beam Coupling in Photorefractive $Bi_{12}SiO_{20}$ Crystals with Moving Gratings: Theory and Experiments", *Jour. Appl. Phys.*, **58**, 45 (1985).

21. M. Cronin-Golomb, B. Fischer, J. O. White and A. Yariv "Theory and Application of Four-Wave Mixing in Photorefractive Media", *IEEE Jour. Quant. Elec.*, **QE-20**, 12 (1984).

22. P. Yeh, "Fundamental Limit of the Speed of Photorefractive Effect and its Impact on Device Applications and Material Research", *Appl. Opt.*, **26**, 602 (1987).

23. A. R. Tanguay, Jr., "The Czochralski Growth and Optical Properties of Bis-

muth Silicon Oxide", Ph.D. dissertation, Yale University, New Haven, Conn.,(1977).

24. G. C. Valley and M. B. Klein, "Optimal Properties of Photorefractive Materials for Optical Data Processing", *Opt. Eng.*, **22**, 704 (1983).

III. THE PHOTOREFRACTIVE INCOHERENT TO COHERENT CONVERTER

I. Introduction

High performance spatial light modulators (SLMs) are essential in many optical information processing and computing applications in order to convert incoherent images to coherent replicas suitable for subsequent processing [1,2]. A typical spatial light modulator consists of a photosensitive element to capture the incoherent light image and an optical modulator element to impress the incoherent image onto a coherent readout beam. A particularly important class of spatial light modulators employs photorefractive crystals that combine both photosensitive and electro-optic modulation functions within the same medium. Examples of electro-optic spatial light modulators that utilize photorefractive crystals include the Pockels Readout Optical Modulator (PROM) [3] and the PRIZ [4].

During operation of the Pockels Readout Optical Modulator, the input image-bearing beam creates photoinduced carriers which are longitudinally separated by an applied bias electric field. This charge separation produces a space-variant division of the applied field across the electro-optic crystal and one or more dielectric blocking layers as shown in Figure 3.1a. The local birefringence of the medium depends on the longitudinal component of the local electric field, and hence can be sensed by a polarized readout beam observed through an exit analyzer. In the PRIZ,

the same charge generation and separation process is utilized, with the exception that the crystallographic orientation is chosen to emphasize readout sensitivity to the transverse components of the induced electric field distribution, as shown in Figure 3.1b.

The PROM and the PRIZ are typically limited in spatial frequency response to an order of 10 l/mm at their optimum optical exposure [5] and hence are limited to relatively modest bandwidth optical processing and computing applications. The physical configurations of the PROM and PRIZ devices do not lend themselves readily to exploitation of the remarkably high spatial bandwidths available in holographic configurations, in which the input image is encoded on a spatial carrier (as shown in Figure 3.1c). Even when utilizing the same electro-optic crystal as in the PROM and PRIZ (typically Bismuth Silicon Oxide (BSO)), holographic recording configurations employing transverse applied electric fields and no blocking layers have been shown to exhibit spatial frequency bandwidths in excess of 2000 l/mm [6]. However, such purely holographic recording requires the input of image dependant information on one of two coherent input beams, and as such cannot be directly utilized for performing the incoherent to coherent conversion function.

A fourth distinct type of photorefractive spatial light modulator has been independently proposed by Kamshilin and Petrov [7] and by the author and his coworkers [8-10], which combines the incoherent to coherent conversion function with holo-

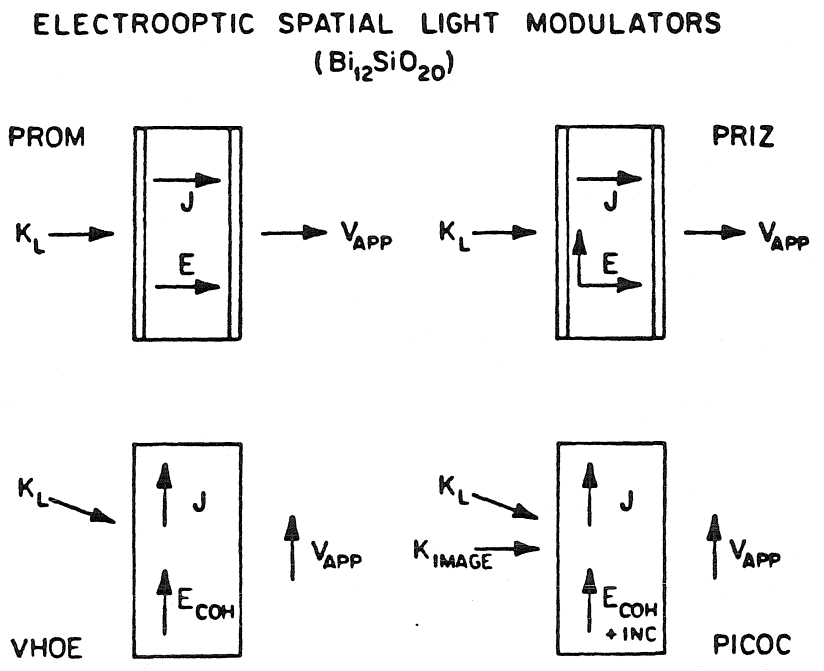

Fig. 3.1 Schematic Diagram of Four Spatial Light Modulators Using Bi_12SiO_20: a) Volume Holographic Optical Element (VHOE) b) PROM c) PRIZ d) Photorefractive Incoherent to Coherent Converter (PICOC)

graphic recording process, and as such exhibits several advantages of each. As in the holographic recording case, a transverse applied electric field is used in conjunction with two uniform coherent writing beams to produce a volume grating that is then selectively modified by a third incoherent beam encoded with the information content to be stored or converted. This configuration is shown schematically in Figure 3.1d. This Photorefractive Incoherent to Coherent Optical Converter (PICOC) [8-10] is a device capable of recyclable real time operation, is characterized by an enhanced spatial frequency response, and is much simpler to construct than the PROM or PRIZ. In addition, the PICOC device configuration allows its use in many quasi-holographic techniques (such as optical phase conjugation), which in turn leads to potentially novel optical information processing and computing architectures [11-13].

The photorefractive incoherent to coherent conversion process is described in the following section along with alternative sequencing schemes and optical implementations. Section 3 analyzes the steady state response of the conversion process through both the Kukhtarev model and a higher order perturbation model similar to that described in chapter 2. Important criteria such as the linearity and frequency response of the converter are discussed. In section 4, the perturbation analysis is extended to analyze the temporal response of PICOC and its implications on various sequencing architectures. Conclusions and further research regarding PICOC

are presented in section 5.

III.2 Photorefractive Incoherent to Coherent Conversion

III.2.1 Physical Principles

The photorefractive incoherent to coherent optical conversion (PICOC) process is perhaps best understood as an extension of the more familiar holographic recording process in a photorefractive medium. The physical principles governing such recording are briefly reviewed in this section while greater mathematical detail is presented in following sections and the appendix. This extension of the recording process to include PICOC allows for at least three different temporal modes for sequencing the coherent grating with respect to the incoherent image. These modes are identified and compared in this section. In addition, two alternative optical architectures are defined, and converted images generated by one representative configuration are presented.

In the photorefractive incoherent to coherent optical conversion (PICOC) process, an incoherent image is focused in the volume of the photorefractive material in addition to the coherent beams that form a uniform grating. In regions where the incoherent image has a high intensity distribution, the space charge field pattern resulting from the coherent grating will be erased. Conversely, in regions where the incoherent image is weak, the space charge grating will remain relatively unaffected. This spatial modulation of the coherent grating by the incoherent image can then be

transferred onto a coherent readout beam by reconstructing the holographic grating. In regions where the grating remains unaffected, *i.e.* the incoherent image is dark, the diffracted output will be bright. In the erased regions, *i.e.* where the incoherent image is bright, the diffracted light will be attenuated. The spatial modulation of the coherent reconstructed beam will then be a negative replica of the input incoherent image as shown in Figure 3.2. It should be noted here that a related image encoding process can be implemented non-holographically by premultiplication of the image with a grating [15].

III.2.2 Modes of Operation

The ability of photorefractive crystals to store the charge patterns written on the material allows PICOC to operate in several different modes. These include the grating erasure mode (GEM; Fig. 3.3), the grating inhibition mode (GIM; Fig. 3.4), and the simultaneous erasure/writing mode (SEWM; Fig. 3.5).

In the grating erasure mode (GEM), shown schematically in Figure 3.3, a uniform grating is first recorded by interfering two coherent writing beams in the photorefractive crystal. The writing beams are turned off, and this grating is then selectively erased by incoherent illumination of the crystal with an image-bearing beam. A probe beam is then used to reconstruct a coherent replica of the incoherent image.

In the grating inhibition mode (GIM), shown schematically in Figure 3.4, the

PHOTOREFRACTIVE INCOHERENT-TO-COHERENT OPTICAL CONVERSION:

Selective Grating Erasure

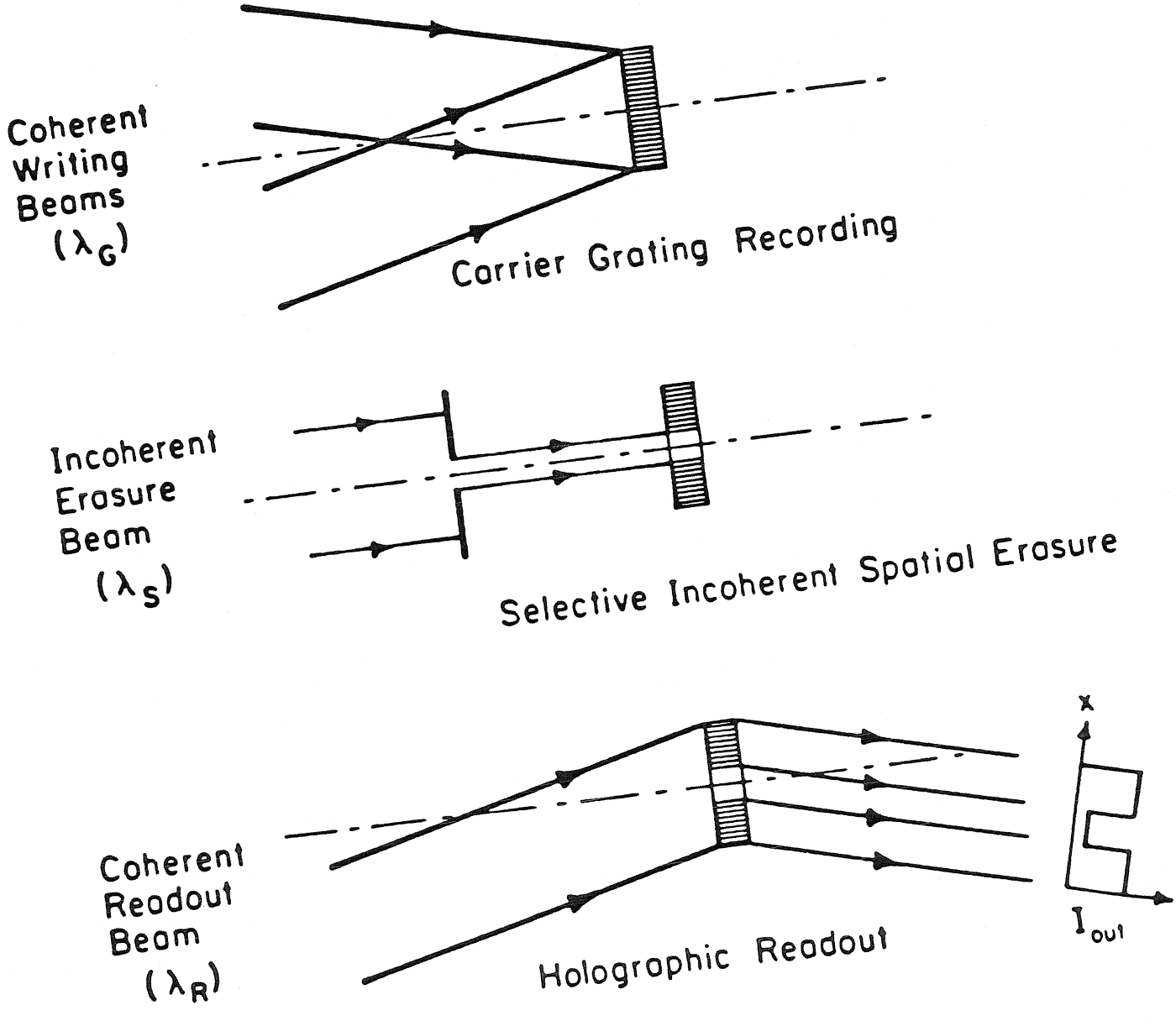

Fig. 3.2 Principle of Operation of PICOC

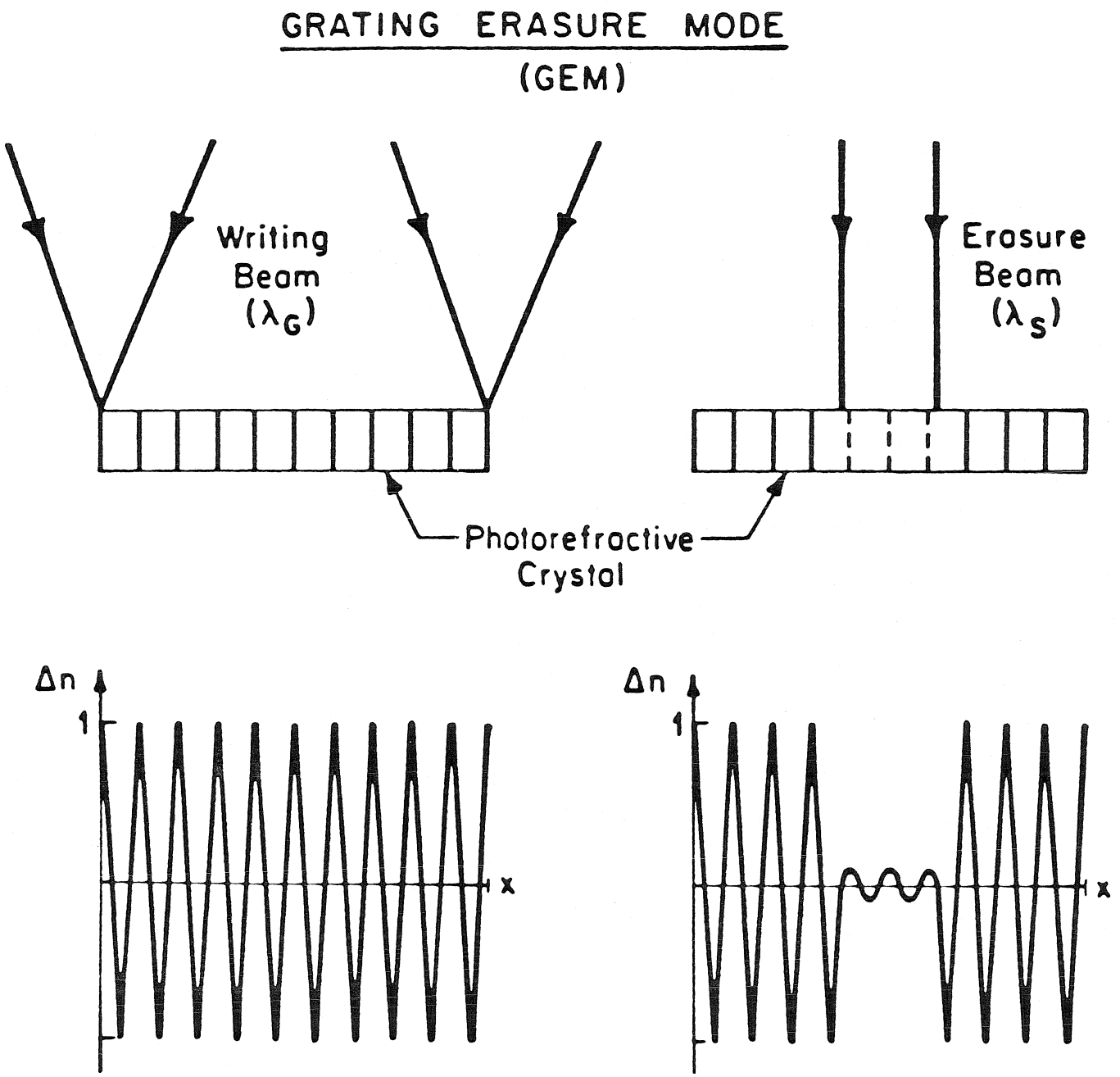

Fig. 3.3 Grating Erasure Mode (GEM)

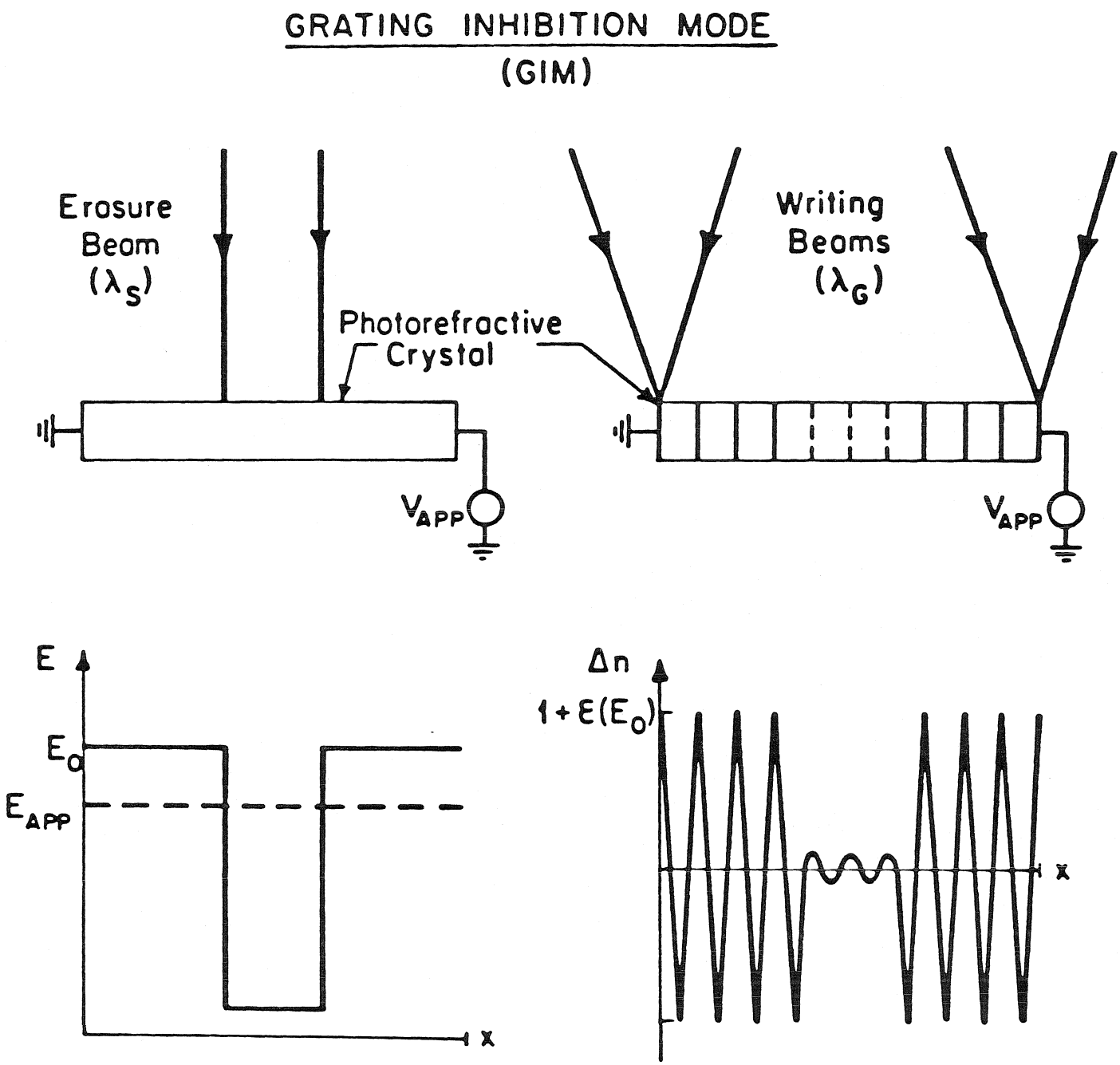

Fig. 3.4 Grating Inhibition Mode (GIM)

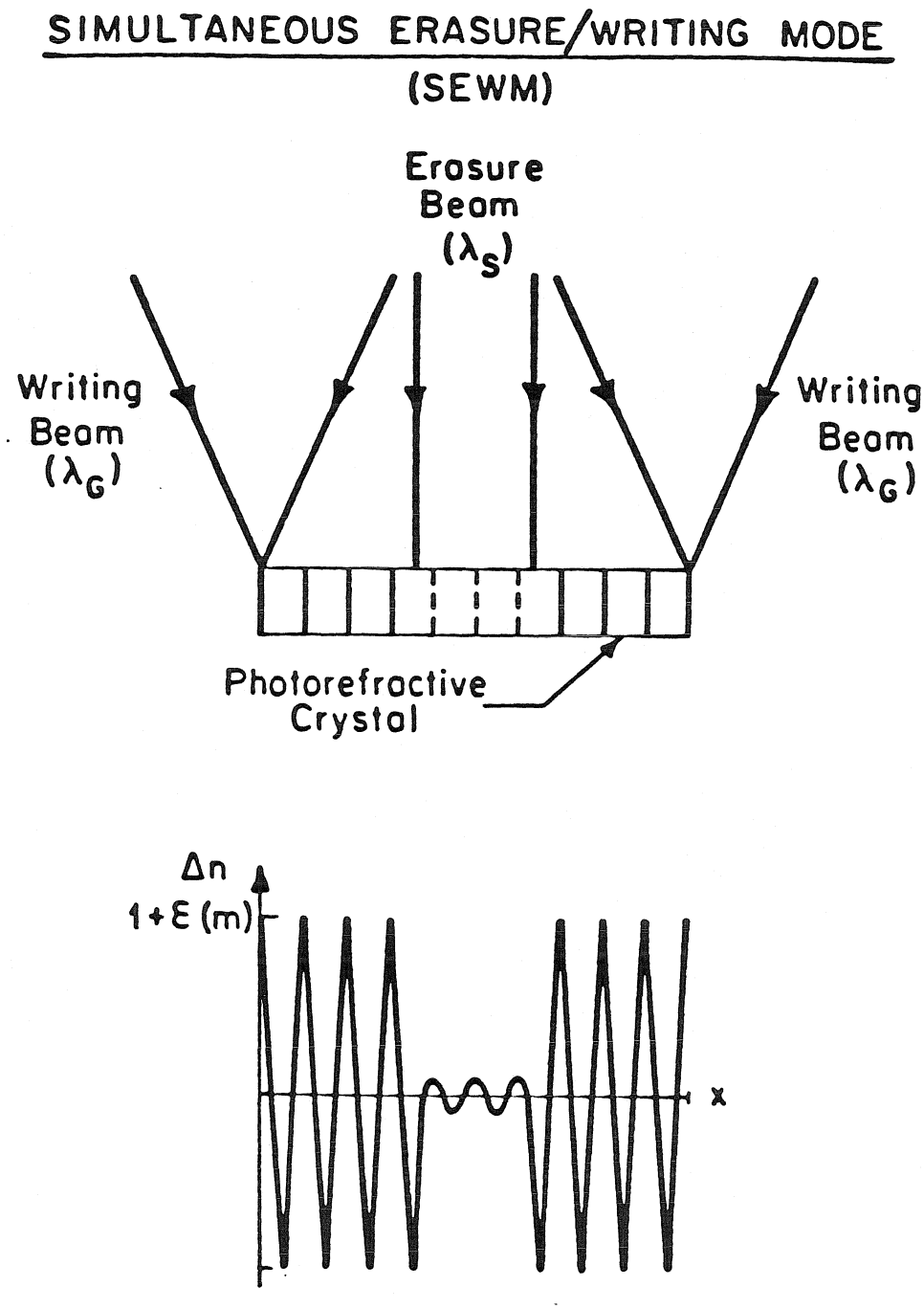

Fig. 3.5 Simultaneous Erasure/Write Mode (SEWM)

crystal is pre-illuminated with the incoherent image-bearing beam prior to grating formation. This serves to selectively decay (enhance) the applied transverse electric field in exposed (unexposed) regions of the crystal. After this pre-exposure, the coherent writing beams are then allowed to interfere within the crystal, causing grating formation with spatially varying efficiency due to significant differences in the local effective applied field.

In the simultaneous erasing/writing mode (SEWM) shown in Figure 3.5, the incoherent image modulation, the cohrent grating formation, and the readout function are performed simultaneously. A stable conversion of the incoherent image is produced after the space charge fields within the crystal have reached steady state.

A major difference between the first two operating modes and SEWM lies in light sequencing required by each of the modes. In GEM and GIM, no useful steady state condition exists. Prolonged exposure to the incoherent beam in GEM results in an erasure of the previously recorded coherent grating. As a result, no light will diffracted and conversion will not occur. Likewise in GIM, prolonged exposure to the coherent grating would lead to erasure of the information previously recorded by the incoherent image. Consequently, an important operating parameter in analyzing these two modes is the optical exposure (energy per unit area) required for optimum conversion of the incoherent image. In the case of SEWM, however, both the incoherent and coherent beams are simultaneously incident on the photorefractive

crystal. As a result, conversion can occur in the steady state regime. Thus the important parameter for this mode is the optical power of the incident light beams.

The ability of SEWM to convert incoherent images to their coherent replicas, despite prolonged exposure, allows one to construct a simplified experiment which requires no temporal sequencing of the incident beams. Because of its experimental convenience and analytical simplicity, SEWM is emphasized in this thesis. More detailed discussions of GEM and GIM are given in the temporal analysis described in section 3.4.

III.2.3 Experimental Implementation

The implementation of PICOC is a modification of the non-degenerate four-wave mixing geometry to include simultaneous exposure by an incoherent image-bearing beam (Fig. 3.6). This configuration requires a readout wavelength separate and distinct from the coherent grating writing wavelength, which then allows the readout wavelength to be selected for significantly reduced grating erasure rates. Thus, the grating inhibition mode (GIM) and the grating erasure mode (GEM) are best implemented in this configuration. One drawback of the nondegenerate four-wave mixing implementation lies in the difficulty of aligning the probe beam. Since the wavelength for writing and read out of the recorded pattern differs, the Bragg angle for the two beams will not be the same (as shown in Figure 3.6).

An alternative method of reconstructing the hologram consists of retroreflecting

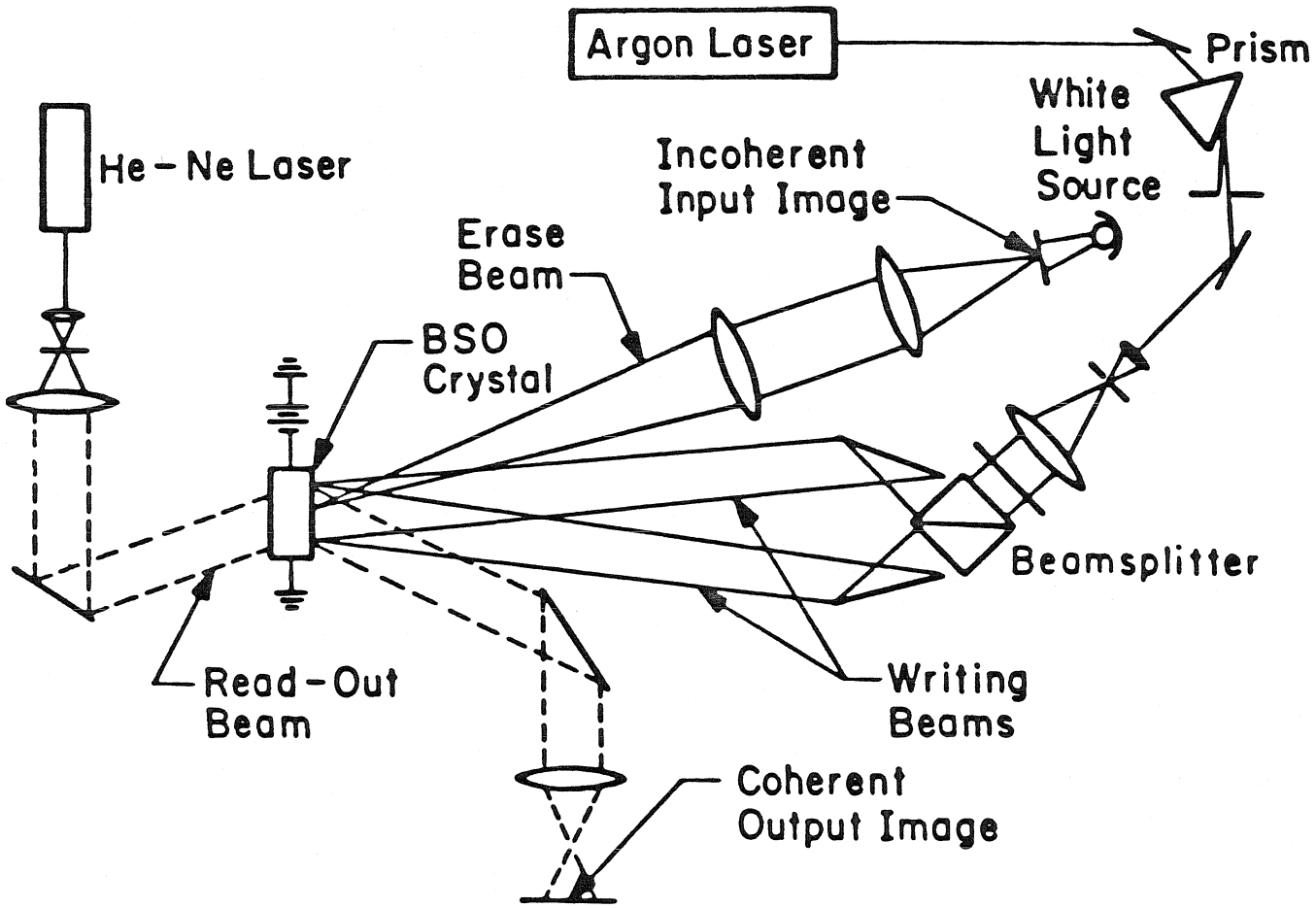

Fig. 3.6 Optical Implementation of PICOC using Nondegenerate Four-Wave Mixing Architecture

one of the writing plane waves and using it as a readout beam. This degenerate four-wave mixing architecture (shown in Fig. 3.7) has the advantage of easier optical alignment, as the readout beam is readily Bragg aligned by the retroreflecting of one of the two coherent grating writing beams. It has the disadvantage that since the readout beam is at the same wavelength as the coherent grating writing beams, the process of reconstruction simultaneously erases the grating structure being probed. Thus, this implementation can be utilized for the simultaneous erasure/writing (SEWM), and can be adopted for the grating erasure mode (GEM) and the grating inhibition mode (GIM) only by significantly reducing the probe beam intensity, with a correspondingly reduced readout signal intensity.

As a specific example of the PICOC process, a non-degenerate four-wave mixing configuration was utilized, in which the coherent writing beams and the incoherent image-bearing beam were made to illuminate the same face of a 2 mm thick crystal of bismuth silicon oxide (BSO) obtained from Crystal Technology Inc. An electric field of 6kV/cm was applied along the $< \bar{1}10 >$ axis as shown in Figure 3.8. A 300 l/mm grating was written by the 488 nm line of an argon laser with the grating wave vector oriented parallel to the applied bias field to maximize the diffraction efficiency. The image bearing light source was either a Xenon arc lamp, a tungsten lamp, or the 514 nm line of the argon laser. The average coherent grating intensity was 0.4 mW/cm^2 and the image-bearing light intensity was typically 8.0 mW/cm^2.

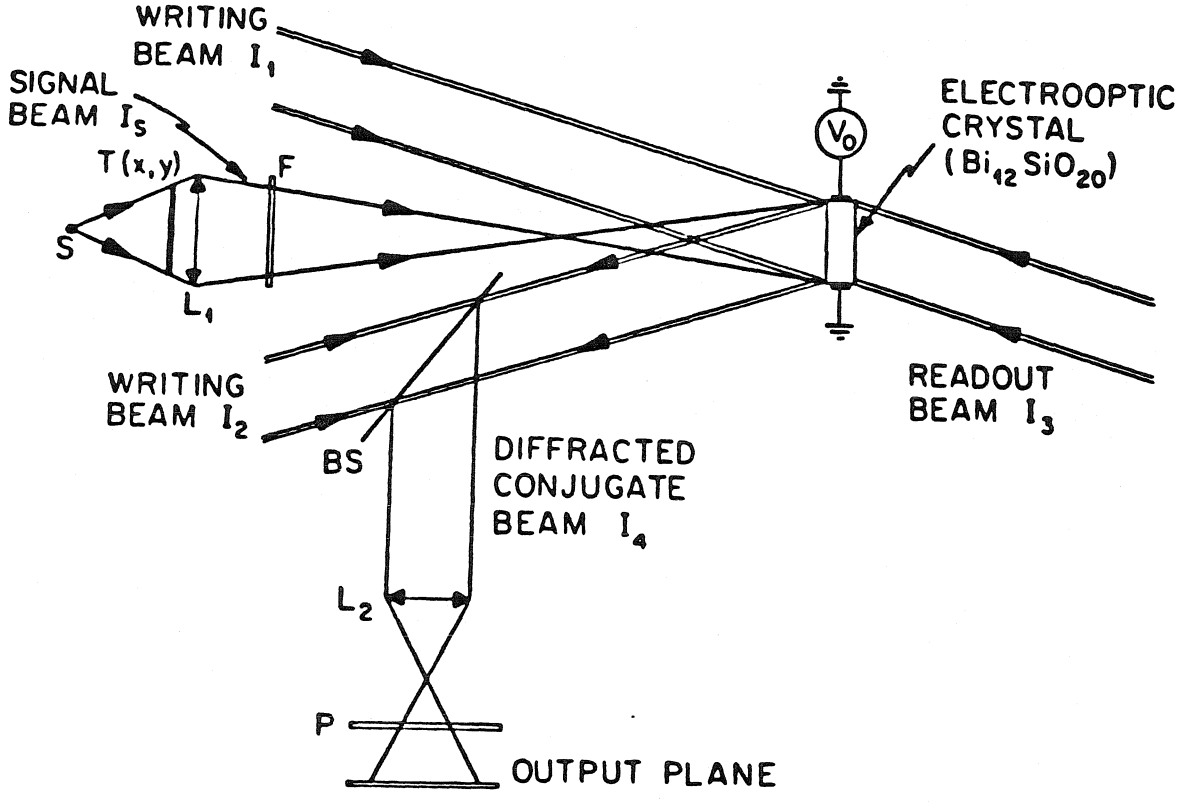

Fig. 3.7 Optical Implementation of PICOC using Degenerate Four-Wave Mixing Architecture

The coherent grating writing beams were polarized orthogonal to the applied electric field. An auxillary beam, utilizing the 633 nm line of a He-Ne laser, was used to read out the information recorded in the crystal. The average intensity of the readout beam was 5 mW/cm^2. A polarizer was inserted at the output to minimize coherent optical scatter from the crystal [16].

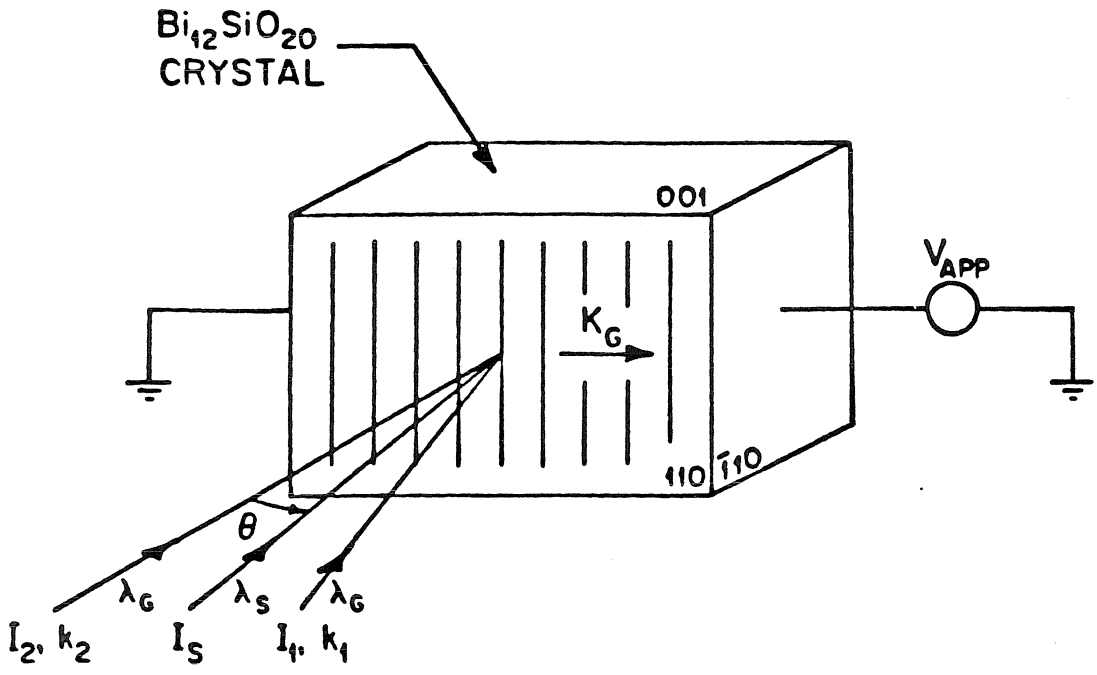

Fig. 3.8 Crystal Orientation Used in PICOC

Sample converted images obtained from two binary transparencies (a spoke target and a U.S. Air Force resolution target) and from two black-and-white slides with continuous gray scale are shown in Figure 3.9. The original transparency and its converted image have reversed contrast, as explained by Figure 3.2. An approximate resolution of 15 l/mm, as determined from the resolution target image, was achieved without optimization factors such as the Bragg readout condition. Further optimization of the optical beam orientations results in striking enhancement of the resolution up to the order of 50 l/mm. This is discussed in section III.3.3 below. Similar images of comparable quality have also been recorded in a bismuth silicon oxide crystal in which the $< 001 >$ axis is aligned parallel to the coherent grating wave vector and to the applied bias electric field.

Having discussed the physical principles, modes of operation and experimental demonstration of the PICOC process, a mathematical model is now formulated through which specifications of the converter can be analyzed. The analytical model is based on the Kukhtarev model [17] for the recording process in photorefractive crystal which was reviewed in section II.3. This method allows one to derive an analytic expression for the dynamic and steady state response of PICOC in the low modulation depth regime.

A higher order model similar to one discussed in section II.4 is also applied to the PICOC process and presented in section III.3.4. Numerical analysis utilizing

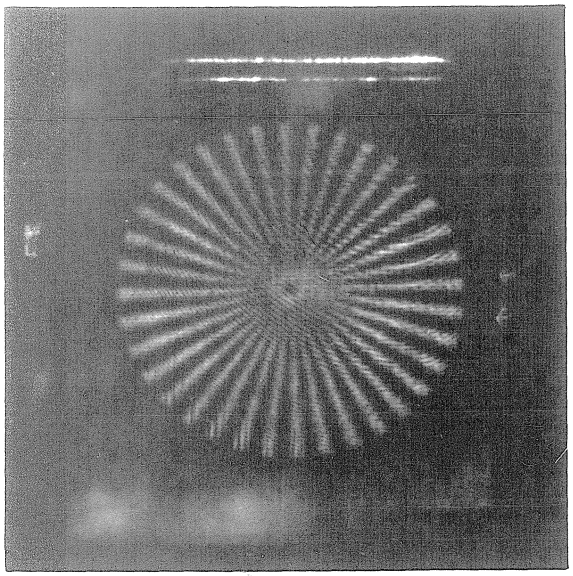

(a)

(c)

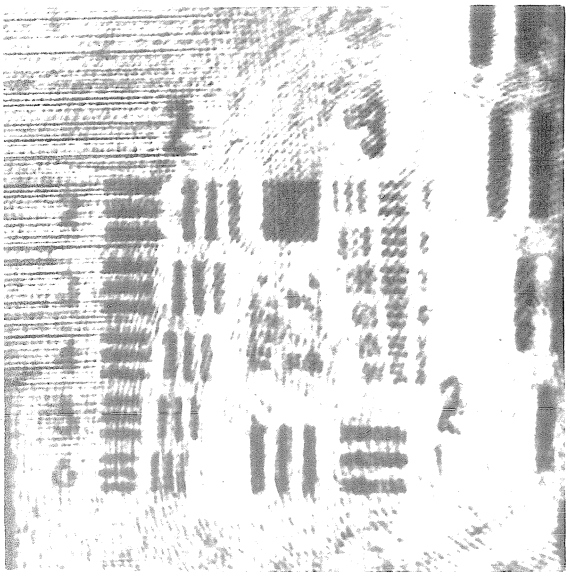

(b)

(d)

Fig. 3.9 Examples of PICOC Conversion of Binary and Gray-Level Images: a) Spoke Target, b) Air Force Resolution Target, c) Incoherent Graduate Student, and d) Airplane.

this model allows one to derive the space charge profile within the photorefractive crystal under different operating conditions. In addition, this allows one to predict the steady state response of the converter in the high modulation depth regime.

The following section presents the steady state analysis of PICOC and discusses important issues such as linearity and spatial frequency response of the converter. The temporal analysis of PICOC is presented in section III.4 with more detailed studies on the different operating modes of the coverter.

III.3 Steady State Analysis of PICOC

During the recording process, a space charge electric field E(x) is formed in the photorefractive crystal in response to the combined illumination by a coherent grating light beam $I_g(x)$ and an incoherent image beam $I_s(x)$. The recording process can be analyzed using the Kukhtarev model [17] (section II.3) to predict the recorded index change subject to the two simultaneous intensity patterns. The results obtained by using a perturbation expansion on Kukhtarev's equations are presented in the next section. The implications of these results on the nonlinear transfer function of the conversion process are explored in section III.3.2. Issues affecting the resolution of the recording process are discussed in section III.3.3. Results of numerical analysis performed on the higher order model are shown in section III.3.4. The temporal response of the converter is discussed in the following

section III.4.

III.3.1 Two Grating Recording

When an incoherent image beam is present simultaneously with the coherent grating, as in the simultaneous erase/writing mode (SEWM), then additional terms corresponding to harmonics of the spatial frequencies of the illuminating intensity must be incorporated into the analysis. Let us consider the recording of a coherent grating with frequency k_g and an incoherent grating with frequency k_s. The light intensity incident on the crystal is then

$$I(x) = I_0(1 + m_g cosk_g x) + I_1(1 + m_s cosk_s x). \qquad [3.1]$$

The presence of both gratings in the crystal and the nonlinearities in the photorefractive process results in the recording of a space charge with additional harmonic components. The dominant components in the harmonic expansion are the k_g and k_s orders due to the presence of the two intensity gratings incident on the photorefractive crystal. If these were the only two spatial frequencies recorded in the photorefractive crystal, then the incoherent image would not modulate the coherent grating and conversion would not be possible. However, due to the nonlinearities in the recording process, the intermodulation terms $k_g \pm k_s$ and possibly higher order terms are also recorded in the crystal. As a result, when two sinusoidal grating are

recorded on the crystal, the resulting space charge field is

$$E(x,t) = E_{01}e^{ik_s x} + [E_{10} + E_{11}e^{ik_s x} + E_{1-1}e^{-ik_s x}]e^{ik_g x} + \text{higher order terms.} \quad [3.2]$$

In this notation, E_{pq} is the amplitude of the Fourier component of the space charge field at the spatial frequency $(pk_g + qk_s)$. It is important to note that the subscript notation used in this chapter is different from that used in the higher order model (section II.4) to denote the double Fourier-power series expansion. The space charge field described in equation 3.2 will give rise to an diffracted intensity pattern of the form

$$I_{out} = I_{10} + 2I_{11}cos(k_s x). \quad [3.3]$$

Thus, the incoherent sinusoidal pattern results in a modulation of the diffracted output and the incoherent image is impressed on the coherent diffracted beam. The far field diffraction pattern, shown in Figure 3.10, shows the spatial Fourier components which arise when two gratings are written on the photorefractive crystal. The I_{10} and I_{01} orders arise from the diffraction of the incident probe beam by the two fundamental gratings (k_s and k_g). In addition, the I_{11} order is created by a nonlinear interaction between the two fundamental modes and it is this term that is responsible for the incoherent to coherent conversion that occurs in the crystal. Hence, the photorefractive incoherent to coherent conversion (PICOC) process must be analyzed by examining how the intermodulation term E_{11} depends on dif-

ferent parameters such as incident intensity and spatial frequency, as well as its relationship with the other first order harmonic components.

The analysis of PICOC using the Kukhtarev model is based on a Fourier expansion solution to the material equations governing the photorefractive process (Eqs. 2.13-2.16). In this case, however, two intensity gratings are being transcribed on the crystal. By using mathematical techniques similar to those described by Kukhtarev *et al.*,[17] the space charge field components at the two fundamental frequencies can be analytically solved to first order and are found to be

$$E_{10} = -0.5\frac{m_g s_g I_0}{s_g I_0 + s_s I_1}\left[\frac{E_0 + iE_d[k_g]}{1 - i(E_0 + iE_d[k_g])/E_q[k_g]}\right] \qquad [3.4]$$

$$E_{01} = -0.5\frac{m_s s_g I_0}{s_g I_0 + s_s I_1}\left[\frac{E_0 + iE_d[k_s]}{1 - i(E_0 + iE_d[k_s])/E_q[k_s]}\right] \qquad [3.5]$$

where E_0 is the applied bias field and s_g and s_s are the absorption cross sections at the coherent and incoherent frequencies, respectively. $E_d[k]$ and $E_q[k]$ are the characteristic diffusion and trap limited saturation field described in section II.3 and rewritten as functions of the grating spatial frequency below.

$$E_d[k] = \frac{k_B T k}{e} \qquad [3.6]$$

$$E_q[k] = \frac{eN_{Deq}^{+}}{\epsilon k}. \qquad [3.7]$$

These expressions correspond closely to the space charge field generated by a single intensity grating in a photorefractive crystal as predicted by the Kukhtarev analysis.

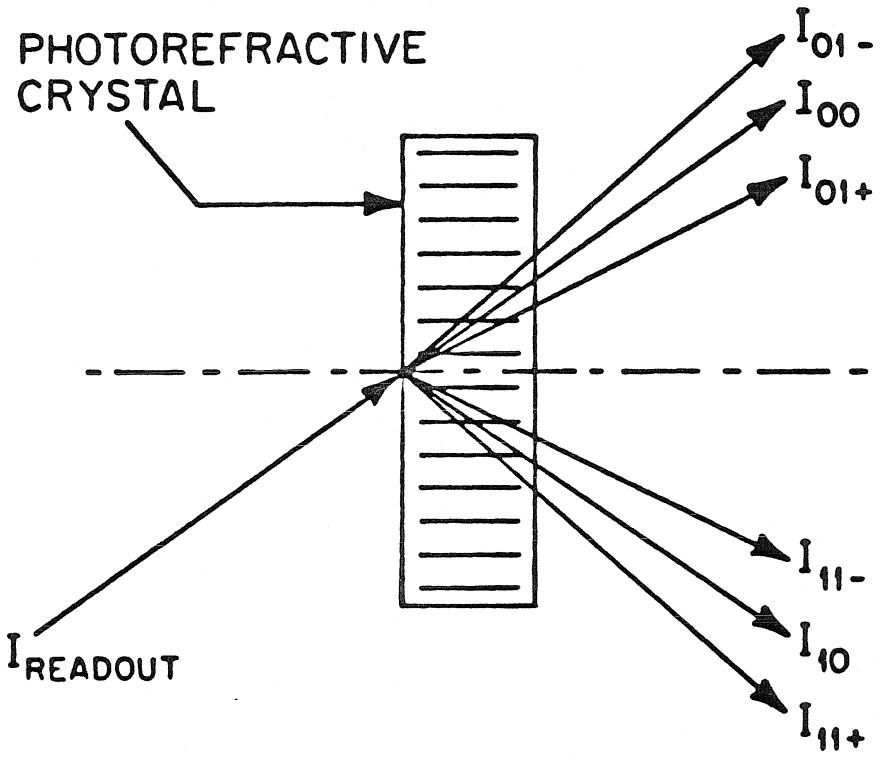

Fig. 3.10 Spatial Fourier Components Generated by Conversion of an Incoherent Sinusoidal Image

In this case, however, the space charge fields are proportional not to the modulation depth of each sinusoidal intensity component but rather to an effective modulation depth due to the presence of a DC intensity component in both beams. The space charge field can thus be described in terms of an effective modulation depth

$$m_g^{eff} = m_g\left[\frac{s_g I_0}{s_g I_0 + s_s I_1}\right] \qquad [3.8]$$

$$m_s^{eff} = m_s\left[\frac{s_s I_1}{s_g I_0 + s_s I_1}\right] \qquad [3.9]$$

which accounts for the reduction in the original modulation depth due to the presence of both incoherent and coherent beams simultaneously on the crystal.

Using the material parameters for a BSO crystal (shown in Table 2.1), the expressions for the fundamental space charge fields can be further simplified by assuming incoherent and coherent spatial frequencies of less than 200 l/mm and an applied field 2kV/cm< E_0 < 15kV/cm. In this case, the trap limited saturation field E_q > 26 kV/cm and is much greater than the applied field E_0. The applied field is in turn much greater than the diffusion field E_d, which is less than 0.8 kV/cm for the spatial frequencies of interest. The lowest harmonics of the space charge field can then be simplified to

$$E_{10} = -0.5 m_g^{eff} E_0 \qquad [3.10]$$

$$E_{01} = -0.5 m_s^{eff} E_0. \qquad [3.11]$$

In order to analyze the steady state response of the photorefractive incoherent to coherent optical converter, an expression for the intermodulation term must be

found. By carrying a perturbation analysis to a higher order the E_{11} term can be derived analytically. The complete expression for this term is shown in the Appendix III.A.1. Using the same assumptions for a low spatial frequency and high bias field as above, the expression for E_{11} can be simplified to

$$E_{11} = \frac{m_g^{eff} m_s^{eff}}{2} E_0. \qquad [3.12]$$

An identical expression for E_{11} was derived by Marrakchi *et al.* [9] based on the Moharam model [18] which assumes a constant recombination time (see section II.2). This derivation involves an additional linearization of the response in the limit of low modulation depths for m_g^{eff} and m_s^{eff}.

Equations 3.10-3.12 indicate that under the conditions described above, the SEWM response in the steady state limit is predominantly governed by the modulation depths m_g^{eff} and m_s^{eff}. The consequent impact on the overall readout image light intensity and on the modulation transfer function is discussed in the nonlinear transfer response analysis, presented next.

III.3.2 Nonlinear Transfer Response

In order to characterize the nonlinear transfer characteristics of the photorefractive incoherent to coherent process, we would like predict the effect of varying the input parameters characteristics on the output image. We will consider the SEWM mode in the steady state regime with a single coherent frequency grating

and a single incoherent frequency grating and determine the modulation depth of the readout image as a function of the characteristics of the incoherent and coherent input light. A convenient parameter that describes these characteristics is the product BR, where R = I_1/I_0 is the ratio of the average incoherent light image intensity to the average coherent grating intensity and B = s_s/s_g is the ratio of the absorption cross sections at the incoherent and coherent wavelengths. In terms of the actual absorption coefficients of the photorefractive material, the absorption ratio is given by

$$B = \frac{\alpha_s \lambda_s \eta_s}{\alpha_g \lambda_g \eta_g} \qquad [3.13]$$

where $\alpha_{s,g}$ is the absorption coefficient at the signal and coherent grating wavelengths, $\lambda_{s,g}$. $\eta_{s,g}$ is the quantum efficiency of material at the two wavelengths.

With these definitions, the output intensities of the various harmonic components can be rewritten as

$$I_{10} \propto \left[\frac{m_g}{1+BR}\right]^2 \qquad [3.14]$$

$$I_{11} \propto \left[\frac{m_g m_s BR}{(1+BR)^2}\right]^2. \qquad [3.15]$$

Figure 3.11 shows the intensity components I_{10}, I_{11}, and I_{01} as functions of the intensity ratio BR. In this graph, we have assumed that the absorption coefficient ratio B is equal to 0.5. For low levels of image intensity corresponding to low intensity ratios , the coherent grating's charge pattern is not significantly erased by the image beam. In this regime, increasing the incoherent image-bearing light

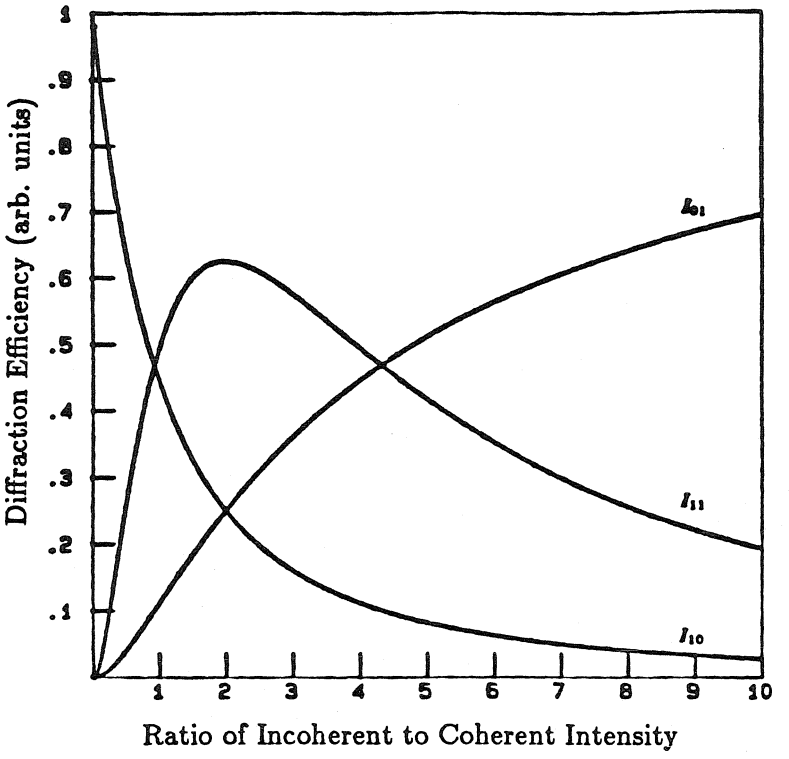

Fig. 3.11 Intensity Components I_{10}, I_{01}, and I_{11} as a Function of the Ratio of Incoherent to Coherent Intensities, R.

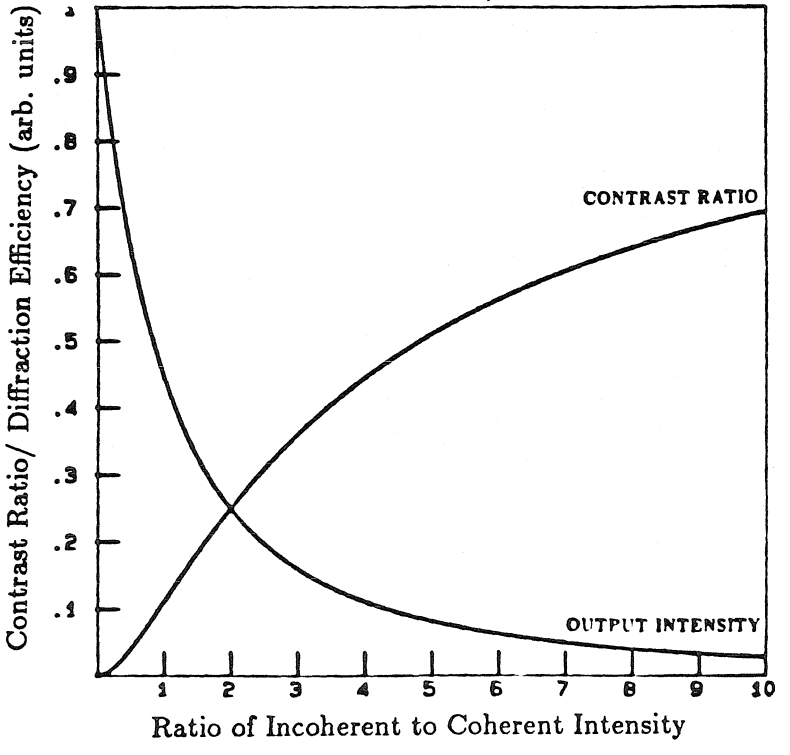

Fig. 3.12 Contrast Ratio vs R

intensity increases the transfer of image modulation onto the space-charge grating profile without destroying that profile. For high levels of incoherent light intensity, corresponding to larger intensity ratios (R), the high intensity of the uniform incoherent image beam,I_1 strongly erases the coherent grating profile leading to a decrease in the I_{10} component and likewise the intermodulation term I_{11}. Hence, over the full range of R values, the I_{11} diffracted component exhibits the peaking behavior shown in Figure 3.11. This peak occurs when the ratio of the incoherent to coherent intensity is equal to the inverse of the absorption cross section, 1/B. In other words, I_{11} peaks when the amount of photons absorbed (causing photoexcitation) from the incoherent beam is equal to the number of photons absorbed from the coherent beam.

As shown from equation 3.3, the diffracted light contains both I_{10} and I_{11} diffracted components. In this case, the output modulation depth is given by the ratio of the modulated component I_{11} to the DC component of the diffracted light I_{10} and is given by

$$m_{out} = \left[\frac{m_s BR}{1+BR}\right]^2 \qquad [3.16]$$

Figure 3.12 shows a theoretical plot of the contrast ratio (I_{11}/I_{10}), as a function of the ratio of the incoherent to coherent intensity (I_1/I_0). The plot demonstrates that the contrast ratio improves steadily with increasing intensity of the image bearing light. However, as also shown in this figure, the overall average diffracted intensity

I_{10} declines with increasing incoherent intensity because the uniform background in the incoherent light erases the coherent grating pattern in the photorefractive crystal. Thus there are two competing mechanisms, output modulation depth and output overall intensity, which result in a performance tradeoff for image transfer PICOC. In one case, high overall diffraction efficiency is possible at the expense of a poorly contrasted output image and in the other case, a well contrasted output can be created only by sacrificing output brightness.

In many optical information processing applications, optimization of the image contrast ratio is desirable within the image intensity constraints implied by the performance tradeoff described above. In other types of signal processing applications such as correlation with a Vander Lugt filer, the DC portion of the output image contained in the I_{10} diffraction component does not contribute to the processing, or can be readily reduced by spatial filtering, whereas maximizing I_{11} is critical to good conversion performance. For these cases, the optimum level of incoherent-image bearing beam intensity is that which maximizes the I_{11} component (*i.e.*, when $I_1=I_0/B$).

To test the predictions of this nonlinear transfer model, the erasure of the readout beam's first diffraction order I_{10} in response to spatially uniform incoherent illumination was measured in the nondegenerate four wave mixing configuration discussed in section III.2.3 with the results shown in Figure 3.13. The grating

was written with the 515 nm line of an argon laser while the 488 nm line was used to simulate a spatially uniform image beam. For comparison, the theoretical prediction based on Kukhtarev's linear expansion is also drawn. The model has been scaled in intensity to match the experimental point at R = 0.6. As expected, the experimental results agree well with theoretical predictions in regions where the modulation depth is low (*i.e*,. R is high). For regions where the modulation depth is near unity, numerical simulations predict that the linear model would underestimate the expected diffracted output. This fact is demonstrated clearly by the deviation between the theoretical and experimental curves in the region near R = 0.

A more challenging test of the theory is to predict accurately the conversion response to a sinusoidally modulated image beam. This can be done with the nondegenerate four-wave mixing geometry described previously. In this case, the coherent grating was written with the 488 nm line of an Argon laser and the 514 nm line passing through a Michelson interferometer was used to generate a sinusoidal spatial modulation as shown in Figure 3.14. The sinusoidal image modulation introduces an additional diffraction order I_{11} not observed in the uniform erasure case. The diffracted light sideband intensity I_{11} was measured as a function of the intensity ratio R and is presented in Figure 3.15 with a theroretical fit corresponding to the analytical form predicted by the perturbation expansion method.

From the position of the experimentally derived peak, one can infer the ra-

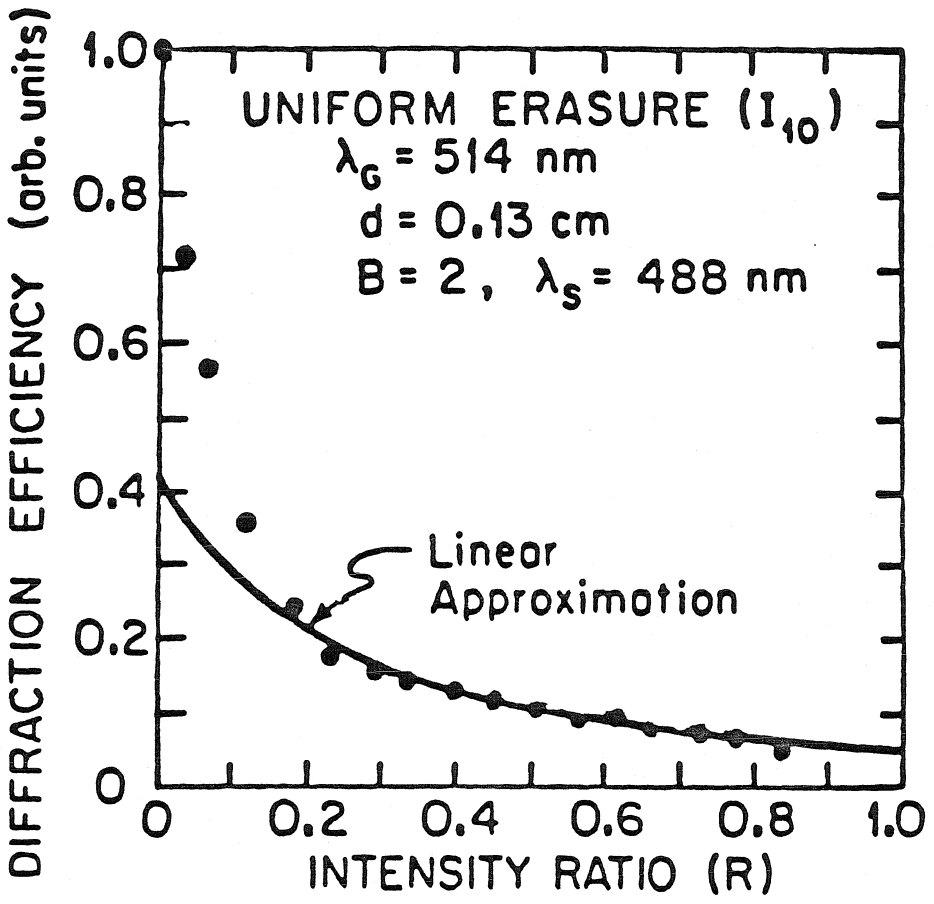

Fig. 3.13 Experimental Diffraction Efficiency of I_{10} vs. R

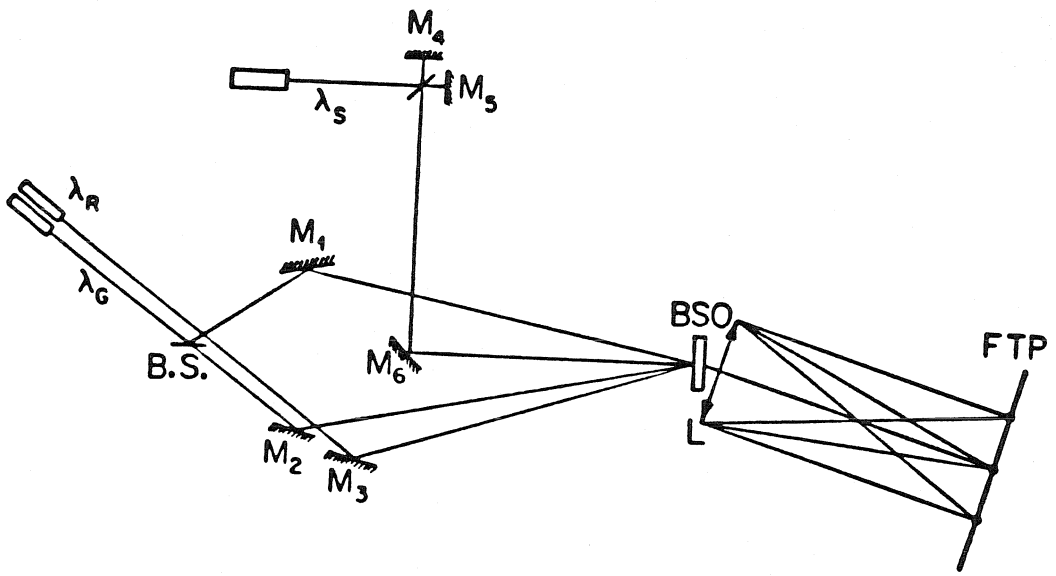

Fig. 3.14 Experimental Arrangement for Sensitivity and Transfer Function Measurements

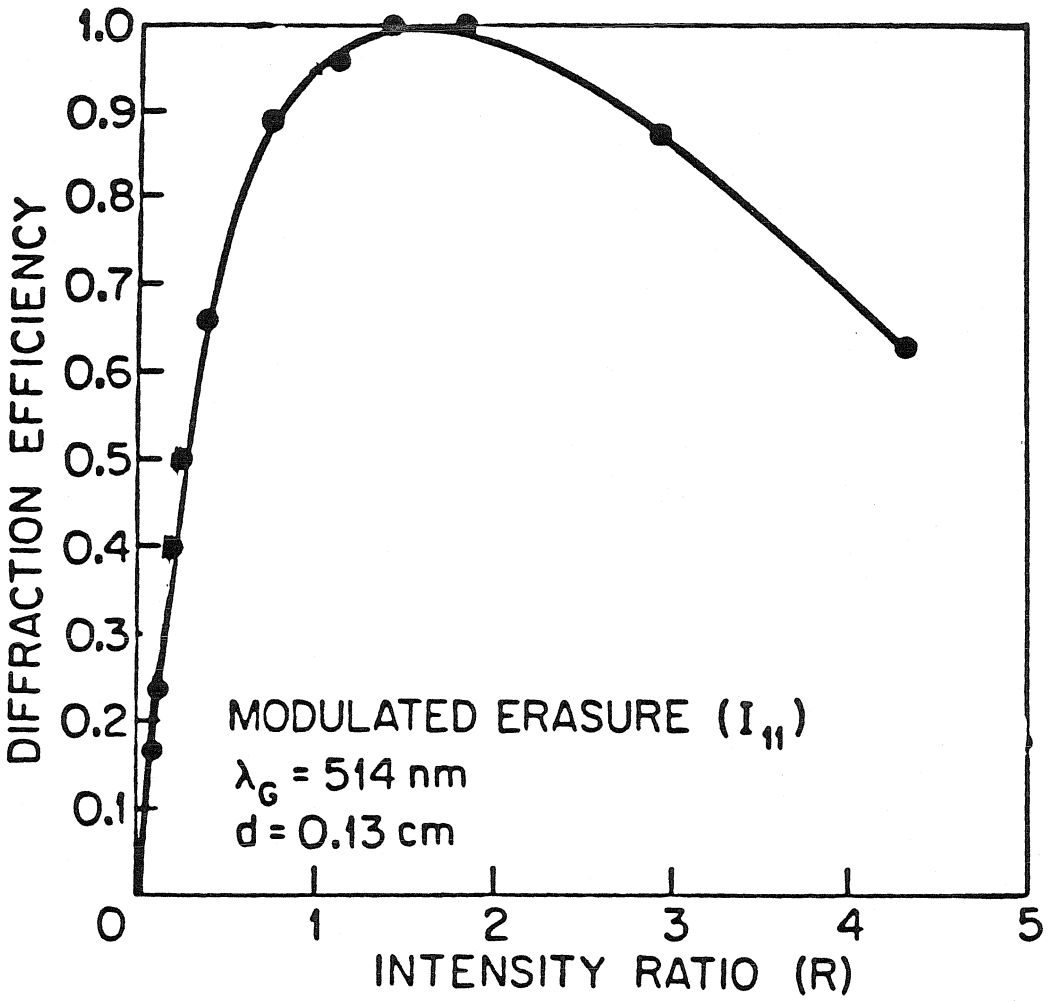

Fig. 3.15 Experimental Diffraction Efficiency of I_{11} vs. R

tio of the absorption cross sections at the writing and reading wavelengths. The experimental results demonstrate that this s_g/s_s ratio is about 2.

III.3.3 Spatial Resolution Issues for the Recording Process

A number of distinct factors influence the ultimate resolution achievable with the PICOC spatial light modulator. These factors can be classified as geometric, configurational, and materials related. The geometric and materials factors deal primarily with the recording of the image and the ability of the photorefractive crystal to store it. The configurational factors deal with reading out the stored image, and how the Bragg requirements for reconstructing a volume hologram affect the spatial resolution of PICOC.

III.3.3.1 Geometrical Limitations

Geometric resolution limitations arise from incorporating an incoherent imaging system in the four-wave mixing geometry and from the finite crystal thickness d required to create a volume holographic grating. These effects are illustrated in Figure 3.16.

Figure 3.16 describes the case for low optical absorption ($\alpha_g d << 1$ and $\alpha_s d << 1$), such that the induced holographic grating has essentially uniform amplitude throughout the volume of the crystal. The optimal focal point occurs at the center of the crystal and is not localized on the front surface of the crystal, as would be the case in

PHOTOREFRACTIVE INCOHERENT-TO-COHERENT OPTICAL CONVERTER: GEOMETRIC CONSTRAINTS

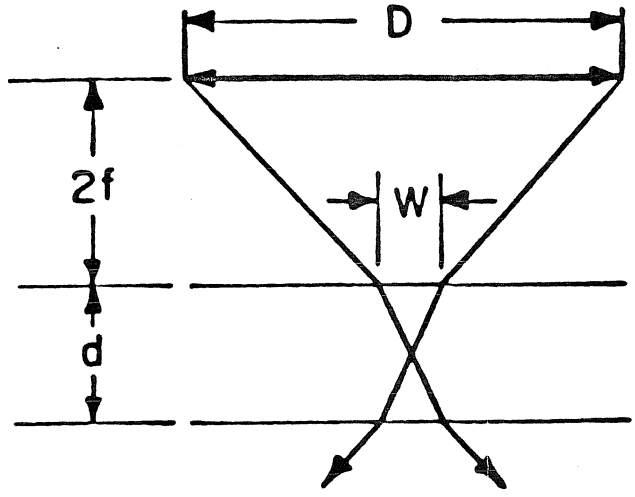

CASE I: $\alpha d < 1$ $\quad R \sim \frac{1}{(W/2)} = \frac{4nF\#}{d}$

EXAMPLE: FOR $n = 2.5$, $d = 1\text{mm}$, $F\# = 5$,

$R = 50$ line pairs/mm

Fig. 3.16 Geometrical Constraints of PICOC Resolution

a highly absorptive media. The spatial frequency response will then be proportional to

$$\Delta f_{geom} = (W/2)^{-1} = \frac{4n_0 F\#}{d} \qquad [3.17]$$

where W is the diameter of the incoherent image beam at the front surface of the crystal, n_0 is the refractive index of the electro-optic crystal. $F\#$ is the F-number of the incoherent imaging system and d is the crystal thickness. As an example, for $n_0 = 2.5$, $d = 1$mm and an F-number of 5, the resolution limit is approximately 50 lines/mm.

III.3.3.2 Material Limitations

An additional resolution limitation results from material-dependent parameter constraints which influence the physics of grating formation, in particular the finite supply of traps N_{Deq}^{+}. As discussed in section II.3, if the trap density is limited, then the space charge field that can be recorded is similarly limited because sufficient space charge cannot be generated to establish higher field strengths. This limitation becomes progressively more severe at higher spatial frequencies and results in a reduction of the the space charge field as the spatial frequency is increased. The finite level of compensating traps leads both to a reduction of the space charge field and to a phase shift as consequences of the finite saturation field. These two effects are discussed in more detail below.

In making the assumptions used to simplify the expressions for E_{11}, we assumed

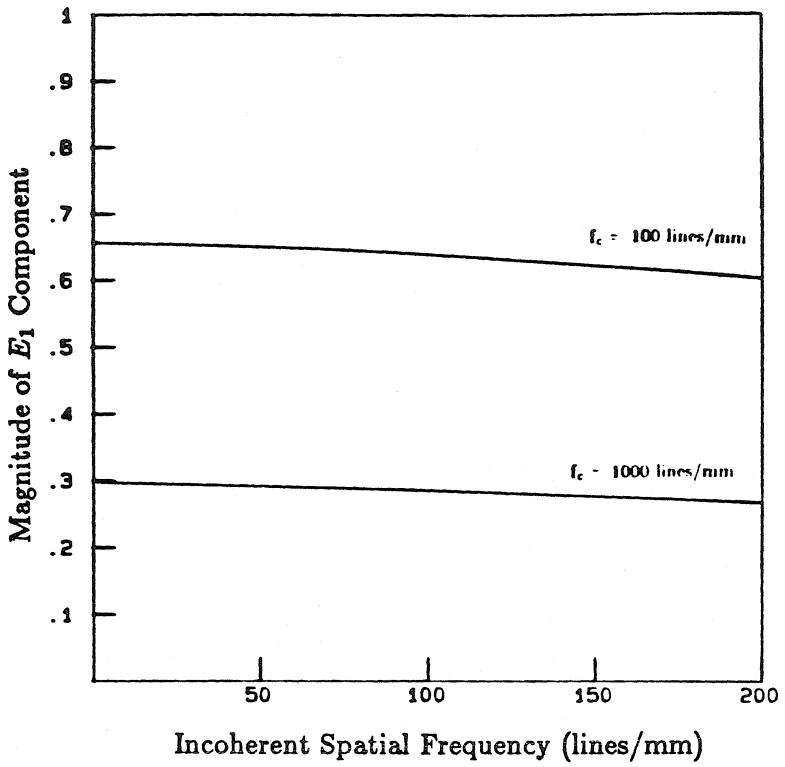

Fig. 3.17 E_{11} Component of Space Charge Field vs Incoherent Spatial Frequency

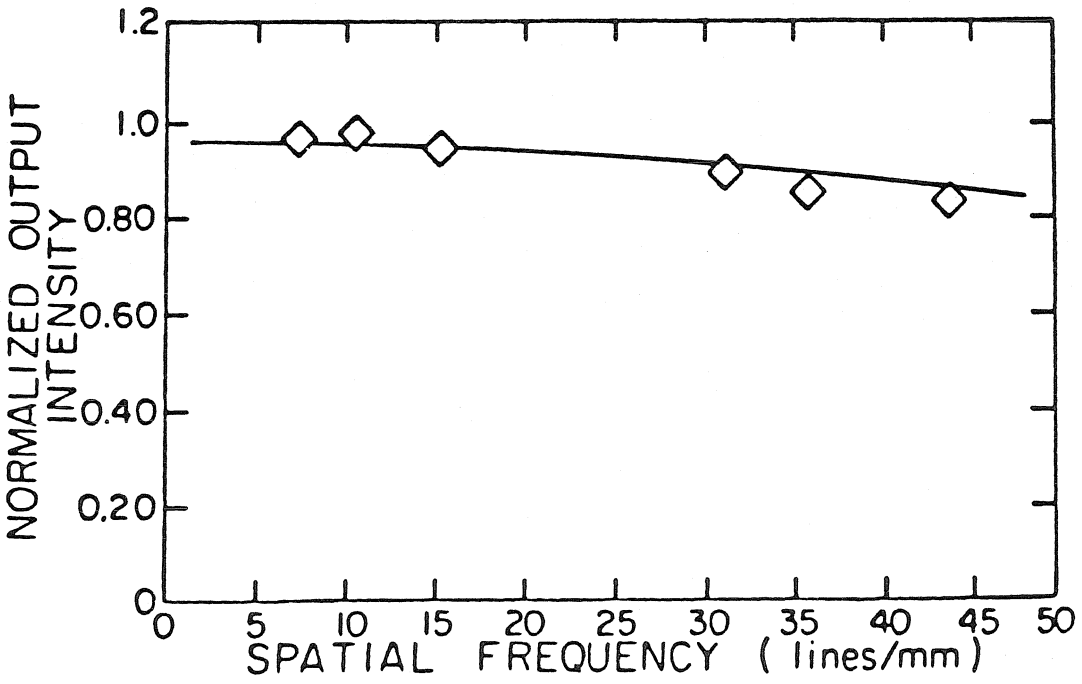

Fig. 3.18 Experimental Diffraction Efficiency of I_{11} vs Incoherent Spatial Frequency

that the spatial frequency of the two gratings are less than 200 lines/mm. The dependence of this intermodulation term on the incoherent spatial frequency is explicitly derived in Appendix III.A.1 (equation A.20). Figure [3.17] shows the E_{11} component of the space charge field as a function of the incoherent spatial frequency at various coherent grating frequencies. As depicted from this figure, the variation over the effective bandwidth of the photorefractive incoherent to coherent converter is negligible especially when compared with the effect induced by the coherent grating spatial frequency.

To verify the predicted high bandwidth of the recording process and to eliminate the depth of focus issues discussed previously, the Michelson interferometer configuration shown in Figure 3.14 was again used to record a sinusoidal image pattern onto a BSO crystal. The ratio of the incoherent image intensity to the coherent image intensity was adjusted experimentally to maximize the intensity of the I_{11} diffraction order. As the image grating frequency was varied, the angular alignment of the readout beam was also varied to maintain optimum Bragg alignment, thereby removing Bragg detuning effects on the readout resolution. Thus the measured diffracted intensity I_{11} corresponds to the strength of the space charge field stored in the crystal, with results as shown in Figure 3.18. A slight decrease in diffraction efficiency with increasing spatial frequency is observed, but the frequency response far exceeds the bandwidths for Bragg detuning, discussed in the

following section.

A far more serious implication of finite density of trap sites is a shift in the phase of the recorded space charge field profile with respect to the incident coherent grating illumination profiled. Considering an equilibrium donor-like trap density, N_{Deq}^{+} of 10^{16} cm^{-3}, a coherent grating frequency of 300 line/mm and an applied bias field of 6kV/cm, the resultant phase shift is of the order of 18^{o}. This phase shift poses no problems for PICOC performance so long as it remains uniform over the full aperture of the photorefractive crystal and the full spatial bandwidth of the incoherent image. On the other hand, an image-induced differential phase shift can prove to be problematic for particular optical processing architectures.

The expression shown in equation 3.15 derives the magnitude of the intermodulation field. An important parameter, however, is the phase relationship between the E_{11} term an the DC component of the diffracted field E_{10}. Should the phase shift between the two space charge field components vary significantly as a function of the spatial frequency of the incoherent grating, this would result in a highly distorted coherent reconstruction of the image. In making the assumptions leading to equation 3.15, we can conclude that there is no phase shift between the intermodulation term and E_{10}. A more detailed analysis based on the full analytical expressions of the two space charge fields (shown in equation A.20) demonstrates that there is indeed a phase shift between the two components. Figure 3.19 shows

the phase shift of the E_{11} intermodulation component as a function of the incoherent spatial frequency at various coherent grating frequencies. From this figure, we can conclude that the phase shift is linearly proportional to the spatial frequency of the incoherent image. Thus, the image that is recorded in the crystal is spatially shifted with respect to the intensity profile of the incoherent image. At a coherent spatial frequency of 100 l/mm, the amount of phase shift is approximately 0.09° per 1 l/mm. This would correspond to a spatial translation of image-induced space charge pattern of 20 μm. Thus for a 1:1 output imaging system, the phase shift induced in the recording process will result in a 20 μm shift of the converted output image. Thus, we can conclude that the phase shift is essentially linear with frequency throughout the bandwidth of the converter and will have negligible effect on the converted image.

III.3.3.3. Resolution Anisotropy

Another issue of affecting resolution that has been predicted by the perturbation series is a moderate anisotropy in the recording of image structures parallel as opposed to perpendicular to the applied bias field for the simultaneous erasure writing mode (SEWM), and a resolution anisotropy for the grating inhibition mode (GIM).

The analysis described above is conducive to an intuitive interpretation of the

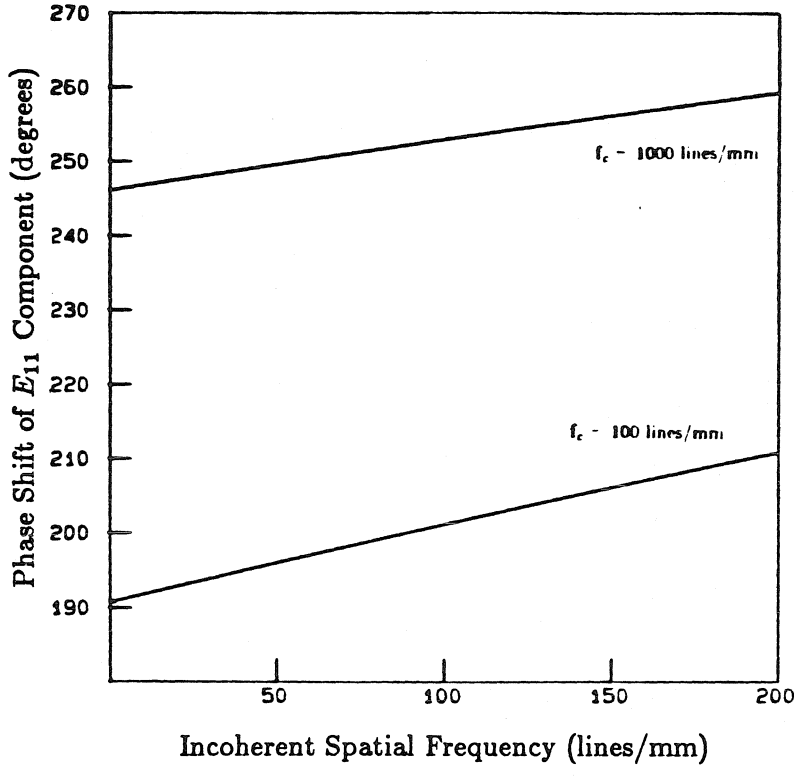

Fig. 3.19 Phase Shift of E_{11} vs Incoherent Spatial Frequency

perturbation terms as a sequence of discrete recording events. For the simultaneous erasure/writing mode (SEWM), two recording paths contribute to the I_{11} diffraction order. In one recording path, the incoherent image writes a space charge field E_{01}, independent of the coherent grating profile. This space charge field then modulates the recording of the coherent grating light beam. This transcription path is analogous to the grating inhibition mode (GIM). In the second SEWM transcription path, the coherent grating profile writes a space charge field E_{10}, which then modulates the recording of the incoherent image-bearing beam. This second path is analogous to the grating erasure mode (GEM). The GEM-like path exhibits perfect isotropy of response to an arbitrary image, but the GIM-like path exhibits a very strong anisotropy with image structures oriented perpendicular to the applied bias field generating much weaker space charge fields than structures oriented parallel to the bias field.

To elaborate, consider an image profile consisting of a single spatial frequency similar to equation 3.1, but oriented such that the wave vector k_s is orthogonal to the applied bias field E_0. Thus the incident image intensity $I_s(y)$ is given by

$$I_s(y) = I_1(1 + m_s cos k_s y) \qquad [3.18]$$

in which the y axis is orthogonal to the applied bias field. This image profile, in combination with the coherent grating profile, induces a space charge field $E(x, y)$

of the form

$$\vec{E}(x,y) = \hat{x}(E_0 + E_{10}e^{ik_g x}) + \hat{y}E_{01}e^{ik_s y} + (\hat{x}E_{11x} + \hat{y}E_{11y})e^{i(k_g x + k_s y)}$$

$$+ (\hat{x}E_{1-1x} + \hat{y}E_{1-1y})e^{i(k_g x - k_s y)} + \text{c.c.} \qquad [3.19]$$

in which $\hat{x}$ and $\hat{y}$ are unit vectors parallel and perpendicular respectively to the direction of the applied field.

Terms such as E_{01} and E_{11y} involve recording a charge pattern along a direction orthogonal to the applied bias field, and hence do not benefit from the enhancement of the photoconductivity due to the applied field. In practice these terms are very much smaller than terms E_{10} and E_{11x}, which involve recording a charge pattern along a direction parallel to the applied bias field. The perturbation method analysis solving for the E_{11x} term is presented in Appendix III.A.2 (equation A.35). It can be shown that if the spatial frequencies of both the incoherent and coherent gratings are less than 200 l/mm, and the applied field is between 2 and 15 kV/cm, the intermodulation term E_{11x} can be approximated by

$$E_{11x} = -0.25 m_s^{eff} m_g^{eff} E_0. \qquad [3.20]$$

This value is reduced by a factor of two compared with the E_{11} term given in equation 3.12 that results when the image wave vector k_s is parallel to the bias field.

It is through this analysis of resolution anisotropy, that the importance of the coherent grating in PICOC is seen. Consider a system such as shown in Figure 3.20.

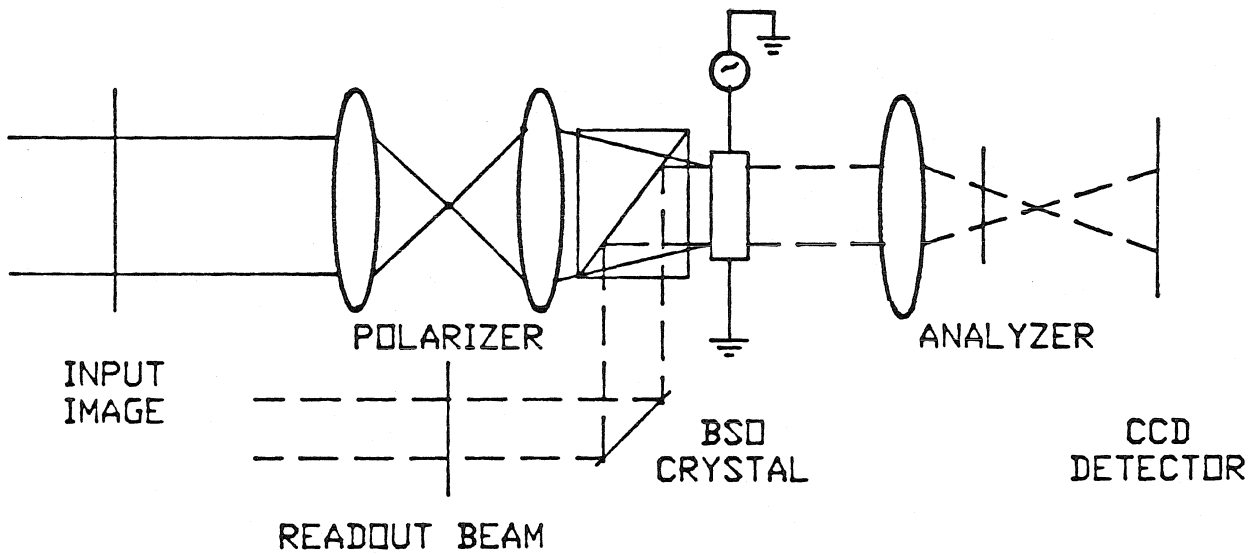

Fig. 3.20 Experimental Set-up for Implementing Conversion Without Coherent Writing Beams (Polarization Modulation)

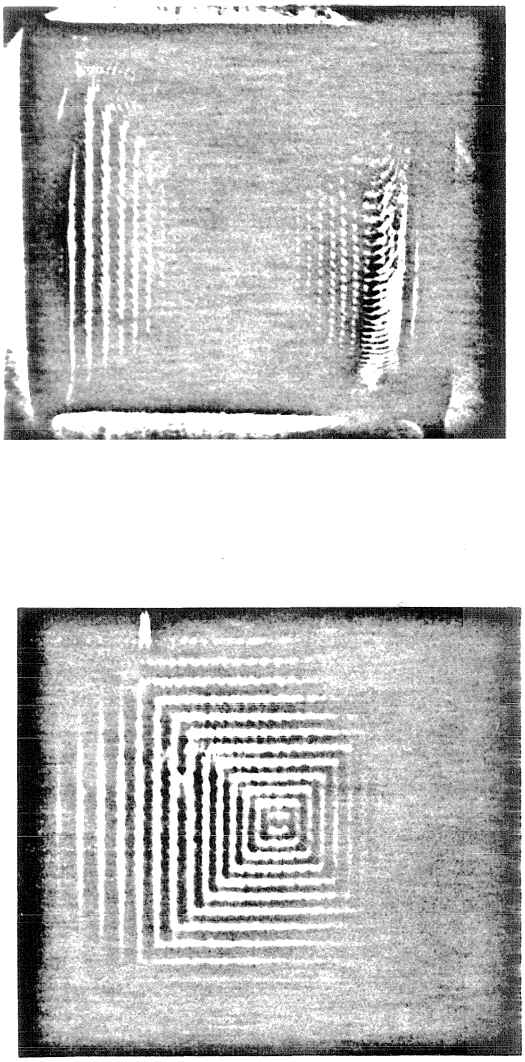

Fig. 3.21 Conversion of Nested Squares Image Using: a) No Coherent Beam (Phase Modulation), and b) With Coherent Beam (PICOC)

In this optical system, an incoherent image is imaged onto the BSO-crystal without the presence of the coherent grating. An auxillary beam is then used to read out the phase information recorded in the crystal through a set of crossed polarizers. The index perturbation induced in the crystal will result in a modulation of the intensity of the coherent light observed through to the polarizer. Figure 3.21a shows the conversion of a nested square image using this optical conversion system. The lines perpendicular to the direction of applied field have an increased index change due to the drift mechanism induced by the field. As for lines parallel to the applied field, the photorefractive process is totally governed by the weaker diffusion process. The result is high index variation for the lines perpendicular to the field and a low variation for lines parallel to the field, as demonstrated in Figure 3.21a. In contrast, if a coherent grating were added to the optical architecture as in the case of PICOC, the nested square image is converted nicely for lines oriented in both directions (Fig. 3.21b).

One immediate consequence of the severe anisotropy in converting without a coherent grating is in the response of the grating inhibition mode (GIM). Since the crystal must first support a space charge field generated by the incoherent image before a coherent grating is brought in, the anisotropy in the image induced field is transferred to the modulation of the coherent grating. As a result, modulation of the coherent grating by an incoherent structure perpendicular to the applied

field will be much more pronounced than modulation by structures parallel to the applied field. Thus, GIM cannot be used to convert two dimensional images to their coherent replicas, but must be constrained to only converting information with Fourier components nearly parallel to the direction of the applied field.

III.3.3.4 Bragg Limitations

In the configuration typically used in PICOC, the phase gratings are thick, and consequently the readout quality is degraded when the Bragg condition is not satisfied. This may occur by a slight angular misalignment of the readout beam or by sub-optimum alignment of the incoherent image beam. This section examines the readout of these phase gratings and its consequences for the performance of PICOC as a spatial light modulator.

Bragg detuning impacts PICOC performance in two ways: the angular alignment sensitivity of the hologram to the coherent readout beam, and the spatial frequency response of the hologram readout as a function of the incoherent image frequency. Consider first the alignment sensitivity to the coherent readout beam. The optimum angle at which a readout beam must be incident on the photorefractive crystal is given by the Bragg condition

$$sin(\theta_B) = \frac{\lambda_R k_g}{4\pi n_0} \qquad [3.21]$$

where θ_B is the Bragg angle, λ_R is the wavelength of the readout beam, $k_g/2\pi$ is the

spatial frequency of the phase grating, and n_0 is the refractive index of the crystal. An angular misalignment $\Delta\theta$ between the readout beam and the optimum Bragg alignment introduces decrease in the light diffracted from the crystal. The overall diffraction efficiency can be characterized through a Bragg mismatch parameter ξ of

$$\xi = \frac{\Delta k d}{2} = 0.5 k_g d \Delta\theta \qquad [3.22]$$

where k_g is the magnitude of the grating wavevector, $\Delta\theta$ is the angular deviation from the Bragg angle, and d the thickness of the volume hologram. Δk is a crystal independent mismatch parameter which is used in characterizing the relative amount of mismatch in a given optical configuration as shown in Figures 3.23 and 24. Assuming a small grating strength, the dependence of the diffraction efficiency on ξ is given by[19]

$$\eta = \eta_0 sinc^2(\xi) \qquad [3.23]$$

where η_0 is the diffraction efficiency when the Bragg condition is satisfied (i.e. $\xi = 0$). Thus, the angular misalignment $\Delta\theta$ needed to reach the first null of this profile occurs when

$$\Delta\theta = \frac{2\pi}{k_g d} = \frac{\Lambda_g}{d} \qquad [3.24]$$

where Λ_g is the wavelength of the grating. For a 2 mm thick photorefractive crystal with a 300 line/mm grating frequency, the angular tolerance is on the order of 0.1^o.

Hence very accurate angular alignment is needed to achieve optimum diffraction efficiency.

One possible alignment of the PICOC system is to orient the readout beam to be Bragg matched precisely to the coherent grating, thereby maximizing the intensity of the I_{10} diffracted order. When an incoherent grating is also incident upon the crystal, the nonlinear recording process creates a new grating with wave vectors $(k_g \pm k_s)$ that does not satisfy the same Bragg condition as the coherent grating wave vector k_g. The resulting I_{11} intensity component is then attenuated by an amount dependent upon the orientation and magnitude of the image wave vector k_s.

The importance of the orientation of k_s on the spatial frequency response of the converter is strinkingly illustrated in Figure 3.22. Two converted images of a 5 line/mm Ronchi ruling are shown at two orthogonal orientations along with their associated coherent Fourier transforms. As can be seen from the figure, a significant difference in resolution exists between cases in which the wave vector of the ruling is parallel or perpendicular to the coherently written grating. As a result, a higher number of diffracted orders can be seen in the direction perependicular to the coherent grating. This difference derives principally from the fact that a different wave vector matching condition exists for these two cases.

Consider the two wave vector matching conditions shown in Figures 3.23 and

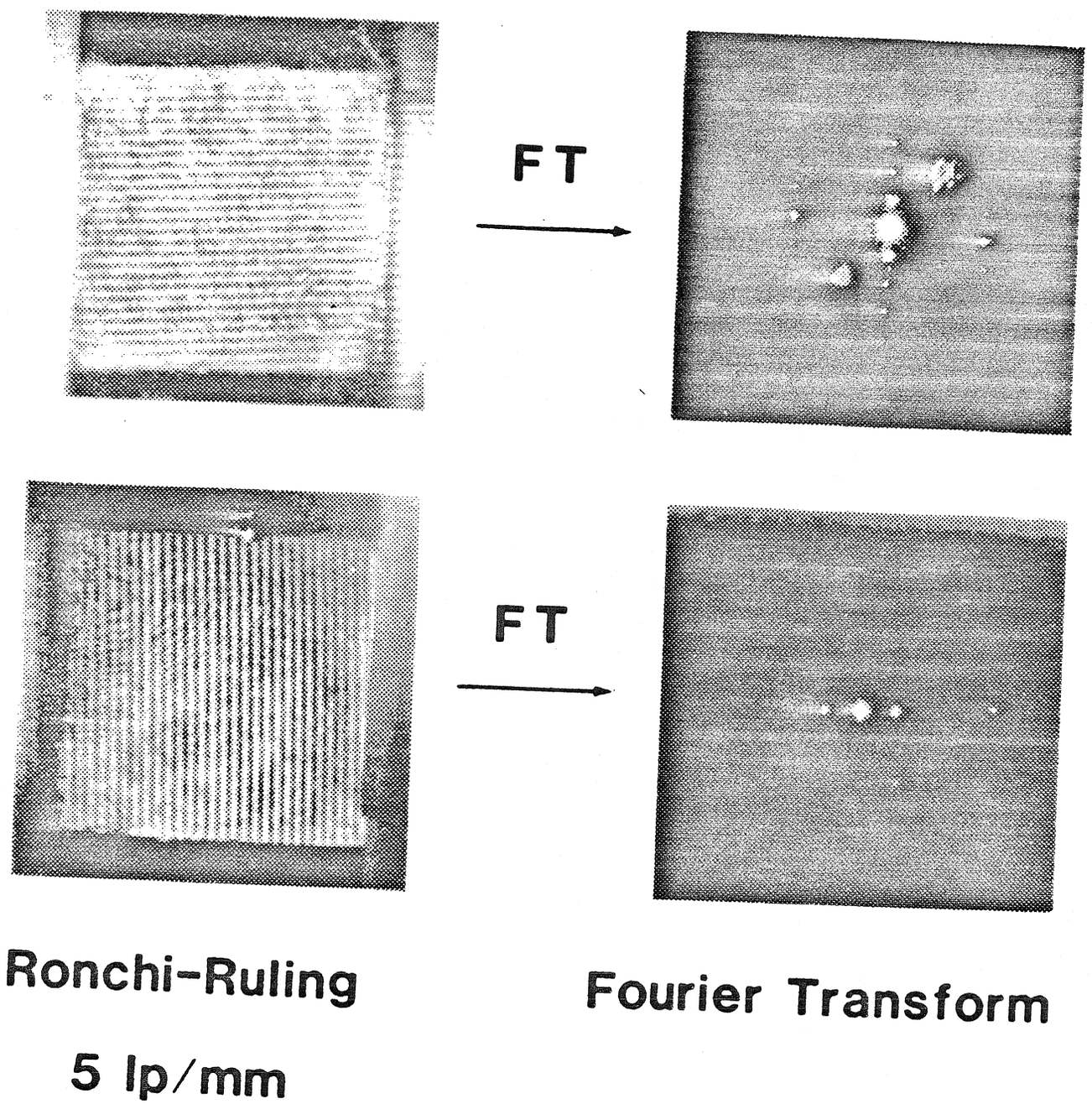

Fig. 3.22 Fourier Transform of a Conversion of a Ronchi- Ruling Image

3.24. In Figure 3.23, the incoherent grating wave vector k_s is parallel to the coherent grating wave vector k_g, a condition achieved by symmetrically orienting the incident coherent beams about the normal to the crystal while simultaneously arranging the incoherent imaging system such that its optical axis is parallel to the crystal normal. In this case, significant Bragg detuning occurs for even small incoherent grating wave vectors.

Let the spatial bandwidth of the readout process be defined as that spatial frequency f_s for which the magnitude of the I_{11} diffracted intenstiy component is attenuated to 25% of its peak value. As determined for equation 3.23, this occurs when the Bragg mismatch parameter $\xi = 1.9$. From equation 3.22, 25% attenuation will then occur when the amount of angular deviation is given by

$$\Delta\theta = \frac{1.9}{\pi f_g T} \qquad [3.25]$$

where f_g is the spatial frequency of the coherent grating. Taking the derivative of the Bragg condition results in a relationship between the spatial frequency of the incoherent image and the consequent angular mismatch

$$\Delta f_s = \frac{2n_0 cos\theta_B}{\lambda}\Delta\theta. \qquad [3.26]$$

Substituting equation 3.25 in 3.26 gives the spatial bandwidth of the incoherent image Δf_s

$$\Delta f_s = 1.2\frac{n_0}{f_g \lambda T} cos\theta_B. \qquad [3.27]$$

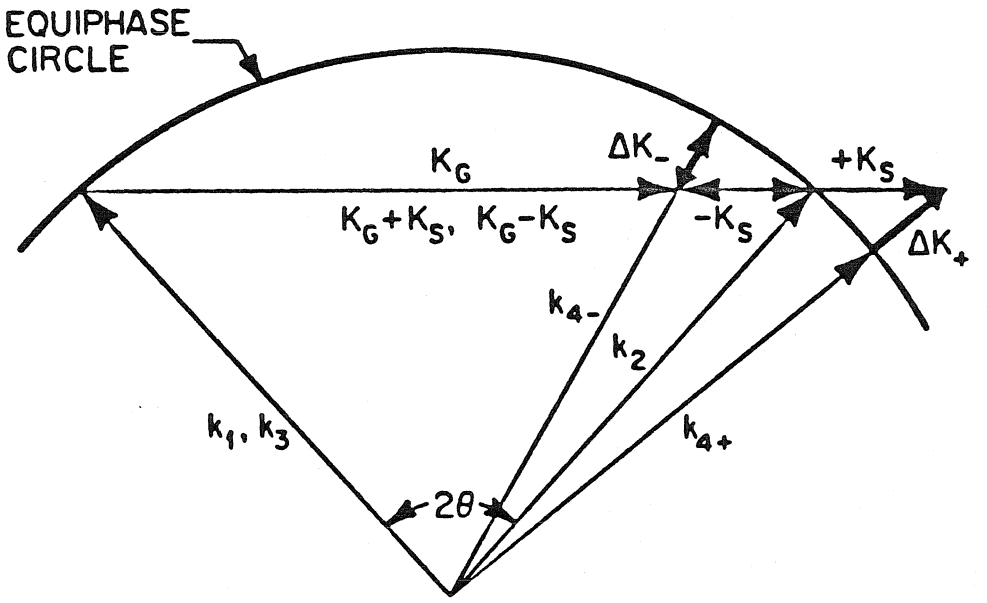

Fig. 3.23 Phase Matching Diagram for the Bisecting Configuration

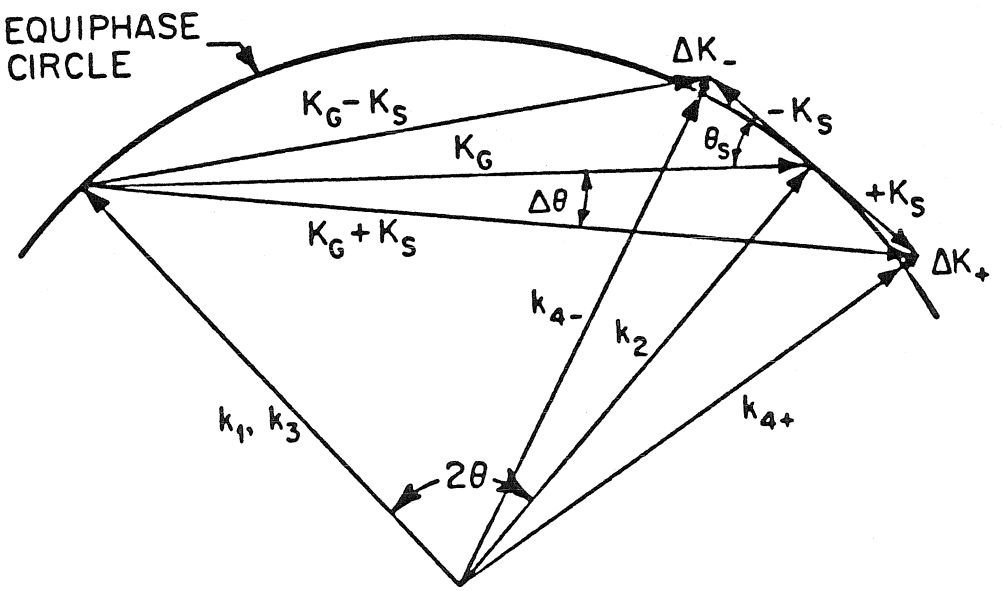

Fig. 3.24 Phase Matching Diagram for the Tangential Configuration

For the parameters used in our experiments (n_0 = 2.5, f_g = 300 lines/mm, T = 2mm, and λ = 488nm), this bandwidth is calculated to be on the order of 8 lines/mm. Note that doubling the crystal thickness d to increase the diffraction efficiency by almost a factor of four has the adverse effect of reducing the spatial bandwidth by a factor of two for this alignment configuration.

Compare now the resolution performance associated with the alignment of Figure 3.24 with that for Figure 3.23. In Figure 3.24, the incoherent grating wave vector is arranged to lie tangent to the circle defined by the readout wave vector. In this case Δk, which is given by the distance between the intermodulation grating wave vector and the equiphase circle is minimized. As a result, the angular deviation that can occur before serious Bragg detuning occurs is significantly increased, yielding a much larger incoherent spatial bandwidth. Such a wave vector tangency condition is automatically satisfied when the incoherent image wave vector is normal to the coherent grating wave vector as it is when recording an incoherent grating in the y orientation normal to the plane of incidence.. In addition, the wave vector tangency condition can be satisfied when the central ray of the incoherent image beam is aligned parallel to the diffracted probe light. A typical PICOC set-up achieving this tangency condition is shown in Figure 3.25.

In the tangential geometry, the addition of an image frequency f_s shifts the direction of the combined wave vectors ($k_g \pm k_s$) such that the incident readout

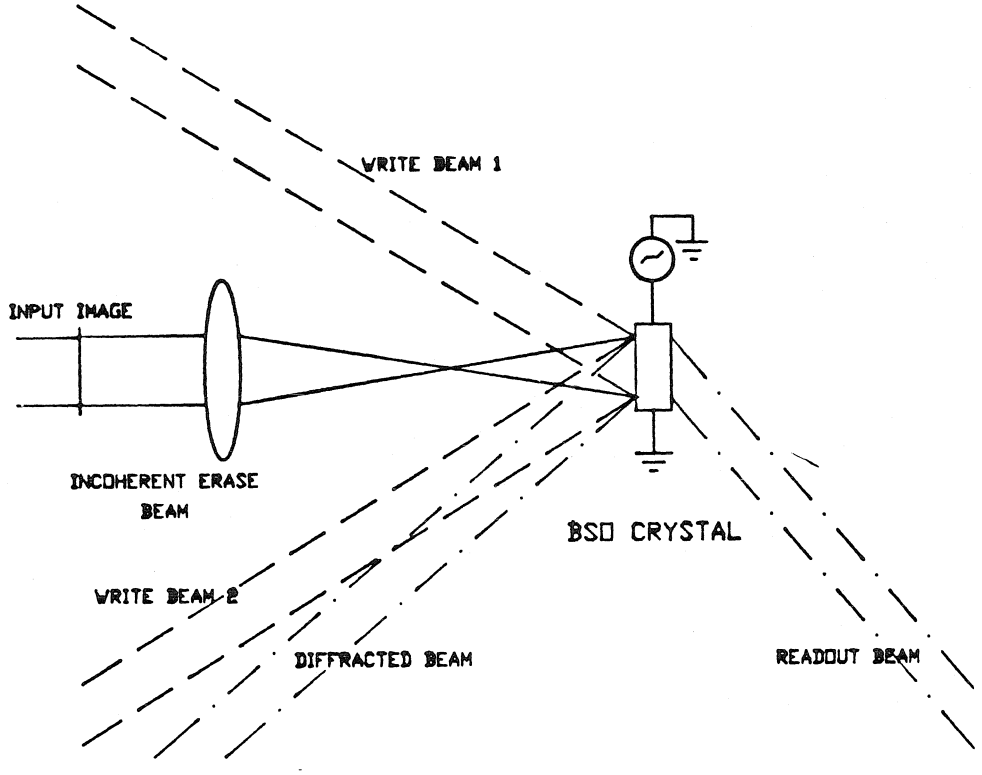

Fig. 3.25 Experimental Arrangement to Achieve Optimum Resolution

light remains almost perfectly Bragg matched over a much broader range of image frequencies. The mismatch parameter in this case can be geometrically calculated and is found to be

$$\Delta k = \left[\sqrt{(2\pi f_s)^2 + (\frac{2\pi n_0}{\lambda})^2} - \frac{2\pi n_0}{\lambda}\right]. \qquad [3.28]$$

Since $1/\lambda >> f_s$, equation 3.28 can be approximated by a binomial expansion.

$$\Delta k = \frac{2\pi\lambda f_s^2}{n_0}. \qquad [3.29]$$

Setting $\xi = 1.9$ and using equation [3.22], the resulting spatial bandwidth for the tangential configuration is

$$\Delta f_s = \sqrt{\frac{1.2 n_0}{\lambda_R d}}. \qquad [3.30]$$

For our experimental configuration, the tangential geometry increases the converter's bandwidth from 8 to 48 lines/mm. It is interesting to note that in addition to the increased bandwidth of the tangential geometry, the spatial resolution is independent of the the coherent grating frequency and that doubling the thickness of the crystal d does not halve the converter's bandwidth as it would for the colinear alignment configuration, but only reduces it by a factor of $\sqrt{2}$.

An important consideration for achieving the tangential matching needed to optimize the spatial bandwidth of the converter is the sensitivity of the system to angular misalignment. It can be shown that for small angular deviations α from

the optimum tangential matching conditon, the Bragg mismatch parameter, ξ, is given by

$$\xi = \pi f_s \alpha d \qquad [3.30]$$

Thus, the angular misalignment of the image beam results in an increased mismatch parameter and consequently a smaller angular bandwidth. For the conditions used in our experiments, an angular mismatch of approximately 0.7^o would result in a decrease in the spatial bandwidth from 48 to 24 lines/mm.

Further experimental tests of the Bragg detuning hypothesis are presented in figures 3.26-3.27, in which the image source was generated by a Michelson interferometer at a coherent wavelength of 514 nm (shown in Figure 3.14). The interferometer was used to alleviate the depth of focus issues discussed previously. In this experiment, the intensity of the diffracted component I_{11} was measured as a function of the spatial frequency of the image source grating. Figure 3.27 shows the response for the geometry in which the incoherent image beam bisects the coherent grating writing beams to achieve the wave vector mismatch condition diagrammed in Figure 3.23. The experimentally derived frequecy response indicate a bandwidth of about 9 lines/mm which agrees reasonably well with the theoretically predicted bandwidth of 8 lines/mm. Figure 3.27 shows the rolloff when the signal beam wave vector is tangent to the equiphase circle as shown in Figure 3.24, giving a much improved frequency response of 45 lines/mm. This again agrees well with the

theoretical bandwidth of 48 lines/mm.

Figure 3.28 shows the response of the converter to changes in the spatial frequency of the signal when its wave vector is oriented perpendicular to the direction of the applied bias field and coherent grating vector. The theoretical bandwidth for this configuration is identical to that of the tangential condition derived above. However, experimental measurements yielded a bandwidth of only 25 lines/mm. This discrepancy is attributed to a misalignment in the path of the incoherent image beam relative to the plane defined by the two coherent writing beams. A deviation of approximately 0.7^o would cause a deterioration of the bandwidth from 48 lines/mm to the observed 25 lines/mm.

To conclude, we have found that the material limitations on the spatial resolution of PICOC are negligible when compared with the geometrical limitations resulting from finite apertures in the incoherent imaging system. These in turn are comparable with the limitations on resolution due to the Bragg sensitivities inherent when recording in a volume hologram. As a consequence of these Bragg sensitivities, the readout beam must be aligned typically within 0.1^o of the optimum and the image bearing beam to within 0.5^o. In addition, the optimum alignment does not consist of bisecting the two beams that record the coherent grating with the incoherent image, but rather aligning the incoherent imaging beam with the diffracted probe thereby achieving the tangency condition necessary for maximum

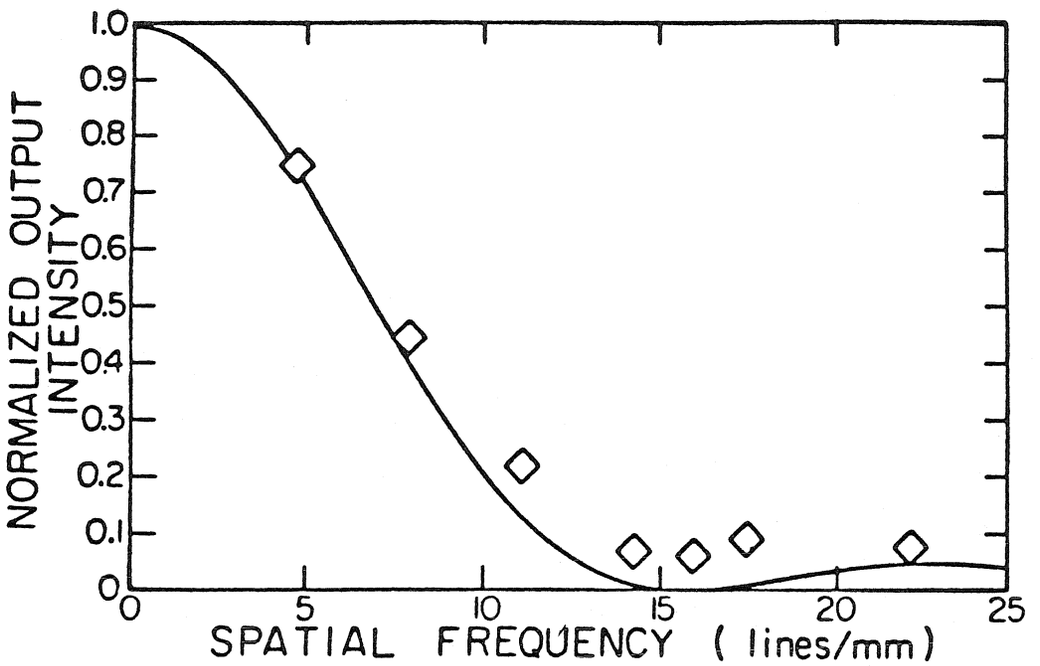

Fig. 3.26 Experimental Measurements of Spatial Resolution in Bisecting Configuration

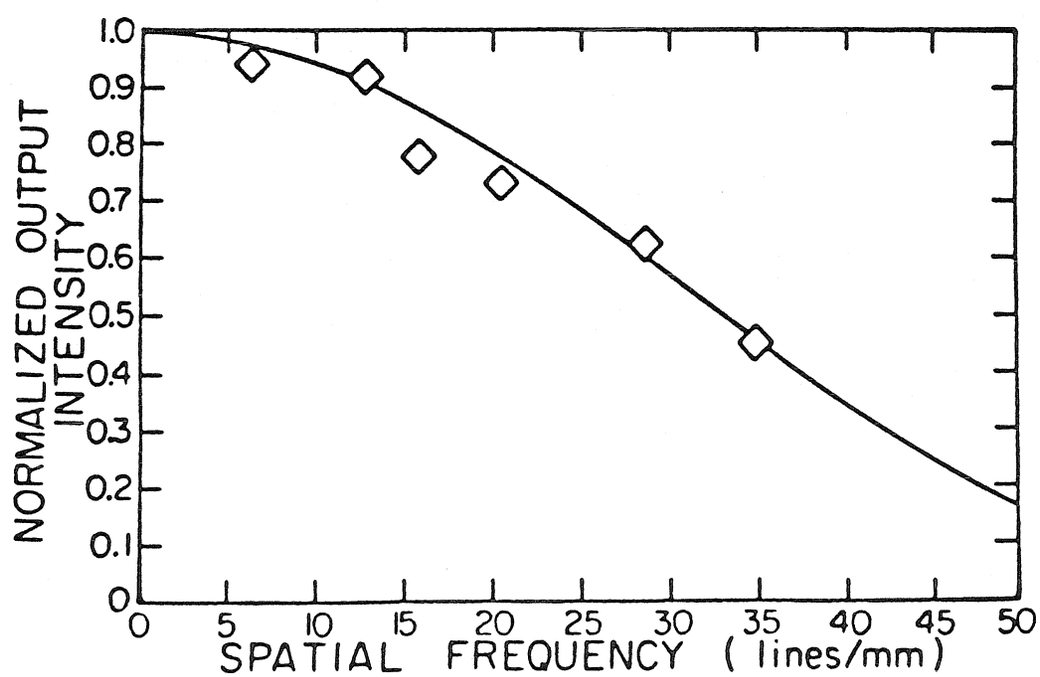

Fig. 3.27 Experimental Measurements of Spatial Resolution in Tangential Configuration

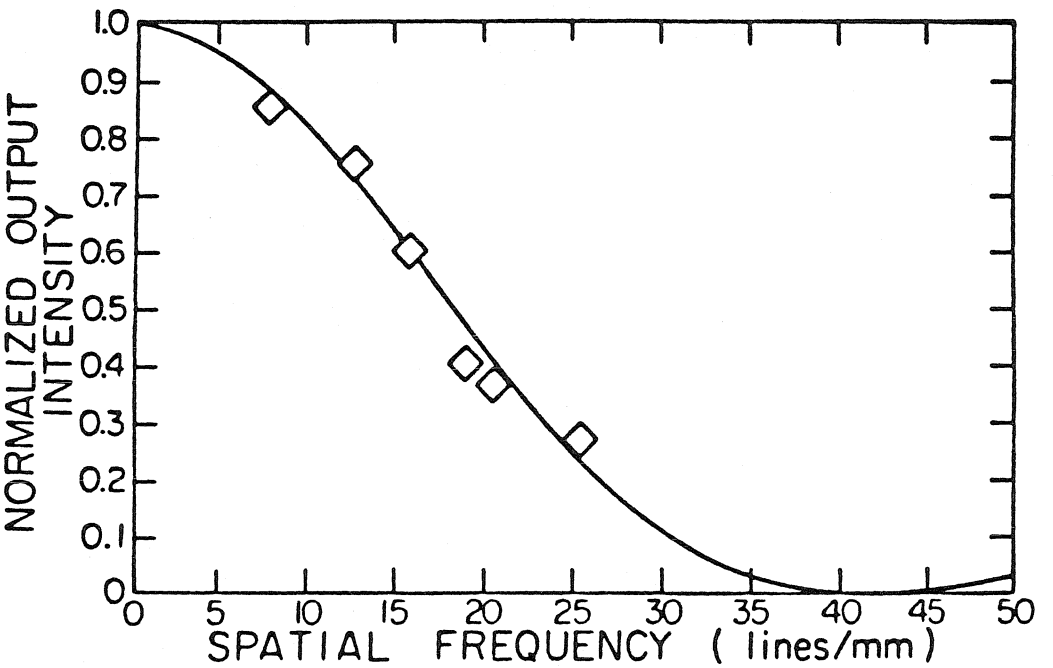

Fig. 3.28 Experimental Measurement of Spatial Resolution in the Direction Perpendicular to the Applied Electric Field

bandwidth.

III.3.4 Higher Order Model

A double perturbation expansion such as the one described in section II.4 can be used to calculate higher order spatial Fourier components of the space charge field in the case of PICOC. In this procedure, numerical methods were used to solve for the first 50 Fourier terms of the space charge field as well as the electron and trap densities. The major difference from the calculations performed in Chapter 2 is the presence of both an incoherent and coherent intensity being recorded in the crystal. In order to simplify the numerical calculations, the coherent spatial frequency was chosen to be a multiple of the incoherent spatial frequency. As a result, accounting of the higher orders of the incoherent gratings could be accomplished at the same time as the Fourir orders of the coherent gratings. Using this technique, it is possible to generate the space charge field that is induced by the two incident gratings. Figure 3.29 shows the space charge profiles that are generated for 6kV/cm applied field, a incoherent frequency of 10 lines/mm, and coherent frequency of 200 lines/mm. Incoherent to coherent intensity ratios of 10, 1, and 0.1 are represented in this figure. From these figures, the modulation of the coherent grating pattern by the incoherent grating is clearly evident resulting in the necessary refractive index profile to perform incoherent to coherent conversion. Figure 3.30 shows the space charge

profiles in the absence of an applied field and the same conditions used to generate Figure 3.29. Again, the profile shows the incoherent grating modulating the high frequency coherent grating.

III.4 Temporal Response of PICOC

A temporal response analysis is necessary for the study of the photorefractive incoherent to coherent conversion process. In the grating inhibition (GIM) and grating erasure (GEM) modes, analysis is necessary to determine the optimum sequencing of the coherent and incoherent light beams. The temporal analysis is also of interest in the simultaneous erasure/writing mode (SEWM) because it clarifies the duration and nature of the transient writing period before a stable response is achieved, and also because it leads to the reciprocity law between the incident light power and the response time of the converter. The analysis reported here is restricted to small modulation regimes for simplicity. The results are modified substantially when operating with large modulation depths and require the use of numerical methods to provide accurate predictions of the dynamic behavior of PICOC.

Let us consider one version of the simultaneous erasure/writing mode (SEWM) for the photorefractive incoherent to coherent optical conversion (PICOC) process. In this example, we assume that a coherent grating of wave vector k_g has been prewritten on the photorefractive crystal and has reached its steady state value. At

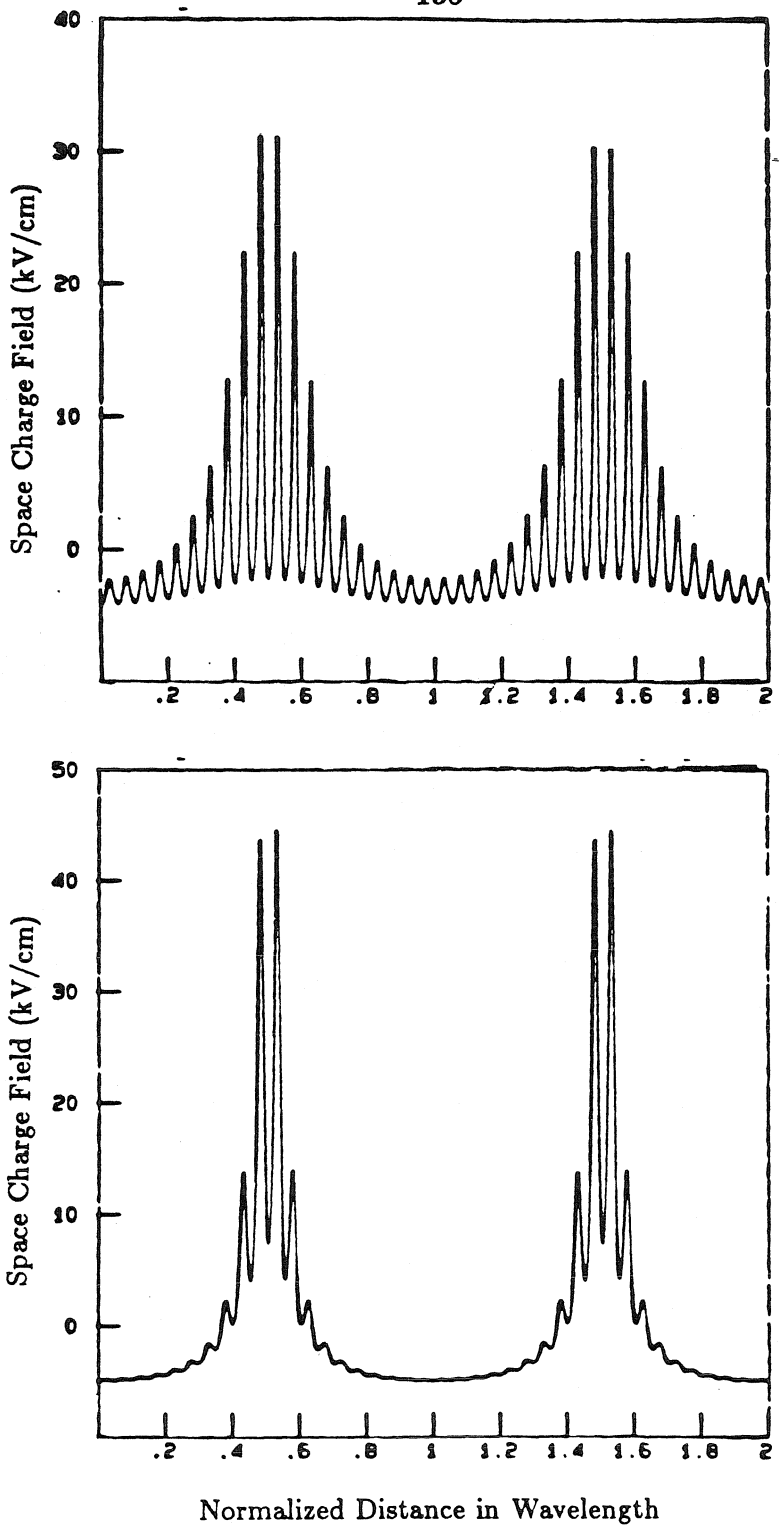

Fig. 3.29 Space Charge Field Profile of Two Grating Incident on a Photorefractive Crystal. E_0=6kV/cm, f_g = 200 l/mm, f_s = 10 l/mm, m_g=1, m_s=1. a) I_s/I_c = 1, b) I_s/I_c = 10, and c) I_s/I_c = 0.1

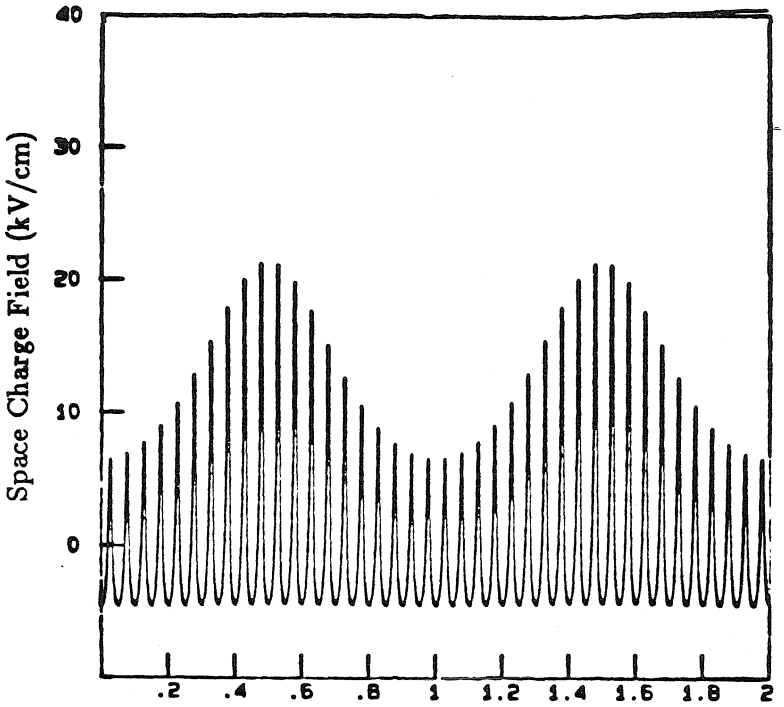
40
30
20
10
0
Space Charge Field (kV/cm)
.2
.4
.6
.8
1
1.2
1.4
1.6
1.8
2
Normalized Distance in Wavelength

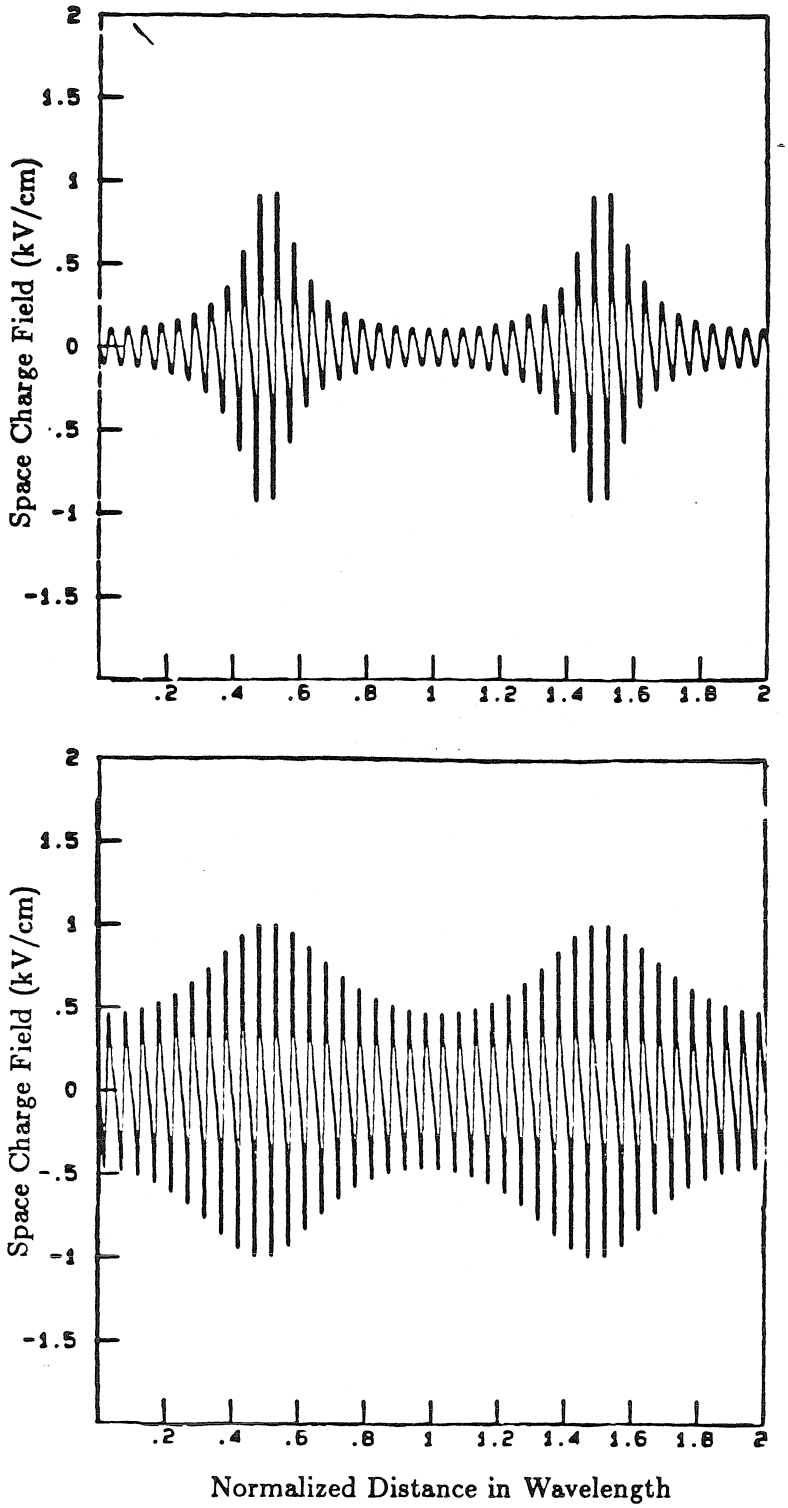

Fig. 3.30 Space Charge Field Profile of Two Grating Incident on a Photorefractive Crystal. E_0=0kV/cm, f_g = 200 l/mm, f_s = 10 l/mm, m_g=1, m_s=1. a) $I_s/I_c = 1$, b) $I_s/I_c = 10$, and c) $I_s/I_c = 0.1$

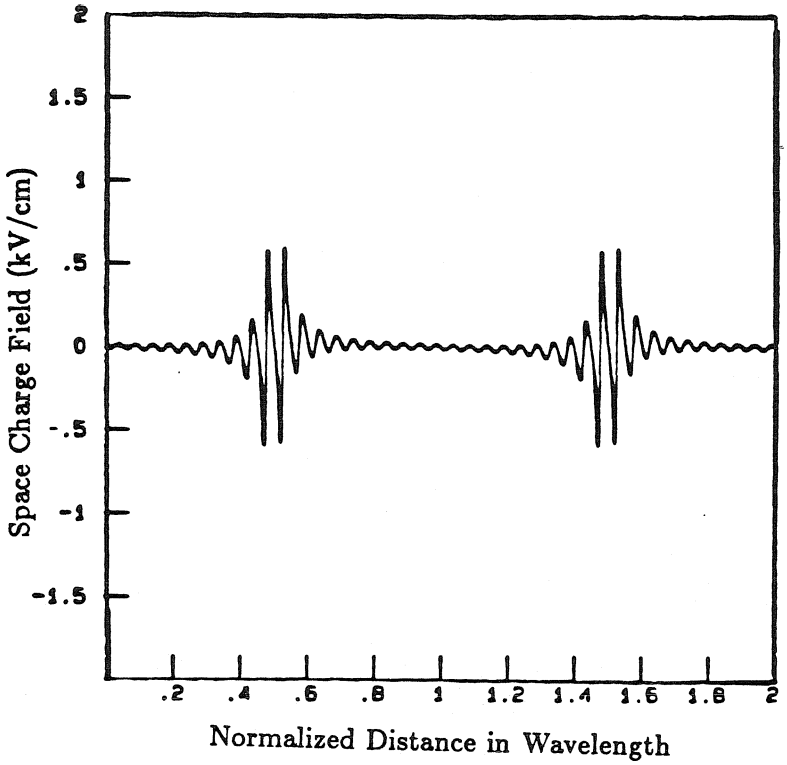
2
1.5
1
.5
0
-.5
-1
-1.5
Space Charge Field (kV/cm)
.2
.4
.6
.8
1
1.2
1.4
1.6
1.8
2
Normalized Distance in Wavelength

time t = 0, a grating with wave vector k_s is turned on. The intensity incident upon the crystal is then described by

$$I(x,t) = \begin{cases} I_0(1 + m_g cosk_g x) & \text{t<0} \\ I_0(1 + m_g cosk_g x) + I_1(1 + m_s cosk_s x) & \text{t>0.} \end{cases} \quad [3.32]$$

The temporal evolution of the various components of the space charge field can be solved for by perturbation techniques, valid for small levels of the modulation depth m_g. The derivations are included in Appendix III.A.3.

The temporal response of the E_{11} intermodulation term arises from the multiplicative nonlinearities inherent in the photorefractive process. Since these nonlinearities generating the E_{11} intermodulation term arises from the product of the space charge field at the two fundamental frequencies, it is expected that the time response for E_{11} would be determined by the temporal evolution of the product of the E_{10} and E_{01} fields. From the Kukhtarev analysis, the time response for the space charge field at the coherent frequency is expected to decay from its initial value to a steady state value with an exponential time constant $\tau[k_g]$. Hence, E_{10} is proportional to

$$E_{10} \propto [(m_g - m_g^{eff})e^{-t/\tau[k_g]} + m_g^{eff}] \quad [3.33]$$

where m_g^{eff} is the effective modulation depth of the coherent grating in the presence of both the coherent and incoherent beams and is given by

$$m_g^{eff} = \frac{m_g I_0}{m_g I_0 + m_s I_1} \quad [3.34]$$

and $\tau[k]$ is the complex time constant of a single frequency grating with wave vector k and is given by the expression [17]

$$\tau[k] = t_0 \frac{1 - i(E_0 + iE_d[k]/E_q[k])}{1 - i(E_0 + iE_d[k]/E_m[k])}. \qquad [3.35]$$

t_0 is the dielectric relaxation time and is given

$$t_0 = \frac{N_{Deq}^+}{\alpha N_D I_0} \qquad [3.36]$$

and the E_d, E_m, and E_q are the characteristic fields for diffusion, drift and trap limited space charge, respectively

$$E_d[k] = \frac{k_B T k}{e} \qquad [3.37]$$

$$E_m[k] = \frac{\sigma N_A}{\mu k} \qquad [3.38]$$

$$E_q[k] = \frac{eN_A}{\epsilon k}. \qquad [3.39]$$

Likewise, the space charge field induced by the incoherent grating rises exponentially from its zero initial condition to its final steady state value with an exponential rise time of $\tau[k_s]$

$$E_{01} \propto m_s[1 - e^{-t/\tau[k_s]}]. \qquad [3.40]$$

The product of equations 3.33 and 3.40 give rise to the time constants which are important in the dynamical behavior of the E_{11} intermodulation term. These time constants are $\tau[k_g]$, $\tau[k_s]$, and their product τ_2, where

$$\tau_2 = \left[\frac{1}{\tau[k_g]} + \frac{1}{\tau[k_s]}\right]^{-1}. \qquad [3.41]$$

The recording of the E_{11} intermodulation component is in fact a recording of a grating at a spatial frequency $k_s + k_g$. Such a grating is characterized by a time constant $\tau[k_s+k_g]$ which is unique to its spatial frequency. The temporal evolution of E_{11} can be considered to be a system with a resonant time constant $\tau[k_s+k_g]$ which is forced by a term proportional to the product of the E_{10} and E_{01} space charge field components. Hence, the E_{11} component will consist of four characteristic time constants $\tau[k_s]$, $\tau[k_g]$, $\tau[k_s + k_g]$ and τ_2 and have the form

$$E_{11} = M_0 + M_1 e^{-t/\tau[k_g]} + M_2 e^{-t/\tau[k_s]} + M_3 e^{-t/\tau[k_g+k_s]} + M_4 e^{-t/\tau_2}. \qquad [3.42]$$

Explicit expressions for $M_0 - M_5$ are presented in the Appendix III.A.3 (Eqns. A.42-A.53). The time independent term M_0 corresponds to the steady state value of E_{11}.

The response time of the system is dependent on four distinct time constants as well as the relative magnitudes of M_1 to M_4. Each of the four time constants, however, is inversely related to the amount of intensity incident on the crystal. Hence, the overall time constant for the E_{11} component can be rewritten as

$$E_{11}(t) = E'_{11}\left(\frac{t}{s_g I_0 + s_s I_1}\right). \qquad [3.43]$$

Thus, the time required to reach saturation is characterized through the following reciprocity law:

$$\tau_{sys} = \frac{G}{s_g I_0 + s_s I_1}. \qquad [3.44]$$

The proportionality constant G involves only material parameters and the applied bias field E_0. As a result, the rate at which new information can be recorded is determined by the total available intensity incident on the crystal.

Similar temporal response analyses have been performed for both the grating inhibition mode (GIM) (Appendix III.B) and the grating enhancement mode (GEM) (Appendix III.C). In the GEM mode, the response time constant of the system is inversely proportional to the incoherent erasing intensity I_1, rather than the sum of the incoherent and coherent intensities. Conversely in the GIM mode, the time constant of the system is inversely proportional to the coherent intensity I_0.

Sample analytical solutions for GEM, GIM, and SEWM are shown in Figures 3.31, 3.32 and 3.33 respectively for a 1 mW/cm^2 average intensity coherent grating beam at 515 nm wavelength with a spatial grating frequency of 200 lines/mm and a small modulation depth m_g, a 1 mW/cm^2 average intensity incoherent image bearing beam at 488 nm wavelength with an image spatial frequency of 10 lines/mm and also with a small modulation depth m_s, an applied bias field of 6kV/cm and with material parameters for bismuth silicon oxide as given in Table 2.1.

Figure 3.31 shows the GEM response for three diffracted light components, I_{10}, I_{01}, and I_{11}. The coherent grating has been recorded to saturation and then turned off before the time interval shown in the figure. The time t = 0 is defined when the image bearing beam is turned on. Thus the coherent grating frequency I_{10} starts

at its saturated level and decays for $t > 0$ because of erasure by the image-bearing beam. The direct recording of the image-bearing beam I_{01} grows from an initial value of zero to its saturation level. Note that the response time for the I_{01} image component, with its much lower spatial frequency, is significantly faster than that for the I_{10} coherent grating component. The image modulated grating component I_{11} exhibits a temporal response which is derived from a combination of the I_{10} and I_{01} response, eventually evolving into a slow decay in time when the incoherent image-bearing light beam erases the coherent grating. The image modulated grating component I_{11} initially shows a very rapid rise, followed by a much slower erasure by the coherent grating beam, eventually decaying to zero for very long recording times. As a result, to convert incoherent image efficiently, the image-bearing light exposure time must be truncated before decay of the intensity begins to occur.

Figure 3.32 shows a similar set of temporal response curves for GIM. The image-bearing light has been recorded to saturation, then turned off before the time interval shown in this figure. Time t = 0 is defined when the coherent grating light is turned on. In this mode, I_{10} starts with zero intensity and gradually grows to saturation, whereas the directly recorded incoherent image-bearing beam I_{01} starts from its saturation level and is quite rapidly erased by the uniform component of the coherent grating light. The I_{11} gradually builds up to its maximum value and is eventually erased when the space charge induced by the image-bearing beam is

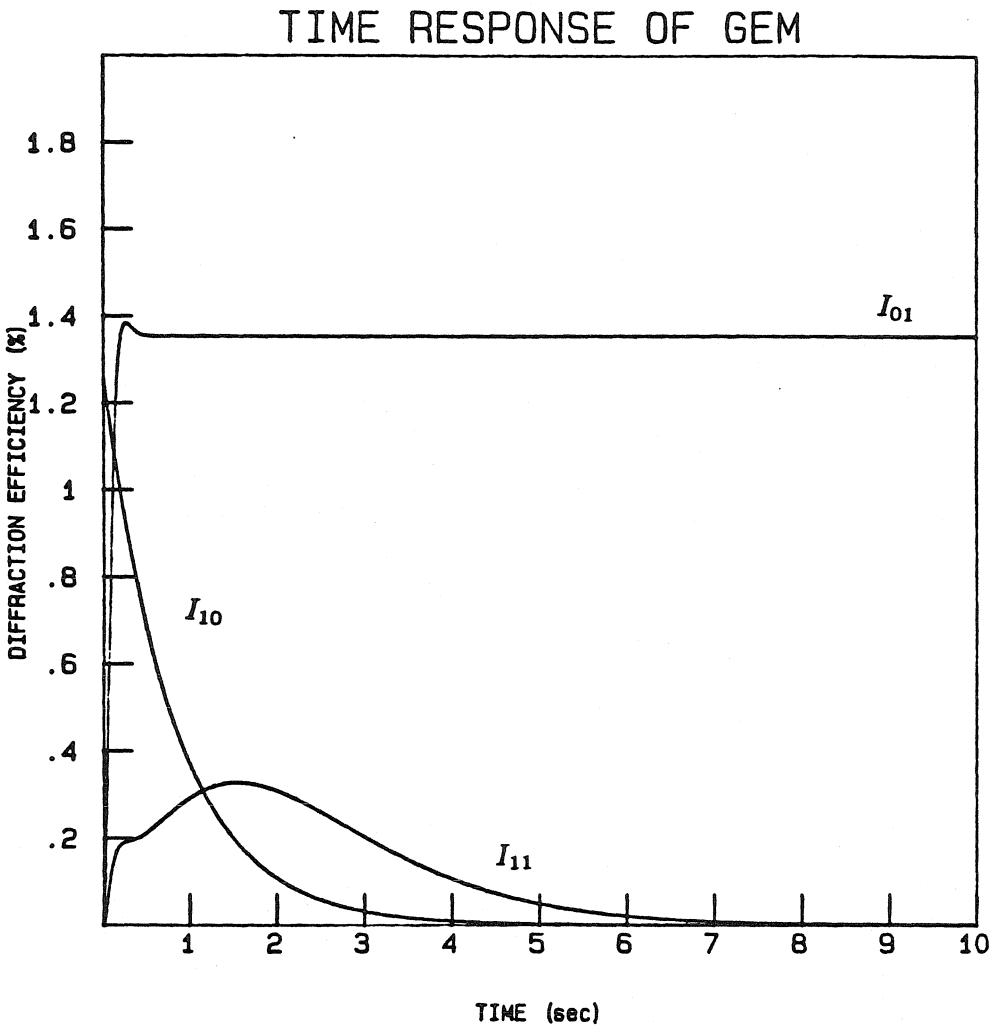

Fig. 3.31 Temporal Response of GEM

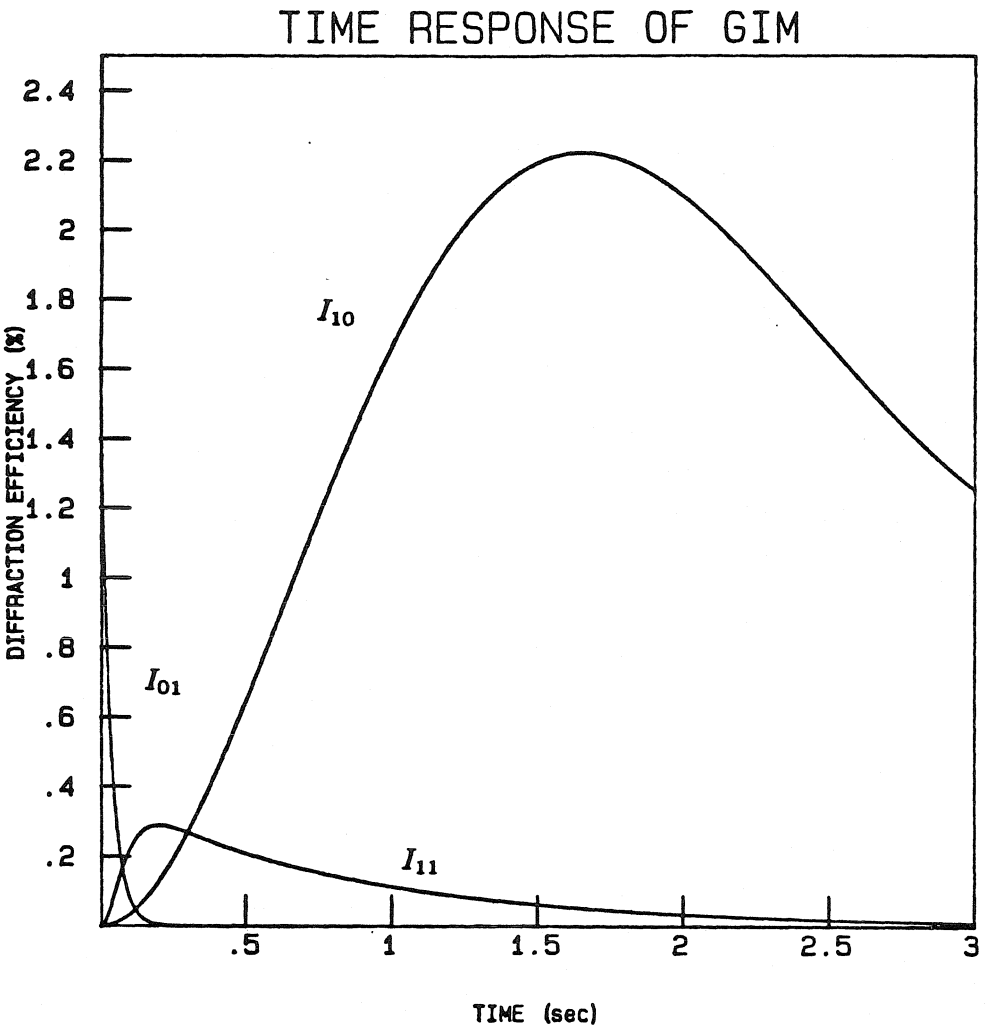

Fig. 3.32 Temporal Response of GIM

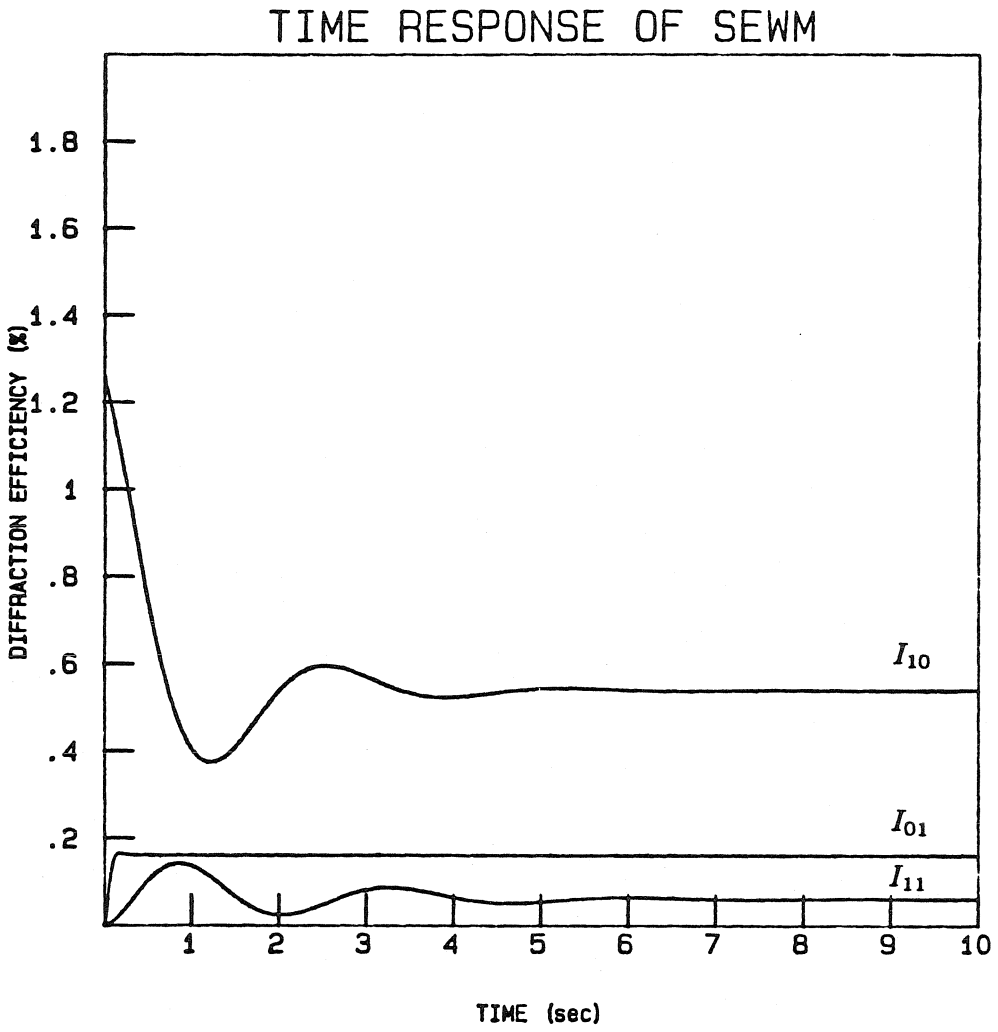

Fig. 3.33 Temporal Response of SEWM

erate a rapid rise in the amplitude of I_{11}, but the strong incoherent illumination eventually erases the coherent grating and hence the diffraction efficiency decreases to a small steady state value.

III.5 Conclusion

Through the use of a photorefractive crystal, an incoherent to coherent optical converter, PICOC, has successfully converted incoherent images into their coherent replicas. The PICOC system is simple, easy to implement, and compares favorably in its performance with other photorefractive spatial light modulators. A mathematical framework has been developed to analyze the performance of the converter. Using this formalism, conditions necessary to achieve high linearity, good contrast ratio, high spatial bandwidth and fast temporal response have been derived.

Despite the simplicity and high spatial bandwidth of the photorefractive incoherent to coherent converter, the converter exhibits two major drawbacks: low diffraction efficiency and slow response time. The efficiency of the converter is primarily due to the choice of material, specifically BSO, which demonstrates a maximum diffraction on the order of 1% for the crystal thicknesses used in our experiments. Other crystals with higher electro-optic coefficients such as $LiNbO_3$:Fe and SBN may be used in place of BSO to improve the efficiency of the converter. Another method of increasing the diffraction efficiency can be accomplished by increasing the thickness of the crystal; however this results in a decrease in the spatial

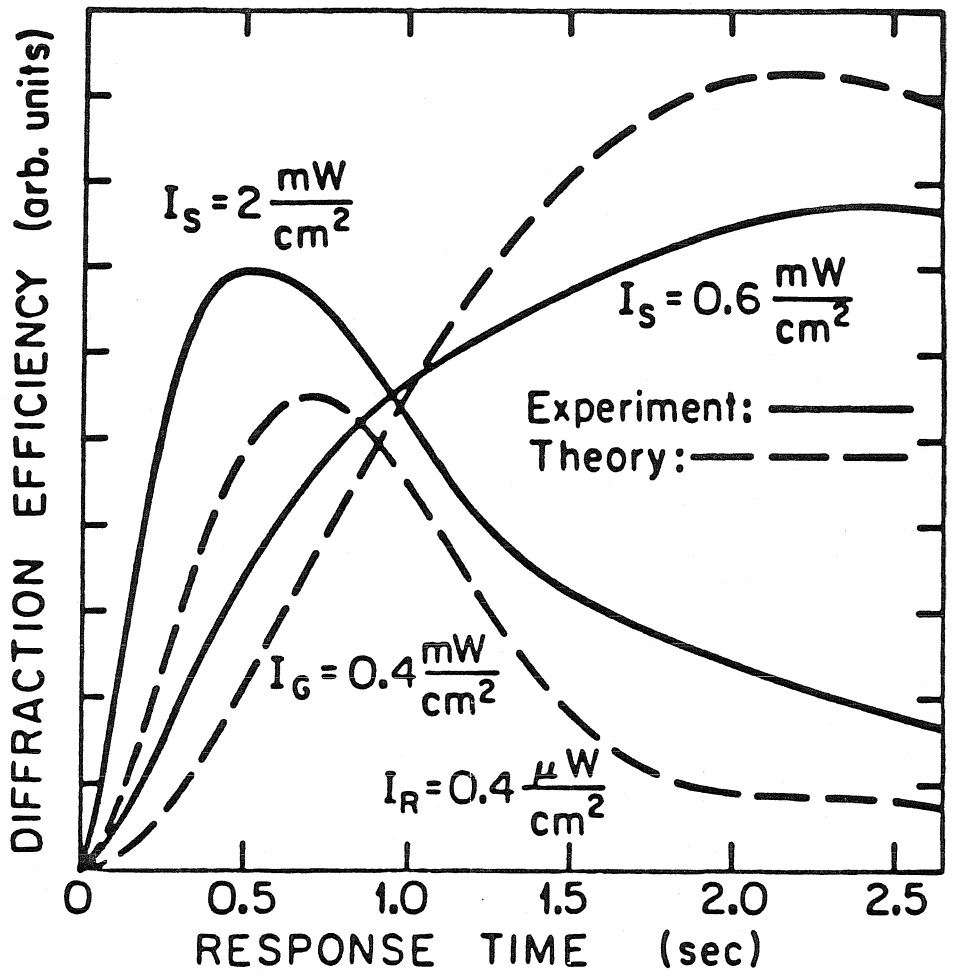

Fig. 3.34 Experimental Results for the Temporal Response of SEWM

bandwidth of the converter. The slow response time of PICOC also results from the choice of the photorefractive material used to implement the converter. It is possible to increase the recording time of the converter by increasing the amount of light incident on the photorefractive crystal. This technique, however, is still limited by the availability of high intensity levels required to achieve a fast writing rate. Faster converters may be implemented by using photorefractive crystals which exhibit inherently fast response times (*i.e.*, GaAs). These crystals, however, are still fundamentally limited by the amount of light incident on the material [20].

APPENDIX

Steady State and Temporal Behavior of the Space Charge Field Components in PICOC

III.A. Simultaneous Erase/Write Mode (SEWM)

In this appendix, the expressions for the lowest order components of the space charge field E_{mn} are presented, both in the steady state as well as its full temporal evolution.

The material equations which characterize the photorefractive process are described in section II.3 and are rewritten below

$$\frac{\partial N_D^+}{\partial t} = s_g N_D I_g - \gamma_r N_D^+ n \qquad [A.1]$$

$$\frac{\partial N_D^+}{\partial t} = -\frac{1}{e}\frac{\partial J}{\partial x} \qquad [A.2]$$

$$\frac{\partial E}{\partial x} = \frac{e}{\epsilon}(N_D^+ - N_A) \qquad [A.3]$$

$$J = \mu e n E + k_B T \frac{\partial n}{\partial x}. \qquad [A.4]$$

In writing the above equations, the effects of dark current is neglected and the fact that $n << N_D^+ = N_A << N_D$, and $\frac{\partial n}{\partial t} << \frac{\partial N_D^+}{\partial t}$ is used to simplify the equations.

III.A.1 Steady State Behavior

In the steady state regime of the simultaneous erasure/writing mode of PICOC, the light incident on the photorefractive crystal is given by

$$I(x) = I_0(1 + m_g cosk_g x) + I_1(1 + m_s cosk_s x). \qquad [A.5]$$

In order to derive the space charge field components which describe the conversion process, we assume that the electric field can be written as

$$E(x) = E_0 + E_{10}e^{ik_g x} + E_{01}e^{ik_s x} + E_{11}e^{i(k_g+k_s)x} + E_{1-1}e^{i(k_g-k_s)x} + \text{c.c.} \quad [A.6]$$

The first term E_0 corresponds to the applied DC field, and the second and third terms E_{10} and E_{01} correspond to the amplitude of the field at the fundamental frequencies of the incident gratings. The last two terms E_{11} and E_{1-1} are the amplitudes of the cross terms generated through the nonlinearities inherent in the photorefractive effect. As discussed in section III.3, without the generation of these intermodulation terms, conversion of the incoherent image to its coherent replica could not occur.

Expressions for the trap, electron, and current densities are also assumed to have forms similar to equation A.6

$$N_D^+(x) = N_{Deq}^+ + N_{D10}^+e^{ik_g x} + N_{D01}^+e^{ik_s x} + N_{D11}^+e^{i(k_g+k_s)x} + N_{D1-1}^+e^{i(k_g-k_s)x} + \text{c.c.} \quad [A.7]$$

$$n(x) = n_0 + n_{10}e^{ik_g x} + n_{01}e^{ik_s x} + n_{11}e^{i(k_g+k_s)x} + n_{1-1}e^{i(k_g-k_s)x} + \text{c.c.} \quad [A.8]$$

$$J(x) = J_0 + J_{10}e^{ik_g x} + J_{01}e^{ik_s x} + J_{11}e^{i(k_g+k_s)x} + J_{1-1}e^{i(k_g-k_s)x} + \text{c.c.} \quad [A.9]$$

By substituting equations A.6-A.9 into the steady state form (d/dt=0) of the material equations A.1-A.4 and combining terms with equal spatial frequency components, one can derive the amplitudes of the various space charge field components.

Combining the nonsinusoidal component leads to the following equation for the background density of electrons

$$n_0 = \frac{s_g N_D I_0 + s_s N_D I_1)}{\gamma_r N_{Deq}^+}. \qquad [A.10]$$

Using equation A.10, the space charge field amplitudes for the components at the two fundamental frequencies k_s and k_g can be found. These terms are very similar to the response of the crystal to an intensity pattern consisting of only a single frequency grating and are found to be

$$E_{10} = -\frac{m_g^{eff}}{2} \frac{E_0 + iE_d[k_g]}{1 - i[E_0 + iE_d[k_g]/E_q[k_g]]} \qquad [A.11]$$

$$E_{01} = -\frac{m_s^{eff}}{2} \frac{E_0 + iE_d[k_s]}{1 - i[E_0 + iE_d[k_s]/E_q[k_s]]} \qquad [A.12]$$

in which

$$m_g^{eff} = m_g\left[\frac{s_g I_0}{s_g I_0 + s_s I_1}\right] \qquad [A.13]$$

$$m_s^{eff} = m_s\left[\frac{s_s I_1}{s_g I_0 + s_s I_1}\right]. \qquad [A.14]$$

$E_q[k]$ and $E_d[k]$ are the space charge limited and diffusion limited space charge fields and are functions of the spatial frequency of the gratings

$$E_q[k] = \frac{eN_{Deq}^+}{\epsilon k} \qquad [A.15]$$

$$E_d[k] = \frac{k_B T k}{e}. \qquad [A.16]$$

In addition to the space charge field components, one can also derive the trap and electon densities at the fundamental frequencies (*i.e.*, $N^+_{D10}, N^+_{D01}, n_{10}$ and n_{01}). Because of the nonlinearities in the material equations, expressions for these components are important in deriving the amplitudes of the intermodulation terms E_{11} and E_{1-1}.

Consider the E_{11} component. By collecting terms with spatial frequency components $(k_s + k_g)$ and combining the steady state forms of equations A.2 and A.4, the following set of equations can be derived:

$$(N^+_{D11} n_0 + N^+_{D0} n_{11}) = (N^+_{D10} n_{01} + N^+_{D01} n_{10}) \qquad [A.17]$$

$$i\mu e(k_s+k_g)(n_{11}E_0+n_0E_{11})-k_BT(k_s+k_g)^2 n_{11} = -i\mu e[(k_s+k_g)(n_{10}E_{01}+n_{01}E_{10})] \qquad [A.18]$$

$$E_{11} = \frac{-ie}{(k_s+k_g)\epsilon} N^+_{D11}. \qquad [A.19]$$

By substituting equations A.11 and A.12 as well as the explicit expressions for N^+_{D10}, N^+_{D01}, n_{10} and n_{01} into equations A.17-A.19, the amplitude of E_{11} can be derived. In the steady state regime, this amplitude is

$$E_{11} = \frac{m_g^{eff} m_s^{eff}}{4}[C_1[k_s+k_g, k_g]D_1[k_g]D_2[k_s]+C_1[k_s+k_g, k_s]D_1[k_s]D_2[k_g]] \qquad [A.20]$$

where

$$C_1[k_1, k_2] = \frac{E_0 + i(E_d[k1] + E_q[k2])}{1 - i(E_0 + iE_d[k1])/E_q[k1]} \qquad [A.21]$$

$$D_1[k] = \frac{E_0 + iE_d[k]}{E_0 + i(E_d[k] + E_q[k])} \qquad [A.22]$$

$$D_2[k] = \frac{iE_q[k]}{E_0 + i(E_d[k] + E_q[k])}. \qquad [A.23]$$

If the spatial frequency of both the coherent and incoherent gratings is less than 200 lines/mm and the applied field is between 2 and 15 kV/cm, then $E_q >> E_0 >> E_d$. In this regime, $D_1[k] = E_0/iE_q[k], D_2 = 1$ and $C[k1, k2] = iE_q[k2]$. As a result E_{11} simplifies to

$$E_{11} = \frac{m_g^{eff} m_s^{eff}}{2} E_0. \qquad [A.24]$$

III.A.2 Steady State Analysis in Two Dimensions

In this section, we consider the effect of an incoherent intensity grating oriented perpendicular to the direction of the applied field. The intensity incident on the photorefractive crystal is given by

$$I(x,y) = I_0(1 + m_g cosk_g x) + I_1(1 + m_s cosk_s y) \qquad [A.25]$$

where the applied field is chosen to be parallel to the x direction. Let us assume that the electric field vector can be written as

$$\vec{E}(x,y) = \hat{x}\left[E_0 + E_{10}e^{ik_g x} + E_{11x}e^{i(k_g x + k_s y)} + E_{1-1x}e^{i(k_g x - k_s y)}\right] + \hat{y}\left[E_{01}e^{ik_s x} + E_{11y}e^{i(k_g x + k_s y)} + E_{1-1y}e^{i(k_g x - k_s y)}\right] + \text{c.c.} \qquad [A.26]$$

where $\hat{x}$ and $\hat{y}$ are the unit vectors parallel and perpendicular to the applied field, repectively. The expressions for the electron and trap densities have the same form

as those in equations A.7 and A.8 In addition to the material equations given in equations A.1-A.4, another constraint, given by Faraday's Law

$$\nabla \times E(x,y) = 0 \qquad [A.27]$$

is used to solve for the various components of the space charge field. By substituting equation A.26 as well as the corresponding forms for the electron, trap and current densities into A.1-A.4, the steady state expressions for the fundamental field components are found to be

$$E_{10} = -\frac{m_g^{eff}}{2}\frac{E_0 + iE_d[k_g]}{1 - i[E_0 + iE_d[k_g]/E_q[k_g]]} \qquad [A.28]$$

$$E_{01} = -\frac{m_s^{eff}}{2}\frac{E_d[k_s]}{1 + E_d[k_s]/E_q[k_s]]} \qquad [A.29]$$

It is interesting to note that the expression for E_{10} is identical to that described in section A.1 (equation A.11). In contrast, the expression for E_{01} is similar to that of equation A.12 but with the applied field E_0 set to zero. This is result of the incoherent intensity grating being oriented perpendicular to that of the applied field. Similar to the analysis performed in the previous section, expressions for the trap and electron densities at their fundamental frequencies ($N_{D10}^{+}, N_{D01}^{+}, n_{10}$ and n_{01}) can also be found. These terms can be substituted into the equations A.17 and A.18 to solve for the intermodulation term and result in an expression for N_{D11}^{+}. Using the curl equation A.27, the relationship between the E_{11x} and E_{11y} is found

to be

$$E_{11x} = \frac{k_g}{k_s} E_{11y}. \qquad [A.30]$$

Since the spatial frequency of the coherent grating is very much larger than that of the incoherent grating, $E_{11x} >> E_{11y}$. As a result, the relationship between the x component of the intermodulation field E_{11x} and N^+_{D11} is

$$E_{11x} = \frac{-ie}{(k_g + k_s^2/k_g)\epsilon} N^+_{D11} \approx \frac{-ie}{(k_g)\epsilon} N^+_{D11}. \qquad [A.31]$$

Using this relationship and collecting terms with spatial frequency components $k_s + k_g$, the resulting amplitude of E_{11x} is found to be

$$E_{11x} = \frac{m_g^{eff} m_s^{eff}}{4} i E_q[k_g]\big(D_1[k_g]B_1 + B_2 D_2[k_g]\big) \qquad [A.32]$$

where

$$B_1 = \frac{E_q[k_s]}{E_d[k_s] + E_q[k_s]} \qquad [A.33]$$

$$B_2 = \frac{E_d[k_s]}{E_d[k_s] + E_q[k_s]} \qquad [A.34]$$

and $D_1[k]$ and $D_2[k]$ are given in equations A.22 and A.23, respectively.

If the spatial frequency of the coherent grating is less than 200 lines/mm and the applied field is between 2 and 15 kV/cm, then $E_q >> E_0 >> E_d$. As a result, $D_1 = E_0/iE_q[k_g], D_2 = 1, B_1 = 1$, and $B_2 = E_d[k_s]/E_q[k_s]$. As a result E_{11x} simplifies to

$$E_{11x} = \frac{m_g^{eff} m_s^{eff}}{4} E_0. \qquad [A.35]$$

III.A.3 Temporal Response

One of the advantages of using the Kukhtarev model to predict the response of a photorefractive crystal to incident light is its ability to predict the temporal behavior of the refractive index change in the crystal. In this section, the temporal response of the SEWM mode of PICOC is derived. Consider the following sequencing of light intensity which characterizes the simultaneous erasure/write mode:

$$I(x,t) = \begin{cases} I_0(1 + m_g cosk_g x) & t < 0 \\ I_0(1 + m_g cosk_g x) + I_1(1 + m_s cosk_s x) & t > 0 \end{cases} . \qquad [A.36]$$

In this set-up, a coherent grating is recorded on a photorefractive BSO crystal until it has reached steady state. At this time (t = 0), an incoherent grating is imaged onto the crystal in addition to the coherent beam. The temporal evolution of the various components of the space charge can be derived by substituting the time varying forms of equations A.7-A.9 into the time dependent material equations A.1-A.4. By collecting terms with similar spatial frequency components, the amplitudes of the field components can be derived by solving a set of inhomogeneous first order differential equations. In summary, the two components of the space charge field at the fundamental frequencies ($E_{10}(t)$ and $E_{01}(t)$) are given by:

$$E_{10} = [(m_g - m_g^{eff})e^{-t/\tau[k_g]} + m_g^{eff}]\left[\frac{E_0 + iE_d([k_g]}{1 - i(E_0 + iE_d[k_g])/E_q[k_g}\right] \qquad [A.37]$$

$$E_{01} = [m_s(1 - e^{-t/\tau[k_s]})][\frac{E_0 + iE_d([k_s]}{1 - i(E_0 + iE_d[k_s])/E_q[k_s]} \qquad [A.38]$$

where

$$\tau[k] = \frac{N_{Deq}^{+}}{s_g N_D I_0 + s_s N_D I_1} \frac{1}{T[k]} \qquad [A.39]$$

$$T[k] = \frac{E_0 + i(E_d[k] + E_q[k])}{E_0 + i(E_d[k] + E_u[k]} \qquad [A.40]$$

and $E_u[k]$ is the characteristic field due to the drift process which is given by

$$E_u[k] = \frac{\gamma_r N_{Deq}^{+}}{\mu k}. \qquad [A.41]$$

Equation A.37 describes the decay of the coherent grating from its intial strength without the presence of the incoherent beam, to its final steady state value. Likewise, equation A.38 describes the exponential growth of the incoherent grating from its zero initial condition to its steady state value.

In order to derive the intermodulation component of the space charge field, E_{11}, terms with spatial frequency component $k_g + k_s$ are collected. This is similar to the technique used to derive the steady state response. Solutions for the fundamental components are then substituted into the equations to derive the E_{11} component. This intermodulation component is given by:

$$E_{11} = M_0 + M_1 e^{-t/\tau[k_g]} + M_2 e^{-t/\tau[k_s]} + M_3 e^{-t(1/\tau[k_g]+1/\tau[k_s])} + M_4 e^{-t/\tau[k_g+k_s]} \qquad [A.42]$$

where

$$M_0 = \frac{m_g^{eff} m_s^{eff}}{4} \frac{-F_0}{T[k_g + k_s]} \qquad [A.43]$$

$$M_1 = \frac{(m_g - m_g^{eff})m_s^{eff}}{4} \frac{-F_1}{T[k_g + k_s] - T[k_g]} \quad [A.44]$$

$$M_2 = \frac{m_g^{eff} m_s^{eff}}{4} \frac{-F_2}{T[k_g + k_s] - T[k_s]} \quad [A.45]$$

$$M_3 = \frac{(m_g - m_g^{eff})m_s^{eff}}{4} \frac{-F_3}{T[k_g + k_s] - T[k_s] - T[k_g]} \quad [A.46]$$

$$M_4 = -(M_0 + M_1 + M_2 + M_3) \quad [A.47]$$

$$F_0 = [-iE_q[k_g + k_s]][C_3 D_1[k_g] D_2[k_s] + C_4 D_1[k_s] D_2[k_g]] \quad [A.48]$$

$$F_1 = [-iE_q[k_g + k_s]][C_3 D_1[k_g] D_2[k_s] + C_4 D_1[k_g] D_1[k_s](T[k_g] - 1)] \quad [A.49]$$

$$F_2 = [-iE_q[k_g + k_s]][C_3 D_1[k_g] D_1[k_s](1 - T[k_s]) + C_4 D_2[k_g] D_1[k_s]] \quad [A.50]$$

$$F_3 = [-iE_q[k_g + k_s]][C_3 D_1[k_g] D_1[k_s](1 - T[k_s]) + C_4 D_1[k_g] D_1[k_s](T[k_g] - 1)] \quad [A.51]$$

$$C_3 = \frac{E_0 + i(E_d[k_g + k_s] + E_q[k_g])}{E_0 + i(E_d[k_g + k_s] + E_u[k_g + k_s]} \quad [A.52]$$

$$C_4 = \frac{E_0 + i(E_d[k_g + k_s] + E_q[k_s])}{E_0 + i(E_d[k_g + k_s] + E_u[k_g + k_s]}. \quad [A.53]$$

Expressions for $D_1[k]$ and $D_2[k]$ are given in equations A.22 and A.23.

III.B. Temporal Response of the Grating Erasure Mode (GEM)

In the Grating Erasure Mode (GEM), a coherent grating is prewritten on the BSO crystal. At certain point in time (t = 0), the coherent beam is turned off and an incoherent grating is imaged onto the crystal. The nonlinearities in the

photorefractive process give rise to a conversion of the incoherent image into its coherent replica. The sequencing of light intensities in this mode is given by:

$$I(x,t) = \begin{cases} I_0(1 + m_g cosk_g x) & \text{t<0} \\ I_1(1 + m_s cosk_s x) & \text{t>0.} \end{cases} \qquad [B.1]$$

By using the same procedure as that described in the previous two sections, the amplitude of the various space charge field components can be derived. The two components at the fundamental frequencies are given by:

$$E_{10} = (m_g e^{-t/\tau[k_g]} \left[\frac{E_0 + iE_d[k_g]}{1 - i(E_0 + iE_d[k_g])/E_q[k_g]} \right] \qquad [B.2]$$

$$E_{01} = m_s(1 - e^{-t/\tau[k_s]}) \left[\frac{E_0 + iE_d[k_s]}{1 - i(E_0 + iE_d[k_s])/E_q[k_s]} \right] \qquad [B.3]$$

where

$$\tau[k] = \frac{N_{Deq}^{+}}{s_s N_D I_1} \frac{1}{T[k]} \qquad [B.4]$$

$$T[k] = \frac{E_0 + i(E_d[k] + E_q[k])}{E_0 + i(E_d[k] + E_u[k])}. \qquad [B.5]$$

Equation B.2 again describes the temporal evolution of the coherent grating which decays exponentially from its initial value to 0. The evolution of the incoherent grating demonstrating an exponential growth to its steady state value is described in equation B.3. It is important to note that the time constant in this mode is not inversely proportional to the sum of the incoherent and coherent intensities (as in the case of SEWM) but only on the intensity of the incoherent image.

The intermodulation component can also be derived and is given by

$$E_{11} = M_1 e^{-t/\tau[k_g]} + +M_3 e^{-t(1/\tau[k_g]+1/\tau[k_s])} + M_4 e^{-t/\tau[k_g+k_s]} \qquad [B.6]$$

where

$$M_1 = \frac{m_g m_s}{4} \frac{-F_1'}{T[k_g + k_s] - T[k_g]} \qquad [B.7]$$

$$M_3 = \frac{m_g m_s}{4} \frac{-F_3'}{T[k_g + k_s] - T[k_s] - T[k_g]} \qquad [B.8]$$

$$M_4 = -(M_1 + M_3) \qquad [B.9]$$

$$F_1' = -iE_q[k_g + k_s]\Big[C_3[D_1[k_g]D_2[k_s] + D_1[k_g]D_1[k_s](T[k_g] - 1)\Big] \qquad [B.10]$$

$$F_3' = -iE_q[k_g + k_s]\Big[C_4[D_1[k_g]D_1[k_s](1 - T[k_s]) + D_1[k_g]D_1[k_s](T[k_g] - 1)\Big]. \qquad [B.11]$$

III.C Temporal Response of the Grating Inhibition Mode (GIM) of PICOC

In the grating inhibition mode (GIM), an incoherent image is prerecorded on a BSO crystal. After the fields have reached steady state, a coherent grating is recorded on the crystal. The nonlinear interaction inherent in the photorefractive effect creates intermodulation terms which result in the conversion of the incoherent image to its coherent replica. Consider the following sequencing of the incoherent and coherent light beams:

$$I(x,t) = \begin{cases} I_0(1 + m_s cosk_s x & \text{t<0} \\ I_1(1 + m_g cosk_g x & \text{t>0} \end{cases} \qquad [C.1]$$

$$E_{10} = [m_g(1 - e^{-t/\tau[k_g]})]\left[\frac{E_0 + iE_d[k_g]}{1 - i(E_0 + iE_d[k_g])/E_q[k_g]}\right] \qquad [C.2]$$

$$E_{01} = [(m_s e^{-t/\tau[k_s]}]\left[\frac{E_0 + iE_d[k_s]}{1 - i(E_0 + iE_d[k_s])/E_q[k_s]}\right] \qquad [C.3]$$

where

$$\tau[k] = \frac{N^+_{Deq}}{s_g N_D I_0}\frac{1}{T[k]} \qquad [C.4]$$

$$T[k] = \frac{E_0 + i(E_d[k] + E_q[k])}{E_0 + i(E_d[k] + E_u[k]}. \qquad [C.5]$$

Equation C.2 again describes the temporal evolution of the coherent grating which grows exponentially from its 0 to its steady state value. The evolution of the incoherent grating demonstrating an exponential decay from its initial state to 0 is described in equation C.3. It is important to note that the time constant in this mode is not inversely proportional to the sum of the incoherent and coherent intensities (as in the case of SEWM) but only on the intensity of the coherent beam.

The intermodulation component of the space charge field in this mode is

$$E_{11} = M_2 e^{-t/\tau[k_s]} + + M_3 e^{-t(1/\tau[k_g]+1/\tau[k_s])} + M_4 e^{-t/\tau[k_g+k_s]} \qquad [C.6]$$

where

$$M_2 = \frac{m_g m_s}{4}\frac{-F_2'}{T[k_g + k_s] - T[k_s]} \qquad [C.7]$$

$$M_3 = \frac{m_g m_s}{4}\frac{-F_3'}{T[k_g + k_s] - T[k_s] - T[k_g]} \qquad [C.8]$$

$$M_4 = -(M_2 + M_3) \qquad [C.9]$$

$$F_2' = -iE_q[k_g + k_s]C_3\Big[D_1[k_g]D_1[k_s](1 - T[k_s]) + D_1[k_s]D_2[k_g]\Big] \qquad [C.10]$$

$$F_3' = -iE_q[k_g + k_s]C_4\Big[D_1[k_g]D_1[k_s](1 - T[k_s]) + D_1[k_g]D_1[k_s](T[k_g] - 1)\Big] \qquad [C.11]$$

References for Chapter 3

1. D. Casasent, "Spatial Light Modulators", *IEEE* **65**, 143 (1977).

2. A. R. Tanguay, Jr., "Material Requirements for Optical Processing and Computing Devices", *Opt. Eng.* **24**, 2 (1985).

3. B. A. Horwitz and F. J. Corbett, "The PROM- Theory and Applications for the Pockels REadout Optical Modulator", *Opt. Eng.* **17**, 353 (1978).

4. M. P. Petrov, A. V. Khomenko, M. V. Krasin'kova, V. I. Marakhonov and M. G. Shlyagin, *Sov. Phys. Tech. Phys.* **26**, 816 (1981)

5. Y. Owechko and A. R. Tanguay, Jr. "Theoretical Resolution Limitations of Electro-optic Spatial Light Modulators. I. Fundamental Considerastions" *J. Opt. Soc. Am. A* **1**, 635 (1984)

6. J. P. Huignard, J. P. Herriau, G. Rivet and P. Gunter, "Phase Conjugation and Spatial Frequency Dependence of Wavefront Reflectivity in $Bi_{12}SiO_{20}$ Crystals", *Opt. Lett.*, **5**, 102 (1980).

7. A. A. Kamshilin and M. P. Petrov, "Holographic Image Conversion in a $Bi_{12}SiO_{20}$' , *Sov. Tech. Phys. Lett.*, **6**, 145 (1980)

8. Y.Shi, D. Psaltis, A. Marrakchi and A. R. Tanguay Jr. "Photorefractive Incoherent to Coherent Optical Converter", *Appl. Opt.*, **22**, 3665 (1983)

9. A. Marrakchi, A. R. Tanguay, Jr., J. Yu and D. Psaltis, "Physical Characterization of the Photorefractive Incoherent to Coherent Optical Converter" *Opt.*

Eng., **24**, 124 (1985)

10. J. Yu, D. Psaltis, R. V. Johnson, A. R. Tanguay, Jr. and A. Marrakchi, "The Photorefractive Incoherent to Coherent Converter" Springer Verlag, Berlin, Germany (1988).

11. M. W. McCall and C. R. Petts, "Grating Modification in Degenerate Four Wave Mixing", *Opt. Comm.*, **53**, 7 (1985)

12. L. M. Bernardo and O. D. D. Soares, "Selective Erasing on a Hologram in a BSO Photorefractive Crystal", *Appl. Opt.*, **25**, 592 (1986)

13. M. B. Klein, G. J. Dunning, G. C. Valley, R. C. Lind and T. R. O'Meara, "Imaging Threshold Detector Using a Phase Conjugate Resonator in BaTi O_3", *Opt. Lett.*, **11**, 575 (1986)

14. M. Peltier and F. Micheron, "Volume Hologram Recording and Charge Transfer Process in $Bi_{12}SiO_{20}$ and $Bi_{12}GeO_{20}$", *J. Appl. Phys.*, **48**, 3683 (1977)

15. R. Grousson and S. Mallick, "White-light Image Processing with $LiNbO_3$", *Appl. Opt.*, **19**, 1762 (1980)

16. J. P. Herriau, J. P. Huignard and P. Aubourg, "Some Polarization Properites of Volume Holgrams in $Bi_{12}SiO_{20}$ Crystals and Applications", *Appl. Opt.*, **17**, 1851 (1978)

17. N. V. Kukhtarev, V. B. Markov, S. G. Odulov, M. S. Soskin and V. L. Vinetskii, "Holographic Storage in Electro-optic Crystals I. Steady State", *Ferroelectrics*,

22, 949 (1979)

18. M. G. Moharam, T. K. Gaylord, R. Magnusson and L. Young, "Holographic Grating Formation in Photorefractive Crystals with Arbitrary Electron Transport Lengths", *J. Appl. Phys.*, **50**, 5642 (1979)

19. H. Kogelnik, "Coupled Wave Theory for Thick Hologram Gratings", *Bell Sys. Tech. Jour.*, **48**, 2909 (1969).

20. P. Yeh, "Fundamental Limit of the Speed of Photorefractive Effect and its Impact on Device Applications and Materials Research", *Appl. Opt.*, **26**, 602 (1987).

IV. PHOTOREFRACTIVE TIME INTEGRATING CORRELATOR

IV.1. Introduction

Time integrating correlators have been extensively used in the field of optical processing in order to detect temporally varying waveforms [1]. The processing gain of a time integrating correlator is determined by the length of the integration time on the output detector [2]. However, because of the limited dynamic range of the detector, the processing gain is severely limited by the bias that is being integrated at the output along with the signal. In this chapter, an alternative approach to performing the temporal integration of the correlation signals is presented. By using a photorefractive crystal on which to record the correlation, the bias at the output can be removed, thereby utilizing the full dynamic range of the output detector. In addition, because the writing time of the crystal can be made relatively long, the processing gain of the system is increased.

In the following section, the use of a photorefractive crystal as a time integrating detector is analyzed. A review of the standard time integrating correlator is presented in section 3, while the alternative architecture utilizing a photorefractive crystal and experimental results are presented in section 4. Section 5 discusses important issues in characterizing the photorefractive time integrating correlator such as its linearity, dynamic range, and integration time.

IV.2 Photorefractive Crystals as Time Integrating Detectors

The ability to record and erase holograms in real time using photorefractive crystals allows one to optically process temporal signals. In this section, the effect of a temporally varying intensity signal incident on a photorefractive crystal is analyzed. Specifically, it is shown that the crystal acts as a sliding window integrating detector whose integration time is approximately equal to the writing time of the crystal.

Consider an intensity pattern incident on a photorefractive crystal consisting of a grating whose modulation depth varies as a function of time. The intensity incident can be written as

$$I(x,t) = \begin{cases} 0 & \text{t<0} \\ I_0 + \mathrm{Re}\{I_1(x,t)e^{ikx}\} & \text{t>0} \end{cases} \qquad [4.1]$$

where $k/2\pi$ is the spatial frequency of the grating. Using the Kukhtarev model [3], in the low modulation depth regime, the diffracted intensity is given by

$$I_{out}(x,t) = I_R \left| \frac{K_1}{\tau} \int_0^t \frac{I_1(x,t')}{I_0} e^{(t'-t)/\tau} dt' \right|^2, \qquad [4.2]$$

where K_1 is a complex coefficient dependent on the material parameters of the photorefractive crystal, the spatial frequency of the grating, and the applied electric field. The explicit expression for K_1 is given in section 2.3. τ is the complex time constant of the material given in equation 2.4 and it is dependent on the material parameters, spatial frequency, and total intensity (I_0) incident on the crystal. I_R

is the intensity of the readout beam. The above equation can be rewritten in terms of the Fourier components of $I_1(x,t)$

$$I_{out}(x,t) = I_R \left| \frac{K_1}{\tau} \int_{-\infty}^{\infty} \frac{\tilde{I}_1(x,w)}{(1/\tau + iw)I_0} e^{iwt} dw \right|^2 \qquad [4.3]$$

where $\tilde{I}_1(x,w)$ is the temporal Fourier transform of the signal $I_1(x,t)$:

$$\tilde{I}_1(x,w) = \int_{-\infty}^{\infty} I_1(x,t) e^{iwt} dw. \qquad [4.4]$$

Equation 4.3 is recognizable as a low pass filter of the input modulation with a cutoff frequency given by $Re\{1/\tau\}$, which is the inverse of the rise time of a single frequency grating being recorded in a photorefractive crystal as derived in section 2.3. Thus, the response of the crystal to a temporally varying intensity pattern is approximately equivalent to a time integrator with a sliding integration window and has the form of

$$I_{out}(x,t) = \left| \frac{K_1}{\tau} \int_{t-\tau'}^{t} \frac{I_1(x,t')}{I_0} dt' \right|^2 I_R \qquad [4.5]$$

where τ' is the writing time of the grating in the crystal. Hence, the output intensity from the photorefractive crystal is proportional to the square of the integration of the signal $I_1(x,t)$ over a sliding time window of length $\tau' = |\tau|^2 / \text{Re}\{\tau\}$. In the following sections, we will demonstrate an acousto-optic time integrating correlator which utilizes a photorefractive time integrating detector in order to enhance the processing gain of the system and present the output information free of bias.

IV.3 Time Integrating Correlators

Time integration is a powerful technique in optical signal processing and has been used in a wide variety of architectures [2][4]. A one dimensional time integrating correlator is shown in Figure 4.1. This architecture, known as an additive time integrating correlator, utilizes two acousto-optic devices as input devices. When an electrical signal is applied to either of the AODs, the signal modulates a tranducer which launches an acoustic wave through the acousto-optic medium. This wave in turn modulates the refractive index of the material. Through this device, a temporally varying electrical signals can be converted to spatially varying optical signals in the form of a phase hologram.

In the acousto-optic time integrating system, a signal is presented to one AOD, and a second signal is presented to the other. The optical system is aligned such that the diffracted output from each cell is imaged onto the output detector. The two images have acoustic vectors which are counterpropagating with respect to each other and the diffracted orders from both beams are chosen to be upshifted (or downshifted) with respect to the incident beam. Let the inputs to each of the AODs be $s_1(t)$ and $s_2(t)$ respectively. The resulting intensity detected by the output detector is

$$I_o(x,t) = \int_{(t-\tau_d)}^{t} |s_1(t' - x/v)e^{-iwx/v} + s_2(t' + x/v)e^{iwx/v}|^2 dt' \qquad [4.6]$$

where τ_d is the integration time of the detector, w is the center frequency of the

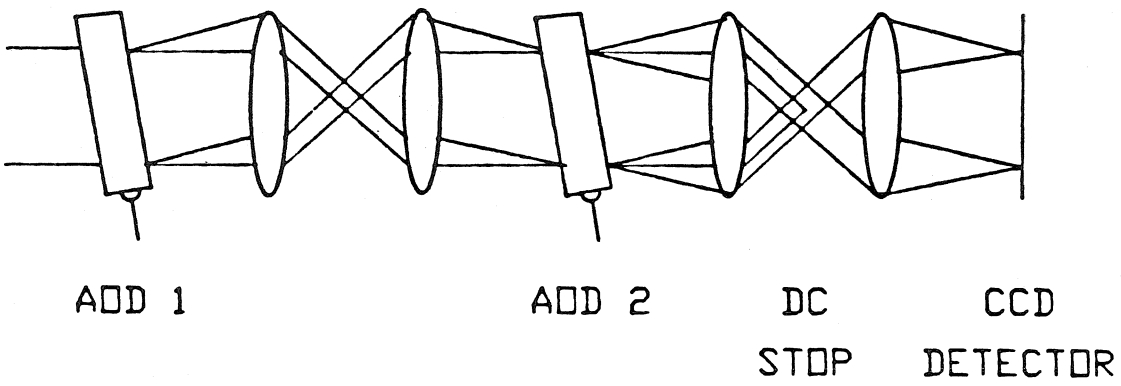

Fig. 4.1 Standard Time Integrating Acousto-Optic Correlator

acoustic wave and v is the acoustic velocity of the AOD. Let us assume that the magnitudes of $|s_1(t)|^2$ and $|s_2(t)|^2$ are constant in time as in the case of bipolar or phase encoded signals. The output intensity is then

$$I_o(x,t) = [|s_1|^2 + |s_2|^2]\tau_d + 2Re\{\left[\int_{t-\tau_d}^{t} s_1(t-x/v)s_2^*(t+x/v)dt\right]e^{i2wx/v}\}. \quad [4.7]$$

Hence the detected output consists of a bias term $|s_1|^2 + |s_2|^2$ and a sliding window correlation of the two input signals which modulates a spatial carrier with frequency

$2w/v$.

This method of producing the correlation creates a two-fold problem. Firstly, the presence of the spatial carrier results in an increase in the resolution required by the output detector. In the absence of a spatial carrier, the detector would require only two or three pixels to sample a correlation peak. This system, however, requires two to three spatial fringes to sample a correlation peak and correspondingly two to three detector elements to sample each fringe. The resolution required will typically be equal to the space-bandwidth product of the input signals. Secondly the bias recorded on the detector decreases the effective dynamic range of the correlator and therefore the overall processing gain of the system. One method which is commonly used to seperate the correlation signal from the bias utilizes the fact that the correlation information modulates a high frequency spatial carrier. Both the correlation information and the spatial carrier are detected and temporally read out. The output of the detector is then electronically filtered to separate the high frequency correlation signal from the lower frequency bias [6]. This method, however, does not diminish the fact that prior to post-processing both the signal and bias are still detected by the detector, thus decreasing the performance of the correlator.

In most signal processing environments, the requirement of the correlator is that it recognizes a signal contaminated by noise. Consider an input signal $s(t)$

which is additively contaminated by a white noise process $n(t)$ (ie. $s_1(t) = s(t), s_2(t) = s(t) + n(t)$). In the standard time integrating correlator, the output is given by

$$V_o(x,t) \propto \int_{(t-\tau_d)}^{t} |(s(t-x/v) + n(t-x/v))e^{-iwx/v} + s(t+x/v)e^{iwx/v}|^2 dt. \quad [4.8]$$

Assuming that the signal and noise terms are sufficiently uncorrelated and that $|n(t)|^2$ is a constant, the output of the integrator is

$$V_o(x,t) \propto [|s(t)|^2 + |n(t)|^2]\tau_d + [\int_{t-\tau_d}^{t} s(t-x/v)s^*(t+x/v)dt]cos(2wx/v). \quad [4.9]$$

Thus the effect of noise on a standard time integrating correlator is an increase in the bias while the strength of the correlation signal remains constant. If the dynamic range of the output detector is DR and the light incident on it has a signal to bias ratio SBR, then the effective dynamic range of the correlator is reduced by a factor given by [5]

$$DR' = DR\left[\frac{SBR}{1+SBR}\right]. \quad [4.10]$$

In most applications, the noise power will far exceed that of the desired signal resulting in a very small signal to bias ratio. Thus, the effective dynamic range will be severely reduced. Consequently, for a given signal strength, the smaller the effective dynamic range of the detector, the faster the detector will saturate and the shorter the integration time. The ability of the detector to accomplish signal recognition is described by its processing gain which is the signal to noise ratio of the output correlation to signal to noise ratio of the input signal. Hence a higher

processing gain implies the ability of the correlator to recognize weaker signals in the presence of noise. It has been shown that the processing gain of a correlation system is given by [2]

$$Gain = \frac{SNR_{out}}{SNR_{in}} = \tau_d BW \qquad [4.11]$$

where BW is the bandwidth of the input signals and τ_d is the integration time of the detector. As a result, the presence of bias reduces the maximum integration time of the detector thereby decreasing the processing gain of the correlator. The integration time of the correlator may always be increased by decreasing the amount of light incident on the detector. However, this will be limited by the amount of dark current and shot noise generated within the detector.

IV.4 Photorefractive Time Integrating Correlator

As mentioned previously, two important attributes for a time integrating detector in a correlator architecture are that the resolution of the device must be high enough to sample the correlation information and the spatial carrier, and that the integrator must have a high dynamic range needed for longer integration times and hence higher processing gains. These needs are nicely satisfied by a photorefractive crystal which demonstrates resolution up to 1000 lines/mm and integration times as long as several seconds.

When a photorefractive crystal is used as the time integrating detector in the

acousto-optic correlator with input signals $s_1(t)$ and $s_2(t)$, the light incident on the crystal is given by

$$I_{inc} = |s_1(t)|^2 + |s_2(t)|^2 + 2Re\{s_1(t - x/v)s_2^*(t + x/v)e^{2iwx/v}\}. \qquad [4.12]$$

Again, considering signals whose power is constant in time and using equation 4.5, the signal diffracted from the photorefractive crystal is given by

$$I_o(x,t) = \left| \frac{K_1}{|s_1(t)|^2 + |s_2(t)|^2} \left[\int_{t-\tau'}^{t} s_1(t - x/v)s_2^*(t + x/v)dt \right] \right|^2 \qquad [4.13]$$

where τ' is the writing time of a grating of frequency $2w/v$ in a photorefractive crystal. Hence, the system produces the magnitude square of the correlation integral. In addition, the absolute intensity of the output is dependent on the signal-to-bias ratio of the writing information.

A schematic diagram of the time integrating correlator which uses a photorefractive detector as an output device is shown in Fig. 4.2. The system can be subdivided into two stages: a standard time integrating architecture incorporating two colinearly aligned acousto-optic devices identical to the system described in the previous section, and a photorefractive time integrating detector with an auxiliary beam used to read out the recorded correlation information.

In our experiment, we used two flint glass acousto-optic devices illuminated with light from an argon ion laser (λ=488 nm). The average intensity incident on the photorefractive crystal was $1\mu W/cm^2$. The acousto-optic cells were driven at

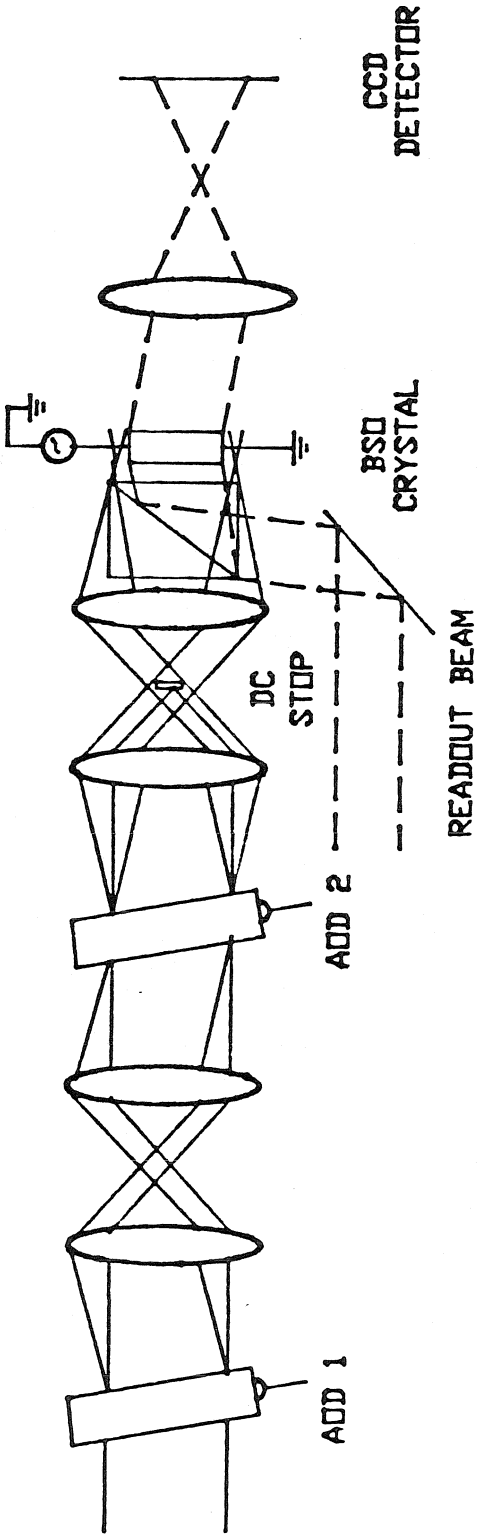

Fig. 4.2 Optical Set-up of Photorefractive Time Integarating Correlator

a center frequency of 70 Mhz and a symmetric linear chirp with bandwidth Δf = 5 Mhz was entered into each Bragg cell to produce an autocorrelation peak. The acoustic velocity in the device was 4 km/sec leading to a Bragg angle of 0.2^o and a grating frequency of 35 lines/mm in the crystal.

A bismuth silicon oxide (BSO) crystal cut in the $< 110 >$ direction and measuring 15x15x2 mm was used as the integrating detector. An electric field of 6 kV/cm was applied transverse to the crystal in order to enhance the diffraction efficiency of the crystal. Cylindrical lenses (not shown in figure) were used to expand the output of the AODs to illuminate the full aperture of the BSO crystal. A He-Ne laser (λ=633 nm) at an intensity of 150 $\mu W/cm^2$ was used to read out the recorded correlation information. The diffracted beam was then imaged onto a 1-dimensional CCD for observation.

The output of a standard time integrating correlator using an electronic detector (CCD) for the noise-free case and equal input amplitudes is shown in Fig. 4.3. As we can see from this figure, the output is composed of a strong bias term in addition to the correlation peak. Since the noise free case gives the highest signal to bias ratio, typical applications of the correlator in a noisy environment would lead to a severe degradation of the output signal, as well as diminish the effective dynamic range of the system. The correlation produced by temporally integrating on the photorefractive crystal is shown in Fig. 4.4. In this case, all the bias due

to temporal integration is removed and any residual bias is due to the dark current from the CCD. It is interesting to notice that because the photorefractive crystal produces the square of the correlation, the output appears as a unipolar signal and as a result does not need a background bias term. In contrast, the output of the standard time integrating correlator is bipolarly represented (Fig. 4.3) and requires the presence of the bias for accurate representation.

The effect of noise on the photorefractive time integrating correlator is very different than that for the standard time integrating correlator. Assuming a reference signal $s_1(t) = s(t)$ and an input signal $s_2(t) = s(t) + n(t)$, contaminated by uncorrelated constant energy noise n(t), the output of the photorefractive time integrating correlator is

$$I_o(x,t) = \left| \frac{K_1}{|s(t)|^2 + |n(t)|^2} \left[\int_{t-\tau_d}^{t} s(t - x/v) s^*(t + x/v) dt \right] \right|^2 . \qquad [4.14]$$

Thus the immediate consequence of adding noise to one of the inputs is an increase in the amount of DC light incident on the photorefractive crystal. Since the diffracted output from the crystal is dependent on the modulation depth of the recorded grating, the result of the additive noise will be a decrease in the intensity of diffracted output. This information, however, will remain free of any output bias. Figures 4.5 and 4.6 show the output of the photorefractive time integrating correlator with an input signal to noise ratio of 0dB and -10dB respectively. In both cases, the presence of a bias floor is entirely due to the buildup of dark current in the output

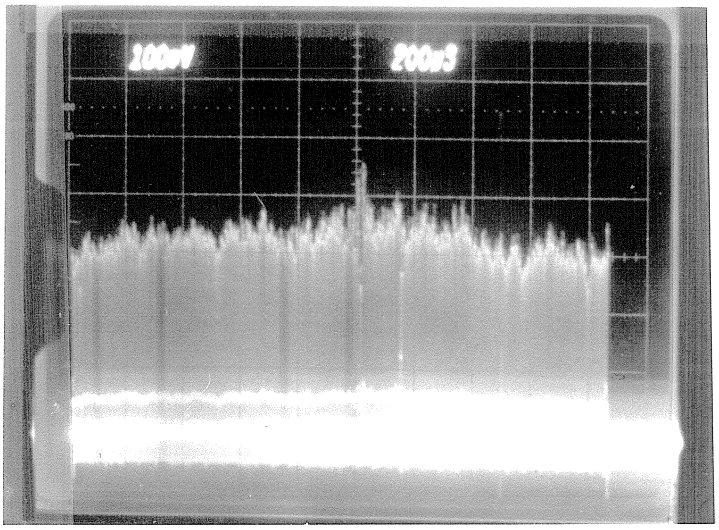

Fig. 4.3 Autocorrelation of Two Chirp Signals in a Standard Time Integrating Correlator Without Noise

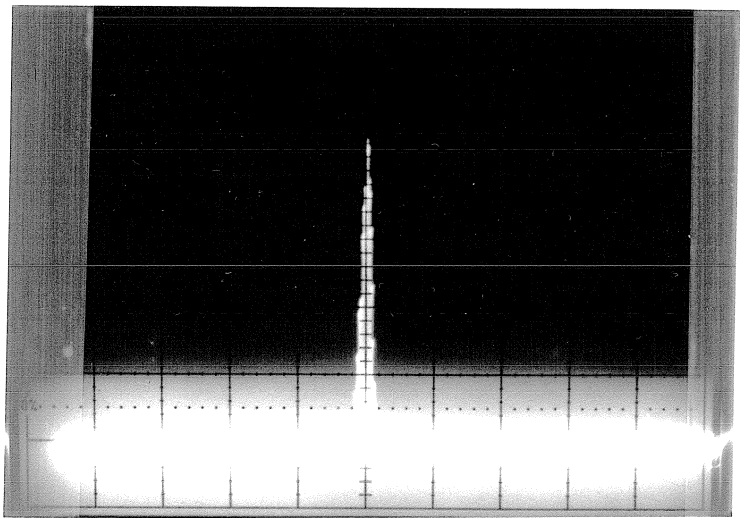

Fig. 4.4 Autocorrelation of Two Chirp Signals in a Photorefractive Time Integrating Correlator Without Noise

CCD detector. The is a result of the long CCD integration times required to detect the weak diffracted image. In practice, the detector dark current can be minimized by increasing the intensity of the readout beam, thereby decreasing the required integration time of the output CCD detector or by thermally cooling the detector.

An additional advantage of the photorefractive time integrating correlator is that the output modulates a coherent light beam. As a result, the correlation information can be used as an input to a coherent optical processing system without the utilization of a spatial light modulator. One example, demonstrated by Hong *et al.* [6], utilizes this correlator architecture in implementing an acousto-optic adaptive system. This particular system was used to descriminate between high temporal bandwidth signals and low bandwidth (or single frequency) jammers and null out the latter.

IV.5 Performance Issues

The experimental results described in the previous section show a dramatic qualitative improvement in the correlation that is obtained when the photorefractive crystal is used instead of the CCD. In this section, we examine certain characteristics of this method which are useful for quantitatively evaluating its performance. Specifically, we examine the linearity, integration time, dynamic range and sensitivity of the correlator.

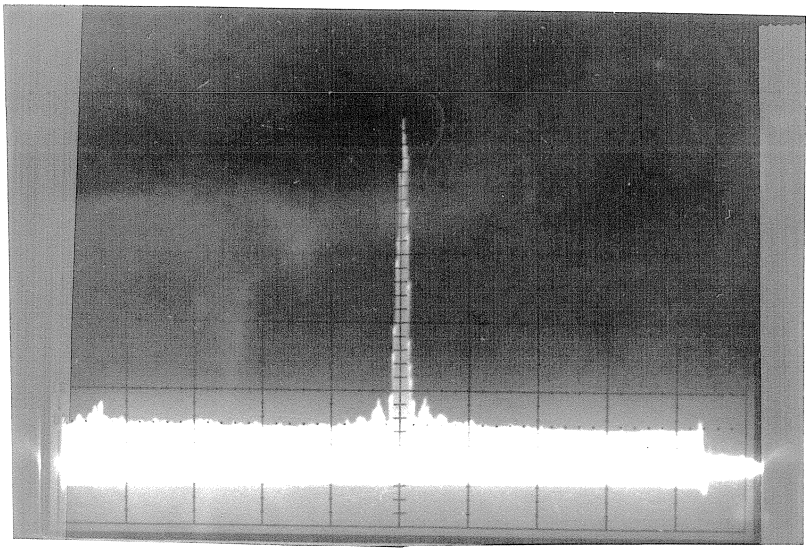

Fig. 4.5 Autocorrelation of Two Chirp Signals in a Photorefractive Time Integrating Correlator (SNR = 0dB)

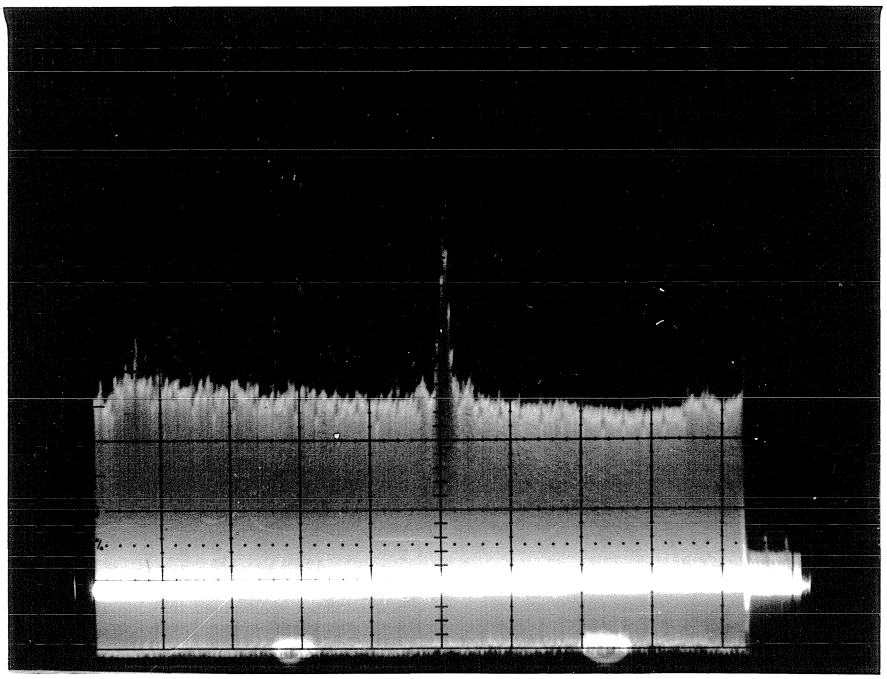

Fig. 4.6 Autocorrelation of Two Chirp Signals in a Photorefractive Time Integrating Correlator (SNR = -10dB)

IV.5.1 Linearity

In a conventional time integrating correlator (coherent or incoherent), the output correlation is basically proportional to the signals applied to the AODs. Nonlinearities occur when the linear dynamic range of the devices used is exceeded, as in the case where the diffraction efficiency of the AOD exceeds several percent or if the integrating detector is driven to saturation. In the photorefractive time integrating processor, the output intensity is a nonlinear, monotonically increasing function of the input voltage. The nonlinearity arises because of the square-law detection at the final readout stage and the recording mechanism in the photorefractive crystal. The nonlinear relationship is studied analytically and is experimentally verified.

Let $v_1(t) = s(t)$ be a fixed reference signal and $v_2(t) = as(t)$ be an input signal of varying amplitude ($0 < a < 1$). Near the correlation peak (x=0) the intensity incident on the photorefractive crystal is

$$I(x,t) \propto (1 + a^2 + 2acoskx)|s(t)|^2. \qquad [4.13]$$

Using equation 4.9, the output intensity at the CCD is proportional to the magnitude square of the modulation depth of the intensity incident on the BSO crystal

$$I_{out} \propto m^2 = \left|\frac{2a}{1+a^2}\right|^2 = \frac{4a^2}{1+a^2}. \qquad [4.14]$$

where m is the modulation depth of the spatial grating. Figure 4.7 is a graph of the output intensity at the correlation peak versus the modulation depth incident on

the crystal. The experimental result is in excellent agreement with the square-law relationship predicted by equation 4.14.

A plot of the output intensity as a function of the amplitude of the input signal a is shown in Fig. 4.8. The nonlinear relationship between the input and output signals is generally a disadvantage since the scaling of signals of varying amplitudes will be nonlinear. This, however, will not cause a problem if the correlator is used only as a signal detection device, since correlation peaks will still be discernible and only the threshold level need be adjusted accordingly to maximize the probability of detection.

IV.5.2 Integration Time

In a conventional time integrating correlator, the integration time is limited by the dark current buildup on the output detector, typically up to several hundred milliseconds. When a photorefractive crystal is used, the integration time is determined by the rise time of the internal space charge field which can easily be made much longer. The correlation can be read out at any rate less than the writing time of the crystal that is convenient for the auxiliary detector array.

The integration time of the photorefractive time integrating correlator is

$$\tau' = \frac{|\tau|^2}{Re\{\tau\}} = \left|\frac{K_2}{I_0}\right| \qquad [4.15]$$

where K_2 is a complex constant depending on the material parameters, spatial

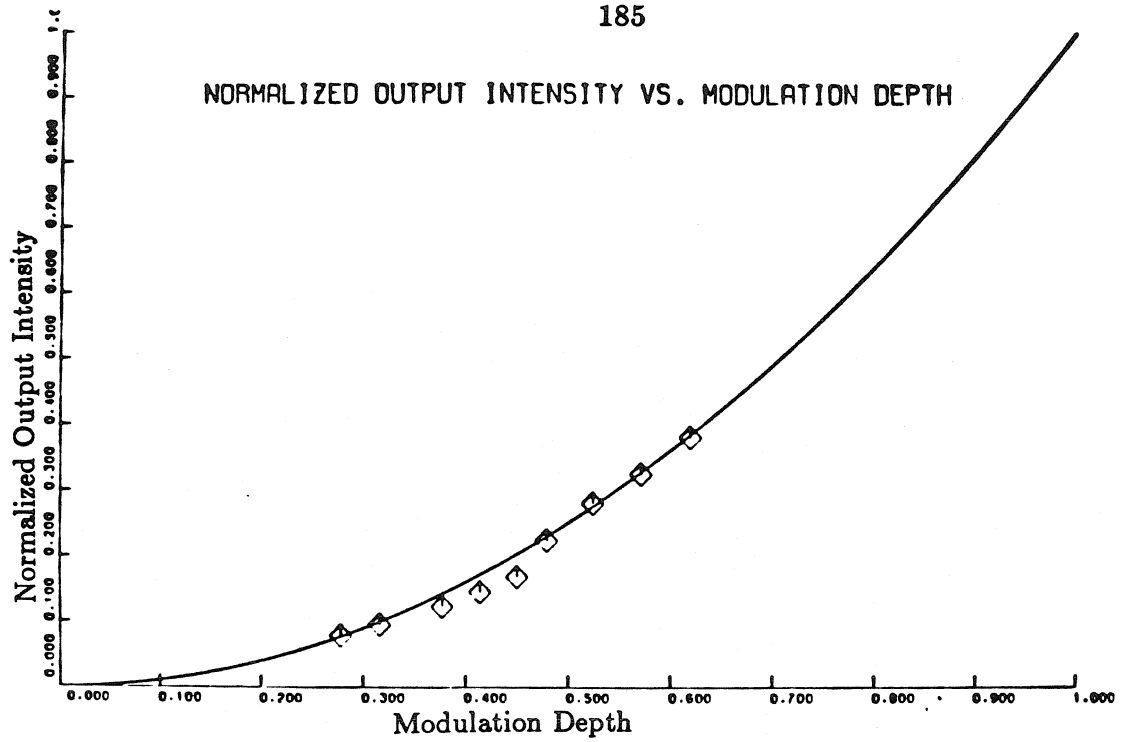

Fig. 4.7 Intensity of Correlation Peak vs. Modulation Depth

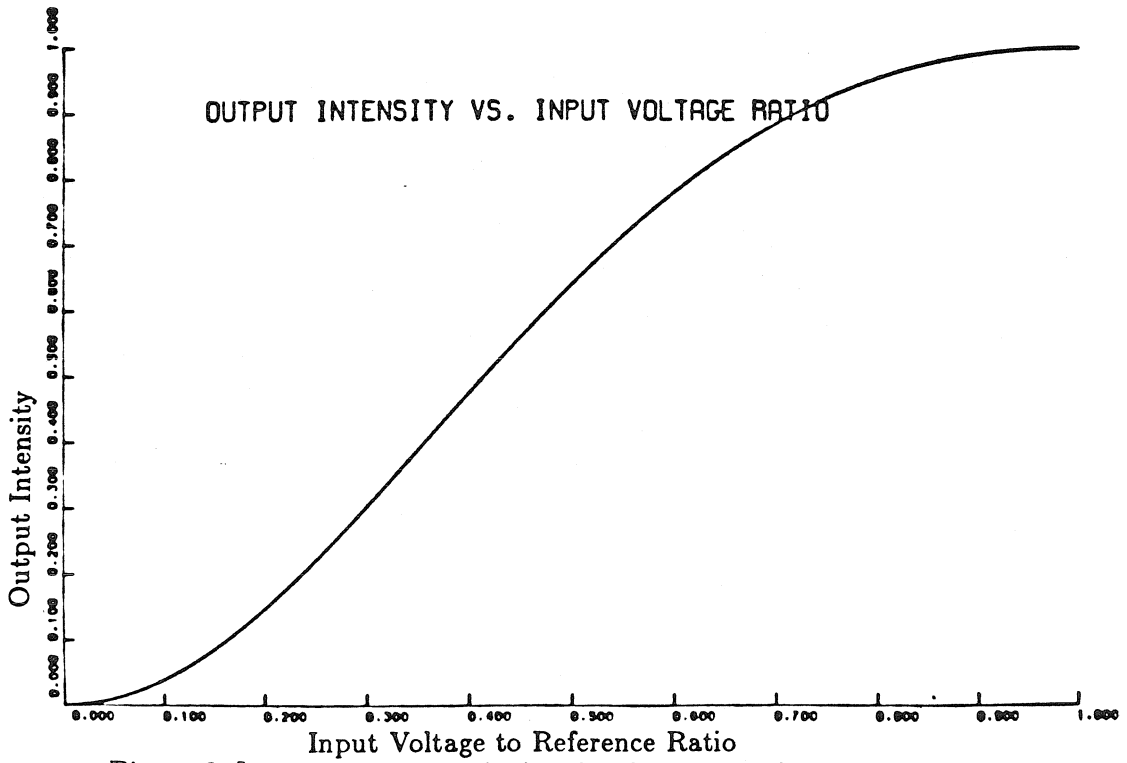

Fig. 4.8 Intensity of Correlation Peak vs. Amplitude of Input Signal

frequency of the carrier, and the applied field only. Thus, the integration time of the correlator can be increased by decreasing the amount of light incident on the photorefractive crystal. This is similar to the integration time of the standard time integrating correlator, where the maximum integration time is inversely dependent on the total intensity incident on the electronic detector. This control is important since the integration time can be matched to the length of the reference signal thereby maximizing the processing gain of the system.

The time response of the correlation peak for different values of average incident intensity is shown in Figure 4.9. Figure 4.10 is a plot of intensity versus the inverse of the experimentally observed rise time which shows excellent agreement between the experiment and the theoretical prediction.

The integration time, however, has a finite range over which it can be adjusted. The maximum integration time is limited by the thermal effects in the crystal. If the rate at which carriers are thermally generated becomes comparable with the rate at which they are photogenerated, the modulation depth of trap density will be reduced. As a result, the diffraction efficiency of the grating will decrease, thereby decreasing the signal to noise ratio at the output and hence the processing gain of the system. In practice the minimum integration time is limited by the maximum light intensity that is available for recording. As seen from the graph, the integration time can be reduced to real time rates of 30 msec. if the incident intensity is made

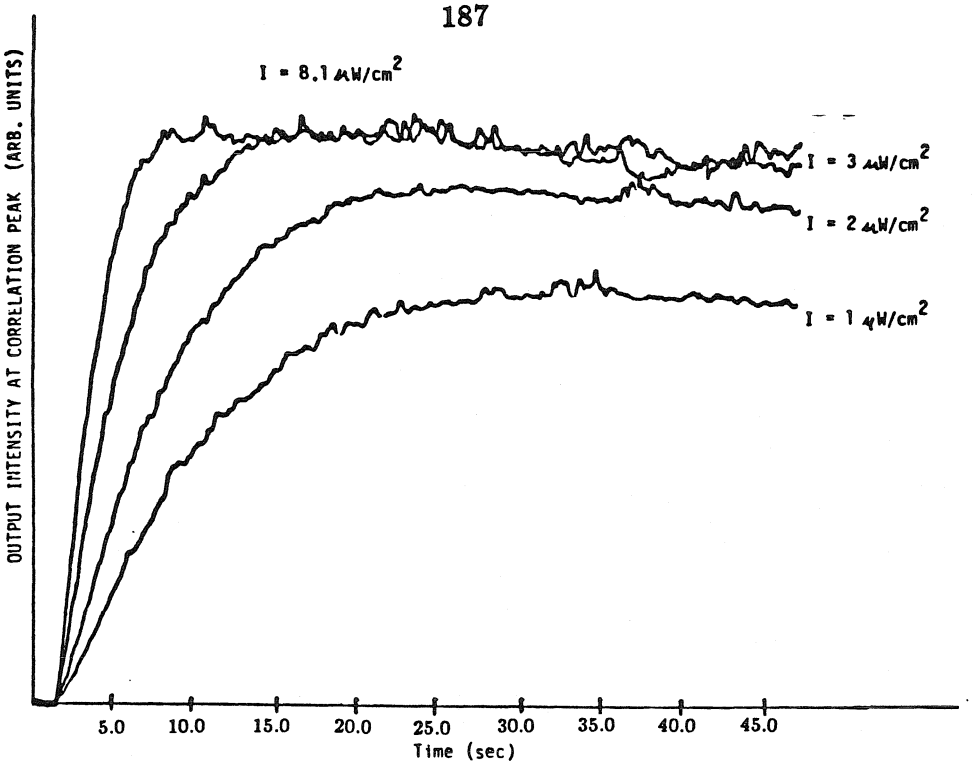

Fig. 4.9 Temporal Response of the Correlation Peak for Various Incident Intensities

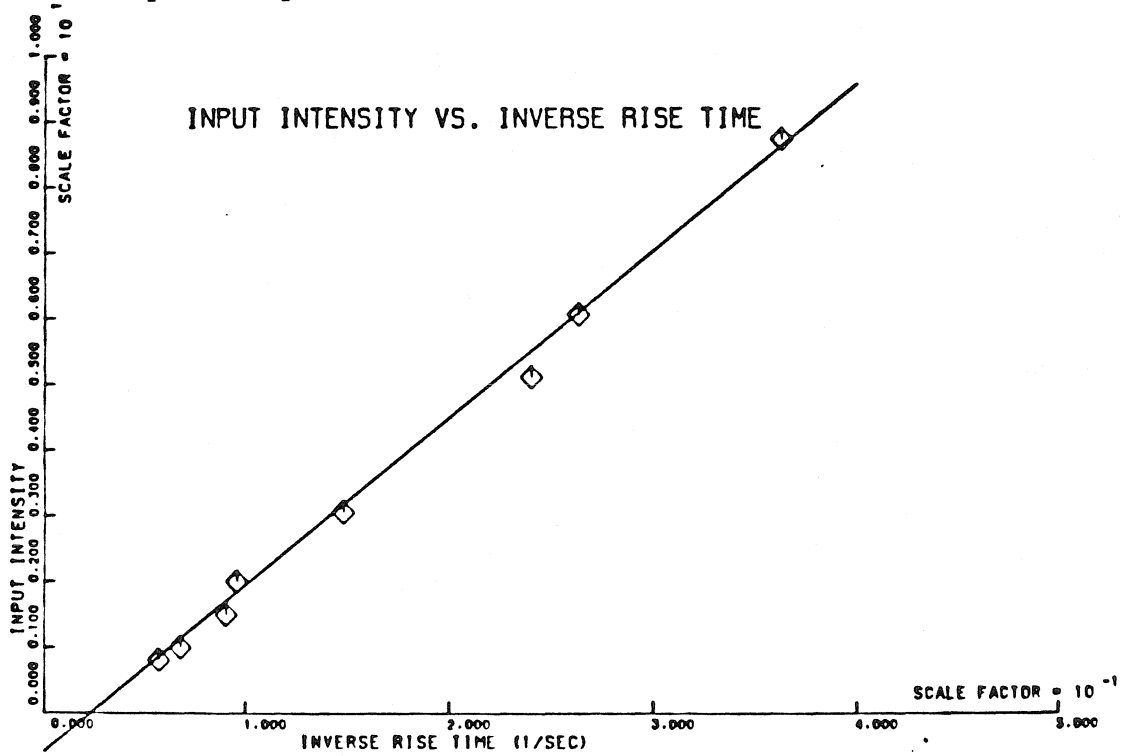

Fig. 4.10 Inverse of Integration Time vs. Incident Intensity

equal to $1mW/cm^2$. This would require very efficient acousto-optics devices and such power level are simply not practical for most applications.

IV.5.3 Dynamic Range and Sensitivity

Since the output of the bias removal correlator is presented without bias, the output dynamic range of the system is essentially equal to the dynamic range of the readout detector array. It is more important to determine the input dynamic range of the detector, that is to say, the minimum signal that can be detected by the correlator in the absence of noise. To achieve this, it is necessary to determine how the dynamic range of the photorefractive crystal affects the dynamic range of the correlator. Let the dynamic range of the photorefractive crystal be defined as $DR_{PR} = m_{max}/m_{min}$, where m_{max} is the maximum modulation depth that can be recorded on the crystal (in our case 1), and m_{min} is the minimum modulation depth for which a diffracted signal is detectable above the output scatter and noise level of the system. Given two input signals $v_1(t) = as(t)$ and $v_2(t) = s(t)$, the modulation depth of the light incident on the crystal is $m = 2a/(1 + a^2)$. Thus for small values of a, the minimum detectable input signal is given by

$$a_{min} = \frac{m_{min}}{2} = \frac{1}{2DR_{PR}}. \qquad [4.16]$$

Hence, the useful range over which a can vary is limited by the dynamic range of

the photorefractive crystal DR_{PR}. Thus, the input dynamic range is given by

$$DR_{in} = \frac{1}{a_{min}^2} = \frac{4}{m_{min}^2}. \qquad [4.17]$$

The most important parameter in determining the system's dynamic range is m_{min}. By adjusting the ratios between the input and reference signals to the correlator, the dynamic range of our experimental system was found to be equal to 23dB. This corresponds to a minimum modulation depth of 0.142. We expect that through careful design this can be substantially improved. At present, not all mechanisms that determine m_{min} are fully understood. It is believed that in addition to the detector noise and scattering from the crystal, the modulation depth is also limited by thermal effects in the material and shot noise arising from currents within the crystal.

Another important aspect of the correlator system is its sensitivity. This parameter is defined to be the minimum input signal to noise ratio that produces a detectable correlation peak. This parameter is also intrinsically related to the minimum detectable modulation depth, m_{min}. Given a reference signal $v_1(t) = as(t)$ and an input signal contaminated by additive white noise $v_2(t) = bs(t) + n(t)$, the modulation depth of the intensity incident on the crystal is

$$m = \frac{2ab|s(t)|^2}{(a^2 + b^2)|s(t)|^2 + |n(t)|^2}. \qquad [4.18]$$

The reference level, a, which maximizes m is given by

$$a_{opt} = \left(b^2 + \frac{|n(t)|^2}{|s(t)|^2}\right)^{1/2} = b\left(\frac{SNR+1}{SNR}\right)^{1/2}, \qquad [4.19]$$

resulting in an optimum modulation depth of

$$m_{opt} = \frac{b}{(b^2 + |n(t)|^2/|s(t)|^2)^{1/2}} = \left(\frac{SNR}{SNR+1}\right)^{1/2}. \qquad [4.20]$$

In practice, optimizing the reference level can easily be achieved by setting the power of the reference equal to the total average power of the input signal (*i.e.* setting $|v_1(t)|^2 = |v_2(t)|^2$). Thus for small input signal-to-noise ratios, the minimum input SNR that produces a detectable correlation peak at the output is

$$SNR_{min} \approx m_{min}^2. \qquad [4.21]$$

Using the minimum modulation depth experimentally derived above, the photorefractive time integrating correlator used in our experiment was predicted to have a sensitivity of -17dB. This value was verified by continuously adding noise to one of the system inputs while adjusting the reference to maximizes the output until the correlation peak in the diffracted output was no longer detectable.

IV.6 Conclusion

We have successfully implemented a time integrating correlator by utilizing a photorefractive crystal as the time integrating detector. This method has been shown to produce the magnitude square of the correlation signal without the bias

term inherent in a standard time integrating architecture . As a result, the absence of bias allows one to lengthen integration times thereby increasing the processing gain of the correlator. As mentioned in the PICOC chapter, photorefractive crystals (specifically BSO) suffer from both low diffraction efficiency and long writing time constants. In this application, we utilized the long writing times to an advantage allowing the construction of a correlator with extremely high processing gains. The system, however, is still plagued by low diffracted output intensities which are exacerbated when the input signals are contaminated by noise. Other crystals with higher electro-optic coefficiencts may be used in place of BSO to improve the diffraction of the photorefractive time integrating detector.

References for Chapter 4

1. R. A. Sprague and C. L. Koliopoulos, "Time Integrating Acousto-Optic Correlator", *Appl. Opt.*, **15** 89 (1976)

2. P. Kellman, "Time Integrating Optical Signal Processing", *Ph.D. Thesis*, Stanford University, 1979

3. N. V. Kukhtarev, V. B. Markov, S. G. Odulov, M. S. Soskin and V. L. Vinetskii, "Holographic Storage in Electro-optic Crystals: I. Steady State" *Ferroelectrics*, **22** 949 (1979)

4. K. Wagner "Time and Space Integrating Acousto-optical Signal Processing", *Ph.D. Thesis*, California Institute of Technology, 1987

5. D. Psaltis, "Incoherent Electro-optic Image Correlator", *Opt. Eng.*, **23** 12 (1984).

6. D. Psaltis and J. Hong, "Adaptive Acousto-optic Filter", *Appl. Opt.*, **23** 19 (1984).

V. CAPACITY OF OPTICAL CORRELATORS

V.1 The VanderLugt Optical Correlator

The VanderLugt correlator, shown in Figure 5.1 has been used extensively in optical processing systems. Among its uses are pattern recognition [3,4], associative memories [5,6], and holographic interconnections [7]. In its original implementation [1], the correlator was used to recognize a stored reference in an input image. In this original configuration, the Fourier transform of the reference image is recorded as a planar hologram. When an input image is presented to the correlator, the Fourier transform of the input is used to read out the recorded reference filter. The diffracted beam is then inverse Fourier transformed to produce the correlation between the input and the reference on the output plane. It can be shown that for an image contaminated by white noise, the VanderLugt correlator is the optimum filter to detect the image [2]. An experimental result obtained with a VanderLugt correlator is shown in Figure 5.2. In this experiment, the Fourier transform of the word GARNET is recorded on the planar hologram. When an input image containing many words is presented to the correlator, an output peak is produced wherever the word GARNET appears in the sentence.

In the system described above, the correlator is only required to produce a peak whenever the input is identical to the reference image. A more complex scenario would be to require the system to differentiate between two classes, each containing

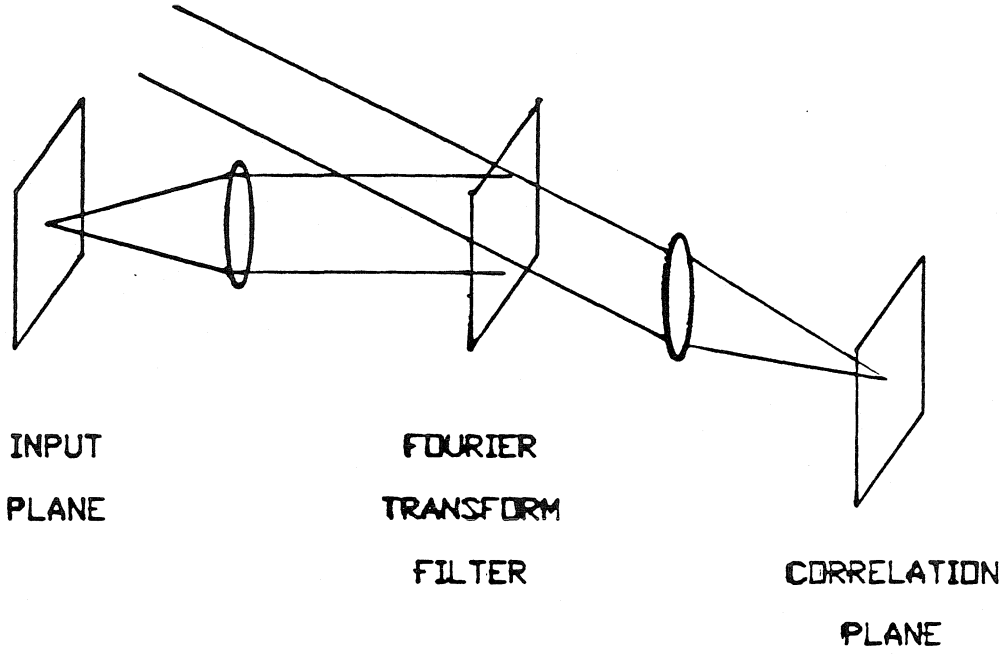

Fig. 5.1 Vander Lugt Correlator

a number of images. In this instance, we would like the correlator to produce a peak if the input image is a member of class I and no peak if it is a member of class II. The information of the images in each class is stored in some fashion in the hologram and the main problem is then to design a filter which accomplishes classification. A number of methods have been developed to perform this task [8-10]. One criterion which characterizes the efficiency of these systems is the capacity of the classifier, which henceforth will be denoted by M. M is defined to be the maximum number of

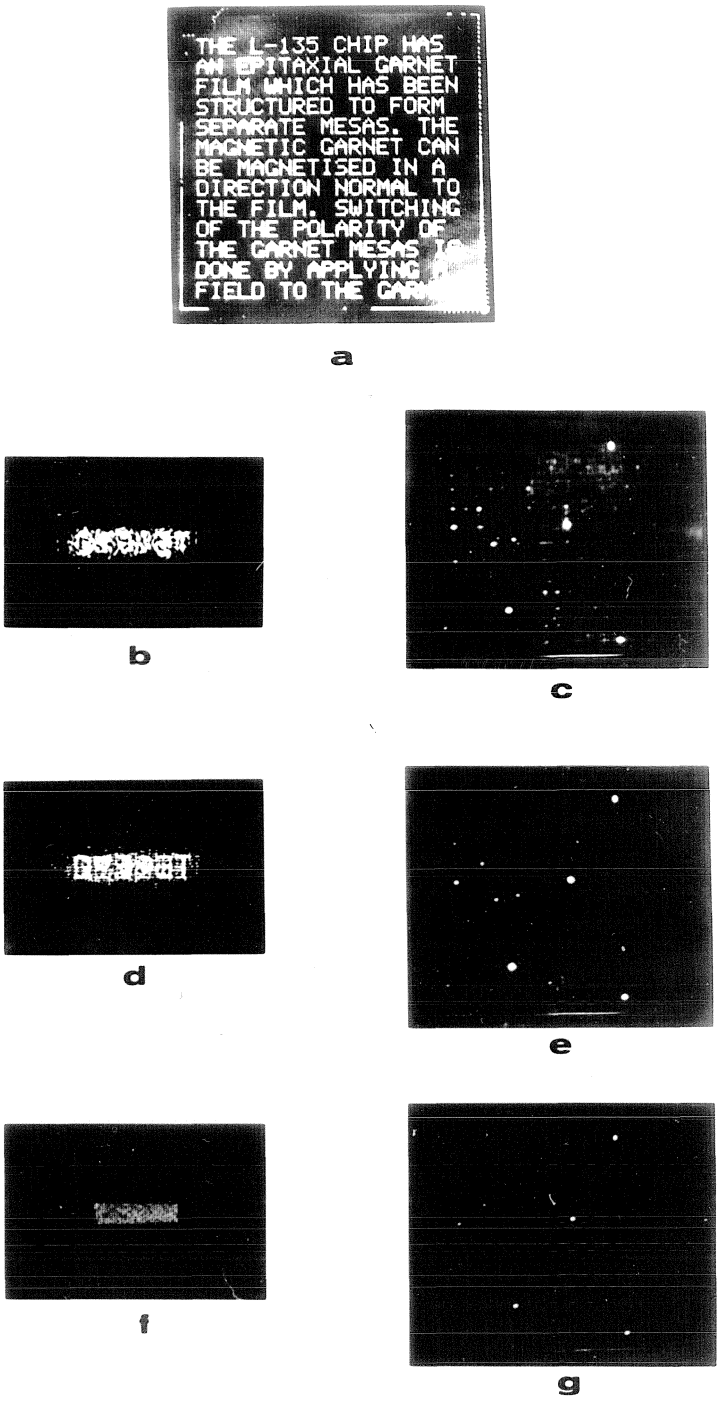

Fig.5.2 Example of a Correlation with a VanderLugt Correlator

images in each class that can be stored in one filter and still perform classification correctly. The capacity of a standard VanderLugt correlator will be addressed in the following section.

In the architecture described above, the reference filter used in perfoming the pattern classification is recorded on a planar medium. Aside from using a plane hologram, it is also possible to store information in a volume hologram, such as a photorefractive crystal. This has two distinct advantages. Firstly, the ability of the photorefractive material to record and erase holograms in real time allows one to update the filter quickly. As a result, the photorefractive crystal can be used to record reconfigurable filters necessary in adaptive or training systems [11]. Secondly, because a volume hologram uses all three dimensions to store information as opposed to only two by planar holograms, it is expected that the volume VanderLugt correlator will demonstrate an increase in storage capacity. However, because of the angular selectivity inherent in the readout of a volume hologram, this increase in capacity comes at the expense of the shift invariance inherent in a planar VanderLugt correlator. The effect of utilizing a volume hologram in a VanderLugt correlator is discussed in section V.3. The capacity of the volume VanderLugt correlator and the tradeoff between capacity and shift invariance is derived in section V.4.

V.2. Capacity of the Planar VanderLugt Correlator

V.2.1 Inner Product Architecture

A common method of performing pattern classification is to calculate the inner product between the input image $x_p(i,j)$ and a reference filter $h(i,j)$ [12,13]

$$y_p = \sum_{i=1}^{\sqrt{N}} \sum_{j=1}^{\sqrt{N}} x_p(i,j)h(i,j) \qquad [5.1]$$

where both $x(i,j)$ and $h(i,j)$ are composed of N pixels. Whether the resulting output y_p exceeds a preset threshold or not determines which class the input image x_p belongs to. This algorithm is easily implemented in a VanderLugt correlator. The correlation between the input image and the reference filter is formed, and the output y_p is determined by detecting the center of the correlation plane. This value is then electronically thresholded to determine the class of the input image.

The major difficulty in implementing this type of pattern classification system is the construction of the reference filter. A number of different methods have been developed to perform classification [8-10]. One simple method of achieving this is to form a linear combination of the images in both classes. Hence

$$h(i,j) = \sum_{p=1}^{M} w_p x_p(i,j). \qquad [5.2]$$

The linear weights w_p are usually found through some optimization or adaptive procedures such as the perceptron learning algorithm [14] or adeline [15] in order to achieve proper classification. The capacity of this system, M, is a well known result in pattern recognition and is given by

$$M = 2N \qquad [5.3]$$

where N is the total number of pixels in each image.

In this section we will consider the standard VanderLugt correlator with a planar hologram in the Fourier plane as a device to classify images. Instead of utilizing a learning algorithm, the filter is constructed by summing up all the images in class I, while ignoring those in class II. Hence,

$$h(x,y) = \sum_{p=1}^{M} w_p x_p(i,j)$$

$$w_i = \begin{cases} 1 & \text{if } \phi_i(x,y) \in \text{Class I} \\ 0 & \text{if } \phi_i(x,y) \in \text{Class II.} \end{cases} \qquad [5.4]$$

This method forms a much simpler reference filter which is easily implemented by exposing a hologram to the images in class I for an equal length of time.

To derive the capacity of this algorithm, let us consider a set of binary, bipolar images, composed of N distinct pixels, denoted by $x^p(i,j)$ $(i,j = 1...\sqrt{N},\ p = 1...2M)$ which may belong to one of two classes, I or II, each class being represented by M samples. The pixels $x^p(i,j)$'s are assumed to be independent, identically distributed random variables with

$$Pr[x^p(i,j) = 1] = Pr[x^p(i,j) = -1] = \frac{1}{2} \qquad [5.5]$$

and

$$Pr[x^p(i,j) = \alpha, x^q(k,l) = \beta] = Pr[x^p(i,j) = \alpha]Pr[x^q(k,l) = \beta]$$

$$\text{for all p} \neq \text{q, i} \neq \text{k, j} \neq \text{l.} \qquad [5.6]$$

We will first derive the capacity using this statistical model for the images to be stored when detection is performed only at the center of the correlation plane (*i.e.*, inner product architecture).

In the inner product architecture, the amplitude transmittance of the Fourier transform hologram in the VanderLugt correlator must be such that all the images that belong to class I produce a correlation peak at the output plane that is strong enough to exceed a predetermined threshold, while all the images in class II must produce a peak that does not exceed the threshold level.

We will calculate the probability that the correlator will misclassify an input image and through this determine the maximum number of images that can be recorded before a certain probability of error is exceeded. Let the input to the correlator be a member of class I. This will correlate with itself and produce a peak with expected value N, In addition, signals due to cross-correlations between the input image and the other images stored in the hologram will also be produced. This may cause errors in image classification. These cross correlation terms have an expected value of 0 and variance of $(M-1)N$ at the correlation peak, where M is the number of images in class II.

If the number of pixels is large and the statistics of the contribution of each pixel to the correlation peak is independent of all other pixels, the central limit theorem can be used to determine the output distribution. The proof of the inde-

pendence argument is presented in reference [16]. Using the theorem, the statistical distribution of the correlation peak approximates with a Gaussian function with mean N and variance $(M-1)N$. Since the threshold level is set to one-half the expected value of the peak, the probability of making an identification error for an input in class I at the center of the correlation plane is

$$\begin{aligned} Pr(y_I < th) &= \sqrt{\frac{2}{\pi}} \int_{-\infty}^{th=N/2} e^{-(x-N)^2/2MN} dx \\ &= \Phi\left(\frac{\sqrt{N}}{2\sqrt{M}}\right) \end{aligned} \qquad [5.7]$$

where Φ is the cumulative Gaussian function. We have also assumed that the number of stored states M is large enough that we can approximate $M-1$ by M. Likewise, if the input is a member of class B, the expected value of the output at the correlation peak will be 0 with variance also MN. Thus, the probability of making an error at the output in this case is also

$$Pr(y_{II} > th) = \Phi\left(\frac{\sqrt{N}}{2\sqrt{M}}\right). \qquad [5.8]$$

In order to derive an expression for the probability that the correlator performs correctly for all input images, it is necessary to show that the statistics of the correlation output due to one input image are independent of the output statistics resulting from other input images. In the limit that N and M become large, it has been proved that the output statistics for different input images become statistically independent [16]. Hence, the probability that the VanderLugt correlator produces

an error for any of the images of class I or II is

$$Pr(\text{Error}) = 1 - \left(1 - Pr(\text{error for one input})\right)^{2M} \qquad [5.9]$$

where the probability of an error for a single input is given by equation 5.8 and 5.9. If the desired probability of error is small, the cumulative Gaussian function can be approximated by its asymptotic form

$$\Phi\left(\frac{\sqrt{N}}{2\sqrt{M}}\right) \approx \frac{e^{-N/8M}}{\sqrt{2\pi}\sqrt{N}/4\sqrt{M}}. \qquad [5.10]$$

If the probability of error for each input is small, the probability of misclassification can be written as

$$Pr(\text{Error}) = 2M\frac{e^{-N/8M}}{\sqrt{2\pi}\sqrt{N}/4\sqrt{M}}. \qquad [5.11]$$

The number of images M can then be solved, giving a bound on the maximum number of images that can be stored in the correlator in order to achieve a desired probability of correct identification. This bound is given as the solution of the following transcendental equation:

$$M = \frac{N}{8log[M^{1.5}/N^{0.5}] + 8logk} \qquad [5.12]$$

where $k = [\sqrt{2\pi}/4]Pr(Error)$. Thus, equation 5.12 can be solved to determine the maximum M for which the correlator will classify inputs correctly with a probability of error no greater than $Pr(Error)$. In the limit that of large N, $log[M^{1.5}/N^{0.5}]$

approaches $logN$ and

$$M = \frac{N}{8logN} \qquad \text{as} \quad N \rightarrow \infty. \qquad [5.13]$$

It is interesting to note that the capacity derived for a simple multiple exposure hologram is less than the $2N$ capacity derived for an arbitrary linear discriminant function. However, this simpler method for constructing the reference filter results in a relatively modest loss in capacity of a factor $16logN$.

V.2.2 Shift Invariant Architecture

An important attribute of a VanderLugt correlator is the ability of the system to recognize shifted versions of the reference image. In order to utilize this shift invariant property in a VanderLugt classifier, detection of a correlation peak must be performed by thresholding over the entire output correlation plane. As a result, by determining the location of the correlation peak, one could determine not only whether the input is a member of a given class, but also whether it is a shifted version of a member of class I. In this situation, the classifying algorithm is given by the following correlation function

$$y_p(i,j) = \sum_{i'=1}^{\sqrt{N}} \sum_{j'=1}^{\sqrt{N}} h(i+i', j+j') x_p(i', j'). \qquad [5.14]$$

The effect of increasing the number of images stored in the reference hologram is demonstrated in Figure 5.3.

This figure shows the output at the correlation plane for $N = 256$ and and $M = 1$,3 and 6. From these figures, it is evident that for the case where only one

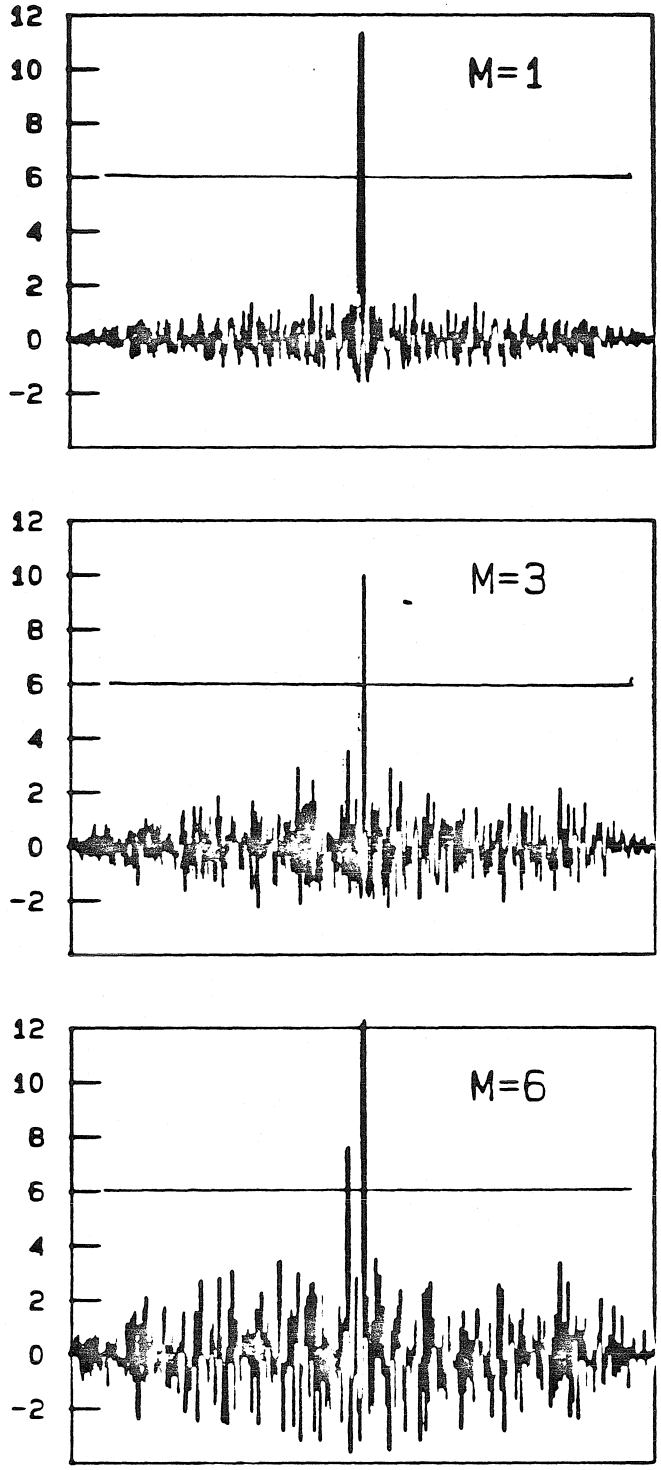

Fig. 5.3 Digital Correlations of a Shift Invariant Filter for N=256 and a) M =1, b) M= 3, and c) M 6

image is recorded in the reference filter, the input image correlates well with the reference, producing a single peak lying above the threshold. When the number of stored images is increased, the sidelobe level also increases. For the case of $M = 3$, even though the sidelobe level has significantly increased, only the correlation peak lies above the threshold value in this example. Hence, the classification of the input is still performed correctly. However, when the number of images is further increased to 6, two peaks now exceed the threshold level. As a result, the correlator will erroneously detect two shifted patterns and can no longer decide whether the input is simply a member of class I or a shifted version of class I.

The derivation of the capacity of the shift invariant VanderLugt correaltor is similar to that of the inner product algorithm derived above. In this situation, however, the probability of error will no longer by given by equation 5.8 and 5.9, but we must take into account the possibility that an output pixel other than the center of the correlation may be incorrect. In this case, by using the multivariate central limit theorem, it can be shown that as the number of pixels N^2 becomes large, the statistics of each output bit become independent of the other output bits [15]. Thus,

$$Pr(\text{error for one input}) = 1 - (1 - \Phi\left(\frac{\sqrt{N}}{2\sqrt{M}}\right)^{N^2}. \qquad [5.15]$$

In this system, we have chosen to restrict the output to an area of N by N pixels, as opposed to the (2N-1) by (2N-1) pixels needed to encompass the whole correlation

output. Since any shifted version of the stored images will produce peaks within this smaller area, the system will still be able to recognize all shifted versions of the images in class I.

Using equation 5.15 in equation 5.9, the probability that the VanderLugt system commits an error in any output bit for any input image to can be approximated by

$$Pr(\text{Error}) = 2MN\frac{e^{-N/8M}}{\sqrt{2\pi}\sqrt{N}/4\sqrt{M}} \qquad [5.16]$$

The number or images M that can now be stored is given by the following transcendental equation

$$M = \frac{N}{8logM^{1.5}N^{0.5} + 8logk} \qquad [5.17]$$

where k=$\sqrt{2\pi}/8$ Pr(Error). In the limit of large N, $N \rightarrow \infty$, the capacity becomes

$$M = \frac{N}{16logN}. \qquad [5.18]$$

Thus the capacity of the shift invariant system is decreased by only a factor of two from that of the non shift invariant system. It is important to point out that even though the shift invariant correlator can classify up to MN images (including their shifted forms), the capacity of the shift invariant correlator is not truly MN, since it is not possible to store MN arbitrary images. Rather, by choosing the first M images, the correlator predetermines all the other stored images to simply be the shifted versions of the original images. In the next section, we investigate the

consequences of using a volume hologram to store the Fourier transform filter. In particular, we will consider the loss of shift invariance introduced by the volume hologram and the ability of the correlator to perform multi-class categorization.

To verify the theoretical capacity of the correlator, 100 computer trials were averaged to determine the capacity for various N. For each trial, two random vectors were generated to form the initial reference filter. Each image was correlated to determine whether classification was performed correctly. If no error occured, a new random image was added to the reference filter and correlation with all the images was done. The number of images in the reference was increased until a misclassification occured. At this point, the capacity was said to be one less than the number of images stored in the reference. Figure 5.4 shows the capacity of both the peak only and shift invariant systems as a function of the number of pixels N in the image. Experimental simulations show good agreement with theoretical predictions. It is important to note that because the simulations were performed in the regime of small N, the transcendental equations for the capacity (Eqs. 5.12 and 5.17) were used to plot the theoretical curves.

V.3 The Volume VanderLugt Correlator

While a planar hologram uses only two dimensions to record information, a volume hologram utilizes all three dimensions for storage. It has been shown that this added dimension results in a large increase in the storage capacity of a volume

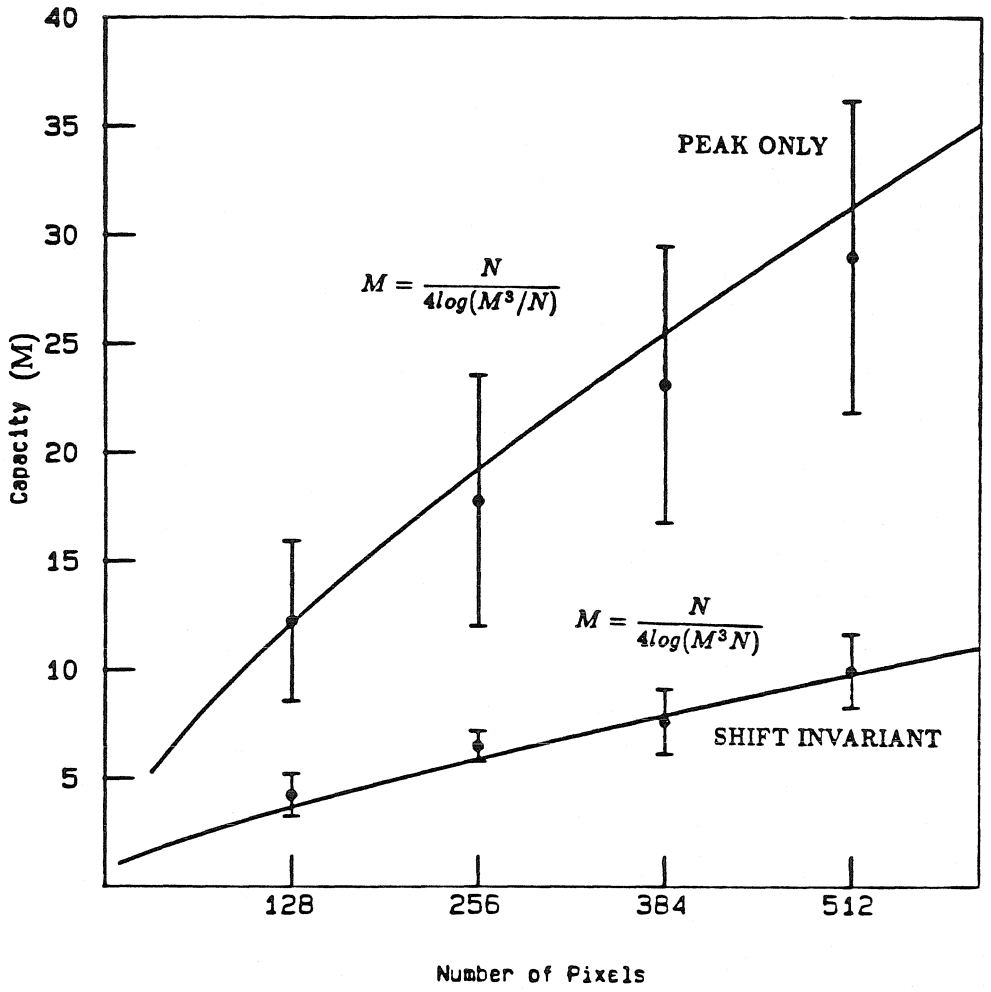

Fig. 5.4 Capacity Curves of the Peak Only and Shift Invariant Filters

hologram [16]. It is then expected that by incorporating a volume hologram in a VanderLugt system, the capacity of the correlator can be greatly increased. An immediate consequence of the gain in capacity is a loss of shift invariance associated with the angular selectivity of volume holograms.

Consider the correlation between two point sources in the volume VanderLugt correlator shown in Figure 5.5. During the recording process, a reference plane wave and the Fourier transform of the point source reference function, which is itself a plane wave are incident on the hologram. The two plane waves record a spatial grating in the hologram whose frequency and phase are determined by the position of the reference point source. When an input point source is presented to the correlator, the Fourier transform of the input, another plane wave, reads out the volume hologram to produce the correlation. If the input point source is perfectly aligned with the reference source, the readout plane wave will be perfectly Bragg matched with the grating recorded in the volume hologram. This will result in a diffracted plane wave which when inverse Fourier transformed will produce a correlation spot at the output plane. Now let the input point be shifted in a direction parallel to the plane of incidence, which is plane formed by the direction of the image and reference beams. If the amount of shift exceeds the Bragg angular bandwidth of the hologram, the readout plane wave will no longer diffract light and no correlation spot will be detected. In contrast to the planar case, shifts of the

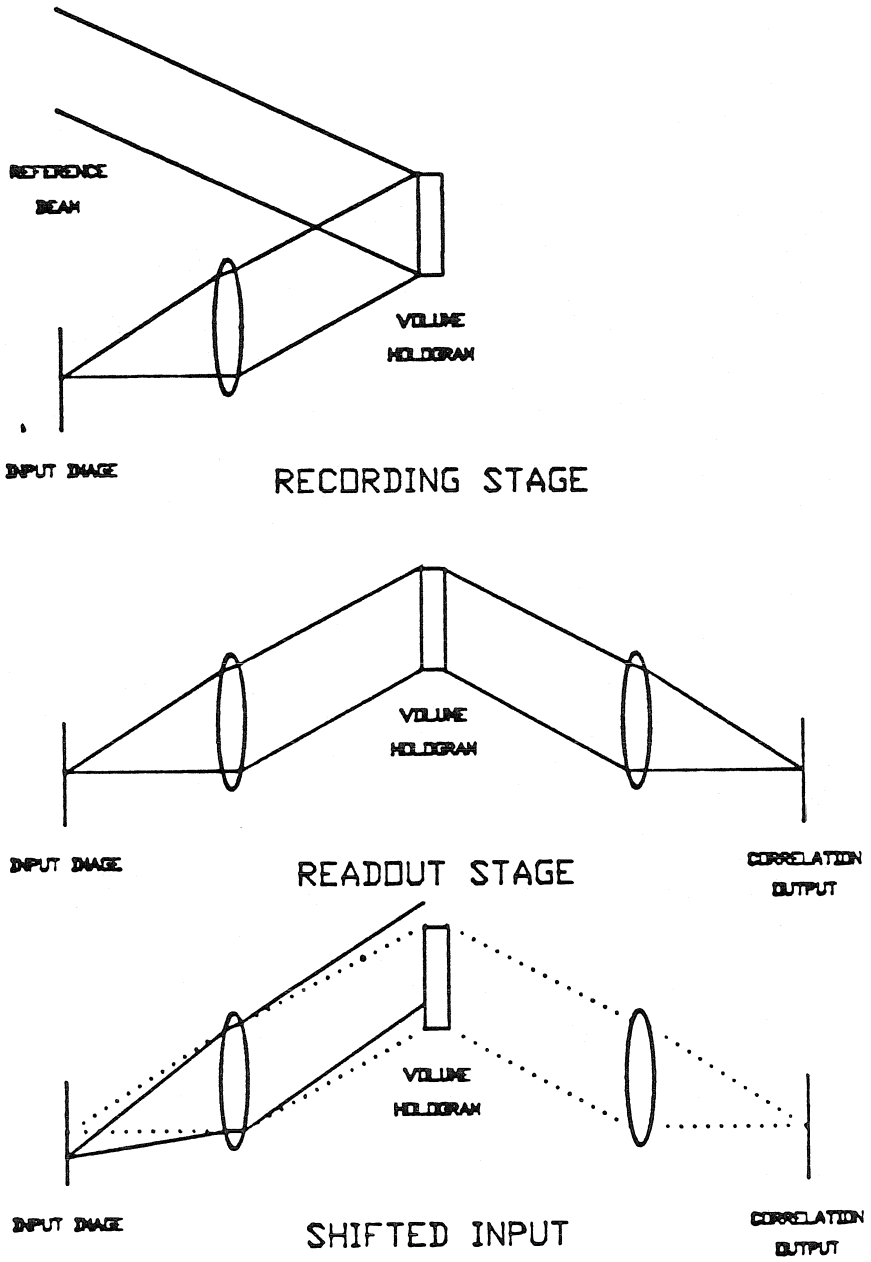

Fig. 5.5 Correlation Between Two Point Sources in a Volume VanderLugt Correlator

input in the direction parallel to the plane of incidence do not result in a shift of the correlation pattern, and shift invariance is lost. In the direction perpendicular to the plane of incidence, however, the volume hologram remains insensitive to angular deviations from the Bragg conditions.

In the next section, we will analyze the response of the volume VanderLugt correlator to an arbitrary input and reference image and derive the degree to which the shift invariant capabilities of the system are lost. Experimental demonstrations of the optical system will also be presented. The capacity of the volume VanderLugt correlator will be derived in section V.4. In addition, we will demonstrate that using a volume hologram to record a series of reference filters allows the correlator to be used as a multi-category classifier.

V.3.1 Mathematical Analysis

The basic difference between a standard VanderLugt correlator utilizing a plane hologram to store the Fourier transform filter, and the system which we wish to analyze, is the angular selectivity present in a volume hologram. In order to account for this property in volume holograms, we will analyze the effect of correlating arbitrary images with the aid of the k-space diagram.

Let us now examine the correlation of a recorded image A(x,y) with an input B(x,y). Each plane wave is represented by a vector in k-space with a length $2\pi/\lambda$ and oriented in the direction of propagation of the plane wave. The z direction

was chosen to coincide with the propagation direction of the reference beam (see Fig. 5.6). The optical axis forming the input arm of the VanderLugt correlator is at an angle θ with the reference beam. Hence, the k vector corresponding to the optical axis of the input arm is $\overrightarrow{a}_0 = k_{x0}\hat{x} + \sqrt{k_0^2 - k_{x0}^2}\hat{z}$, where $k_{x0}/k_0 = sin\theta$ and $k_0 = 2\pi/\lambda$. λ is the wavelength of the readout light.

$A(x,y)$ is placed at the input plane of the image arm as shown in Figure 5.6. The lens is essentially a Fourier transform lens, taking the light from each point at the input and mapping it into a plane wave at the output. The direction of this plane wave is determined by the position of the input point. Let us denote

$$\overrightarrow{k}_a = (k_{x0} + k_x)\hat{x} + k_y\hat{y} + \sqrt{(k_0^2 - (k_{x0} + k_x)^2 - k_y^2)}\hat{z} \qquad [5.19]$$

as the wavevector emitting from a point in the input space. $\hat{x}, \hat{y}$ and $\hat{z}$ are the unit vectors in the k_x, k_y and k_z directions, respectively and k_{x0} is the x component of the propagation direction of the input beam. The amplitude of each wavevector is

$$a(k_x, k_y) = A(-k_x\lambda F/2\pi, -k_y\lambda F/2\pi), \qquad [5.20]$$

where F is the focal length of the Fourier transform lens at the input end of the correlator.

In the recording process, these plane waves interfere with the reference plane wave to form a set of gratings in the volume medium. Let the reference wave be represented in k-space as a single vector of unit amplitude and direction

$$\overrightarrow{k}_r = k_0\hat{z}. \qquad [5.21]$$

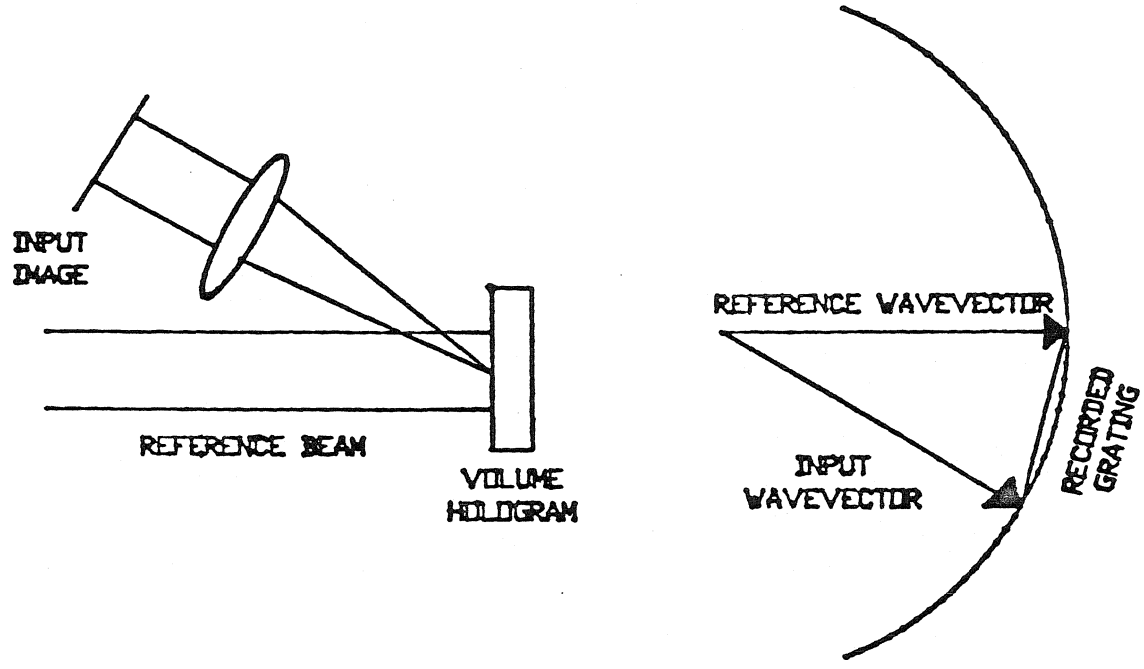

Fig. 5.6 Optical Set-up and Phase Matching Diagram for the Volume Vander Lugt Correlator

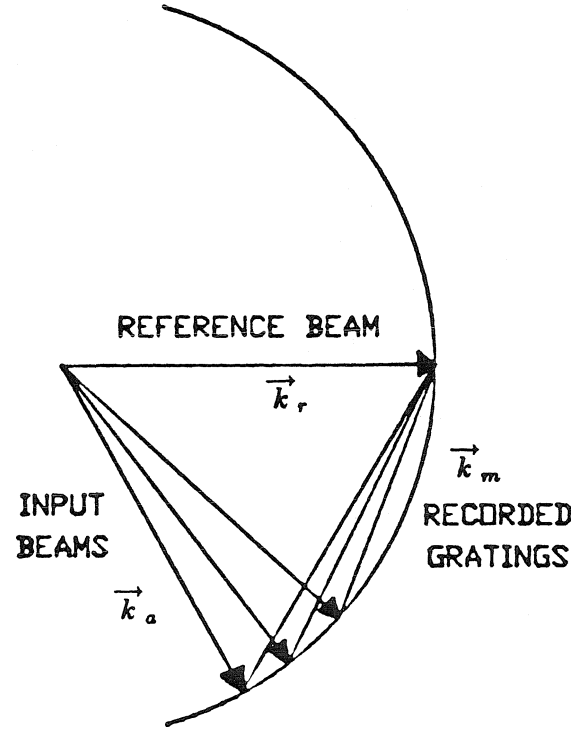

Fig. 5.7 Phase Matching Diagram of the Recording Process in a Volume VanderLugt Correlator

This recording process is described in Figure 5.7, which shows another two dimensional slice of the equiphase sphere containing the reference wave and the corresponding gratings. These grating vectors stored in the volume hologram have a direction given by

$$\begin{aligned}\vec{k}_m &= \vec{k}_r - \vec{k}_a \\ &= -(k_{x0}+k_x)\hat{x} - k_y\hat{y} + (k_0 - \sqrt{k_0^2 - (k_{x0}+k_x)^2 - k_y^2})\hat{z}.\end{aligned} \quad [5.22]$$

For a grating recorded in a photorefractive medium, the induced index change is proportional to the modulation depth of the fringes that are being recorded. The amplitude of the index grating vector $m(k_x, k_y)$

$$m(k_x, k_y) = \frac{Ga(k_x, k_y)}{1 + |A(x,y)|^2} \quad [5.23]$$

where G is a constant relating the relationship between the modulation depth of the incident grating and the actual induced refractive index change. If the total intensity due to the input image is relatively constant over the area of the crystal and much less than the intensity of the reference wave, the stored grating strength can be approximated by

$$m(k_x, k_y) \approx Ga(k_x, k_y). \quad [5.24]$$

Consequently, the resulting index change change is linearly proportional to the plane wave component of the image $A(x, y)$.

To perform a correlation, a new image B(x,y) is placed at the input of the correlator and reads out the stored hologram, as shown in Figure 5.8. The resulting

diffracted light diffracted light propagates through the inverse Fourier transform lens to produce the output correlation. In k-space, this corresponds to a new set of plane waves due to the image B(x,y) attempting to read out the stored gratings $m(k_x, k_y)$. This new set of plane waves have amplitude

$$b(k'_x, k'_y) = B\left(-\frac{k'_x \lambda F}{2\pi}, -\frac{k'_y \lambda F}{2\pi}\right) \qquad [5.25]$$

and propagation direction

$$\overrightarrow{k}_b = (k_{x0} + k'_x)\hat{x} + k'_y\hat{y} + (\sqrt{k_0^2 - (k_{x0} + k'_x)^2 - k'^2_y})\hat{z}. \qquad [5.26]$$

In this case, it is assumed that the optical axis of the readout image $B(x, y)$ is identical to the optical axis of the recording image $A(x, y)$ and is given by $k_{x0}\hat{x} + \sqrt{k_0^2 - k_{x0}^2}\hat{z}$.

When an new input image B(x,y) reads out the stored gratings, a new set of wavevectors $\overrightarrow{k}_c$ will be formed as shown in Fig.[5.8], where

$$\begin{aligned} \overrightarrow{k}_c &= \overrightarrow{k}_b + \overrightarrow{k}_m \\ &= k''_x\hat{x} + k''_y\hat{+}\sqrt{k_0^2 - (k_{x0} + k_x)^2 - k_y^2} \\ &+ \sqrt{k_0^2 - (k_{x0} + k_x + k''_x)^2 - (k_y + k''_y)^2} - k_0 \end{aligned} \qquad [5.27]$$

As shown in Figure 5.9, each vector $\overrightarrow{k}_c$ will contribute to the diffracted beam, $\overrightarrow{k}_d$ by an amount dependent on the amplitude strength of $\overrightarrow{k}_c$ and attenuated by

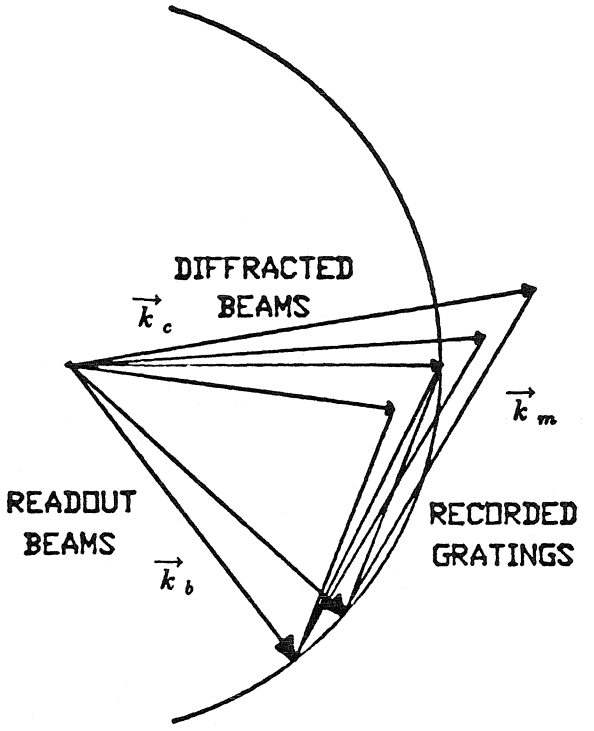

Fig. 5.8 Phase Matching Diagram of the Readout Process in a Volume VanderLugt Correlator .

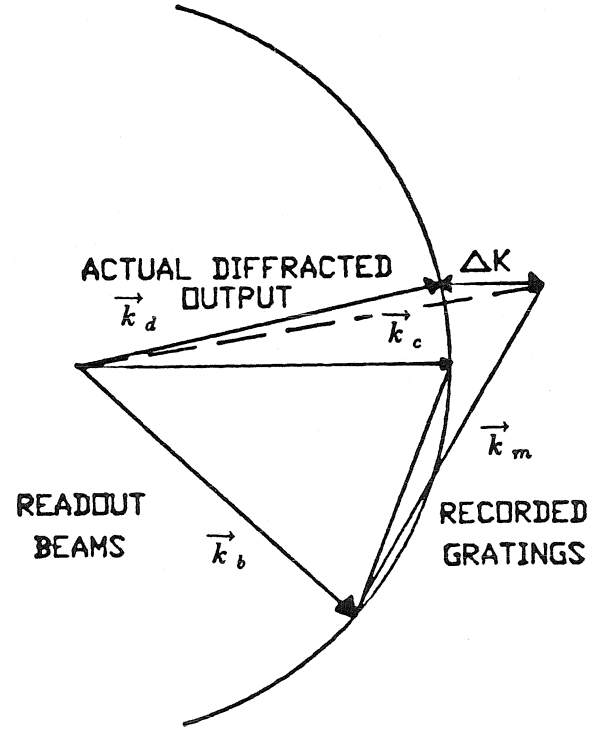

Fig. 5.9 Determination of Δk in the Volume VanderLugt Correlator

the amount of Bragg mismatch Δk, where

$$\begin{aligned}\Delta k &= \vec{k}_d - \vec{k}_c \\ &= (k_0 - \sqrt{k_0^2 - k_x''^2 - k_y''^2} - \sqrt{k_0^2 - (k_{x0} + k_x)^2 - k_y^2} + \\ &\sqrt{k_0^2 - (k_{x0} + k_x + k_x'')^2 - (k_y + k_y'')^2})\hat{z}.\end{aligned} \qquad [5.28]$$

In this expression for Δk, we have assumed a volume hologram which has infinite transverse area and a finite thickness in the z direction. Consequently, the direction of the phase mismatch $\Delta \vec{k}$ also lies in the z direction. Under the assumption that the diffraction efficiency of each diffracted component is small, the strength of the diffracted wavevectors can be approximated by [17]

$$d(k_x'', k_y'') = \int\int b(k_x''+k_x, k_y''+k_y) Ga(k_x, k_y) e^{i|\Delta k(k_x,k_y)|L/2} sinc[|\Delta k(k_x, k_y)L|/2] dk_x, d_y \qquad [5.29]$$

where L is the thickness of the crystal. If the recording angle is large and the spatial extent of the input and output images small, then $k_0, k_{x0} >> k_x, k_y, k_x'', k_y''$. The expression for Δk can then be approximated by the first term of a Taylor expansion:

$$\Delta k = \frac{k_{x0} k_x''}{\sqrt{k_0^2 - k_{x0}^2}}. \qquad [5.30]$$

In this case, the amount of Bragg mismatch Δk becomes independent of the integrating variables k_x and k_y. This results from the approximation that the wavevectors $\vec{k}_a$ and $\vec{k}_b$ lie on a small portion of the equiphase circle which can be approximated

by a straight line in k-space. Hence, $d(k_x'', k_y'')$ can be rewritten as

$$\begin{aligned} d(k_x'', k_y'') &= \int\int a(k_x, k_y) b(k_x'' + k_x, k_y'' + k_y) sinc(\alpha k_x'') exp(i\alpha k_x'') dk_x dk_y \\ &= [a * b](k_x'', k_y'') sinc(\alpha k_x'') exp(i\alpha k_x'') \end{aligned} \quad [5.33]$$

where

$$\alpha = \frac{k_{x0} L}{2\sqrt{k_0^2 - k_{x0}^2}} = L \tan\theta. \quad [5.34]$$

$*$ is the correlation operator and θ is the recording angle between the reference beam and the input images. The resulting output pattern is

$$D(x,y) = \left[A * B(\frac{F_1}{F_2}x, \frac{F_1}{F_2}y) \right] sinc\left[\frac{2\pi\alpha x}{\lambda F_2} \right] exp(i\frac{2\pi\alpha x}{\lambda F_2}) \quad [5.35]$$

where F_2 is the focal length of the inverse Fourier transform lens.

The output intensity is then

$$|D(x,y)|^2 = \left| A * B(\frac{F_1}{F_2}x, \frac{F_1}{F_2}y) \right|^2 sinc^2\left[\frac{2\pi\alpha x}{\lambda F_2} \right]. \quad [5.36]$$

The output diffracted intensity pattern will then be composed of the standard two dimensional correlation pattern with a demagnification factor of F_2/F_1 and which is apodized by a sinc function with width given by

$$W_{apod} = \frac{\lambda F_2}{\alpha}. \quad [5.37]$$

One consequence of using a volume hologram in a Vander Lugt correlator is the loss of shift invariance. In a typical image detection scheme, a set of inputs are

correlated sequentially with a reference image. The output of the correlator is then thresholded to determine whether the input image matches a stored reference. In a standard Vander Lugt correlator any shifts of the input will result in a corresponding shift of the correlation pattern at the output. Recognition and position of shifted forms of the image can then be made by thresholding the entire correlation plane and locating the correlation peak. In the case of the volume VanderLugt correlator, only a portion of the correlation image is produced at the output. If the input is shifted in a direction parallel to the plane of incidence the correlation peak can be shifted outside the correlation band of the system. As a result, shifted inputs which indeed match with the reference image will not produce a correlation peak at the output and, therefore, they will not be recognized.

In the direction perpendicular to the plane of incidence, the shifts in the input will produce correlation peaks which shift within the output correlation band. Consequenty, the system will be able to recognize images which are shifted only in this particular direction. Because of the assumptions made in deriving equation 5.36, the apodizing sinc envelope has no dependence in the direction perpendicular to the plane of incidence (y direction). In reality, the diffracted output is also attenuated in this direction, although to a much smaller degree than in the parallel direction. To estimate the size of this envelope, let us consider the correlation of an arbitrary image $A(x, y)$ with a point source $B(0, 0)$. In addition, we will analyze the envelope

only along the x = 0 axis of the output plane. As a result of these assumptions, we can set $k_x = k_x'' = 0$ and the equation for Δk,the Bragg mismatch (Eq. 5.28) becomes

$$\Delta k = k_0 - \sqrt{k_0^2 - k_y''^2} - \sqrt{k_0^2 - k_{x0}^2 - k_y^2} + \sqrt{k_0^2 - k_{x0}^2 - (k_y + k_y'')^2}. \qquad [5.38]$$

For $k_y, k_y'' << k_0, k_{x0}$, this equation simplifies to

$$\Delta k = \frac{k_y''^2}{2k_0} + \frac{k_y''^2}{2\sqrt{k_0^2 - k_{x0}^2}} - \frac{k_y k_y''}{\sqrt{k_0^2 - k_{x0}^2}}. \qquad [5.39]$$

When this expression is substituted in equation 5.31, and the fact that the input image consists of a point source is used, the diffracted field becomes

$$D(0,y) = A(0, \frac{F_2}{F_1}y) sinc[\frac{2\pi\beta y^2}{\lambda F_2}] exp[i\frac{2\pi\beta y^2}{\lambda F_2}] \qquad [5.40]$$

where

$$\beta = L\left[\frac{1}{k_0} + \frac{1}{\sqrt{k_0^2 - k_{x0}^2}}\right]. \qquad [5.41]$$

The expected height of the correlation band in the direction perpendicular to the plane of incidence is

$$\text{Height} = \frac{\lambda F_2}{\sqrt{\beta}} \qquad [5.42]$$

In general, the height of the correlation band will be much larger than its width. For example, in a system with F = 50cm, λ = 633nm, L = 1mm, and a Bragg angle of 30°, the height of the correlation band is found to be 21.4 mm, while its width is only 0.54 mm.

V.3.2 Experimental Results

To verify the basic operational characteristics of the volume VanderLugt correlator that we predicted, an autocorrelation of an "O" was performed. An iron-doped lithium niobate crystal was used to record the Fourier transform volume hologram. The crystal dimensions were 25 x 25 x 5 mm and was oriented such that the $< 001 >$ axis was parallel to the plane of incidence. The Fourier transform holograms were recorded by interfering the Fourier transform of an image with a reference plane wave. Exposure times ranged from 30 - 60 seconds at a reference intensity of $1 mW/cm^2$. The gratings were then read out with the Fourier transform of a second image producing the correlation at the output plane.

Figure 5.10 shows a computer simulation of the autocorrelation of an O. This is the expected output of the correlator if the reference O had been recorded on a plane hologram.

Figure 5.11a shows the optically generated autocorrelation of an O with the volume VanderLugt correlator described above utilized to perform the correlation. As expected, only the portion of the correlation pattern which lies within the correlation band is visible. As mentioned previously, by shifting the input image parallel to the plane of incidence, different portions of the correlation function can be read out. Figures 5.11b and 5.11c show the correlation of an O with its shifted form showing other sections of the autocorrelation funciton of the object. It is interest-

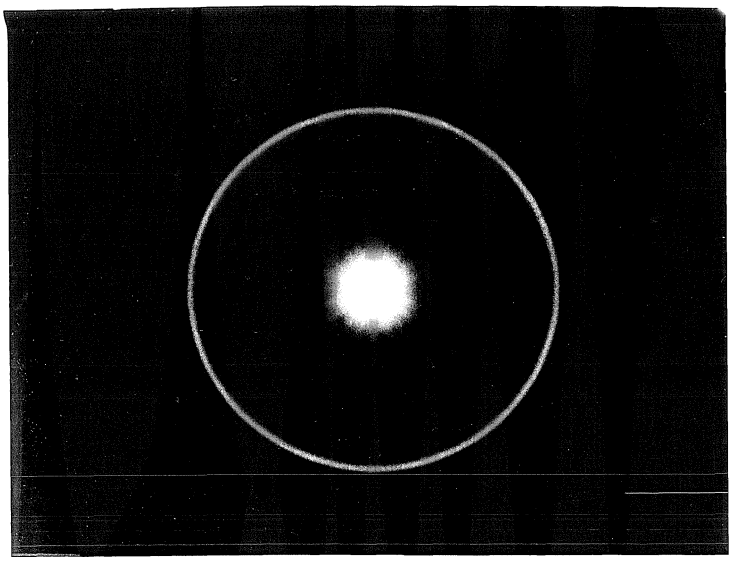

Fig. 5.10 Autocorrelation of an O

ing to note that the reconstruction shown in Figure 5.11b shows a relatively bright dot which lies outside the correlation band. This corresponds to the very bright DC peak lying in the second lobe of the sinc function which multiplies the correlation function.

In the above experiment, a primary Fourier transform lens of focal length 26 cm was used. By increasing the focal length of the primary lens, it is expected that the size of the correlation would decrease and as a result a larger portion of the correlation function would lie within the correlation band. Figure 5.12 shows the

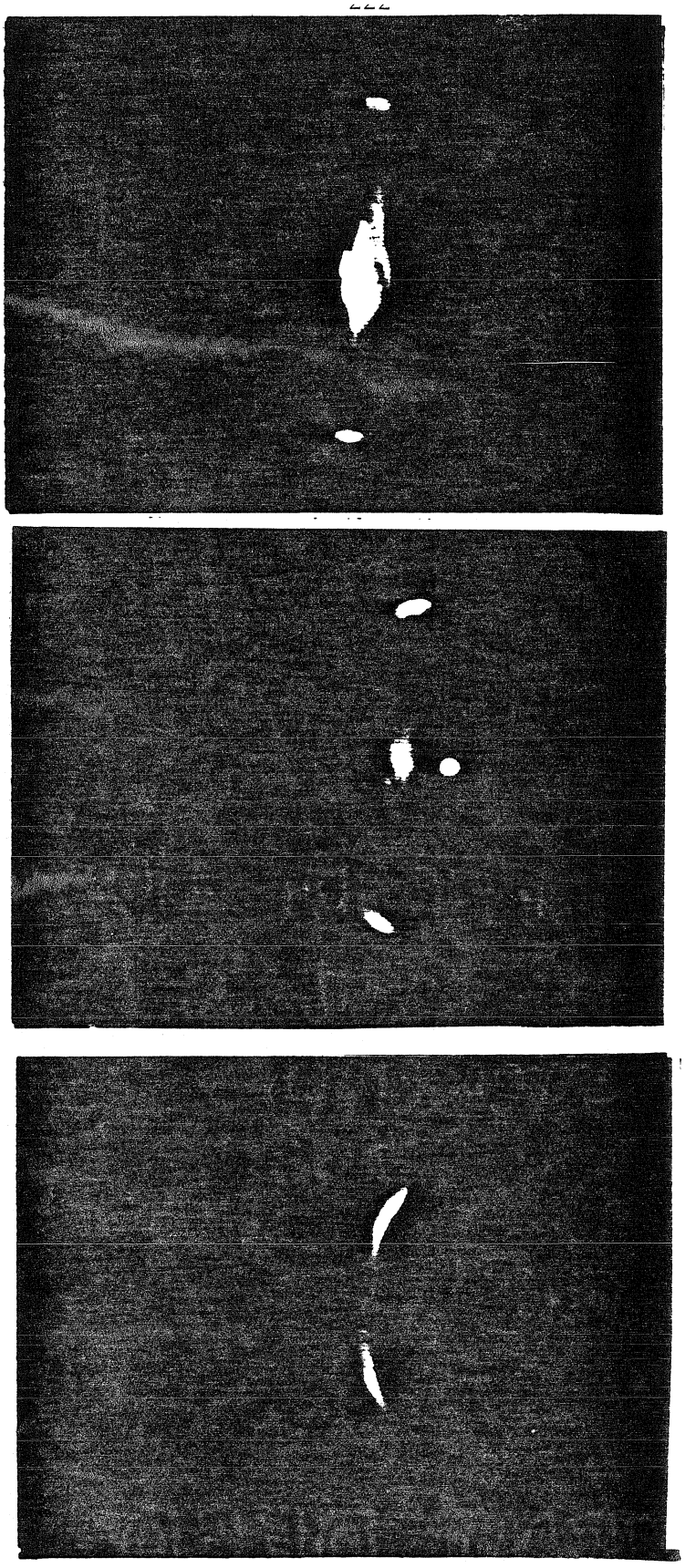

Fig. 5.11 Experimental Outputs of the Autocorrelation of an O Using a Volume VanderLugt Correlator (F_2 = 26cm)

autocorrelation of an O when a primary lens with a focal length of 60 cm is used. In this case, the autocorrelation remains the same, but the portion which is presented at the output has increased. This effect can also be achieved by decreasing the thickness of the crystal.

V.4 Capacity of Volume VanderLugt Correlators

The angular selectivity of the volume holographic recording medium results in a loss of shift invariance as demonstrated in the previous section. This characteristic, however, results in an increase in the capacity of the system, as well as a multi-class descrimination capability [18].

In the typical volume VanderLugt correlator architecture (Fig. 5.13a), a series of filters are recorded on the volume hologram. Each filter will be constructed by interfering the Fourier transform of a reference image with a plane wave at a given angle. Subsequent filters are recorded by interfering each filter with reference beams incident at different angles, each separated by at least the angular bandwidth of the hologram. Because of the Bragg selectivity of the volume hologram, an input image will correlate with all the recorded filters and produce correlation slits which are spatially separated on the output correlation plane (Fig. 5.13b). Each filter can then be used as a discriminator to classify its own class of images. As a result, by determining which slit the correlation peak focuses on, one could simultaneously determine to which of the many classes recorded in the volume hologram the input

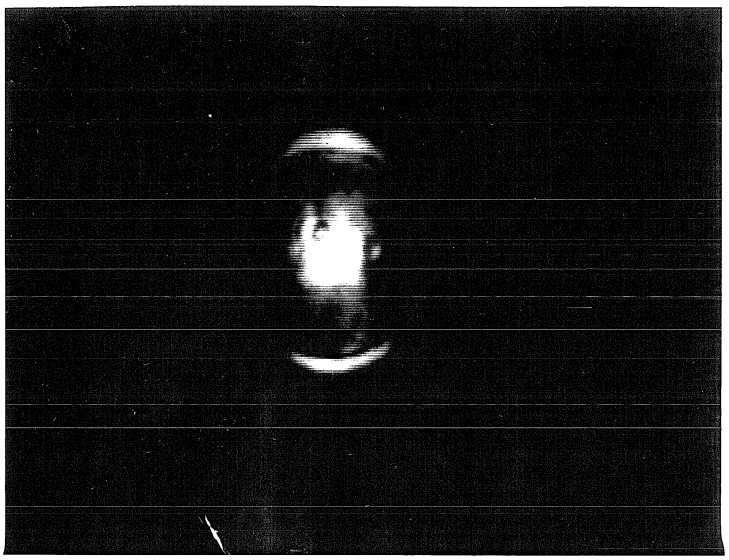

Fig. 5.12 Autocorrelation of an O Using a Volume VanderLugt Correlator (F_2 = 60cm)

image belonged.

Let us now consider the capacity of the volume VanderLugt correlator. If the output of the correlator is still restricted to be NxN pixels, then the total number of filters K that can be stored will be limited by the number of correlation bands which can be fitted in the output correlation plane. This number is given by

$$K = \frac{TLtan\theta}{\lambda F} \qquad [5.43]$$

where L is the dimension of the correlation plane parallel to the plane of incidence and T is the thickness of the hologram. Let us assume that K different filters can be recorded in the volume hologram without cross talk. We will now determine the maximum number of images that can be stored in each of the K classes to achieve a desired probabilty of correct identification. Assume again that the input images consist of randomly chosen, independent, identically distributed, bipolar pixels. Since each of the filters is recorded independently of all the others and each filter does not produce an output away from its respective correlation band, we will first consider the effect of storing multiple images in one of the K filters. For the remainder of the paper we refer to each of these filters and its corresponding correlation output as an output channel. The purpose of the filter corresponding to one output channel is to separate a set of M images belonging to the class it wants to recognize from the images of all the other members of the K-1 classes recognized by the other channels. Let $y_i^{(\gamma)(\beta)}$ be the value at the ith pixel position for the

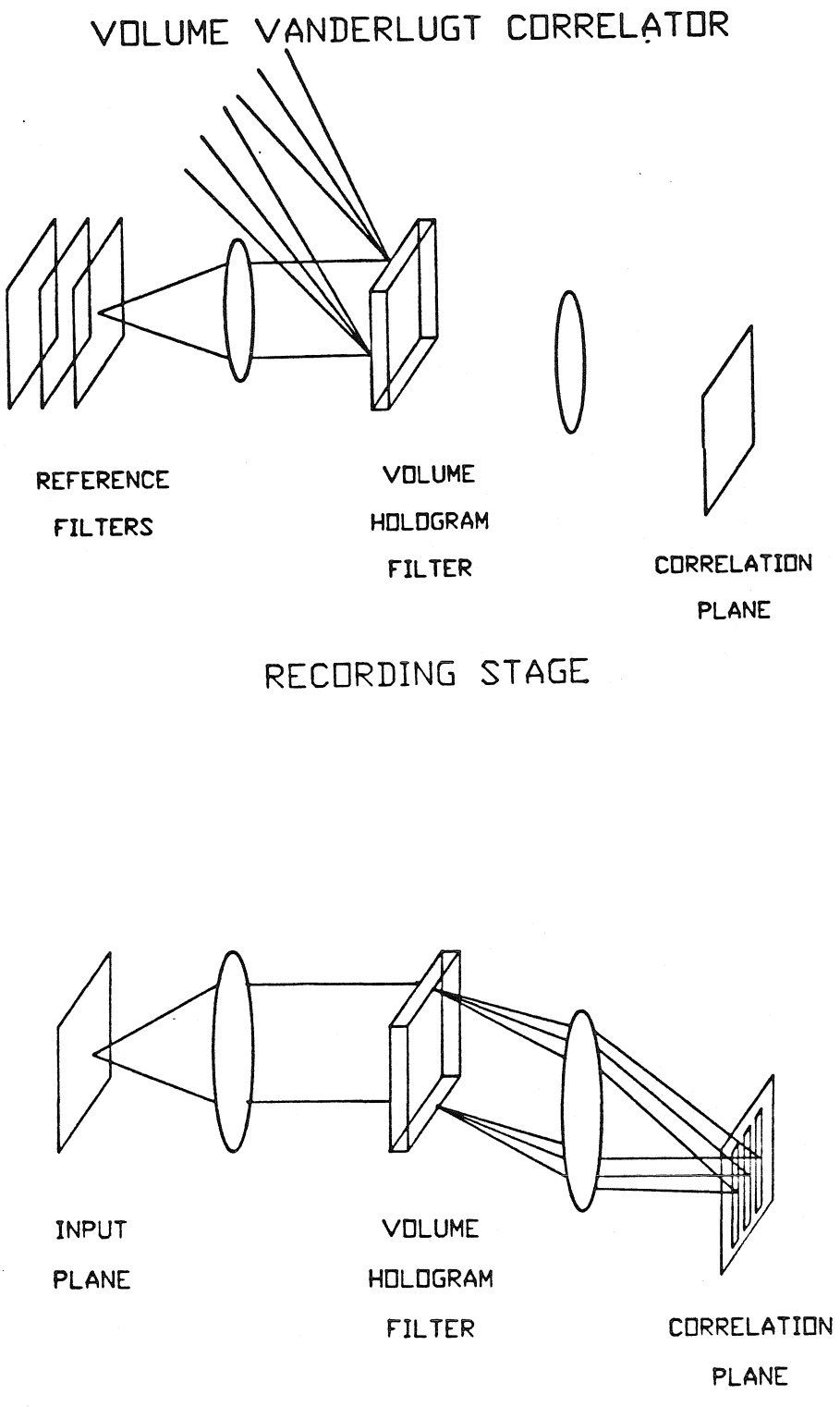

Fig. 5.13 Multi-class Categorization Using a Volume VanderLugt Correlator: a) Recording Stage and b) Readout Stage.

γth input and the βth output channel. In addition, let us again assume that the threshold is set to one half the value of the expected value of a correlation peak, $N/2$. The probability of error for a random input is

$$Pr(y_0^{(\gamma)(\beta)} < th) = Pr(y_i^{(\gamma)(\beta)} > th) = \Phi\left(\frac{\sqrt{N}}{2\sqrt{M}}\right), \qquad i \neq 0. \qquad [5.44]$$

Since the N by N pixels in the output correlation plane is subdivided into K distinct output channels, each band will consists of only N/K output bits. Through the use of the multivariate central limit theorem, the statistics of each N/K output pixel can be shown to be independent of other output bits in the same correlation band [15]. Likewise, the statistics of each correlation output for one input image is independent of the output statistics resulting from other inputs. Assuming that each channel wishes to recognize a class consisting of M images, it is necessary to consider all KM images to determine whether an error occurs in a single channel. Hence, the probability that an error occurs in one of the output channels is

$$Pr(\text{Error in one channel}) = 1 - \left[1 - \Phi\left(\frac{\sqrt{N}}{2\sqrt{M}}\right)\right]^{\frac{N}{K}KM}. \qquad [5.45]$$

Since the statistics of each output channel are independent of other channels, the probability that an error occurs in any channel of the volume VanderLugt correlator is given by

$$Pr(\text{Error}) = 1 - (1 - Pr(\text{Error in one channel})^K. \qquad [5.46]$$

By using the asymptotic form for the cumulative Gaussian function and assuming a small probability of error, equation 5.47 can be approximated by

$$Pr(\text{Error}) = MN^2K\frac{e^{N/8M}}{\sqrt{2\pi}\sqrt{N}/4\sqrt{M}}. \qquad [5.47]$$

Hence, the maximum number of images that can be stored in one output channel is bounded by

$$M = \frac{N}{16logNM^3K + 4log\delta} \qquad [5.48]$$

where $\delta = \sqrt{2\pi}Pr(Error)/K$. In the the limit that $N \rightarrow \infty$, the capacity of each channel approaches

$$M = \frac{N}{16logN + 4logK} \qquad N \rightarrow \infty \qquad [5.49]$$

where K is given by equation 5.44. It is interesting to note that for a crystal of finite thickness (ie K constant), the capacity obtained for one channel of the volume correlator is equivalent to that obtained for the plane hologram correlator (Eqn. 5.18). Hence, the total number of images that can be stored in the volume correlator will be asymptotically bounded by

$$M_{total} = KM = \frac{KN}{16logN} \qquad ([5.50]$$

or K times the capacity of a planar hologram.

V.5 Conclusion

Photorefractive crystals can be used to record volume holograms as the storage medium in a VanderLugt correlator. We have shown that this implementation results in an increase in the capacity of the correlator, when used as a pattern classifier, at the expense of the shift invariance properties characteristic of a planar VanderLugt correlator. In addition, we have demonstrated that by utilizing a volume hologram, multi-class classification can occur simultaneously. The ability of a photorefractive medium also allows one to reconfigure the filter that is recorded in the crystal to adapt to changes in the pattern recognition environment. In addition, the ability to grow extremely thick crystals (up to 1cm) allows one to distinguish between an extremely large number of classes. In the volume VanderLugt correlator architecture described above, a filter for one class is recorded by interference with a single reference plane wave. Subsequent filters are recorded sequentially by exposing the hologram to a filter-reference plane wave pair. The major problem in this implementation is that the hologram is subjected to a large number of exposures which may degrade the quatlity of the output image. In particular, photorefractive crystals with an erasure time on the same order as the write time can only record a limited number of holograms before erasure of holograms written earlier begins to occur.

Studies have been made to determine the maximum number of exposures a photorefractive crystal can record and the optimum exposure schedule that will

result in holograms of equal strength [20]. In addition, it has been shown that through fixing techniques the number of exposures can be significantly increased at the expense of reconfigurability.

References for Chapter 5

1. A. VanderLugt, "Signal Detection by Complex Spatial Filtering", *IEEE Trans Inf Th*, **IT-10**, 139 (1964).
2. J. M. Wozencraft and I. M. Jacobs, *Principles of Communication Engineering*, Wiley and Sons, New York (1965).
3. A. W. Lohmann and D. P. Paris, "Computer Generated Spatial Filters for Coherent Optical Data Processing", *Appl. Opt.*, **7**, 651 (1968).
4. D. Casasent and D. Psaltis, "Scale Invariant Optical Correlation Using Mellin Transforms", *Opt. Comm.*, **17**, 59 (1976).
5. E. Paek and D. Psaltis, "Optical Associative Memory using Fourier Transform Holograms", *Opt. Eng.*, **26**, 428 (1987).
6. D. Gabor, "Associative Holographic Memories", *IBM Jour. Res. Devel.*, **13**, 156 (1969).
7. X. G. Gu, D. Psaltis, J. Yu and H. Lee *to be published*
8. B. Braunecker, R. Hauck and A. W. Lohmann, "Optical Character Recognition Based on Nonredundant Correlation Measurements", *Appl. Opt.*, **18**, 2746 (1979).
9. H. J. Caulfield, "Linear Combinations of Filters for Character Recognition: A Unified Treatment", *Appl. Opt.*, **19**, 3877 (1980).
10. D. Casasent, "Unified Synthetic Discriminant Function: Computational For-

mulation", *Appl. Opt.*, **23**, 1620 (1984).

11. F. Rossenblatt, '*Principles of Neurodynamics: Perceptrons and the Theory of Brain Mechanisms* Spartan Books, Washington D.C., (1961).

12. J. Hong, "Optical Computing for Adaptive Signal Processing and Associative Memories", *Ph.D Dissertation*, California Institute of Technology (1987).

13. T. Cover, "Geometrical and Statistical Properties of Systems of Linear Inequalities with Applications in Pattern Recognition", *IEEE Trans. Elec. Comp.*, **EC-14**, 326 (1965).

14. B. Widrow and M. E. Hoff, "Adaptive Switching Circuits", *1960 IRE WESCON Conv. Rec.*, Part 4, 96-104 (August 1960).

15. F. Mok, "Binary Filters for Optical Computing and Pattern Recognition", *Ph. D. Dissertation*, California Institute of Technology, June 1988.

16. P. J. van Heerden, "Theory of Optical Information Storage in Solids", *Appl. Opt.*, **2**, 393 (1963).

17. H. Kogelnik, "Coupled Wave Theory for Thick Hologram Gratings", *Bell Sys. Tech. Jour.*, **48**, 2909 (1969).

18. C. Guest and C. Gaylord, "Truth Table Lookup Optical Processor Using Binary and Residue Arithmetic", *Appl. Opt.*, **19**, 201 (1983).

19. J. Yu, F. Mok and D. Psaltis, "Capacity of Optical Correlators", *SPIE*, **825-22** (1987).